Evaluation and development of the zone method for modelling metal heating furnaces

Thesis

EVALUATION AND DEVELOPMENT OF THE ZONE METHOD FOR MODELLING METAL HEATING FURNACES

by

Robert James Tucker B.Sc(Hons),M.Sc,M.Inst.Energy

Thesis submitted for the degree of

Doctor of Philosophy

Faculty of Technology

Open University

March 1990

Date of submission: 19th February 1990
Date of award : 2nd July 1990

The Open University,

PO Box 49,

Milton Keynes,

MK7 6AD

To

Hilary

Edward and *William*

ABSTRACT

The zone method of radiation analysis in hot enclosures has been widely applied to the modelling of industrial fuel-fired plant. Many of these models apply a single zone or a longitudinal series of zones (a long furnace model) to represent the hot enclosure. In the latter case, radiation interchange between zones is often ignored in order to reduce the number of geometric exchange areas that must be calculated. If radiation interchange is included, the furnace is often represented as a simple rectangular or cylindrical enclosure in order to facilitate the calculation of these exchange areas. Furthermore, most models only simulate plant operating under steady-state thermal conditions.

In this study, both steady-state and transient long furnace models have been developed which are capable of simulating some of the typical geometries used for metal heating applications. For this purpose, a Monte-Carlo technique has been applied to calculate the radiation exchange areas. Exchange areas calculated by this technique, are compared to those obtained by more accurate numerical integration. Although large errors can occur for some zone pairs, the effect of these errors on predicted thermal performance of furnaces is shown to be insignificant.

The steady-state model (SSZONE) predicts the thermal efficiency and temperatures within a furnace operating

continuously at a constant metal throughput. These conditions are rarely achieved in practical metal heating applications. The transient model (TRZONE) was therefore developed to simulate the cold start-up of a furnace and its performance over a realistic operating period, such as a single or double shift. The effects of changes in metal throughput rate can also be simulated. TRZONE uses a one-dimensional finite difference technique to calculate the non-steady-state thermal conduction through the load and the walls, roof and hearth of the furnace.

Both models have been validated by comparison against experimental data obtained from a continuous steel reheating furnace and a small batch heat treatment furnace. In both cases acceptable agreement was obtained. Finally, examples of the application of these models for practical design have been produced, including an evaluation of alternative methods of flue gas heat recovery on a continuous reheating furnace, and an evaluation of the influence of refractory wall emissivity on furnace thermal efficiency.

ACKNOWLEDGEMENTS

I am indebted to British Gas for their permission to pursue this study, and to John Ward (OU) for providing the opportunity and encouragement to undertake this work through the Open University. I would also like to acknowledge the kind support provided by numerous friends and colleagues at the Midlands Research Station. The furnace measurements were taken with the permission of Ductile Hotmill Ltd., Willenhall, and GKN Forgings Ltd., Bromsgrove.

CONTENTS

LIST OF TABLES

LIST OF FIGURES

NOMENCLATURE

(Note: Other variables not included here are defined within the text.)

A	Surface Area	m^2
a_i, a_j, a_k	Component vectors in x,y,z directions	
$a_{g,n}$	Weighting coefficient for gas emissivity model	
$a_{s,n}$	Weighting coefficient for gas absorptivity model	
$b_{1,n}$, $b_{2,n}$	Temperature coefficients in mixed grey gas model	
B	Square or cube side	m
C_c	Contact conductance	$W/m^2.K$
C_{net}	Net Calorific Value of fuel (mass basis)	MJ/kg
C_p	Specific Heat at constant pressure	J/kg.K
d,D	Diameter	m
D_m	Hydraulic mean diameter	m
$\dot{D}$	Downstream combustion product flow	kg/s
E	Total hemispherical black emissive power	W/m^2
F_{ij}	View factor between surfaces i and j	-
F	Proportion of maximum firing rate	-
$\overline{g_i s_j}$	Gas-surface direct exchange area	m^2
$\overline{g_i g_j}$	Gas-gas direct exchange area	m^2
$\overline{G_i S_j}$	Gas-surface total exchange area	m^2
$\overline{G_i G_j}$	Gas-gas total exchange area	m^2
$\overrightarrow{G_i S_j}$	Gas-surface directed flux area	m^2

$\overleftarrow{G_iS_j}$	Surface-gas directed flux area	m^2
$\overrightarrow{G_iG_j}$	Gas-gas directed flux area	m^2
H	Incident radiation flux	W/m^2
h	Convective heat transfer coefficient	$W/m^2.K$
$\dot{G}$	Fluid momentum	N
I(T)	Specific Enthalpy (ref.288 K) at temp.T	J/kg
i_b	Black body radiation intensity	$W/m^2.ster$
λ	Thermal conductivity	W/m.K
K	Attenuation coefficient	m^{-1}
$k_{g,n}$	Absorption coefficient of grey gas	$m^{-1}atm^{-1}$
k_n	Absorption coef. of gas in mixed grey gas model	
L	Length	m
L_m	Mean beam length	m
M	Number of surface zones in model	
$\dot{m}$	Mass flow rate	kg/s
NZONE	Number of volume zones	
NX	Total number of surface and gas zones	
NWALL	Parameter for number of wall elements per zone	
Nu	Nusselt number	-
p	Partial pressure	atm
p_w, p_c	Partial pressure water vapour and carbon dioxide	
P_b	Proportional band	
Pr	Prandtl number	-
$\dot{q}$	Heat flux	W/m^2
$\dot{Q}$	Heat transfer or release rate	W
r, r_c	Distance traversed by beam through gas	m
R_a	Air-fuel mass ratio	-

R_x, R_y	Random numbers used in Monte-Carlo technique	
Re	Reynolds number	-
$\overline{s_i s_j}$	Surface to surface direct exchange area	m^2
$\overline{S_i S_j}$	Surface to surface total exchange area	m^2
$\overrightarrow{S_i S_j}$	Surface to surface directed flux area	m^2
T	Temperature	K
T_{sp}	Set point temperature	K
t	Time	s
t_d	Turn down ratio	-
$\dot{U}$	Upstream combustion product flow	kg/s
V	Volume	m^3
x,y,z	Co-ordinate distance	m
W	Leaving radiation flux	W/m^2

Greek and special symbols :

α	Absorptivity	-
ε	Emissivity	-
ρ	Density	kg/m^3
ρ	Reflectivity	-
η	Craya - Curtet parameter	-
σ	Stefan-Boltzmann constant ($=5.6687 \times 10^{-8}$)	$W/m^2.K$
τ	Transmissivity	-
θ	Circumferential angle	rad
η	Cone angle	rad
η_{eff}	Recuperator effectiveness	-
ϕ	Recirculation ratio	-
μ	Dynamic viscosity	Ns/m^2

Subscripts :

a	Air
c	Combustion products exit (flue) temperature
d	Door
G	Fuel gas
g	Combustion products in zone
i,j	General subscript , zone label
L	Load
w	Wall
λ	Wavelength

Superscripts :

o	Initial condition
1	Current condition

CHAPTER 1

Background and General Introduction

1.1 Overall Objectives

Natural gas is widely used for the heating of metals, and Table 1.1 gives examples of some of the common heating processes used by manufacturing industry. Many of these applications lie in the range 500 - 1300^{o}C. There is also a general recognition of the need for energy conservation by these industries in order to reduce manufacturing costs and to maintain competitiveness. This stimulates the development, by burner and furnace manufacturers, of replacement or retrofit equipment for improving the efficiency of high temperature fuel using plant. In order to identify and evaluate methods of energy conservation in these processes, there is a demand for reliable thermal design techniques. Thermal performance is a function of several interdependent heat transfer processes occurring within the furnace chamber and can be predicted by mathematical models.

In these models, the equations describing the heat transfer in the furnace are formulated and solved together with the equations for mass and energy conservation. The model provides a numerical simulation of the overall heating process and can then be used to evaluate the influences of operating

Table 1.1 Typical performance characteristics of some natural gas-fired furnaces.

Process or Furnace Type	Operating Temperature (°C)	Specific Energy Consumption GJ/Tonne
A. Iron & Steel Industry		
Reheating for rolling		
Pusher furnaces	1150 - 1350	1.25 - 1.85
Rotary hearth furnaces	1150 - 1280	1.65 - 2.05
Walking beam furnaces	1050 - 1100	1.25 - 1.65
Reheating for forging		
Bogie hearth (large forgings)	1250 - 1300	2.05 - 4.35
Short-pusher furnaces (L/B < 4)	1200 - 1300	3.5 - 6.80
Long-pusher furnaces (L/B > 6)	1200 - 1300	2.25 - 4.35
Die-forge furnaces	1200 - 1300	6.0 - 8.65
Heat-treatment furnaces		
Bogie-hearth large annealers	800 - 900	1.65 - 4.35
Continuous normalising or hardening	800 - 1000	1.85 - 2.45
Continuous tempering	450 - 700	1.25 - 1.85
Coiled strip annealers	600 - 900	0.60 - 1.45
Lift-off annealers	650 - 850	1.65 - 2.05
Tube and bar annealers	900 - 950	1.05 - 2.45
B. Non-Ferrous Metal Industry		
Pusher furnaces (copper)	800 - 900	0.8 - 1.45
Brass re-heating	700 - 800	0.8 - 1.65
Brass melting	1000	4.35 - 5.15
Aluminium reverberatory melting	750	4.35 - 5.15
Aluminium crucible melting	750	4.35 - 6.00

and design characteristics on thermal performance, and in particular, the prediction of energy consumption and thermal efficiency. A mathematical model should also be capable of accurately predicting the load temperature uniformity and its thermal history in the furnace so that the consequences of any design or operating changes on the quality of the heated product can be evaluated.

It is the purpose of this project to develop mathematical models for the accurate thermal design and simulation of natural gas fired furnaces used for heating metals. These models must be flexible enough to be adapted easily to a wide range of geometries and applications. They must also be capable of simulating furnaces operating both continuously and under the non-idealised transient operating patterns met with in industry such as single or double shift operation, cold start-up and intermittent production delays.

Mathematical models for furnace design already exist and have been widely published. However, they normally only simulate steady state or continuous operation. This project aims to extend the range of application to the modelling of non-steady furnace operation. Both steady-state and transient models will therefore be developed. Moreover, to simplify their formulation, existing models often approximate the furnace chamber geometry as a cylindrical or rectangular enclosure. More complex geometries are found in practice. This work will

therefore also be extended to more closely represent some of these geometries.

In order to verify their accuracy the models will be validated by comparison with data from controlled performance tests on furnaces.

1.2 Energy Use In Metal Heating Processes

Throughout the manufacturing and engineering sectors of industry natural gas is used for heating metals for hot forming or heat treatment. Stock metal is supplied in the form of large ingots, slabs or blooms from the primary ferrous and non-ferrous production processes. It then undergoes numerous stages of reheating and hot rolling in order to produce a material of a desired cross sectional shape.

Hot rolling produces metal in the form of bar, rod, strip, wire, billets etc., which is supplied to all sectors of the engineering and manufacturing industries. Much of this material is then further reheated for hot forming into semi-finished products by such processes as hot cropping, forging, pressing etc. In order to impart the correct metallurgical quality to the product, this will be followed by one or more stages of reheating for heat treatment such as hardening, tempering and annealing. Thus, numerous and

diverse reheating operations are involved in the manufacture of metal goods.

A guide to the overall energy demand for metal reheating and heat treatment can be obtained from the Department of Energy Statistics [1] for 1980. The relevant statistics are reproduced in Table 1.2 which gives the pattern of delivered energy in PJ (1 PJ = 10^{15} J) supplied to:

a) The iron and steel industry for secondary and post-finishing operations (this will include a large proportion for hot rolling and excludes energy use in iron and steel making and ingot casting.

b) The engineering industry for direct process energy for temperatures exceeding 400^{o}C (this will include a large proportion for forging and heat treatment processes).

(Not included in Table 1.2 are figures for secondary finishing of non-ferrous metals which in [1] are combined with the overall figures for non-ferrous smelting and refining processes).

Figure 1.1 shows the pattern of energy consumption at 'point-of-use' in the manufacture of metal products. Natural gas accounts for the largest proportion of energy supply.

Table 1.2 Pattern of Energy Usage in the UK in 1980

in the Metal Industries (1 PJ = 10^{15}J)

	PJ - Delivered Energy					
	Solids	Liquids	Gases		Electricity	Total
			Natural	Other		
Iron & Steel Industry						
Secondary & Post Finishing Operations	-	22.4	22.0	17.7	15.9	78.0
Engineering (Direct Process Use >400^{o}C)						
Mechanical engineering	0.9	1.8	3.2		1.2	7.1
Instrument engineering	-	0.1	0.2		0.2	0.5
Electrical engineering	-	0.7	2.0		0.9	3.6
Shipbuilding & marine engineering	-	0.5	0.8		1.1	2.4
Vehicle manufacture	0.3	0.5	4.5		4.2	9.5
Other metal manufacture	0.1	0.4	7.3		3.6	11.4
Total (all engineering)	1.3	4.0	18.0		11.2	34.5
Total (Iron & Steel & Engineering)	1.3	26.4	40.00	17.7	27.1	112.5
%	1.1	23.5	35.6	15.7	24.1	

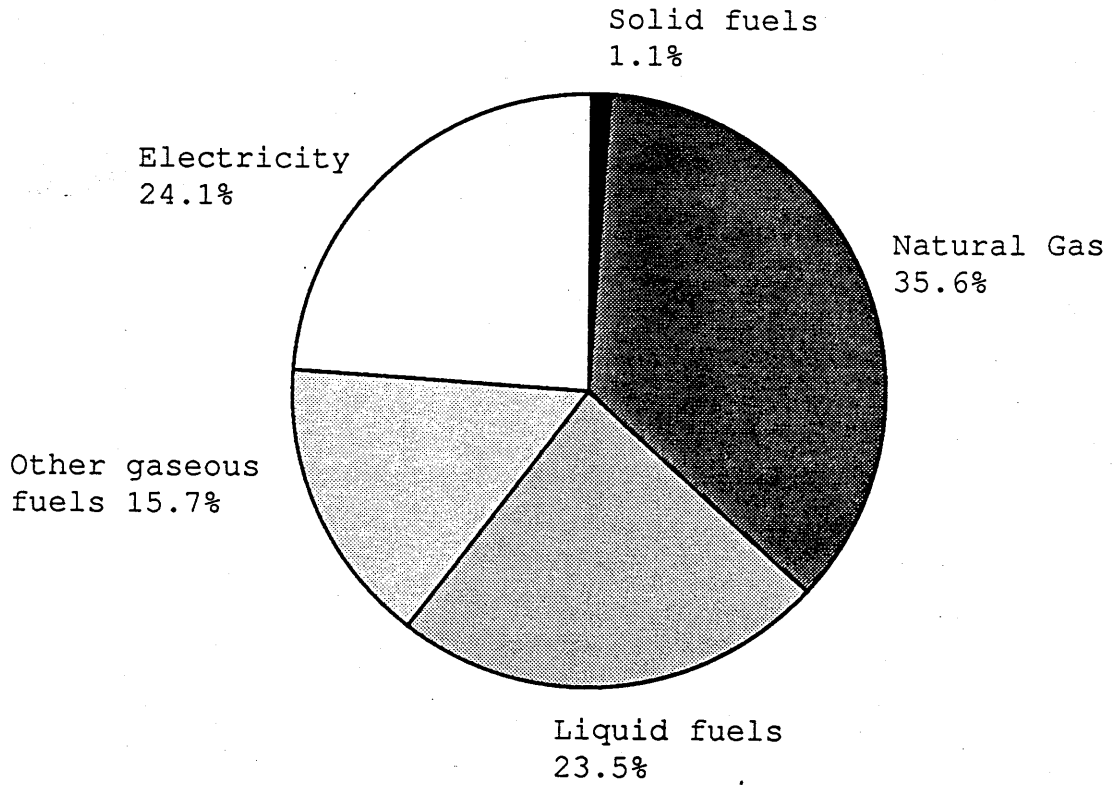

Figure 1.1. Pattern of delivered energy by fuel type in the UK in 1980 for the manufacture of metal products. [1]

Because of the high temperatures of many of these processes specific energy consumption is high (see Table 1.1), and many opportunities exist for cost effective energy saving schemes. As a guide to the extent of these opportunities, the Energy Efficiency Office of the Department of Energy has, as part of the Energy Efficiency Demonstration Scheme, compiled statistics on the population, annual fuel consumption and potential energy savings in the heat treatment of metals [2]. An estimated 9 PJ of energy is consumed annually in 21,500 furnaces of which approximately half are heated by natural gas. Average savings of 30% are also estimated for these processes by waste heat recovery, improvements in thermal insulation and improved controls. Unfortunately, similar figures are not available for other metal heating processes.

1.3 Furnaces for Metal Heating Processes

Fossil fuel fired furnaces for metal heating can be broadly classified as either directly or indirectly fired. Directly fired furnaces include the majority of types used by industry and it is their design which is the subject of this thesis. They are distinguished from indirectly fired furnaces by the combustion products and/or flame being in direct contact with the metal undergoing heating. In indirectly fired furnaces, the combustion products are separated from the metal by, for example, a muffle or radiant tube.

A broad classification is also made based on the method of

operation, with batch (or intermittent) and continuous furnaces representing the two extremes of working practice.

In batch furnaces, the cold material is loaded into the furnace which may or may not be pre-heated. Whilst stationary, the load undergoes the required heating cycle, when all of the material is discharged and replaced by a new cold charge. In a continuous furnace, the material is transported through in a steady feed whilst it undergoes heating (Figure 1.2). The material may be in continuous form (e.g. sheet or strip) or discrete (e.g. billets, slabs, castings etc.) which are transported on a 'one piece in, one piece out' basis through the furnace.

In practice, many furnaces operate between these two extremes. For example batch furnaces may be charged with several billets or ingots which are removed and replaced one at a time. Although the material remains stationary during heating, thermally the furnace more closely resembles a continuous process without the temperature cycling inherent in batch heating of single pieces. Continuous furnaces may also be worked semi-continuously as the following working pattern commonly observed on many forging furnaces illustrates:

i) Discharge of hot billets occurs at the maximum rate that can be forged and at a rate exceeding the continuous output capacity of the furnace.

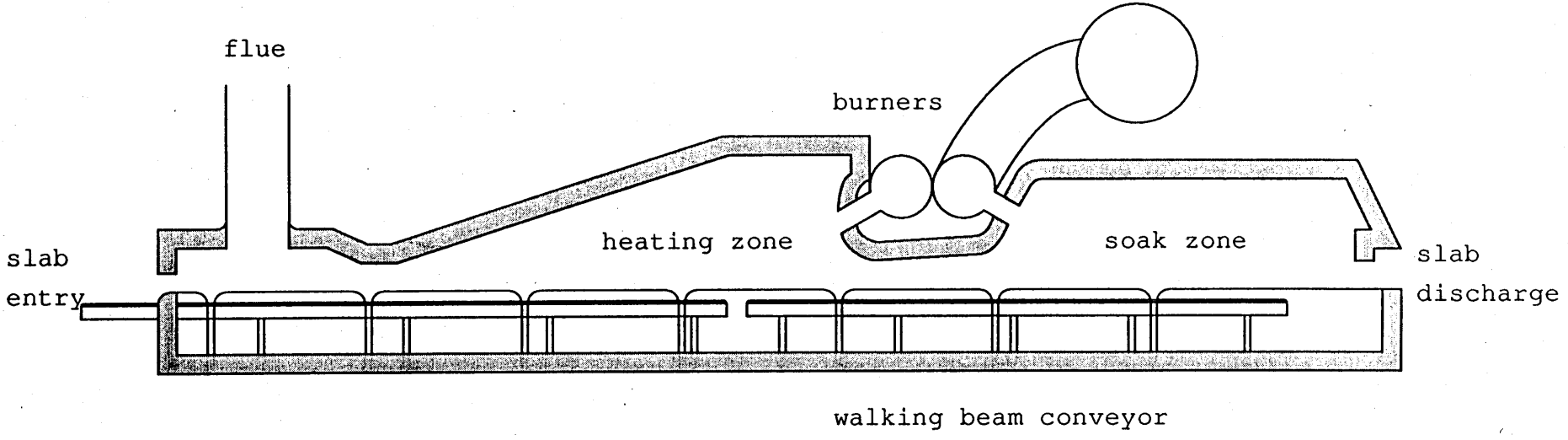

Figure 1.2. A sectional view of a continuous slab reheating furnace incorporating a walking beam conveyor for stock transport.

ii) Because the installed thermal output cannot sustain this rate, the furnace and billet temperatures drop to an unacceptable level, and forging is suspended for a period to let the temperatures recover.

iii) Forging recommences at the maximum rate for a period and the cycle is repeated.

With this mode of operation, the furnace undergoes significant temperature cycling with billets often being overheated to ensure that the high peak output rates can be achieved. Such operation is detrimental to both furnace efficiency and product quality.

Continuous furnaces can be categorised further by the method of load transport employed. Common types are:

i) Pusher furnaces - pushing billets either along a dense refractory hearth, or on cooled skid rails.
ii) Walking beam furnaces
iii) Car bottom or bogie hearth furnaces
iv) Rotary hearth furnaces

Counterflow operation is often practised in continuous furnaces to achieve maximum utilisation of the combustion product enthalpy. Figure 1.2 illustrates this principle whereby the incoming cold material is continuously recovering

heat from the hot combustion products flowing in the opposite direction. This is referred to as load recuperation.

An idealised counterflow furnace would comprise burners and flue at the discharging and charging ends of the furnace respectively. This ensures that a high temperature differential between the load and the combustion products is maintained throughout the length of the furnace and also that thermal efficiency is not thermodynamically limited by the discharge temperature of the heated load. By increasing furnace length, flue exit temperature can be reduced below the load discharge temperature.

In order to achieve control over the heating profile along a counterflow furnace, these furnaces may often be divided into separate temperature control zones commonly referred to as 'soak', 'heating' and 'pre-heating' zones. This is often applied when heating thick section material where conduction into the metal may limit its rate of heating in the furnace.

It is beyond the scope of this work to give a more detailed classification of the wide range of furnaces employed in the metal processing industries. More comprehensive descriptions are found elsewhere [3,4]. However, typical performance characteristics are given in Table 1.1 for a number of natural gas fired furnaces and processes in the ferrous and nonferrous industries. The high specific fuel consumption (SFC)

indicated for forging furnaces is generally a consequence of the intermittent working patterns referred to previously. Reheating for rolling is generally carried out in large load recuperative furnaces which also often employ flue gas heat recovery techniques. This, together with the more continuous nature of the rolling process leads to lower specific fuel consumption. The lower consumption of heat treatment processes is primarily due to the lower process temperatures when compared to those for forging and rolling.

1.4 Heat Transfer in Furnaces

The mechanisms of heat transfer in a fossil-fuel-fired furnace are shown schematically in Figure 1.3. The primary transfer of heat from the combustion products occurs by non-luminous and luminous gaseous radiation and by forced convection. Non-luminous radiation is the dominant mode of transfer in the majority of natural gas fired furnaces. Convective heat transfer is promoted in some designs of rapid heating furnaces [5], by ensuring a high combustion product flow velocity over the load and wall surfaces in the chamber. The combustion products radiate and convect to the load surface directly and also to the surrounding furnace refractory surfaces (e.g. walls, roof etc.). With ideal adiabatic walls, all of the heat received by the walls is reflected or re-radiated back into the furnace chamber towards the load. However, in

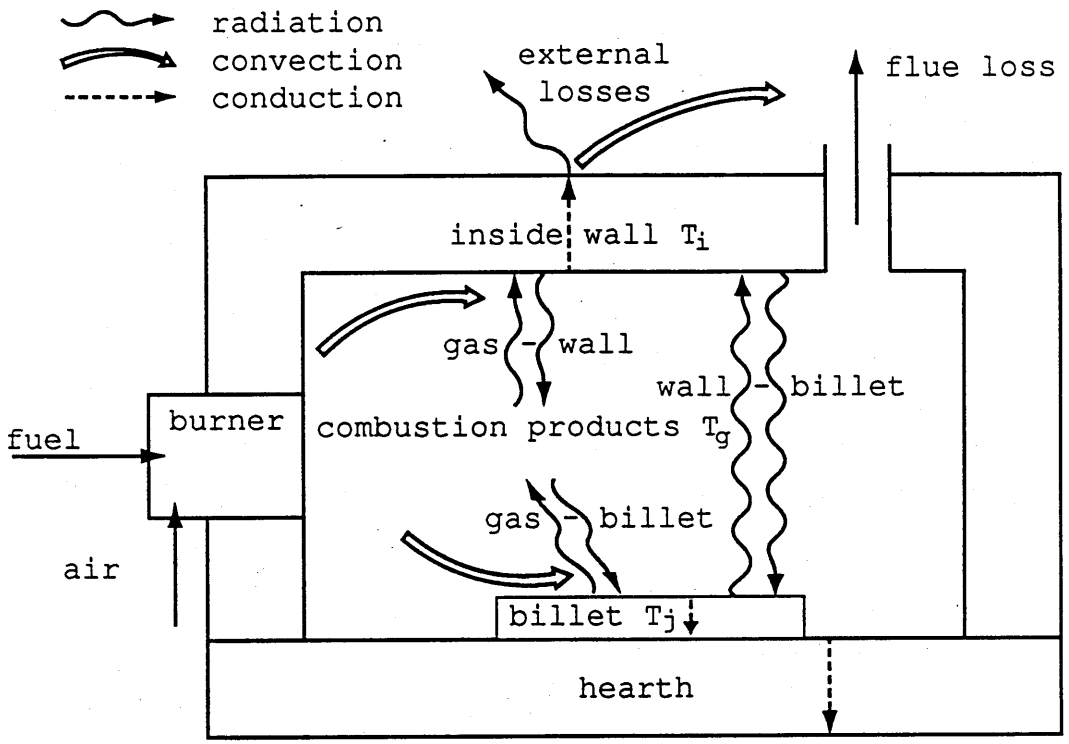

Figure 1.3. The mechanisms of heat transfer in a simple billet reheating furnace.

practice some of the received heat is lost into the refractories. Part of this can be lost through the walls to the ambient environment outside and the remainder can be stored in the structure. Storage losses are significant in a cold furnace when it is first switched on since the structure must absorb considerable energy in order to achieve thermal equilibrium. Under steady-state conditions the loss through the walls is sufficient to balance the radiant and natural convection heat transfer from the outer furnace casing. In a well insulated furnace this loss is a relatively small fraction of the thermal input (typically 5%).

Non-luminous gaseous radiation occurs due to changes in the rotational and vibrational energy levels of heteropolar molecules in the gas stream, of which CO_2 and H_2O are the most important on account of their high concentrations. CO and CH_4 do also radiate but due to their low concentrations in stoichiometric or fuel lean systems, their overall contribution is generally small. The gaseous radiation has a strong wavelength identity with a non-grey spectral distribution typified by the spectral emissivity of carbon dioxide shown in Figure 1.4.

Radiation is emitted at specific wavelengths in all directions from point sources within the flowing hot combustion products. Some of this radiation is re-absorbed by the heteropolar molecules before it arrives at any of the bounding wall or

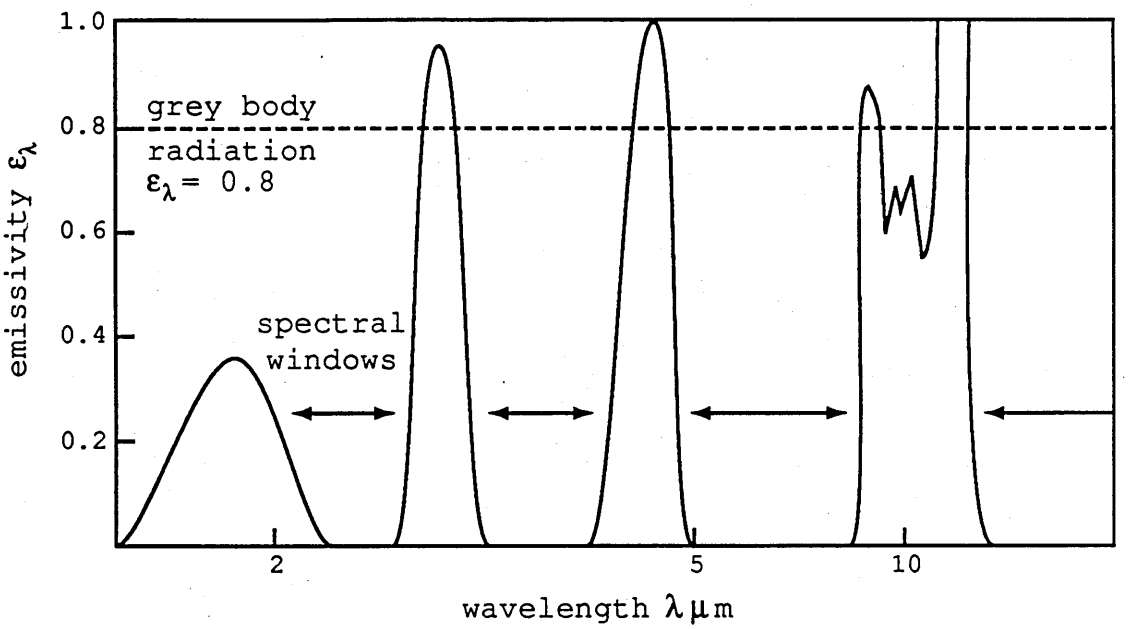

Figure 1.4. The low resolution spectral emissivity of carbon dioxide.

load surfaces. The radiation that is transmitted however, is either absorbed or reflected at the receiving surface depending on the surface emissivity (ε) or reflectivity (ρ). Reflected radiation maintains its original wavelength identity and is therefore more easily re-absorbed by the gas. The absorbed radiation heats the refractories so that these surfaces re-emit radiation with a spectral distribution which approximates to that for a grey body also shown in Figure 1.4. This re-emitted radiation has a greater chance of transmission through the combustion products and to other neighbouring surfaces, since it contains substantial energy at wavelengths conforming to the non-absorbing 'windows' in the gaseous radiation spectrum. Thus, the net radiation arriving at the load surface comprises of the following:

(i) Directly transmitted radiation from the combustion products.

(ii) Reflected radiation from the furnace walls conforming to the spectral distribution of the original gaseous emission.

(iii) Emitted and reflected radiation off the furnace walls approximating to a grey body spectral emission.

Luminous radiation occurs due to the temporary formation of soot in the flame as a result of local regions of fuel-rich combustion. In furnaces where the flame occupies a large

proportion of the chamber volume this can contribute significantly to the overall radiant emission from the combustion products. It also has a more grey spectral distribution when compared to the non-luminous emission and consequently has a lower transmittance to surface radiation. Thus, the mechanism and character of radiation transfer to the load when a luminous flame is present is altered with a greater proportion of the received radiation arriving directly from the flame itself. However, in most natural gas fired furnaces radiation is predominantly non-luminous particularly if efficient burners are used with good air and fuel proportioning and mixing.

The load therefore receives heat by radiation and convection either directly from the combustion products or indirectly by re-radiation off the internal chamber surfaces. In the case of a solid load such as steel billets, blooms, slabs etc., this received heat is transferred internally by conduction. The bottom unheated surface of the load inevitably lags in temperature behind the top directly heated surface due to the conductive resistance of the material and because of heat loss into the supporting hearth or load transport mechanism.

CHAPTER 2

Design and Modelling Techniques for Furnaces

2.1 Survey of Design Techniques

The literature relating to the thermal design of furnaces is extensive and it is therefore only possible to present a brief summary of the different approaches applied in practice. Each approach has its own merits depending on the designers needs, practical experience or mathematical and computational ability. The approach adopted also depends on the particular aspect of the plant performance which is most crucial, for example, the flow patterns in the furnace, the flame behaviour, or the uniformity of radiant heating.

2.1.1 Design by Experience

In its simplest form, design relies heavily on practical experience derived from proven designs of furnaces. As an example of this approach, the length of a continuous furnace is often governed by the minimum load residence time that will ensure acceptable uniformity of heating, and this is often calculated using rule-of-thumb values for the minimum heating time per unit thickness or diameter of material. This determines the surface area of the material in the furnace and the maximum heat flux that can be imparted to the load. Heat

flux itself may be estimated from prior knowledge of a similar furnace, with a simple fourth power temperature correction applied for any difference in furnace or load temperatures.

With respect to heat flux in furnaces, Mawhinney [6] has analysed production data from a wide range of metal heating and heat treatment furnaces and with the aid of simple heat transfer equations has correlated the heat flux to the load to the ratios of load to refractory surface area for various categories of furnaces and heating applications. Such techniques are only reliable if slight changes are made to the proven design. They do not provide sufficient flexibility for design innovation or optimisation. However, in practice, furnace manufacturers rely heavily on such an approach so that furnace designs for many years evolved only gradually.

2.1.2 Early Theoretical Approaches

Trinks [7] published the first comprehensive theoretical approach to the design of modern industrial furnaces covering the mechanical and thermal design of virtually all types of furnaces still in use today. This work was based on the best available techniques and data for calculating convective and radiative heat transfer, and steady-state and transient conduction. These techniques were used to determine the fuel economy or heating capacity of both batch and continuous furnaces. A comprehensive description is given of the

calculation of all terms that must be included in a furnace energy balance. Since this work predates the widespread availability of computers, the techniques were limited in their sophistication by the ability to perform hand calculations and not by a lack of understanding of the thermophysical processes involved.

The concept of 'zoning' a furnace chamber was introduced by Trinks for predicting the steady-state behaviour of continuous counterflow furnaces. The division of the chamber into sections of assumed uniform gas, wall and load temperature was applied to predict heating profile and fuel consumption. Luminous and non-luminous gaseous radiation was calculated using the concept of a mean beam length, first introduced by Hottel and Egbert [8]. The interaction between the flame and the wall in the transfer of heat by radiation to the load was also described and simple formulae were presented to relate the load heat transfer to the flame emissivity. The empirical technique described previously for predicting minimum load residence time was replaced by a transient conduction calculation for the load using charts (e.g. Heisler [9]), and simple graphical or numerical techniques. The use of these techniques for calculating wall conduction in intermittently operated furnaces was also presented.

Trinks clearly understood the influence of non-steady operation on the specific fuel consumption of continuous

furnaces and recognised the limitation of a steady-state design approach for these situations. For example, Figure 2.1, reproduced from Trinks [7] was meant to explain the noted general under-prediction of fuel consumption compared to the wide ranging measured data which can occur.

'.....let point 2 indicate the point as obtained from the operating record, while point 4 represents the fuel consumption that might be expected from theoretical calculations. But it is quite possible that the furnace is driven very lightly, say at point 1, half the time (on account of trouble in mill or at the shear, lack of steel, or trouble in the gas producer) and driven very hard, say at point 3, the rest of the time, so as to maintain tonnage of the mill. Then the resultant average point must lie at 2 instead of at 4.'

This same figure is also used to illustrate the difference in fuel consumption when heating thin and thick section steel. The conduction lag within a thick steel load gives rise to an elevated surface temperature, and in order to maintain an average temperature head in the furnace, the chamber temperature must be increased to compensate. Consequently, the fuel consumption is higher than for the same output rate of thin steel at the same average discharge temperature.

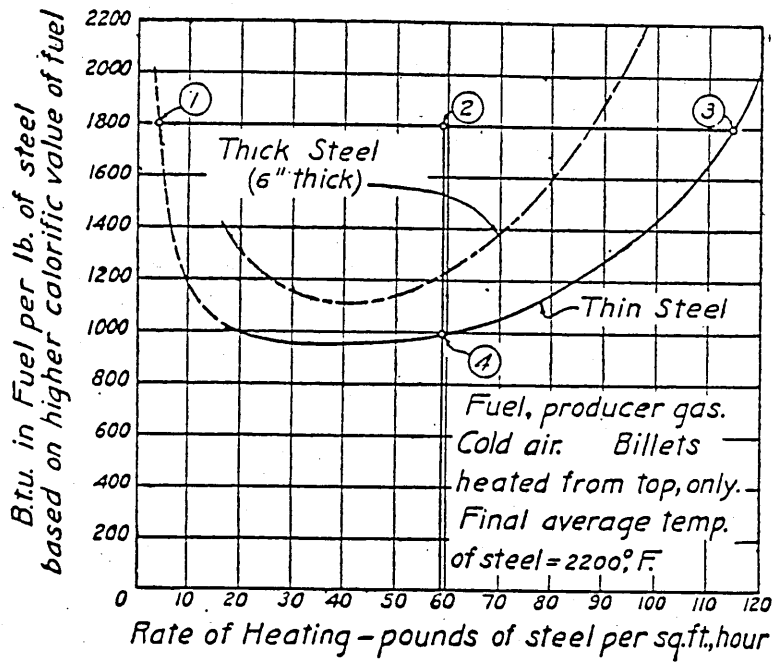

Figure 2.1 **The variation of specific fuel consumption of a continuous steel reheating furnace against rate of heating (after Trinks [7]).**

2.1.3 Mathematical Modelling Techniques

Thermal radiation is the dominant mode of heat transfer in most high temperature fuel-fired furnaces. Modern day methods for radiation calculation include the zone, flux and Monte Carlo techniques. A thorough review of these techniques is presented by Viskanta and Menguc [10].

Hottel and Sarofim [11] originally developed the zone method and this technique is now extensively applied to the design of industrial furnaces, boilers and chemical feedstock heaters. The technique considers the furnace chamber as an assembly of gas and surface zones of uniform temperature. Equations describing the radiation exchange between zones are developed. The formulation of these equations requires knowledge of the opto-geometric exchange coefficients and the fourth power temperature differences between the zones. The exchange coefficients allow for the effects of total system geometry, non-grey gaseous emission and absorption, and for grey diffuse reflection off all surfaces in the radiating enclosure. Energy balance equations are written for each zone in terms of all the zone temperatures (which may or may not be known). These equations also include terms for the convective heat transfer and for the enthalpy release and transport within and across zone boundaries. The geometric disposition of zones is included in the calculation of inter-zone radiation exchange using the concept of the total exchange area, a coefficient

dependent on the mutual view factor of a zone pair and their reflectivities.

The zone method has been applied to a wide range of furnace mathematical models. The simplest of these is the well-stirred model employing a single gas zone. The long furnace model uses a series of connected zones to provide a one dimensional representation. Two- and three- dimensional zone models can also be applied. In the zone models, the chemical heat release, concentration and mass flows in and across each zone, and surface convective heat transfer coefficients must be specified in the input data. This data can be obtained from direct furnace measurements, from empirical correlations or from physical modelling experiments [12,13,14].

Thus, the zone method does not provide a total system description of the thermophysical processes involved. Attempts to overcome this limitation have resulted in the development of two-dimensional and three-dimensional computational fluid dynamic models which predict the interdependent phenomena of multi-component fluid flow, chemical kinetics and heat transfer within turbulent combusting flows. Using finite difference approximation schemes, the partial differential equations describing the conservation of momentum, mass and energy have been solved [15,16] using various models for the turbulence and combustion kinetics and with various treatments for thermal radiation transfer. The latter is generally

handled using flux models [17], or the discrete transfer method [18]. These techniques can be easily adapted to the finite difference solution techniques used by computational fluid dynamic models.

The application of these complex models to furnace design is progressing rapidly as the limitations of computing capacity, speed and cost are being eroded. However, their success is currently limited by difficulties in correctly modelling turbulence in chemically reacting flows and the behaviour of turbulent transport and convection close to surfaces. Before these models can be applied as a general design tool they must also be validated against accurate experimental data.

2.3 Choice of Modelling Technique

The preceding brief review shows that the techniques for furnace modelling and design are varied in their complexity and flexibility. The simplest techniques have only limited accuracy and do not provide detailed information. Computational fluid dynamic models, appear to offer a complete solution but the cost and availability of computing that they require can be prohibitive for many industrial designers. The output is also dependent on the sub-models for simulating the turbulence and chemical kinetics in the flame. Their accuracy for general purpose design has yet to be established.

It is necessary to identify the information that is required by the designer, and the important physical parameters governing plant thermal performance, in order to choose the correct and most appropriate modelling technique.

The modern natural gas fired metal reheating furnace generally employs high intensity nozzle-mixing burners. The air is introduced with a dynamic pressure at the burner nozzle which assists rapid mixing with the fuel. The high velocity, hot reacting gas stream generated downstream of the burner produces a short, non-luminous flame which occupies a small fraction of the overall furnace chamber volume. The high velocity also ensures good mixing with the fully-burnt gases inside the chamber, thus producing a well-stirred region of uniform temperature and concentration. The designer of these furnaces is often not interested in the problem of flame behaviour or mixing except in so far as these factors affect the flame stability under the specified operating and turndown range of the burner.

Because of the high temperatures, radiant transfer between the surfaces and the gases in the chamber is usually the dominant mechanism of heat transfer although convective heating is of similar magnitude in some designs of rapid heating furnaces [5]. The emissivities of the furnace lining material and of the load, and the non-grey emissivity of the combustion products in the furnace chamber have an important influence on

the levels of received heat flux at the load. A reliable model for the radiation transfer is therefore required and this should be capable of simulating the non-grey absorbing atmosphere and the multiple reflections at the various surfaces. The well-stirred and long furnace zone models satisfy these requirements.

A principal objective of the present study is the simulation of the non-steady state behaviour of the load and walls in the furnace. The treatment of the transient thermal conduction into the walls and load and of the non-steady transport of the load through the furnace must therefore be linked to the model. The non-steady-state boundary conditions preclude the use of computational fluid dynamic models because of their large computing demands and long run times. The simple zone models can however be easily linked to a transient conduction calculation without excessive demands on computing time.

For the reasons outlined above, the zone method has therefore been selected as the most appropriate technique for the types of furnaces and metal heating applications to be modelled.

2.4 Background to Zone Modelling

The main objectives of the current work is therefore concerned with the development of the radiation calculation, and the application of the zone method to furnaces with

non-steady-state boundary conditions.

The majority of published techniques for metallurgical furnace design have employed the single well-stirred gas zone model or the long furnace model, and these models will form the basis of this study for two reasons:

1. These models have been proven to give reliable predictions for many designs of industrial furnaces.

2. By using the single zone and long furnace models simple assumptions regarding flow and combustion phenomena can be made. It is not the intention of this project to study the complex interactions between the flow, combustion and radiation on the thermal performance, for which a multi-dimensional zone model or a computational fluid dynamic model would normally be applied, but to concentrate on a development of the radiation calculation and the transient performance simulation.

2.5.1 The Single Gas Zone Model

This model comprises an isothermal radiating gas of uniform composition surrounded by isothermal surfaces. This is often referred to as the 'well-stirred' zone model and is analogous to the well stirred reactor in chemical engineering design. This model provides a reliable prediction of the overall heat

transfer in many real furnaces. The momentum supplied by air blast burners on many industrial furnaces is sufficient to ensure reasonably well-stirred conditions within the chamber, which justify assigning single values to the composition and temperature of the gas. The exit temperature of the combustion products from the zone is also usually assumed to be equal to the mean radiating temperature in the zone.

Treatment of the surfaces in the model can be simplified by assuming that the sink and refractory are intimately mixed ('speckled') such that the relative view factors between the surfaces are independent of position. Various well-stirred models derived from these basic assumptions are described by Hottel and Sarofim [11].

2.5.2 The Long-Furnace Model

Although the well-stirred model is found to yield accurate prediction of overall heat transfer, it gives no information on the spatial variation of heat flux within a furnace. In many practical situations it is unreasonable to assign a single temperature to represent the sink. An example is a counterflow furnace where cold charge enters and hot charge leaves the furnace. The long furnace model is an approximation to a plug flow model wherein temperatures are allowed to vary in the longitudinal direction. The furnace is represented as a longitudinal series of connected well-stirred

zones (Figure 2.2). Long furnace models are derived assuming radial or cross sectional uniformity. Longitudinal temperature variation is represented as a series of step changes along the length.

It is often assumed that there is no radiation exchange across zone boundaries in a long furnace model. This assumption eliminates the need to compute all of the geometric configuration factors (exchange areas) between the surface and volume zones within the model ; only those exchange areas relating to radiation between the gas and the surfaces within each zone need be evaluated. It is well known however, that for greater predictive accuracy, the simulation of radiation interchange between zones should be taken into account.

2.6 Zone Modelling of Metal Reheating Furnaces

A sample of some of the published methods of application of the well stirred and long furnace zone models to metallurgical furnace design follows.

The majority of publications relate to reheating furnaces for rolling. These furnaces have attracted greatest attention because of the quantity of energy consumed in this sector and because of the importance of temperature uniformity in rolling.

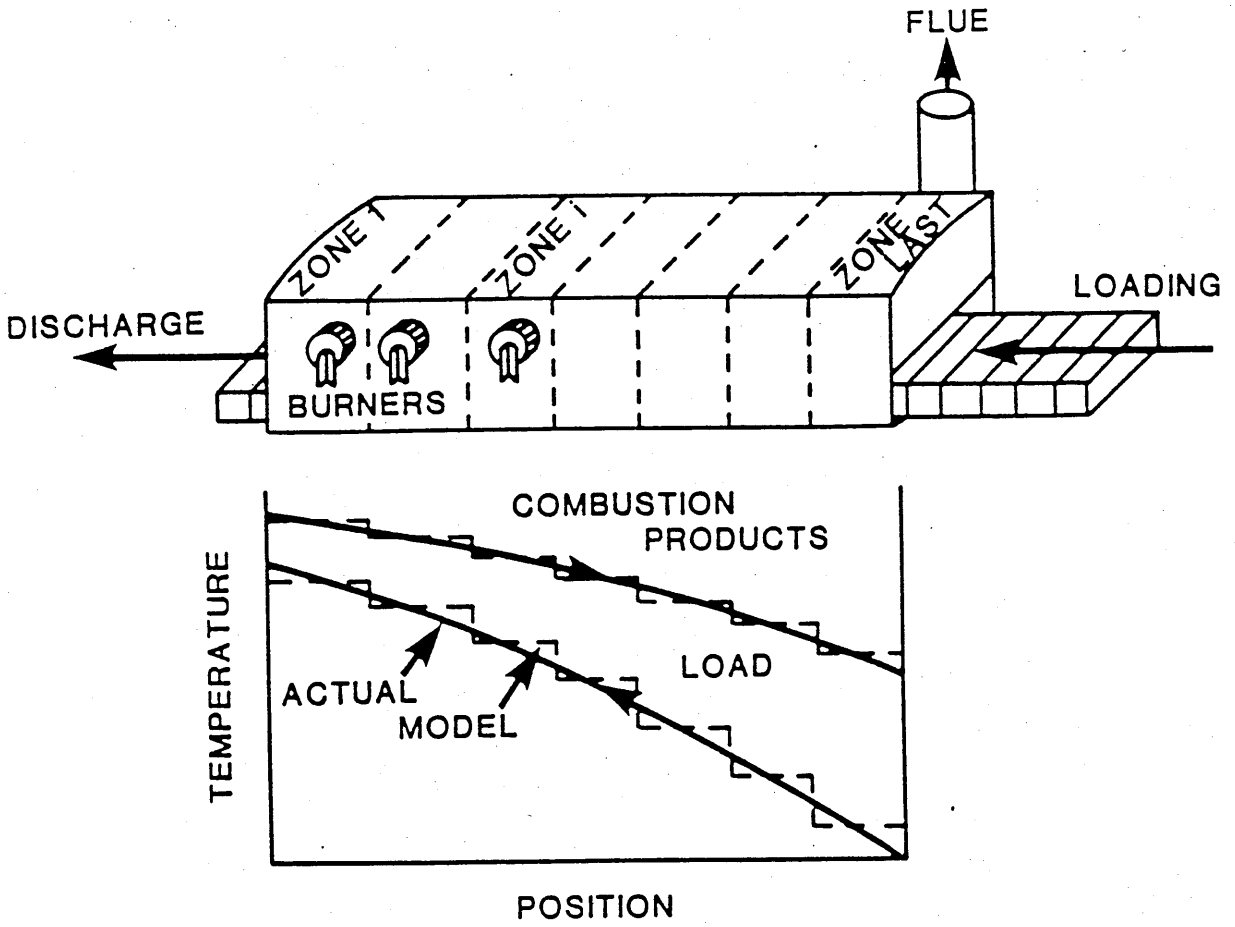

Figure 2.2 The long furnace model.

Salter and Costick [19], describe a steady-state two-dimensional model for predicting the temperature distribution in billets heated in large multi-zone continuous reheating furnaces. The radiant heat flux distribution to the steel billets is calculated by superimposing a two-dimensional grid over the longitudinal cross section of each furnace control zone. The temperature and extinction coefficient of the flame and gases in the furnace are defined by the user at each point in the input to the model. This is the major limitation of this work. The heat transfer into the steel is then computed by steady state calculations of the radiant interchange between grid points representing volume elements, wall and steel surface elements, simultaneously with the transient solution of the one-dimensional vertical conduction into the steel. The model treats the walls as adiabatic, convective heat transfer is ignored, all surfaces are assumed to be black, and the combustion products are assumed to be grey. Use of the model is stated to be dependent on the initial specification of the flame and gas temperature profiles. It is not capable of predicting fuel input rate.

Fitzgerald and Sheridan [20], applied the zone method for predicting heat transfer and temperature distribution in two gas-fired steel reheating furnaces and compared the predictions with measurements from 2 pilot scale furnaces. Longitudinal interchange is taken into account in these models. Steady-state conditions were assumed although the

one-dimensional transient conduction in the steel was solved simultaneously with the zone heat fluxes. Variable thermal properties were taken into account in the steel. Radiant interchange factors were derived from the data of Hottel and Cohen [21] assuming that the combustion products behave as a grey absorbing medium. A rectangular furnace was represented by the 8 zone long furnace model with equal zone sizes. A conventional furnace with a sloping roof was modelled as a two-dimensional configuration of 12 zones (2 zones vertically) but with a stepped geometry representing the roof. Good agreement with the measurements was reported from these two models. They require specification of the fuel, air and steel throughput rates as well as the furnace geometry and combustion product flow and mixing patterns.

Salter and Costick [19] and Fitzgerald and Sheriden [20] only considered transient conduction in the steel charge. Tucker and Saimbi [22] and Klima et al [23] describe models where the non-steady conduction through the furnace wall is also taken into account. In [22] a long furnace model which neglects interzone radiation exchange, is applied to continuous and batch furnaces to simulate both cold starts and intermittent working practice. The models apply a one-dimensional finite difference conduction algorithm to the wall, billet and hearth, taking the temperature variation of conductivity and specific heat into account. A simple 1 grey plus 1 clear gas model is applied to represent the combustion products. The

geometry of each zone is also represented in such a way that total exchange areas are calculated solely from the areas of the wall and load surfaces and from the mean beam length for the zone.

In [23], a model is described comprising of longitudinal well-stirred and plug flow zones to represent the fired and unfired regions respectively, of the furnace. An approximate allowance for interzone radiant exchange is applied using a constant interchange coefficient. The wall surfaces are assumed to be black. Variation of the configuration of well-stirred and plug flow zones was investigated by comparing the predicted billet temperature profile against measurements. Transient furnace operation with variable fuel flow rates was also simulated.

A single well-stirred zone model has been applied by Lucas et al [24] and Lucas and Barber [25] based on the same radiative model as in [22], to predict the performance of the convective rapid heating furnaces developed by the Gas Council. These models utilised convective heat transfer coefficients derived from physical modelling simulation using mass transfer techniques in isothermal models of these furnaces. The naphthalene sublimation and the electrochemical techniques were used to measure mass transfer coefficients from which heat transfer coefficients were derived using the Chilton - Colburn analogy between heat and mass transfer. The

mathematical model predicted the fuel consumption and cycle times for the heating of cylindrical billets fired tangentially in a cylindrical furnace chamber. The high combustion product recirculation around the billet justified the decision to use a single well-stirred zone. By solving the heat balance equations over discrete time steps, the model calculated the transient one-dimensional radial temperatures in the billet simultaneously with the combustion product and wall temperatures in the zone. In [24], a steady-state wall heat loss is assumed at each time step. This model accurately predicted billet heating times compared to data from a furnace with fully warmed refractory, but was unable to simulate cold start-up or intermittent operation. The model was therefore extended to include for the transient conduction on the wall [25]. Predicted times for heating a succession of billets to forging temperature starting with a cold furnace are shown to decrease progressively and reach a minimum value when the refractory has become fully warmed. This corresponded closely to the times predicted assuming a steady-state wall loss.

2.7 Limitations of Existing Approaches

It is apparent from the literature that the main limitations of most published work is the mathematical representation of furnace chamber geometry and the non-grey radiative properties of the combustion products. Radiant interchange is either neglected as in [22] or is treated in a simplified manner as

in [23]. Fitzgerald and Sheriden [20] using a two-dimensional zone model provides a more complete description of chamber geometry although sloping surfaces are approximated by a stepped rectangular zone arrangement. Furthermore, the majority of the published models treat the combustion product emissivity as grey [19,20 and 23] or at best apply a one grey plus one clear gas representation of emissivity [22,24 and 25] in accordance with the equations described by Hottel and Sarofim [11]. The limitations of one grey plus one clear gas representation will be described in Section 3.5.

In the literature survey three different approaches to modelling transient furnace behaviour are identified :

i) In [19] and [20], a steady-state furnace calculation is linked to a one-dimensional transient conduction analysis in the load.

ii) In [22], [23] and [25] the furnace heat transfer is re-calculated over successive time steps simultaneously with the one-dimensional transient temperature profiles through the wall and load.

iii) In [24] a similar approach to ii) is adopted whereby the furnace heat transfer is recalculated over successive time steps, but the wall is assumed to be at thermal equilibrium at each time step. The calculated equilibrium temperatures in

the wall do however vary at each time step as the load temperature varies. Since this approach offers little saving in computation at the possible expense of inaccuracy in predicted transient performance, it has not been adopted in this current work.

2.8 Specific Objectives of this Project

Because of the limitations the previously published models, the following specific objectives of this project were identified:

i) Development and validation of both steady-state and transient long furnace models for metal reheating furnace simulation. This will include development of the radiation calculation with allowance for interzone radiation exchange.

ii) Determination of the effects of chamber geometry and comparison of its approximate and correct zonal representation on predicted thermal performance. A rectangular representation of a complex furnace geometry will be compared to an accurate zonal representation.

iii) Determination of the significance of interzone radiation exchange. A comparison of a long furnace model with and without interzone radiation will be made.

iv) Evaluation of the sensitivity of predicted performance to some of the physical input parameters which often retain a high degree of uncertainty e.g. wall emissivity, density and conductivity, load emissivity.

v) Evaluation of the sensitivity of predicted performance to calculation time step, zone size and the accuracy of calculated exchange areas.

CHAPTER 3

Furnace Radiation Calculation Using the Zone Method

3.1 Background

The zone method is widely attributed to Hottel and Sarofim [11]. The basis of the method involves subdivision of the radiating enclosure into isothermal volume and surface zones. On each zone, a total energy balance is written including the radiation arriving at it from all other zones in the enclosure. These equations are written in terms of exchange factors known as *directed flux areas* (denoted $\overrightarrow{GG}$, $\overrightarrow{GS}$, $\overleftarrow{GS}$ and $\overrightarrow{SS}$ for gas to gas, gas to surface, surface to gas and surface to surface exchange respectively). The one-way radiant energy transfer between a zone pair is proportional to their mutual directed flux area. The net exchange between a pair of zones can then easily be written. For exchange between gas and surface zones i and j for example,

$$\dot{Q}_{i \rightleftharpoons j} = \overrightarrow{G_i S_j}.E_i - \overleftarrow{G_i S_j}.E_j \qquad 3.1)$$

where E is the black hemispherical emissive power of the volume or surface zone ($= \sigma T^4$).

Corresponding expressions can be written for gas to gas and surface to surface exchange. The directed flux areas allow for all possible radiation paths between i and j including multiply reflected radiation and re-radiation off all non-black surfaces in the enclosure. The attenuation and emission of radiation by a non-grey gas in the volume zones is also included in the directed flux areas. The energy transfer to a particular zone is incorporated into an overall energy balance equation on that zone, taking account of all other modes of energy transfer. Such equations can be written for all gas and surface zones, thus giving a set of simultaneous non-linear equations which can be solved to determine the temperature and heat flux at each zone. The major task in the zone method is the evaluation of the temperature dependent directed flux areas for all zone pair combinations. This will be described in detail in this chapter.

By applying the theory developed by Hottel and Sarofim [11], the directed flux areas can be computed from more fundamental sets of exchange factors which, by their definition, are independent of temperature (see Table 3.1). The directed flux areas are computed from *total exchange areas* (designated $\overline{SS}$, $\overline{GG}$ and $\overline{GS}$), which in turn are computed from *direct exchange areas* (designated $\overline{ss}$, $\overline{gg}$ and $\overline{gs}$). Their significance for radiation calculation is that for an enclosure comprising of a grey gas and grey surfaces whose radiant properties (gas attenuation coefficient K and surface emissivities ε) are

Table 3.1 The exchange areas in the zone method of radiation analysis

Exchange Area	Designation	Function of:
Direct Exchange Areas	$\overline{gg}$, $\overline{gs}$, $\overline{ss}$	Geometry $k_g p$
↓ ← ε(surfaces)		
Total Exchange Areas	$\overline{GG}$, $\overline{GS}$, $\overline{SS}$	Geometry ε(surfaces) $k_g p$
↓ ← Mixed Grey Gas Model		
Directed Flux Areas	$\overrightarrow{GG}$, $\overrightarrow{GS}$, $\overleftarrow{GS}$, $\overrightarrow{SS}$	Geometry ε(surfaces) $k_g p$ Temperatures
↓		
Total Energy Balance Equations		

independent of temperature, the total and direct exchange areas are themselves independent of temperature and therefore need only be computed once for a given configuration of zones. In the definitions that follow, these assumptions are invoked. Abandonment of the grey gas restriction introduces the complication that gas emissivity and absorptivity are no longer equal and that absorptivity is dependent on the temperature of the emitting source. The non-grey temperature dependent behaviour of the combustion products is introduced later in the formulation of the directed flux areas.

3.2 Direct Exchange Areas

3.2.1 Surface-Surface Exchange ($\overline{s_i s_j}$)

The fraction of radiation emitted by a surface zone i (E_i) that is directed towards a surface zone j ($\dot{Q}_{i\rightarrow j}$) is proportional to their mutual direct exchange area, thus:

$$\dot{Q}_{i\rightarrow j} = \overline{s_i s_j}.E_i \qquad 3.2)$$

The surface-surface direct exchange area is by definition independent of surface emissivity, ε (or reflectivity ρ) but includes allowance for beam attenuation between the surfaces by an intervening grey gas. It is therefore dependent on the mutual geometric orientation of the two surfaces and on the attenuation or extinction coefficient K of the intervening

grey gas. K is dependent on the concentration or partial pressure of the constituent absorbing grey gas.

$$K = k_g.p \qquad 3.3)$$

The direct exchange area is also independent of system temperature provided k_g is constant.

Consider two differential surface elements dA_i and dA_j, Figure 3.1(a):

The flux from dA_i which is emitted in the direction of dA_j

$$= E_i dA_i \cos\theta_i/\pi \quad \text{W/steradian} \qquad 3.4)$$

The solid angle subtended by dA_j at dA_i

$$= dA_j \cos\theta_j/r^2 \quad \text{steradian} \qquad 3.5)$$

The fraction τ transmitted by the intervening grey gas

$$= \exp(-Kr) \qquad 3.6)$$

assuming that K is uniform between the two surfaces.

a) Surface-surface exchange b) Volume-surface exchange c) Volume-volume exchange

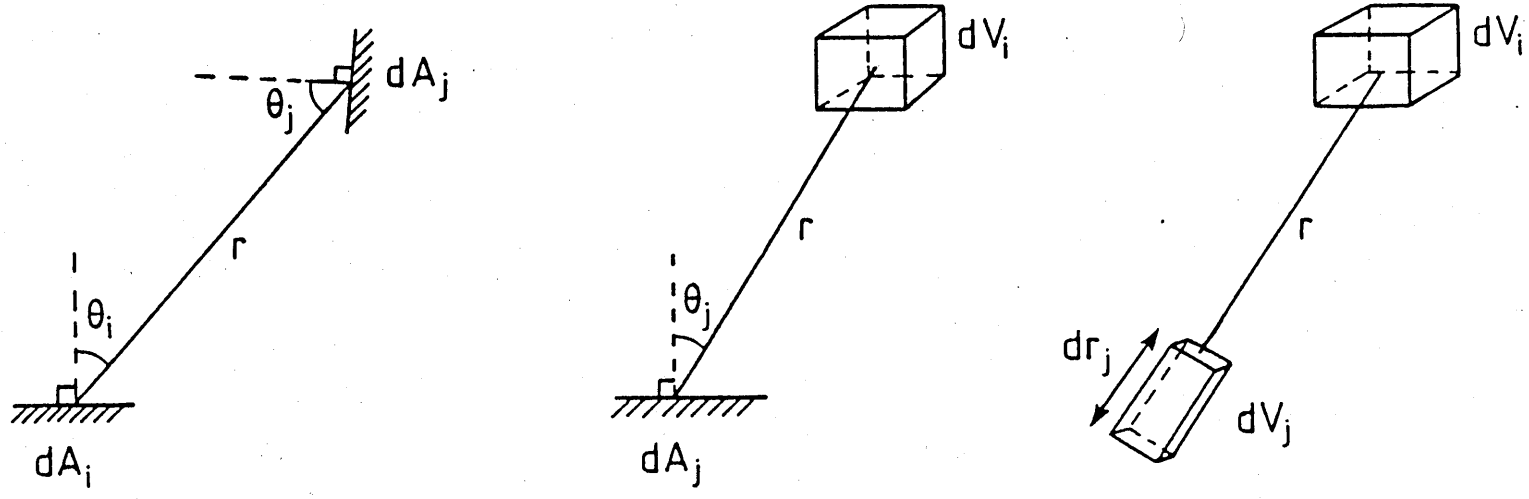

Figure 3.1 Direct exchange between differential surface and volume elements in a radiating enclosure.

The radiant energy leaving dA_i which is directly intercepted by dA_j is the product of terms 3.4), 3.5) and 3.6) thus,

$$\dot{Q}_{i\to j} = E_i dA_i \cos\theta_i dA_j \cos\theta_j \exp(-Kr)/\pi r^2 \qquad 3.7)$$

The formulation of $\overline{s_i s_j}$ for exchange between finite surfaces A_i and A_j follows from equations 3.2) and 3.7),

$$\overline{s_i s_j} = \int_{A_i}\int_{A_j} \frac{\cos\theta_i \cos\theta_j \exp(-Kr)}{\pi r^2} dA_j dA_i \qquad 3.8)$$

From the symmetry of the integral it follows that,

$$\overline{s_i s_j} = \overline{s_j s_i}$$

3.2.2 Volume-Surface Exchange ($\overline{g_i s_j}$)

The direct exchange area between a volume zone i and a surface zone j describes the proportion of radiation emitted from all points within i that arrives at j. Conversely, it represents the proportion of radiation emitted by j that is absorbed within i. As for the surface-surface exchange,

$$\overline{g_i s_j} = \overline{s_j g_i}$$

Consider a differential volume element dV_i within zone V_i, Figure 3.1(b):

The emission from the volume in 4π steradians

$$= \quad 4K_i dV_i E_i \qquad 3.9)$$

The fraction directed towards differential surface dA_j on A_j

$$= \quad dA_j \cos\theta_j / 4\pi r^2 \qquad 3.10)$$

The fraction (τ) transmitted through an intervening gas of extinction coefficient K_i

$$= \quad \exp(-K_i r) \qquad 3.11)$$

Thus, the radiant energy leaving dV_i which is directly intercepted by dA_j is given by the product of terms 3.9), 3.10) and 3.11) thus,

$$\dot{Q}_{i \to j} = \frac{K_i dV_i E_i dA_j \cos\theta_j \exp(-K_i r)}{\pi r^2} \qquad 3.12)$$

The direct exchange area between V_i and A_j is therefore obtained by integration as follows:

$$\overline{g_i s_j} = \frac{\dot{Q}_{i\to j}}{E_i} = \int_{V_i}\int_{A_j} \frac{K_i \cos\theta_j \exp(-K_i r)}{\pi r^2}\, dA_j dV_i \qquad 3.13)$$

3.2.3 Volume-Volume Exchange ($\overline{g_i g_j}$)

Consider a differential volume element dV_i radiating to a rectangular element dV_j which is aligned parallel to r, Figure 3.1(c). Also assume that both differential elements are within a gas of uniform extinction coefficient K. Of the total radiation $4KdV_iE_i$ emitted by dV_i, a fraction equal to $(dA_j/4\pi r^2)\exp(-Kr)$ crosses dA_j into the receiving element dV_j where dA_j is the surface area of the element normal to r. The fraction of this radiation absorbed in dV_j is Kdr_j. Hence,

$$\dot{Q}_{i\to j} = \frac{K^2 dV_i (dA_j dr_j)\exp(-Kr)}{\pi r^2} E_i \qquad 3.14)$$

Replacing $dA_j dr_j$ by dV_j and integrating, the direct exchange area between finite volume zone V_i and V_j therefore becomes:

$$\overline{g_i g_j} = \frac{\dot{Q}_{i\to j}}{E_i} = \int_{V_i}\int_{V_j} \frac{K^2 \exp(-Kr)}{\pi r^2}\, dV_j dV_i \qquad 3.15)$$

3.3 Total Exchange Areas

3.3.1 Definition

The direct exchange areas only consider incident radiation at a surface. The radiation *absorbed* by the surface is a function of its emissivity. Furthermore, the radiation arriving at a surface or gas zone comprises both directly transmitted radiation and multiply reflected radiation off all non-black surfaces forming the enclosure. The net exchange between a pair of surfaces i and j with allowance for reflected radiation within the enclosure is proportional to their total exchange area $\overline{S_i S_j}$ such that,

$$\dot{Q}_{i \leftrightharpoons j} = \overline{S_i S_j}(E_i - E_j) \qquad 3.16)$$

Similarly, total exchange areas can be defined for gas-surface and gas-gas exchange,

$$\dot{Q}_{i \leftrightharpoons j} = \overline{G_i S_j}(E_{g,i} - E_j) \qquad 3.17)$$

and,

$$\dot{Q}_{i \leftrightharpoons j} = \overline{G_i G_j}(E_{g,i} - E_{g,j}) \qquad 3.18)$$

The total exchange areas provide a complete characterisation of the effects of system geometry and of surface emissivities

and gas absorptivities on the radiative transport between zones.

For the grey system defined above, each total exchange area is independent of temperature and need only be calculated once for a given geometry, assuming constant surface emissivities and a constant grey gas attenuation coefficient. It is also independent of the simultaneous occurrence of other modes of heat transfer.

3.3.2 The Calculation of Total Exchange Areas

The arrays of gas-gas, gas-surface and surface-surface total exchange areas are calculated from the corresponding arrays of direct exchange areas by consideration of the radiative energy balance on each zone. The method of calculation follows which is based on a simplification of the method described by Noble [26] for an absorbing, emitting and scattering medium.

Consider a grey surface element of emissivity ε and at a temperature T. The element is part of an enclosure of unspecified geometry or optical character at this point in the derivation. The radiant flux from the surface through an imaginary surface just external to it comprises of two components, εE due to emission and R a reflected component due to partial reflection of the incident flux H coming from the surroundings.

If W is defined as the leaving flux, then:

$$W = \varepsilon E + R$$

$$W = \varepsilon E + \rho H \qquad 3.19)$$

Now consider this surface element to be part of an enclosure of arbitrary geometry having diffusely reflecting (grey Lambert) walls. An optically uniform grey absorbing and emitting medium (the gaseous atmosphere), which is also assumed to be non-scattering is confined within the enclosure. Let the enclosure be sub-divided into M surface zones and L volume zone each considered to be isothermal. The following equation can be written describing the radiant balance at surface zone i:

$$A_i H_i = \sum_{j=1}^{M} \{\overline{s_i s_j} W_j\} + \sum_{j=1}^{L} \{\overline{s_i g_j} E_{g,j}\} \qquad 3.20)$$

Radiation incident on i	=	Radiation ariving directly at i from all surfaces (including i)	+ Radiation arriving directly at i from all volume zones.

The equations for 3 surface elements confining a single grey gas zone (i.e. M=3 ; L=1) can be written thus,

$$A_1H_1 = \overline{s_1s_1}\, W_1 + \overline{s_1s_2}\, W_2 + \overline{s_1s_3}\, W_3 + \overline{s_1g}\, E_g$$
$$A_2H_2 = \overline{s_2s_1}\, W_1 + \overline{s_2s_2}\, W_2 + \overline{s_2s_3}\, W_3 + \overline{s_2g}\, E_g$$
$$A_3H_3 = \overline{s_3s_1}\, W_1 + \overline{s_3s_2}\, W_2 + \overline{s_3s_3}\, W_3 + \overline{s_3g}\, E_g$$

or in matrix form,

$$\begin{bmatrix} A_1 & 0 & 0 \\ 0 & A_2 & 0 \\ 0 & 0 & A_3 \end{bmatrix} \cdot \begin{bmatrix} H_1 \\ H_2 \\ H_3 \end{bmatrix} = \begin{bmatrix} \overline{s_1s_1} & \overline{s_1s_2} & \overline{s_1s_3} \\ \overline{s_2s_1} & \overline{s_2s_2} & \overline{s_2s_3} \\ \overline{s_3s_1} & \overline{s_3s_2} & \overline{s_3s_3} \end{bmatrix} \cdot \begin{bmatrix} W_1 \\ W_2 \\ W_3 \end{bmatrix} + \begin{bmatrix} \overline{s_1g} \\ \overline{s_2g} \\ \overline{s_3g} \end{bmatrix} \cdot E_g$$

which can be written for a general system in shorthand form as follows:

$$\mathbf{AI} \cdot \mathbf{H} = \overline{\mathbf{ss}} \cdot \mathbf{W} + \overline{\mathbf{sg}} \cdot \mathbf{E_g} \qquad 3.21)$$

where,

$$\mathbf{W} = \varepsilon\mathbf{I} \cdot \mathbf{E} + \rho\mathbf{I} \cdot \mathbf{H} \qquad 3.22)$$

AI , **εI** , **ρI** are the diagonal matrices of elements A_i, ε_i, ρ_i

For example:

$$\mathbf{AI} = \begin{bmatrix} A_1 & 0 & \cdots\cdots & 0 \\ 0 & A_2 & 0 \cdots & 0 \\ \vdots & \vdots & \vdots & \\ 0 & 0 & 0 & A_m \end{bmatrix}$$

The net radiative flux leaving each surface zone i is:

$$\dot{Q}_i = A_i(W_i - H_i)$$

$$= \varepsilon_i A_i(E_i - H_i) \qquad 3.23)$$

Again, matrix notation for the set of M surfaces becomes,

$$\dot{\mathbf{Q}} = \mathbf{AI}.(\mathbf{W} - \mathbf{H})$$

$$= \varepsilon\mathbf{AI}.(\mathbf{E} - \mathbf{H}) \qquad 3.24)$$

Similarly, the following radiation energy balance on a volume element i can be written:

$$4\ K_i V_i H_{g,i} = \sum_{j=1}^{M} \{\overline{g_i s_j} W_j\} + \sum_{j=1}^{L} \{\overline{g_i g_j} E_{g,j}\} \qquad 3.25)$$

Radiation absorbed by V_i from all directions	=	Radiation leaving all surfaces which is absorbed by V_i	+	Radiation leaving all volume zones (including V_i), which is absorbed by V_i.

In matrix form for the L equations,

$$4\ \mathbf{KVI}.\mathbf{H_g} = \overline{\mathbf{gs}}.\mathbf{W} + \overline{\mathbf{gg}}.\mathbf{E_g} \qquad 3.26)$$

In equations 3.21) - 3.26) , $\mathbf{E}$, $\mathbf{H}$, $\mathbf{W}$ and $\dot{\mathbf{Q}}$ are M vectors whilst $\mathbf{E_g}$ and $\mathbf{H_g}$ are L vectors. $\overline{\mathbf{ss}}$ and $\overline{\mathbf{gg}}$ are the symmetric (M x M) and (L x L) arrays of direct exchange areas. In accordance with normal matrix notation the first and second subscripts refer to the row and column indices respectively. The matrix $\overline{\mathbf{sg}}$ is therefore an M row x L column array of surface to gas direct exchange areas and $\overline{\mathbf{gs}}$ is its transpose L x M matrix.

From the definition of the total exchange areas it is possible to write the following radiant heat balance between leaving and arriving energy at each surface and volume zone using the total exchange areas and emissive powers rather than direct exchange areas and leaving fluxes (W):

Surface zone balance ($\dot{Q}_i$ = net radiation from zone):

$$\dot{Q}_i = \varepsilon_i A_i E_i - \sum_{j=1}^{M} \{\overline{S_i S_j} E_j\} - \sum_{j=1}^{L} \{\overline{S_i G_j} E_{g,j}\} \qquad 3.27)$$

Volume zone balance ($\dot{Q}_{g,i}$ = net radiation absorbed by i):

$$\dot{Q}_{g,i} = \sum_{j=1}^{L} \{\overline{G_i G_j} E_{g,j}\} + \sum_{j=1}^{M} \{\overline{G_i S_j} E_j\} - 4K_i V_i E_{g,i} \qquad 3.28)$$

also,

$$\dot{Q}_{g,i} = 4K_i V_i (H_{g,i} - E_{g,i}) \qquad 3.29)$$

In matrix notation, these can be written as follows:

$$\dot{Q} = \varepsilon AI.E - \overline{SS}.E + \overline{SG}.E_g \qquad 3.30)$$

$$\dot{Q}_g = \overline{GG}.E_g + \overline{GS}.E - 4KVI.E_g \qquad 3.31)$$

$$\dot{Q}_g = 4KVI.(H_g - E_g) \qquad 3.32)$$

Derivation of algebraic terms for $\overline{SS}$, $\overline{SG}$ and $\overline{GG}$ now follows from manipulation of equations 3.21) to 3.32) :

Substitute W from equation 3.22) into 3.21),

$$AI.H = \overline{ss}.(\varepsilon I.E + \rho I.H) + \overline{sg}.E_g$$

giving,
$$H = R.\overline{ss}.\varepsilon I.E + R.\overline{sg}.E_g \qquad 3.33)$$

where,
$$R = [AI - \overline{ss}.\rho I]^{-1}$$

Similarly substitute W from equation 3.22) into 3.26):

$$4KVI.H_g = \overline{gs}.(\varepsilon I.E + \rho I.H) + \overline{gg}.E_g$$

giving,

$$H_g = [4KVI]^{-1}.[\overline{gs}.(\varepsilon I.E + \rho I.H) + \overline{gg}.E_g] \qquad 3.34)$$

Substitute equation 3.33) for H into equation 3.34):

$$H_g = [4KVI]^{-1}.[\overline{gs}.(\varepsilon I.E + \rho I.R.\overline{ss}.\varepsilon I.E + \rho I.R.\overline{sg}.E_g) + \overline{gg}.E_g]$$

Rearranging,

$$H_g = [4KVI]^{-1}.\overline{gs}.(\varepsilon I + \rho I.R.\overline{ss}.\varepsilon I).E + [4KVI]^{-1}.\overline{gs}.(\rho I.R.\overline{sg}).E_g + [4KVI]^{-1}.\overline{gg}.E_g \qquad 3.35)$$

Substitute equation 3.33) for H into equation 3.24) gives:

$$\dot{Q} = \varepsilon AI.(E - R.\overline{ss}.\varepsilon I.E - R.\overline{sg}.E_g)$$

Comparison with equation 3.30) yields:

$$\overline{SS} = \varepsilon AI.R.\overline{ss}.\varepsilon I \qquad 3.36)$$

$$\overline{SG} = \varepsilon AI.R.\overline{sg} \qquad 3.37)$$

Similarly, substitute 3.35) for H_g into 3.32). Comparison with equation 3.31) gives:

$$\overline{GG} = \overline{gs}.\rho I.R.\overline{sg} + \overline{gg} \qquad 3.38)$$

Thus, the arrays of surface to surface, surface to gas and gas to gas total exchange areas can be evaluated from these simple matrix formulae.

3.4 Reciprocity

The net exchange rate of radiation between two surface zones i and j must be zero when $T_i = T_j$ and thus,

$$\overline{S_iS_j} = \overline{S_jS_i}$$

This relationship is also true for gas-surface and gas-gas total exchange areas and for all corresponding direct exchange areas, thus:

Total exchange areas:

$$\overline{S_iS_j} = \overline{S_jS_i} \qquad \overline{G_iS_j} = \overline{S_jG_i} \qquad \overline{G_iG_j} = \overline{G_jG_i}$$

Direct exchange areas:

$$\overline{s_is_j} = \overline{s_js_i} \qquad \overline{g_is_j} = \overline{s_jg_i} \qquad \overline{g_ig_j} = \overline{g_jg_i}$$

3.5 Summation Rules for Total and Direct Exchange Areas

The following important relationships between the sets of total exchange areas must hold. When all zone temperatures are equal all $\dot{Q}$ and $\dot{Q}_g$ terms in the enclosure are zero, all E and E_g terms are equal, and from equations 3.27) and 3.28) the following rules can therefore be derived:

$$\varepsilon_i A_i = \sum_{j=1}^{M} \overline{S_i S_j} + \sum_{j=1}^{L} \overline{S_i G_j} \qquad 3.39)$$

and,

$$4\, K_i V_i = \sum_{j=1}^{L} \overline{G_i G_j} + \sum_{j=1}^{M} \overline{G_i S_j} \qquad 3.40)$$

Provided the system is grey and optical properties are independent of temperature, these rules will also apply when zone temperatures are not equal since all terms in equations 3.39) and 3.40) are independent of temperature under these conditions.

Similar rules can be derived for direct exchange areas from consideration of equations 3.20) and 3.25) thus:

$$A_i = \sum_{j=1}^{M} \overline{s_i s_j} + \sum_{j=1}^{L} \overline{s_i g_j} \qquad 3.41)$$

and,

$$4K_iV_i = \sum_{j=1}^{M} \overline{g_i s_j} + \sum_{j=1}^{L} \overline{g_i g_j} \qquad 3.42)$$

These summation rules are useful for checking the calculated total and direct exchange areas for a given enclosure. If these summation rules are not obeyed, then a residual error in the calculated energy balance at each zone will arise or at worst, no solution will be found.

3.6 The Representation of a Real Furnace Gas

The foregoing definitions of direct and total exchange areas assume that the participating gaseous medium separating the surfaces is grey and that the grey gas attenuation coefficient (K) is independent of temperature. This assumption is not satisfied for combustion gases comprising of H_2O and CO_2 whose emissivities are very wavelength and temperature dependent. Because of their non-greyness, temperature dependence extends to both the source of emitted radiation as well as to the gas itself. The form of the equations for calculating radiative heat transfer in an enclosure is however greatly simplified if the grey gas assumption can be retained. This can be achieved by representing the emissivity of a real gas as an *a*-weighted summation of the emissivities of a number of grey gases. The total emissivity of a grey gas is given by:

$$\varepsilon_g = 1 - \exp(-k_g pL) \qquad 3.43)$$

where L is the radiation beam length.

The simplest representation of a non-grey gas is the one clear, one grey gas model. The 'clear gas' component represents the windows in the spectrum between the strong emission bands. In this case the total emissivity is given by:

$$\varepsilon_g = a_{g,1}(1 - \exp\{-k_{g,1} pL\})$$

where,

$$a_{g,1} = \frac{\varepsilon^2_{g,L}}{2\varepsilon_{g,L} - \varepsilon_{g,2L}}$$

and,

$$a_{g,o} = 1 - a_{g,1}$$

$a_{g,o}$ and $a_{g,1}$ are the grey-gas weighting coefficients and $\varepsilon_{g,L}$ and $\varepsilon_{g,2L}$ are the calculated emissivities at beam length L and 2L respectively. The above equations do not give an accurate fit to emissivity over the wide range of T and pL encountered in a typical furnace . Consequently, as the solution progresses over each iteration or time step, and zone temperatures change, new values of $\varepsilon_{g,L}$ and $\varepsilon_{g,2L}$ are

calculated from curve fits to T and pL and these are used to recalculate new weighting coefficients.

The total emissivity of a real gas can be represented more accurately and over a wider range of conditions by assuming a larger number of grey gas components. This is expressed mathematically as:

$$\varepsilon_g = \sum_{n=1}^{N} a_{g,n} \left[1 - \exp(-k_{g,n} \cdot pL)\right] \qquad 3.44)$$

where, $$\sum_{n=1}^{N} a_{g,n} = 1$$

The total emissivity of CO_2 and H_2O and of mixtures of the two gases corresponding to fuel derived combustion products, has been accurately expressed by a sum of a few grey gases plus one gas with zero absorption coefficient ($k_{g,1} = 0$).

The important advantage in representing a real gas in this way is that it has been found that $k_{g,n}$ may be held constant and independent of temperature, and that the temperature dependence of ε_g over a wide range can be totally carried by variation of the weighting coefficients $a_{g,n}$. Correlations of this form to measured emissivity data have been derived by Taylor and Foster [27] and Truelove [28] for combustion products comprising of p_c and p_w in the ratios of 1:1 and 1:2.

These ratios correspond approximately to the products of fuel oil and of natural gas combustion respectively. Temperature dependence of ε_g was correlated to acceptable accuracy by assuming that:

$$a_{g,n} = b_{1,n} + b_{2,n}T_g \qquad 3.45)$$

where T_g is the gas temperature in degrees Kelvin.

The correlation coefficients $k_{g,n}$, $b_{1,n}$ and $b_{2,n}$ for a 3 term (2 grey + 1 clear gas) and a 4 term (3 grey + 1 clear gas) fit are given in Table 3.2 for a p_w/p_c ratio of 2. The fit of these correlations to published emissivity data are shown in Figures 3.2 and 3.3. These data are for p_c = 0.1 and for a total pressure of 1 atm. p_c and p_w will vary according to the excess air level and this will lead to changes in emissivity due to pressure broadening effects. Correction factors to the combustion product emissivity due to variations in these partial pressures are given by Hottel and Sarofim [11]. These indicate that the degree of correction is small (<5%) for the normal variations in partial pressures expected in practice. No correction is therefore applied in this work.

The absorptivity $\alpha_{g,s}$ of a gas at T_g to blackbody radiation from a surface at T can be fitted in a like manner, thus:

$$\alpha_{g,s} = \sum_{n-1}^{N} a_{s,n}[1 - \exp(-k_{g,n}\cdot pL)] \qquad 3.46)$$

Table 3.2 **Grey gas parameters used in the correlations for CO_2 and H_2O mixture emissivities [28].**

$p_W/p_C = 2$

$a_{g,n} = b_{1,n} + 10^{-3}.b_{2,n}.T$

n	$b_{1,n}$	$b_{2,n}$ (K^{-1})	$k_{g,n}$ ($m^{-1}atm^{-1}$)
2 grey + 1 clear gas model:			
1	.437	.0713	0
2	.39	-.0052	1.88
3	.173	-.0661	68.8
3 grey + 1 clear gas mode:			
1	.423	.0433	0
2	.285	.0513	0.89
3	.227	-.0676	15.5
4	.065	-.027	240.0

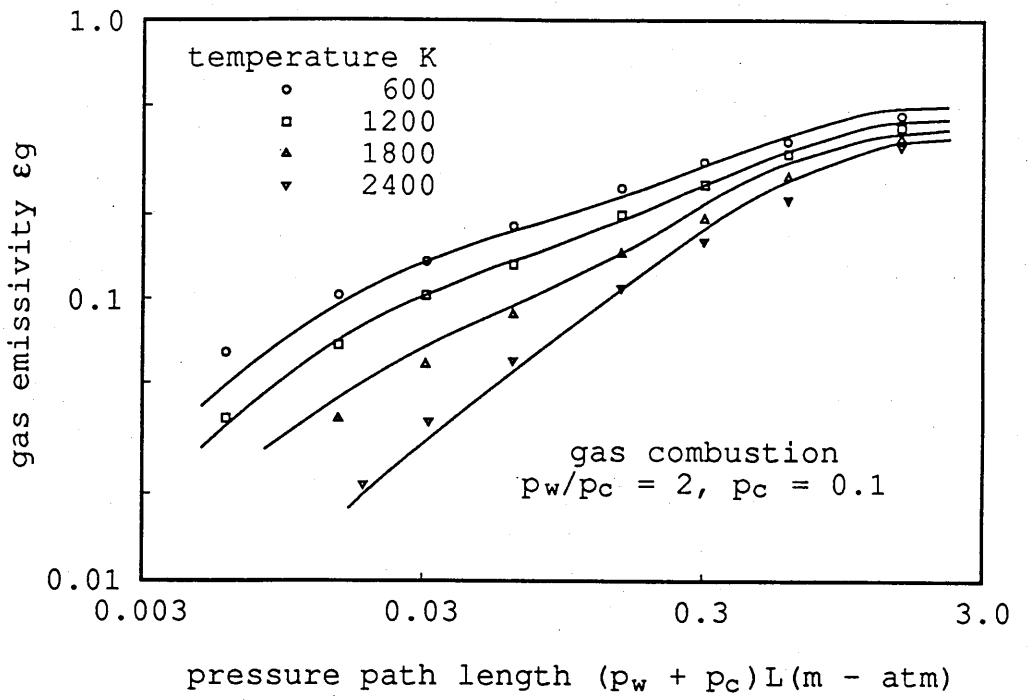

Figure 3.2. Three term fit (1 clear + 2 grey gases) to total emissivity of natural gas combustion products. [28]

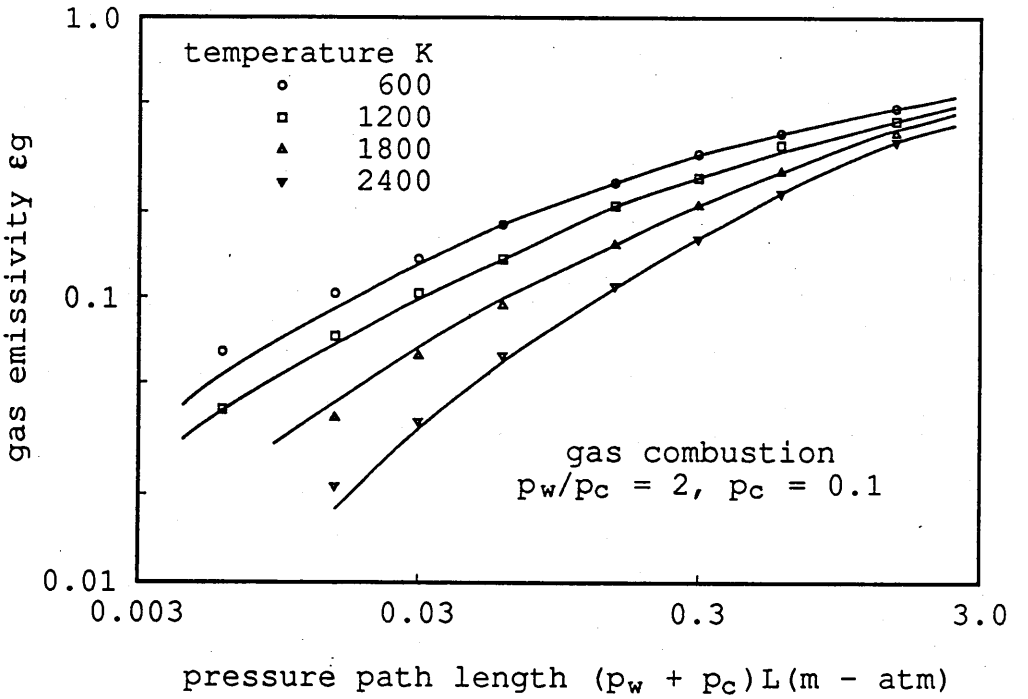

Figure 3.3. Four term fit (1 clear + 3 grey gases) to total emissivity of natural gas combustion products. [28]

where, $\sum_{n=1}^{N} a_{s,n} = 1$

and, $a_{s,n} = b_{1,n} + b_{2,n}T$

To acceptable accuracy, $a_{g,n}$ and $a_{s,n}$ are found to be dependent only on the temperature of the emitter (i.e. gas temperature in the case of emissivity and source emitter temperature in the case of absorptivity).

3.7 Directed Flux Areas

It has been shown how the emissivity and absorptivity of a non-grey gas can be correlated against pL and T by an a-weighted summation of a small number of grey gases plus one clear gas. If the set of all total exchange areas are calculated for each of the grey and clear gases within such a model, the radiant flux between any two zones can also be represented by the same a-weighted summation of the independent contributions of each gas. The net flux between a gas zone i at temperature $T_{g,i}$ and a surface zone j at $T_{s,j}$ for example is given by,

$$\dot{Q}_{i \leftrightarrows j} = \sum_{n=1}^{N} a_{g,n}(T_{g,i})\{\overline{G_i S_j}\}(K_n).E_{g,i} - \sum_{n=1}^{N} a_{s,n}(T_{s,j})\{\overline{G_i S_j}\}(K_n).E_{s,} \qquad 3.47)$$

where each summation is over the N component gases in the mixed grey and clear gas model with $\overline{G_iS_j}(K_n)$ evaluated with $K_1 = 0$, $K_2 = k_{g,2}(p_w+p_c)$, $K_n = k_{g,n}(p_w+p_c)$.

The definition of all directed flux areas follows by comparison of this equation with equation 3.1) thus:

$$\overrightarrow{G_iS_j} = \sum_{n=1}^{N} a_{g,n}(T_{g,i}) \{\overline{G_iS_j}\}(K_n) \qquad 3.48(a)$$

$$\overleftarrow{G_iS_j} = \sum_{n=1}^{N} a_{s,n}(T_{s,j}) \{\overline{G_iS_j}\}(K_n) \qquad 3.48(b)$$

and for surface-surface transfer,

$$\overrightarrow{S_iS_j} = \sum_{n=1}^{N} a_{s,n}(T_{s,i}) \{\overline{S_iS_j}\}(K_n) \qquad 3.48(c)$$

$$\overleftarrow{S_iS_j} = \sum_{n=1}^{N} a_{s,n}(T_{s,j}) \{\overline{S_iS_j}\}(K_n) . \qquad 3.48(d)$$

and gas-gas transfer,

$$\overrightarrow{G_iG_j} = \sum_{n=1}^{N} a_{g,n}(T_{g,i}) \{\overline{G_iG_j}\}(K_n) \qquad 3.48(e)$$

$$\overleftarrow{G_iG_j} = \sum_{n=1}^{N} a_{g,n}(T_{g,j}) \{\overline{G_iG_j}\}(K_n) \qquad 3.48(f)$$

The weighting coefficients in each case are given as follows:

$$a_{g,n}(T_{g,i}) = b_{1,n} + b_{2,n} \cdot T_{g,i} \qquad 3.49(a)$$

$$a_{s,n}(T_{s,i}) = b_{1,n} + b_{2,n} \cdot T_{s,i} \qquad 3.49(b)$$

where $b_{1,n}$, $b_{2,n}$ and $k_{g,1}$, $k_{g,2} \ldots . k_{g,n}$ are the coefficients in the mixed grey gas model.

3.8 The Total Energy Balance

A total energy balance can now be written on each volume and surface zone in the enclosure in terms of the zone temperatures (T) and their hemispherical black-body emissive powers (E).

The balance on surface zone i can be written as follows, which includes the convective heat transfer from the contiguous gas zone at temperature T_g :

$$\sum_j \overrightarrow{S_j S_i} \cdot E_{s,j} + \sum_j \overrightarrow{G_j S_i} \cdot E_{g,j} - A_i \varepsilon_i E_{s,i} + A_i h_i (T_g - T_{s,i}) = \dot{Q}_i \qquad 3.50)$$

where $\dot{Q}_i$ is the net heat transfer rate into the surface. For an adiabatic surface, $\dot{Q}_i = 0$. In practice $\dot{Q}_i$ will equal a loss to a heat sink or to the ambient environment.
The balance on a gas zone i is written as follows:

$$\sum_j \overrightarrow{G_jG_i}.E_{g,j} + \sum_j \overrightarrow{S_jG_i}.E_{s,j} - 4K_iV_iE_{g,i} +$$

$$\dot{m}_{G,i}C_{net} + \dot{Q}_{enth,i} - \dot{Q}_{conv,i} = 0 \qquad 3.51)$$

where,

$\dot{m}_{G,i}C_{net}$ - is the rate of net heat input to the zone from the combustion of $\dot{m}_{G,i}$ kg/s of fuel (assuming complete combustion).

$\dot{Q}_{enth,i}$ - is the rate of arrival minus departure of sensible enthalpy of the products of combustion flow through zone i.

$\dot{Q}_{conv,i}$ - is the convective heat transfer to all contiguous surface zones.

$4K_iV_iE_{g,i}$ - equals the rate of emission of radiant energy from the gas within i which can be expanded for a multiple grey gas model as follows:

$$4K_iV_iE_{g,i} = 4\sum_{n=1}^{N} a_{g,n}k_{g,n}(p_w+p_c)_iV_iE_{g,i} \qquad 3.52)$$

CHAPTER 4

Description of the Steady-State and Transient Models

4.1 Introduction

Generalised steady-state and a transient long furnace models have been written based on the zone method described in Chapter 3. The specification and description of these models is now described in Chapters 4-6. For convenience the abbreviations SSZONE for the steady-state model and TRZONE for the transient model are employed.

4.2 Zone Numbering in SSZONE and TRZONE

The zoning arrangement is illustrated in Figure 4.1. It comprises of a single row of NZONE gas zones of equal width and of equal length in the longitudinal (x) direction. There is an equal load surface area in each zone, which is centrally placed on the floor or hearth of the furnace. By specification of the parameter NWALL in the models, two alternative options can be selected for the configuration of the internal surfaces.

In its simplest form (NWALL = 2), the roof, side walls and exposed hearth surrounding each gas zone are assumed to be one isothermal surface of common material of construction. An

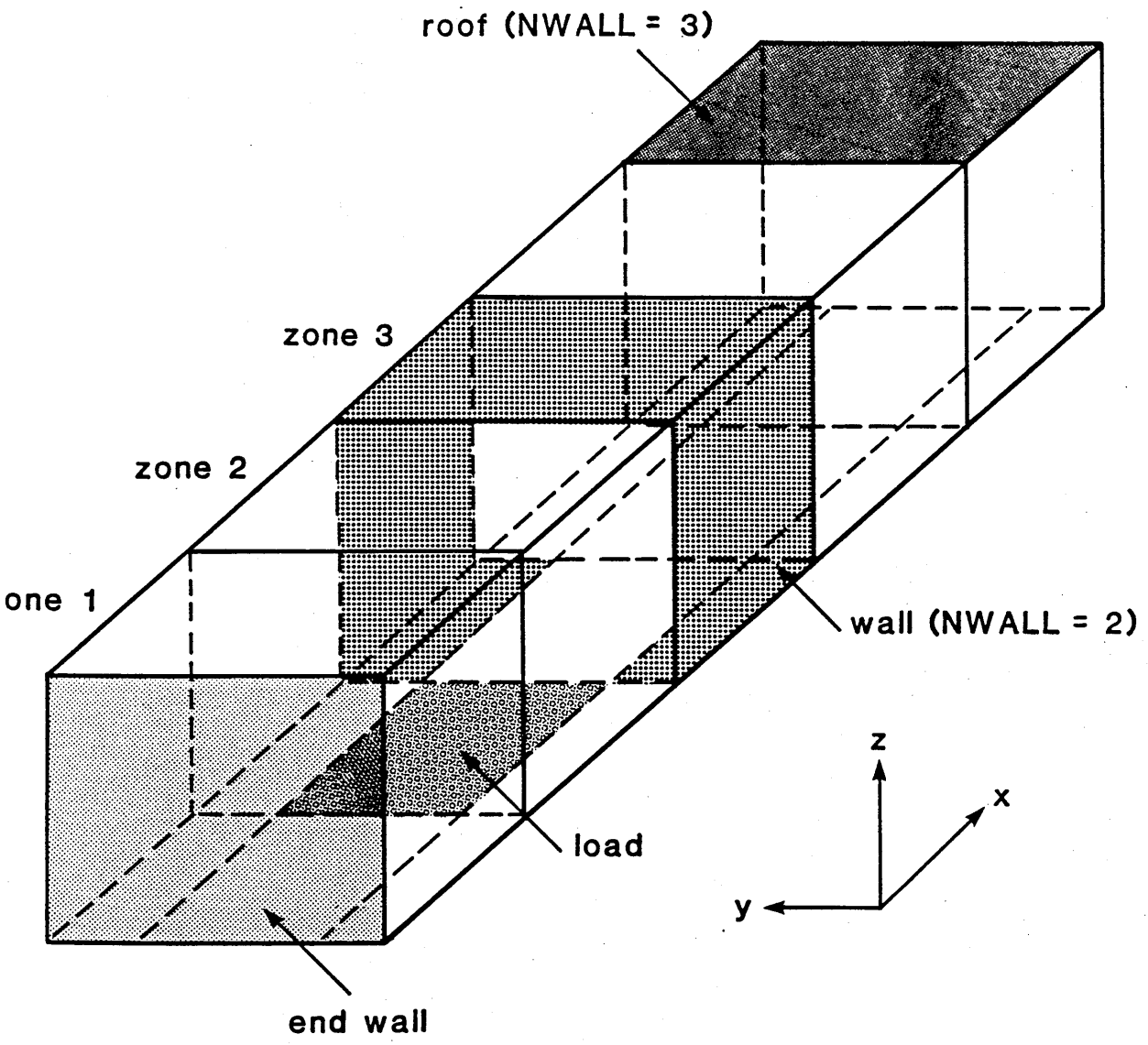

Figure 4.1 The arrangement of surface and gas zones in SSZONE and TRZONE

alternative zoning arrangement (NWALL = 3) can be selected whereby the roof is treated as a separate zone. In either case the end walls are treated as separate surfaces.

The width (y - dimension) of both the furnace and the load are assumed to be constant along the length. To facilitate exchange area calculation between zones, the height of all zones was also initially assumed to be constant giving a rectangular furnace geometry. This restriction was later relaxed with the development of a Monte-Carlo method for exchange area calculation (see Chapter 9).

4.3 Choosing the Zone size

A compromise has to be reached between maximising the number of zones (NZONE), and thereby increasing the accuracy of the model, and minimising the computation time. In practice, selection of the zone length may be dictated by the requirements of the model to accurately represent the following:

- the number and position of burners
- the length and number of temperature control zones
- flue positions
- the geometry or longitudinal profile of the furnace

4.4 Outline of the Preliminary Computation Procedure

Both SSZONE and TRZONE start with a common list of input parameters which are needed to calculate the large number of total exchange areas for each zone pair (see Table 3.1).
These parameters are :

- Number of zones (NZONE).
- Zone length, width and height.
- NWALL
- Surface emissivities
- Excess air level (this defines p_{H2O} and p_{CO2}).

Initially, the direct exchange areas are calculated using all of this input data excepting the surface emissivities ; the direct exchange areas are calculated by the methods to be described in Chapters 7 to 9 and these are assigned to arrays as follows:

$\overline{ss}$ - for $k_g = k_{g,1} = 0$ (ie. the clear gas component)
$\overline{gg}$ - for $k_g = k_{g,2}$ (ie. the first grey gas component)
$\overline{gs}$ - for $k_g = k_{g,2}$ (ie. the first grey gas component)
$\overline{ss}$ - for $k_g = k_{g,2}$ (ie. the first grey gas component)
$\overline{gg}$ - for $k_g = k_{g,3}$ (ie. the second grey gas component)
$\overline{gs}$ - for $k_g = k_{g,3}$ (ie. the second grey gas component)
$\overline{ss}$ - for $k_g = k_{g,3}$ (ie. the second grey gas component)

These are then used with the surface emissivities, to compute the corresponding arrays of total exchange areas using equations 3.36)-3.38). After a checking and correction procedure (described in Chapter 10) to ensure that the summation and reciprocity rules are obeyed, the arrays of total exchange areas are written to a file for subsequent access by SSZONE and TRZONE.

4.5 Physical Assumptions

In the development of SSZONE and TRZONE, the following physical assumptions have been made.

1) In accordance with the requirements of the zone method, the gas zones are assumed to be well stirred thus implying uniform composition and temperature. The surrounding surface zones are similarly assumed to be isothermal. For simplicity, gas composition is assumed to be uniform throughout the furnace chamber.

2) Surfaces are assumed to be grey and diffusely reflecting (i.e. grey Lambert surfaces).

3) The combustion products are assumed to be non-luminous. Their non-grey nature is considered to be important and is represented by a multiple grey and clear gas model.

4) Radiant interchange between zones is considered to be important. Correct representation of the internal furnace geometry is considered important.

5) Convective heat transfer at the surface zones, although included, accounts for less than 5% of the total heat transfered within most conventional furnaces. Therefore, convective heat transfer coefficients do not need to be accurately specified and can be calculated from experimental correlations for simple flow configurations.

6) Variation of the thermal properties of the furnace and load materials over the wide range of temperatures encountered is considered to be significant.

7) Combustion is assumed to be completed at the point of entry of the thermal input to a zone. This is approximated by many modern industrial gas burners which make use of the thrust provided by the combustion air to generate high rates of mixing within the burner quarl or tunnel. Therefore, a heat release pattern does not need to be specified within each zone.

CHAPTER 5

The Steady-State Model (SSZONE)

5.1 Specification of SSZONE

SSZONE predicts the performance of a furnace which is operating continuously at a constant firing and production rate. It predicts the energy (gas) consumption on a natural gas fired furnace given the load throughput rate and discharge temperature. Although SSZONE simulates a furnace operating under idealised conditions, it will represent a real furnace that has been running for a prolonged period of continuous operation as occurs with some larger reheating applications.

In SSZONE, it is assumed that the load enters the furnace at zone NZONE and is discharged hot from zone 1 at a specified temperature and throughput rate. The load is also assumed to be at uniform temperature throughout its thickness i.e. infinite thermal conductivity in the load is assumed.

Although the total rate of fuel input is computed, the relative distribution of fuel to each zone must be specified in the input data. Similarly, the distribution of the combustion products exhausted to atmosphere from each zone must be specified.

The output from the model includes all surface and gas zone temperatures and heat fluxes, together with the computed rates of useful energy transfer to the load.

A steady-state value for the heat flux ($\dot{q}_{loss}$) through the wall, roof and hearth surfaces to the ambient environment is specified in the input data. Calculation of the external wall temperatures is thereby ignored. Furnace wall insulation should normally be designed to ensure a maximum outside surface temperature (typically <100^{o}C). It would therefore seem appropriate to equate this to a heat flux and thus avoid the solution of additional equations for the heat transfer by conduction through the insulation and by natural convection and radiation off the external surface. Since wall losses are usually a small fraction (<5%) of the thermal input to a furnace, this simplified treatment of the insulation losses is justified. By avoiding the need to solve for the external insulation temperatures at each zone, a larger number of zones can be employed in the model for the same demands on computer memory and time.

5.2 The Heat Balance Formulation in SSZONE

Total energy balance equations are written for each gas and surface zone including terms for arriving and leaving radiation, convection, conduction and enthalpy transport. The

total number of surface zones for which a balance equation must be formulated is given by,

$$M = NZONE \times NWALL + 2 \qquad 5.1)$$

These equations generally comprise of NZONE equations for load surfaces with the remainder (M-NZONE) being stationary wall and roof surfaces. The energy balance equation for an internal roof or wall surface zone i is given as follows:

$$\underset{(A)}{\sum_{j}^{M} \overrightarrow{S_j S_i} \sigma T_j^4} + \underset{(B)}{\sum_{j}^{L} \overrightarrow{G_j S_i} \sigma T_{g,j}^4} \underset{(C)}{- A_i \varepsilon_i \sigma T_i^4} \underset{(D)}{+ A_i \dot{q}_{conv,i}} \underset{(E)}{- A_i \dot{q}_{cond,i}} = 0 \qquad 5.2)$$

For a load surface zone i:

$$\underset{(A)}{\sum_{j}^{M} \overrightarrow{S_j S_i} \sigma T_j^4} + \underset{(B)}{\sum_{j}^{L} \overrightarrow{G_j S_i} \sigma T_{g,j}^4} \underset{(C)}{- A_i \varepsilon_i \sigma T_i^4} \underset{(D)}{+ A_i \dot{q}_{conv,i}} \underset{(E)}{- A_i \dot{q}_{cond,i}} = \underset{(F)}{\dot{m}_L (I_L(T_i) - I_L(T_k))} \qquad 5.3)$$

where L = NZONE and M is as defined above.

In equations 5.2) and 5.3), the terms A to F are as follows:

A and B are the sum of the arriving radiation from all surface zones (including i), and all gas zones respectively.
C is the leaving radiation from i.

D is the convective heat transfer between i and the contiguous gas zone whose temperature is T_g. This is given by,

$$A_i \dot{q}_{conv,i} = A_i h (T_g - T_i) \qquad 5.4)$$

The calculation of h will be dealt with in Section 5.5.

E is the conduction through the insulation where $\dot{q}_{cond,i}$ is specified in the input data. It is equal to the combined flux due to radiation and natural convection between the outer casing of the furnace and the ambient environment. In the case of the load zone, $\dot{q}_{cond,i}$ equals the conduction through the hearth of the furnace.

F in the load heat balance equation, equals the enthalpy gained by the load as it moves to i from the downstream zone k (with respect to the direction of load transport). $I_L(T)$ is the specific enthalpy of the load material and $\dot{m}_L$ is the mass throughput of load. $I_L(T)$ is described by a polynomial in (T) dependent on the type of load. Data and polynomials for a number of common metals are given by Tucker and Rhine [30].

NZONE energy balance equations can also be written for each gas zone i as follows:

$$\underset{(A)}{\sum_{j}^{L} \overrightarrow{G_j G_i} \sigma T_{g,j}^4} + \underset{(B)}{\sum_{j}^{M} \overleftarrow{G_i S_j} \sigma T_j^4} - \underset{(D)}{\dot{Q}_{conv,i}} - \underset{(C)}{4 K_i V_i \sigma T_{g,i}^4}$$

$$+ \underset{(G)}{\dot{m}_{G,i}(C_{net} + R_a I_a (T_a))} + \underset{(H)}{\dot{Q}_{enth,i}} = 0 \qquad 5.5)$$

Terms A,B and C represent the same terms as defined in the surface energy balance equations.

Term D in this case is the sum of the convective transfer to all contiguous surface zones.

Term G equals the enthalpy input to i due to combustion of $\dot{m}_{G,i}$ kg/s natural gas entering the zone plus the enthalpy input in $\dot{m}_{G,i} R_a$ kg/s combustion air at temperature T_a. It is assumed that 100 % heat release due to combustion occurs at the point of input to the zone. T_a can be calculated from the effectiveness and the inlet flue gas temperature of a heat recovery device (see section 5.6).

Term H equals the sensible enthalpy input minus output to the zone due to the transport of the combustion products flowing through i, see Figure 5.1. This includes the rate of sensible

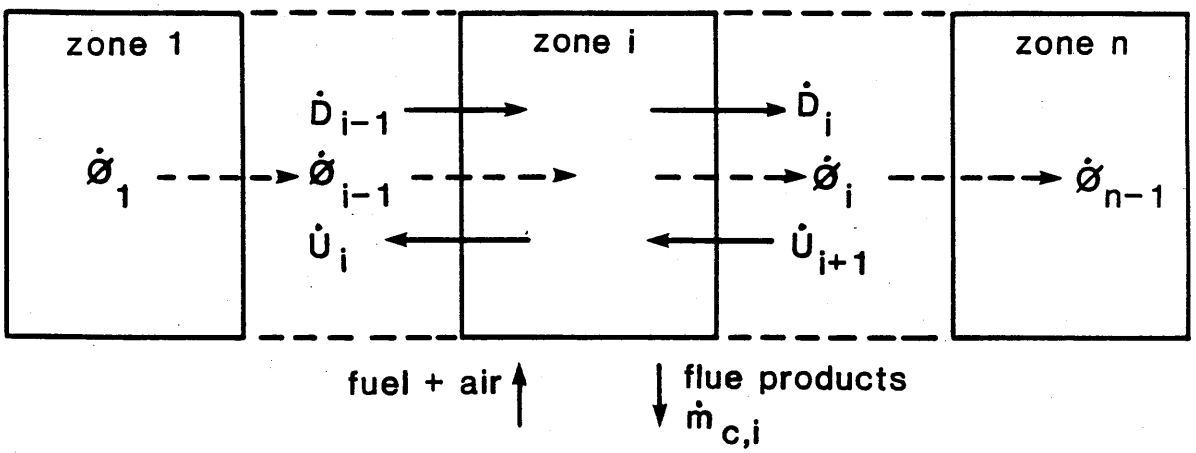

$\dot{D}_{i-1}$, $\dot{D}_i$ = downstream flow components kg/s

$\dot{U}_i$, $\dot{U}_{i-1}$ = upstream flow components kg/s

$\dot{\varnothing}_i$ = net downstream flow from i kg/s

Figure 5.1 The flow field specification across a zone

enthalpy arriving minus that leaving i from adjacent gas zones, minus the enthalpy loss from i through a flue (if present at that position), or due to leakage from the furnace.

5.3 The Solution procedure.

The energy balance equations for each zone, which are non-linear in temperature, are solved simultaneously using an iterative solution procedure for all unknown variables. These equations are rearranged into the general form,

$$f_i(T_1, T_2, \ldots\ldots T_n) = 0 \qquad 5.6)$$

where f_i is the energy balance equation for surface or gas zone i, and T_1, T_2 etc are the surface and gas zone temperatures.

A total of NX equations can be written and solved for NX unknown variables, where NX is the total number of surface and gas zones in the model, and is given by,

$$NX = M + NZONE \qquad 5.7)$$

A general solution procedure based on the Newton technique was selected for this purpose. The Newton method solves all

equations simultaneously. Initially however, a Gauss-Seidel procedure was tried. Both techniques are described in detail in Appendix 1.

A comparison of the solutions obtained by the two methods was made for a simple 5 zone model. The following observations were made:

i) The Gauss-Seidel method required 35 cycles to achieve a convergence to within 0.1 degrees K. At convergence, the absolute sum of the residuals on all heat balance equations was 30.4 Joules.

ii) The general Newton method required 4 iterations to achieve the same convergence at which the sum of the residuals was 2.84 Joules.

iii) Inspection of a sample of the variables solved by the two techniques is given in Table 5.1, which shows that there is significant difference between the solutions, above 30 deg K in some cases. Since the sum of the residuals is much smaller with the general Newton method, it can be assumed that this is achieving a more accurate solution. Inspection of the individual residuals on each equation confirmed that all equations were being solved within an acceptable limit. The Gauss-Seidel method clearly provides insufficient correction

Table 5.1 A comparison of the solutions of the heat balance equations by the general Newton method and by Gauss-Seidel iteration.

l = load surface zone ; *g* = gas zone ; *ew* = end wall

w = wall zone (= side walls and exposed hearth) ; *r* = roof

Zone number I	First guess	Second guess	Newton solutiom TOL = 0.1 T(I)	Residual	Gauss-Seidel Solution T(I)	Residual
1(*ew*)	1600	1000	1760	-.156	1736	-2.09
2(*w*)	1600	1000	1759	-.089	1736	-2.03
4(*l*)	1523	1523	1705	.26	1676	-1.66
6(*r*)	1550	950	1688	-.338	1663	-1.78
7(*l*)	1276	1276	1579	.0805	1545	-1.2
9(*r*)	1500	900	1578	.0783	1553	-1.2
10(*l*)	1029	1029	1364	-.0853	1326	-.6
12(*r*)	1450	850	1463	.104	1440	-.906
13(*l*)	782	782	1055	-.01	1020	-.25
15(*r*)	1400	800	1393	.029	1371	-.789
16(*l*)	535	535	679	-.0393	658	-.0156
17(*ew*)	1400	800	1408	.0788	1386	-.797
18(*g*)	1800	1400	2020	-.000405	2011	-.0142
19(*g*)	1800	1400	1919	-.00106	1905	-.0142
20(*g*)	1800	1400	1818	-.00133	1800	-.0138
21(*g*)	1800	1400	1716	.00178	1696	-.0142
22(*g*)	1800	1400	1619	-.00269	1598	-.0133
				R_{sum}=2.84		R_{sum}=30.4

to the variables once the solution is approached. Thus the same convergence criterion is satisfied because the corrections to T_j are so small at each cycle.

iv) As a final test of the validity of the general Newton method, the initial guesses were changed dramatically to the values shown in column 4 of Table 5.1. The same solution was achieved with a sum of residuals of 2.91.

Thus, the Newton method was selected as the chosen solution procedure. It also has the advantage over the Gauss-Seidel method, that solution need not be restricted to unknown temperatures only. The Gauss-Seidel technique only works because the heat balance about each zone j is dominated by the unknown temperature T_j. With the Newton technique, if one of the temperatures is known, such as the load discharge temperature, this can be replaced by an alternative unknown variable such as fuel flow rate.

In SSZONE, all surface and gas zone temperatures excepting the load discharge temperature from zone 1 are unknown. The latter is specified in the input data to the model. In the solution procedure, the fuel flow rate is substituted for the load discharge temperature to complete the list of NX unknown parameters to be determined.

The energy balance equations include the directed flux areas which are computed from the a-weighted summation of the total exchange areas. As zone temperatures change after each iteration towards a solution, the directed flux areas must be re-calculated since the a-weighting coefficients are temperature dependent (see Chapter 3).

The Newton solution procedure for solving a system of simultaneous non-linear equations is described in detail in Appendix 1.

5.4 The calculation of $\dot{Q}_{enth,i}$

With reference to Figure 5.1 , $\dot{Q}_{enth,i}$ can be expanded as follows:

$$\dot{Q}_{enth,i} = \dot{D}_{i-1}I_{g,i-1} + \dot{U}_{i+1}I_{g,i+1} - (\dot{U}_i+\dot{D}_i)I_{g,i} - \dot{m}_{c,i}I_{g,i} \qquad 5.8)$$

where $I_{g,i}$ is the specific enthalpy of the combustion products in zone i.

$\dot{D}$ and $\dot{U}$ are downstream and upstream components of mass flow, and these are specified in the input data.

5.5 The calculation of Convective Heat Transfer

The convective transfer $\dot{Q}_{conv,i}$ between a gas at T_g and a contiguous surface zone i at T_i is calculated from the simple expression,

$$\dot{Q}_{conv,i} = hA_i(T_g - T_i) \qquad 5.9)$$

where h is the convective heat transfer coefficient which is determined from simple dimensionless correlations available in the literature. These are of the general form,

$$Nu = aRe^bPr^c \qquad 5.10)$$

where $Nu = h\,D/\lambda$; $Re = \rho Du/\mu$; $Pr = C_p\mu/\lambda$

In SSZONE and TRZONE , the Dittus-Boelter correlation [29] was applied where the constants a = 0.023 , b = 0.8 and c = 0.4 This correlation applies to fully developed and turbulent flow in a pipe where Re > 20 000. In most furnaces, the flow is transitional (2000 < Re < 20 000) and developing. Transitional flows often have a strong buoyancy component giving rise to so called 'mixed-convection', particularly where large temperature gradients exist at the surfaces. Simple correlations for h do not exist for these complex flows. Some allowance can however be made for developing flow downstream of a sharp edged entrance. Using the following

relationship [29], the mean coefficient h_m over the entry length x=0 to x=L is related to the fully developed value h_∞ at $L=\infty$ as follows:

$$h_m/h_\infty = 1 + (D/L)^{0.7} \qquad 5.11)$$

h_m is related to the local coefficient h_x by,

$$h_m = 1/L \cdot \int_{x=0}^{L} h_x.dx \qquad 5.12)$$

The local coefficient h_x can be related to the fully developed coefficient h_∞ as follows,

$$h_x = h_\infty(1 + .3(D/x)^{.7}) \qquad 5.13)$$

Where the main flow direction is from zone 1 to NZONE, then x is equal to the distance from the end wall in zone 1 to the centre of the zone for which h_x is being calculated. For flow in the opposing direction, x relates to the distance from the end wall in zone NZONE.

Because of the dominance of radiation, convective heat transfer in high temperature furnaces usually only accounts

for a small percentage (approximately 5%) of the total heat transfer from the combustion gases. The above correlation with an entry correction term for developing flows is therefore considered acceptable for the level of precision required.

The properties substituted into Re and Pr are calculated at the gas zone temperature T_g which is representative of the bulk fluid temperature. The length term in Nu and the entry correction term is equal to the hydraulic mean diameter D_m calculated as follows,

$$D_m = 4A_S/P \qquad 5.14)$$

where A_S is the cross sectional area of the furnace perpendicular to the flow direction, and P is the perimeter. These terms can either be specified in the input data or they can be calculated from the geometry of the furnace.

In SSZONE, h_X is repeatedly re-calculated using these correlations as the flow rates and temperatures in each zone change at each iteration towards the solution. The convective heat transfer coefficient can alternatively be specified as a fixed value in the input data which remains constant irrespective of the current temperatures and flow rates. This

feature can be useful in the following two ways:

i) to carry out sensitivity checks on the effects of zero, or arbitrarily low or high convective heat transfer coefficients,

ii) to input coefficients determined from other sources eg. physical modelling experiments or hot measurements.

5.6 The Calculation of Air Temperature

The air preheat temperature to a zone with combustion in it is calculated from a fixed effectiveness value (η_{eff}) relating to a given heat recovery device. η_{eff} is defined as the energy recovered in the air as a fraction of the maximum recoverable within an infinitely long counterflow heat exchanger, thus:

$$\eta_{eff} = \frac{(\dot{m}C_p)_{air}\ (T_{a,out}-T_{a,in})}{(\dot{m}C_p)_{min}\ (T_{c,in}-T_{a,in})} \qquad 5.15)$$

$T_{a,out}$ and $T_{a,in}$ are the air outlet and inlet temperatures respectively.
$T_{c,in}$ is the inlet combustion products temperature.
$(\dot{m}C_p)_{air}$ is the heat capacity flow rate of the air.
$(\dot{m}C_p)_{min}$ is the lower of the heat capacity flow rates of the air and combustion products streams. Where all of the

combustion products derived from the air are returned through the heat recovery device, then this term equals $(\dot{m}C_p)_{air}$.

Hence,

$$\eta_{eff} = \frac{(T_{a,out}-T_{a,in})}{(T_{c,in}-T_{a,in})} \qquad 5.16)$$

and, $$T_{a,out} = \eta_{eff}(T_{c,in}-T_{a,in}) + T_{a,in} \qquad 5.17)$$

Two alternative methods of heat recovery can be selected in the input data, as follows (Figure 5.2):

i) Local heat recovery on zone i representing recuperative or regenerative burners for example. In this case $T_{c,in} = T_{g,i}$ and $T_{a,out}$ is the preheat temperature for air supplied to zone i only. The air preheat temperature at each zone may in this case be different depending on the value of $T_{g,i}$.

ii) Heat recovery from the main flue for example, which receives combustion products from all flues specified in the model and preheats the combustion air to the furnace to the same temperature irrespective of the firing zone. In this case,

$$T_{c,in} = \Sigma \dot{m}_{c,i}T_{g,i} / \Sigma \dot{m}_{c,i} \qquad 5.18)$$

which equals a mass flow weighted average of all exit flue gas temperatures from the zones.

a) Local heat recovery on zone i

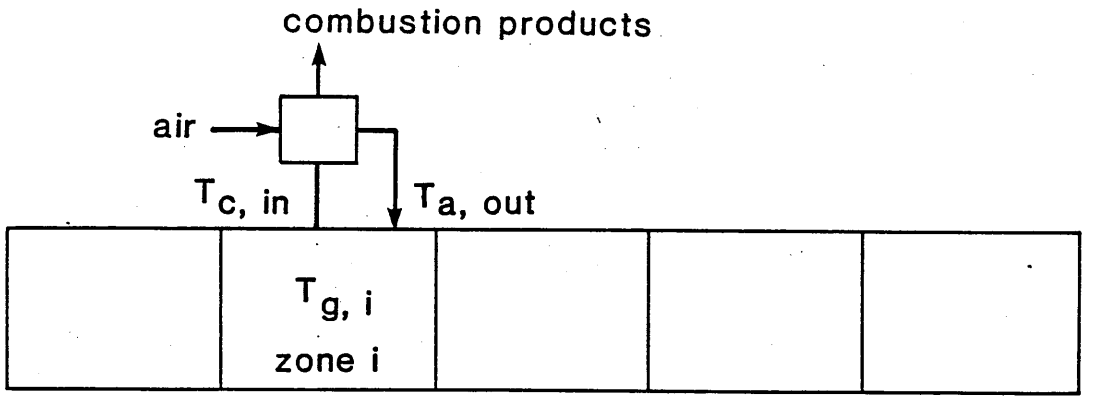

b) Heat recovery from main flue

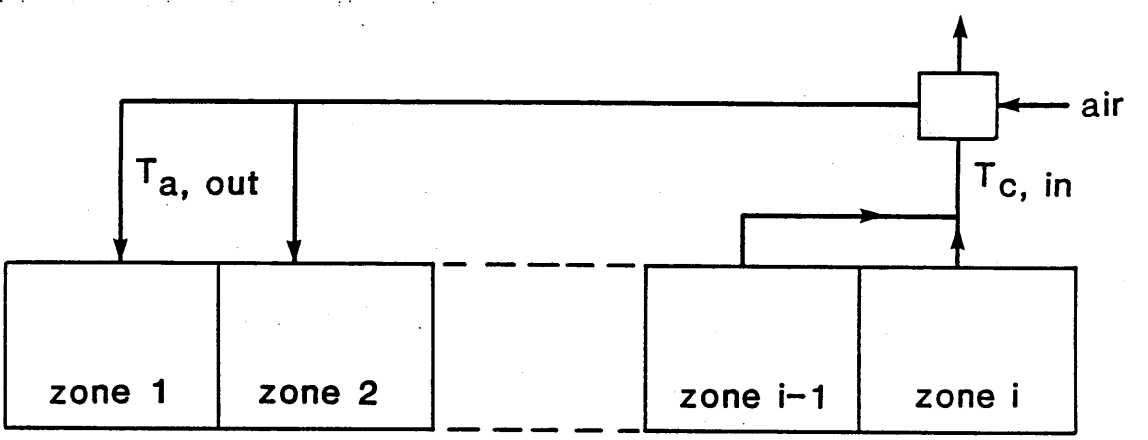

Figure 5.2 The representation of combustion air preheating in a long furnace model.

5.7 The Calculation of Door Losses

Open doors on furnaces can result in considerable heat loss by radiation which can significantly reduce the thermal efficiency of high temperature plant. Combustion product leakage or, if the furnace operates under suction, cold air ingress through the door can also contribute to a reduction in thermal performance. A method is now described for allowing for radiation loss from a single door of area A_d in SSZONE. Because of the difficulties of calculating leakage or air ingress through doors, no attempt is made to allow for these although air leakage can simply be represented in SSZONE by specifying an additional flue loss from the zone containing the door.

To avoid the necessity of simulating the door as an extra surface zone, and therefore calculating the exchange areas to it, the door was assumed to occupy a fixed fraction (A_d/A_N) of a specified surface zone N of surface area A_N and to 'share' its exchange areas.

The presence of a door does not affect the quantity of radiation arriving at zone N from all other zones in the enclosure. It does however reduce the radiation that is both reflected and re-emitted from N. The reduction in reflected radiation can be simulated by specifying an increased surface

emissivity for zone N when the exchange areas are calculated. For this purpose, a corrected emissivity is applied equal to an area weighted average of the true surface emissivity and that of a hole with an emissivity of 1.0 representing the door, thus:

$$\varepsilon_N' = A_d/A_N + (1-A_d/A_N)\varepsilon_N \qquad 5.19)$$

where ε_N is the emissivity of the refractory in zone N, and ε_N' is the corrected emissivity allowing for a door.

The emitted radiation is assumed to be reduced by a factor $(1-A_d/A_N)$. The radiation from surface N with black emissive power E_N to all other gas and surface zones in the enclosure then becomes:

$$\dot{Q} = (1-A_d/A_N).(\sum_j \overleftarrow{G_jS_N} + \sum_j \overleftarrow{S_jS_N}).E_N \qquad 5.20)$$

The radiation loss through the door is therefore,

$$\dot{Q}_{door} = A_d/A_N.(\sum_j \overleftarrow{G_jS_N} + \sum_j \overleftarrow{S_jS_N}).E_N \qquad 5.21)$$

which represents the decrease in emission from zone N on account of the fraction (A_d/A_N) of its area having an

effectively zero radiant emission.

This treatment of the door loss is similar in concept to the speckled enclosure model of Hottel and Sarofim [11]. The geometric position and orientation of the door in zone N is assumed to be intimately mixed with the surface.

CHAPTER 6

The Transient Model (TRZONE)

6.1 Specification of TRZONE

In practice the mode of operation of most furnaces is transient. Modelling of their true thermal behaviour under real production conditions demands the use of a transient mathematical model. The purpose of TRZONE is to simulate the time varying thermal performance of a furnace for the following situations:

i) During its start up from cold

ii) During the period when the furnace is operating but when the temperatures of the walls, hearth and load are still approaching their thermal equilibrium values (i.e. steady-state)

iii) When a delay in production occurs or when other operating parameters such as output temperature are changed.

TRZONE is also capable of simulating,

i) A batch furnace where the whole of the load is replaced by cold material at each recharging operation.

ii) A continuous furnace through which the load is indexed zone by zone at discrete time intervals. As for SSZONE the load enters the furnace at zone NZONE and leaves at zone 1.

The thermal efficiency of furnaces operated under the above conditions is strongly influenced by the rate of heat conduction into the insulation and the resident load in the furnace. The zone model is therefore linked to an analysis of the transient conduction into the wall, hearth and load.

To represent real operating practices, the model simulates the modulation and control of the thermal input to each zone in response to a given control parameter (e.g. load discharge temperature, roof temperature etc.), as well as any scheduled change or delay in throughput specification.

TRZONE predicts the following time varying data:

i) Thermal consumption and useful energy output. This includes the time and thermal consumption to start of discharge of the load and the thermal consumption during production delays.

ii) The surface and internal temperatures of the walls, hearth and load. Unlike SSZONE, the temperature differences between the hot face of the load and the cold face in contact with the hearth are calculated.

From the data given in i), it is possible to compute the efficiency of the furnace. Two definitions of efficiency can be applied to the analysis of furnaces operated under transient conditions:

1) *Overall efficiency* equals the energy output in the discharged load divided by the energy input, both referenced to zero time (ie.the furnace start-up).

2) *Running efficiency* equals the energy output in the discharged load over a defined time period, divided by the energy input over the same period. The running efficiency of a continuously operated furnace approaches the steady state efficiency.

6.2 The Heat Balance Formulation in TRZONE

In TRZONE, the zone energy balance solutions are linked to a series of one-dimensional transient conduction calculations through the furnace insulation, the hearth and the load in each zone. In this way, the effects of both the finite conduction and of the changes in heat storage in the solid structures are simulated. A simplified flow diagram for the computation procedure is shown in Figure 6.1. The transient conduction analysis is carried out using the Crank-Nicolson finite difference solution technique of the following one-dimensional partial differential equation:

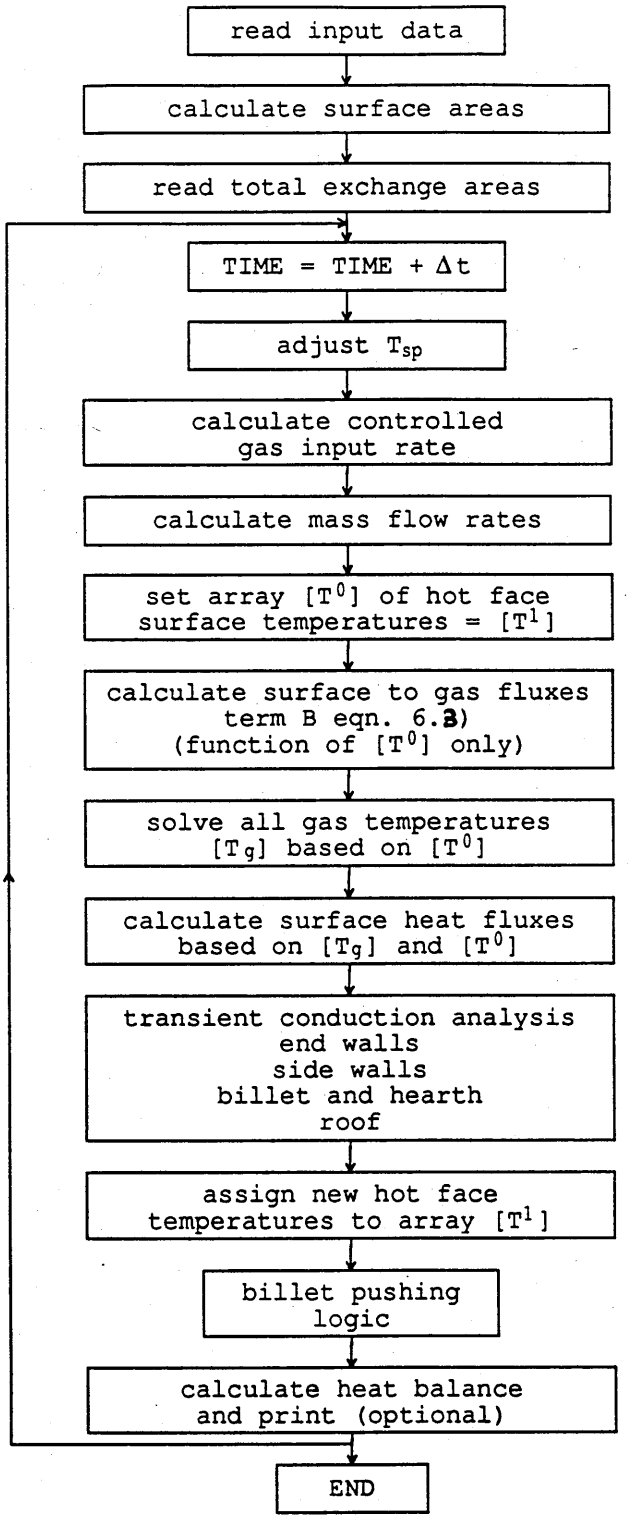

Figure 6.1 Simplified computer flow diagram for TRZONE.

$$(C_p\rho)\frac{\delta T}{\delta t} = \frac{\delta}{\delta x}\left(\lambda \frac{\delta T}{\delta x}\right) \qquad 6.1)$$

The solution assumes a constant heat flux ($\dot{q}$) into the hot face at x = 0 , and assumes a convective boundary at x=L , thus:

$$-\lambda\left(\frac{\delta T}{\delta x}\right)_{x=0} = \dot{q} \quad \text{and} \quad -\lambda\left(\frac{\delta T}{\delta x}\right)_{x=L} = h(T_L - T) \qquad 6.2)$$

The finite difference solution time step is equal to the simulation time step in TRZONE. The formulation of the finite difference solution is described in Appendix 2. The technique allows changes to be made to these boundary conditions at each time step. The heat flux ($\dot{q}$) to each surface is calculated using the zone model and assuming the internal surface temperatures calculated at the last time step. These are designated as (T_i^o). Since surface temperatures are fixed at each time step, only the gas zone heat balance equations need to be solved using the zone method. In the formulation of the gas zone energy balance equations, the thermal capacity of the combustion products in each zone is considered negligible compared to the energy contained in the products flowing through the zone, and to the heat capacity of the surrounding solid structures.

For a model comprising of N gas zones and M surface zones, the energy balance equation on gas zone i is:

$$\underset{(A)}{\sum_{j}^{N} \overrightarrow{G_j G_i} \sigma T_{g,j}^4} + \underset{(B)}{\sum_{j}^{M} \overleftarrow{G_i S_j} \sigma T_j^4} - \underset{(C)}{\dot{Q}_{conv,i}} - 4K_i V_i \sigma T_{g,i}^4$$

$$+ \dot{m}_{G,i}[C_{net} + R_a I_a(T_a)] + \dot{Q}_{enth,i} = 0 \qquad 6.3)$$

In equation 6.3), all surface temperatures T_j used to calculate terms (B) and (C) are constant and equal to the hot face temperatures of the surface zones calculated at the previous time step after the conduction analysis (T_i^o). Hence, a system of N non-linear simultaneous equations in $T_{g,j}$ must be solved at each time step using the Newton-Raphson technique (see Appendix 1). The initial guesses for $T_{g,j}$ in this solution procedure are set equal to the gas zone temperatures calculated at the preceding time step ($T_{g,j}^o$), and which in general will be close to the solution for all $T_{g,j}$ at the current time step.

6.3 Conduction Calculation

In the finite difference technique, allowance can be made for the significant variations of the specific heat (C_p) and conductivity (λ) of the load and insulation materials. This is

particularly important because these materials may commonly be heated from ambient to over 1300 ^{o}C during a single firing. The variation of c_p and λ with temperature are described by simple polynomial expressions [30], which can be automatically accessed by the transient conduction subroutine. The transient conduction solution domain is discretised into spatial increments representing internal points in the conducting material. This technique enables multi-layer structures to be simulated. A very useful example of this is the simulation of ceramic fibre veneer on dense refractory. A typical furnace simulation would include the start up of a furnace from cold. In this case all node temperatures are initialised to a preset ambient value (normally 15 ^{o}C).

6.4 Furnace Temperature Control

At the end of each time step, various parameters are checked, and depending on their value, changes can be made to the operating conditions. For example, the gas rate to designated zones is modulated in response to a calculated internal wall,roof or load surface temperature, thereby simulating a desired control strategy. Idealised two position or proportional control of temperature is simulated based on deviation about a preset temperature (T_{sp}) as shown in Figure 6.2, and using a simple algorithm relating the firing rate, as a proportion (F) of the maximum value, to the deviation about T_{sp}. Within the proportional control band illustrated in

F = Proportion of maximum firing rate

t_d = Proportional turn down

T_{sp} = Set point temperature

P_b = Proportional band

i) Proportional control

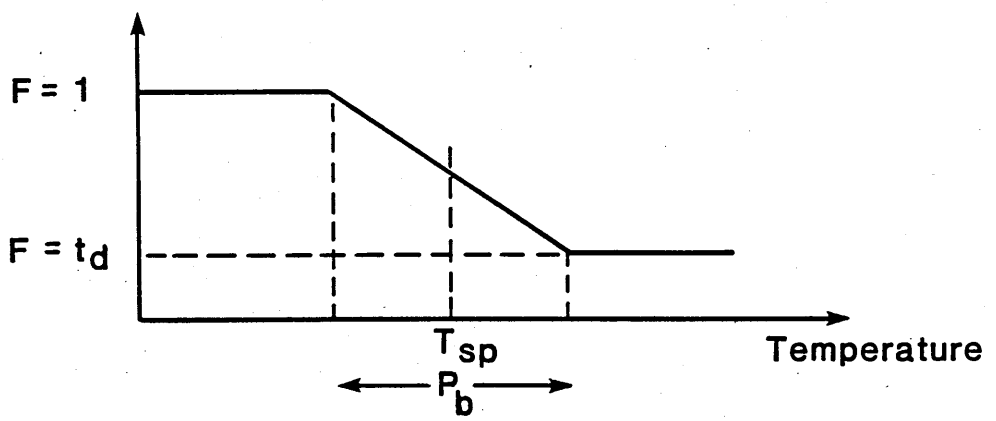

ii) high-low or on - off control

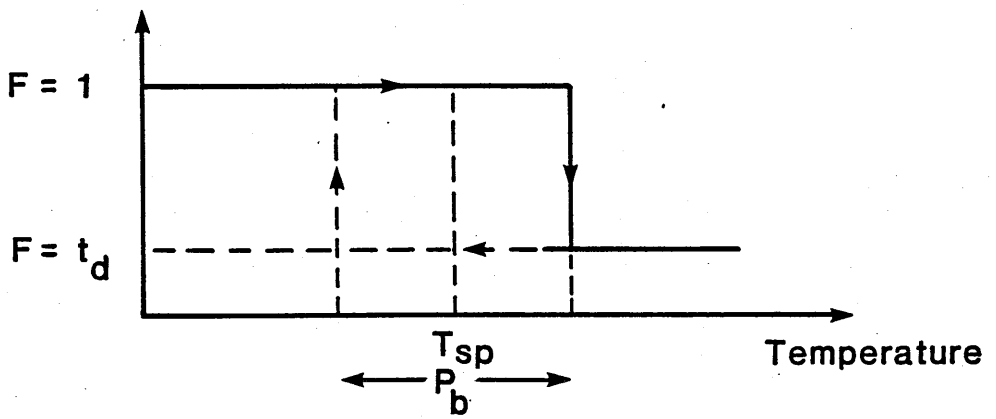

Figure 6.2 The strategey for gas input rate control

Figure 6.2, F is related to temperature T as follows:

$$F = bT + c \qquad 6.4)$$

where $b = (t_d - 1)/P_b$

and $c = (t_d + 1)/2 - (t_d - 1)T_{sp}/P_b$

6.5 Load Discharge Simulation

At the end of each time step, the surface temperature of the load and the elapsed simulation time are checked to determine whether conditions are satisfied for discharge of the load to occur. In the case of a model of a batch furnace for example, all node points representing the load would be re-initialised to a specified input value. In TRZONE, the load movement between zones can be handled by reassigning the node temperatures to new zone locations. At a time when load discharge occurs, all temperatures at nodes J in the steel in zone I, are reassigned to zone I-1 . Thus,

```
T(1,J)   = T(2,J)   all J
   :          :
T(I-1,J) = T(I,J)   all J
   :          :
T(N,J)   = TIN      all J
```

where TIN is the load inlet temperature to zone N.

A discharge or 'push' occurs at a multiple of time steps and at a frequency determined by the specified load throughput rate and the zone size. The latter governs the mass of load in each zone and therefore the mass transferred at each push. For example, in a model of a continuous furnace wherein the load in 1 zone is moved at each push, then the pushing interval is calculated by the following FORTRAN logic:

```
IFREQ = CHARG/WPT/TSTEP*3600.                    6.5)
```

where, CHARG = weight of load in each zone (kg)

WPT = load throughput (kg/hr)

TSTEP = the calculation time step (sec)

IFREQ is the number of time steps between pushes. IFREQ is an integer variable and is therefore 'rounded down' to the nearest integer value. Since the actual pushing interval may not be an exact multiple of time steps, TSTEP is then readjusted as follows:

```
TSTEP = CHARG/WPT*3600/IFREQ                     6.6)
```

CHAPTER 7

Background to the Calculation of Exchange Areas

7.1 Introduction

As discussed in the introduction to Chapter 3, the major computational task in the application of the zone method to furnace design is the calculation of the large number of directed flux areas and the corresponding total and direct exchange areas between all possible zone pairs. It was evident therefore that for a mathematical model to be easy to use, and flexible enough to handle the large number of likely geometries, the methods of calculation of exchange areas needed to be reviewed and evaluated.

The simple furnace models used by Lucas [24] and Saimbi and Tucker [22] ignore the radiation transfer between zones. These models only consider interchange between two surfaces and the gas within each zone. Since results from a simple model of this form are to be compared to those from SSZONE, the method of calculating the direct exchange areas by these models will be reviewed in this chapter.

For exchange area calculation assuming interzone radiation exchange, two approaches were applied, namely,

i) calculation of the direct exchange area integrals (equations 3.8,3.13 and 3.15) by numerical integration,

ii) calculation by the Monte Carlo method.

These techniques will be described separately in chapters 8 and 9. The calculation of the total exchange areas from the direct exchange areas will then be discussed in chapter 10.

The radiant energy balance equations formulated in SSZONE and TRZONE in the previous two chapters assume that interzone radiation occurs. These equations can easily be re-written so that intra-zone radiation only is considered [30]. The physical basis and method of calculation of the exchange areas for this simple model will now be described.

7.2 Assumptions of the simple model

The following assumptions were made in the development of the simple long furnace model:

a) There is zero net radiation transfer across the imaginary boundaries between adjacent gas zones. The only heat transfer across these boundaries is the enthalpy transported in the combustion gases and the load.

b) Each gas zone is assumed to be surrounded by two surfaces only, representing the wall (surface 2) and the load (surface 1). Consequently, the radiative exchange between wall, load and gas within each zone involves only six directed flux areas ($\overrightarrow{GS}_1$, $\overleftarrow{GS}_1$, $\overrightarrow{GS}_2$, $\overleftarrow{GS}_2$, $\overrightarrow{S_1S_2}$, $\overleftarrow{S_1S_2}$).

The calculation of these total exchange areas is further simplified by assuming that:

c) Surface 1 is unable to see itself, since the load is usually a flat or convex surface.

d) All points on surface 2 have an equal view of surface 1 and vice-versa.

e) Radiation attenuation and emission by the gas can be calculated assuming a mean path length for radiation transfer given by,

$$L_m = 3.5\ V/A \qquad 7.1)$$

where V = the volume of the zone

A = the bounding area of the zone

This model is similar in concept to Hottel and Sarofim's speckled enclosure model [11] wherein the load and refractory

are assumed to be intimately mixed. However, assumption c) above provides an additional constraint on the geometry. Assumptions c) - e) are only rigorously obeyed in a system comprising of an absorbing gas enclosed between either a pair of infinite parallel plates, or a pair of concentric cylindrical surfaces where the load is represented by the inner convex surface.

The above assumptions enable the total exchange areas within a given zone to be calculated from the surface areas, emissivities and the mean beam length only, and avoids evaluating the complex multiple integrals describing the true geometry of the zone. Simple algebraic expressions for total exchange area calculation are now derived.

7.3 Calculation of total exchange areas

A zone in the above model comprises of an absorbing gas of mean radiating beam length L_m, surrounded by two grey surfaces of emissivities ε_1 and ε_2 (the load and the refractory wall) whose mutual view factors are given by:

$F_{11} = 0$ i.e. the load cannot see itself

$F_{12} = 1$ i.e. the load can see nothing but refractory

Since $A_1F_{12} = A_2F_{21}$ then $F_{21} = A_1/A_2$

and since $F_{21} + F_{22} = 1$ then $F_{22} = 1 - A_1/A_2$

If the participating gas in the zone is assumed to be grey with a mean transmittance τ given by:

$$\tau = \exp\{-k.pL_m\} \qquad 7.2)$$

then the following direct exchange areas can be defined,

$$\overline{s_1 s_1} = A_1 F_{11} \tau = 0 \qquad 7.3)$$

$$\overline{s_1 s_2} = A_1 F_{12} \tau = A_1 \tau = \overline{s_2 s_1} \qquad 7.4)$$

$$\overline{s_2 s_2} = A_2 F_{22} \tau = (A_2 - A_1)\tau \qquad 7.5)$$

and the matrix of direct exchange areas is therefore complete. Equation 3.36) is now applied to derive the corresponding 2 x 2 matrix of total exchange areas,thus,

$$\overline{\mathbf{SS}} = \mathbf{AI} \,.\, \mathbf{R} \,.\, \overline{\mathbf{ss}} \,.\, \varepsilon\mathbf{I} \qquad 3.36)$$

where $\mathbf{R} = [\mathbf{AI} - \overline{\mathbf{ss}}.\rho\mathbf{I}]^{-1}$

Substitution into the terms in square brackets and its inversion to give **R** is first carried out as follows:

$$\mathbf{R}^{-1} = \begin{bmatrix} A_1 & 0 \\ 0 & A_2 \end{bmatrix} - \begin{bmatrix} 0 & A_1\tau \\ A_1 & (A_2-A_1)\tau \end{bmatrix} \cdot \begin{bmatrix} \rho_1 & 0 \\ 0 & \rho_2 \end{bmatrix}$$

$$= \begin{bmatrix} A_1 & -A_1\rho_2\tau \\ -A_1\rho_1\tau & A_2-(A_2-A_1)\rho_2\tau \end{bmatrix} \qquad 7.6)$$

The inverse of this matrix (**R**) is given by [31],

$$(\mathbf{R}^{-1})^{-1} = \frac{\text{adj}(\mathbf{R}^{-1})}{|\mathbf{R}^{-1}|} = \mathbf{R} \qquad 7.7)$$

where adj $(\mathbf{R}^{-1})$ is the matrix adjoint to $\mathbf{R}^{-1}$ and $|\mathbf{R}^{-1}|$ is the second order determinant associated with the matrix $\mathbf{R}^{-1}$.

The adjoint matrix adj$(\mathbf{R}^{-1})$ is the transpose of the matrix of cofactors of $(\mathbf{R}^{-1})$ which is given by:

$$\text{adj}(\mathbf{R}^{-1}) = \begin{vmatrix} A_2-(A_2-A_1)\rho_2\tau & A_1\tau\rho_2 \\ A_1\tau\rho_1 & A_1 \end{vmatrix} \qquad 7.8)$$

Substitution of eqn.7.7) into eqn.3.36) yields:

$$\overline{\mathbf{SS}} = \frac{\mathbf{AI} \cdot \text{adj } \mathbf{R}^{-1} \cdot \overline{\mathbf{ss}} \cdot \varepsilon\mathbf{I}}{|\mathbf{R}^{-1}|}$$

Expansion of the denominator yields:

$$\mathbf{R}^{-1} = A_1(A_2-(A_2-A_1)\rho_2\tau\,)-A_1^2\tau^2\rho_1\rho_2$$

Expansion of the numerator gives the following matrix:

$$\begin{bmatrix} A_1^3\varepsilon_1^2\rho_2\tau^2 & A_1^2\varepsilon_1\varepsilon_2\tau(A_2-(A_2-A_1)\rho_2\tau \\ & +\varepsilon_1\varepsilon_2A_1^2\tau^2\rho_2(A_2-A_1) \\ A_1^2A_2\varepsilon_1\varepsilon_2\tau & A_1^2A_2\varepsilon_2^2\tau^2\rho_1 \\ & +A_1A_2\varepsilon_2^2(A_2-A_1)\tau \end{bmatrix}$$

thus,

$$\overline{S_1S_2} = \overline{S_2S_1} = \frac{A_1^2A_2\varepsilon_1\varepsilon_2\tau}{A_1(A_2-(A_2-A_1)\rho_2\tau)-A_1^2\tau^2\rho_1\rho_2}$$

Division by $A_1A_2\tau$ gives:

$$\overline{S_1S_2} = \overline{S_2S_1} = \frac{A_1\varepsilon_1\varepsilon_2}{A_1/A_2\rho_2(1-\rho_1\tau)+1/\tau-\rho_2} \qquad 7.10)$$

For surface to gas total exchange areas, eqn 3.37) is applied:

$$\overline{\mathbf{SG}} = \varepsilon\mathbf{AI}.\mathbf{R}.\overline{\mathbf{sg}}$$

$$= \frac{\varepsilon\mathbf{AI} \cdot \mathrm{adj}(\mathbf{R}^{-1}) \cdot \overline{\mathbf{sg}}}{|\mathbf{R}^{-1}|}$$

where $$\overline{\mathbf{sg}} = \begin{vmatrix} \overline{gs}_1 \\ \overline{gs}_2 \end{vmatrix}$$

$\overline{gs}_1$ and $\overline{gs}_2$ are given by application of the sum rules, thus:

$$\overline{gs}_1 + \overline{s_2s}_1 = A_1 \qquad \overline{gs}_2 + \overline{s_2s}_1 + \overline{s_2s}_2 = A_2$$

therefore,

$$\overline{gs}_1 = A_1 - \overline{s_2s}_1 = A_1 - A_1\tau = A_1(1-\tau)$$

$$\overline{gs}_2 = A_2 - A_1 - (A_2-A_1)\tau = A_2(1-\tau)$$

Expansion of the numerator in eqn 3.44) gives the following (1 x 2) matrix:

$$\begin{bmatrix} A_1^2\varepsilon_1(1-\tau)(A_2-(A_2-A_1)\rho_2\tau)+A_1^2A_2\varepsilon_1\tau\rho_2(1-\tau) \\ A_1^2A_2\varepsilon_2\tau\rho_1(1-\tau)+A_1A_2^2\varepsilon_2(1-\tau) \end{bmatrix}$$

from which,

$$\overline{GS}_1 = \frac{A_1^2\varepsilon_1(1-\tau).[A_2+A_1\rho_2\tau]}{A_1(A_2-(A_2-A_1)\rho_2\tau)-A_1^2\tau^2\rho_1\rho_2}$$

Division by $A_1A_2\tau$ gives:

$$\overline{GS}_1 = \frac{A_1\varepsilon_1(1-\tau)/\tau\ [1+A_1/A_2.\rho_2\tau]}{A_1/A_2\rho_2(1-\rho_1\tau)+1/\tau-\rho_2}$$

$$= \frac{A_1\varepsilon_1[A_1/A_2\rho_2(1-\tau)+1/\tau-1]}{A_1/A_2\rho_2(1-\rho_1\tau)+1/\tau-\rho_2} \qquad 7.11)$$

Similarly,

$$\overline{GS}_2 = \frac{A_2\varepsilon_2[A_1/A_2\rho_1(1-\tau)+1/\tau-1]}{A_1/A_2\rho_2(1-\rho_1\tau)+1/\tau-\rho_2} \qquad 7.12)$$

Thus, the relevant surface-surface and gas-surface total exchange areas are defined by equations 7.10, 7.11 and 7.12. Using a mixed grey gas model, the calculated total exchange areas can then be substituted into equations 3.48, to derive the directed flux areas, which are implemented into the surface or gas zone heat balance equations.

CHAPTER 8

Exchange Area Calculation by Numerical Integration

8.1 Introduction

The integral expressions for direct exchange areas (equations 3.8,3.13 and 3.15) when K = 0, are not analytically solvable, except for the simplest of geometric configurations or for optically thin media (see Hottel & Sarofim p.262 [11]). Numerical integration provides the most accurate alternative method of solution. Its accuracy can be reliably tested by successively reducing the integration step until satisfactory convergence is obtained. It therefore provides a standard against which more approximate methods such as the Monte Carlo technique, to be described in Chapter 9, can be compared.

A simple numerical integration technique has been adopted to calculate exchange areas within the rectangular furnace enclosure shown in Figure 8.1. Each gas zone is subdivided into N_x x N_y x N_z cubic elements of side B metres. The bounding surfaces are accordingly subdivided into square elements of side B (Figure 8.2). Subroutines have been written to calculate the complete set of direct exchange areas ($\overline{gg}$,$\overline{gs}$ and $\overline{ss}$) for all zone pairs in the enclosure and for each grey and clear gas component. The direct exchange areas are calculated by a simple summation of exchange areas between

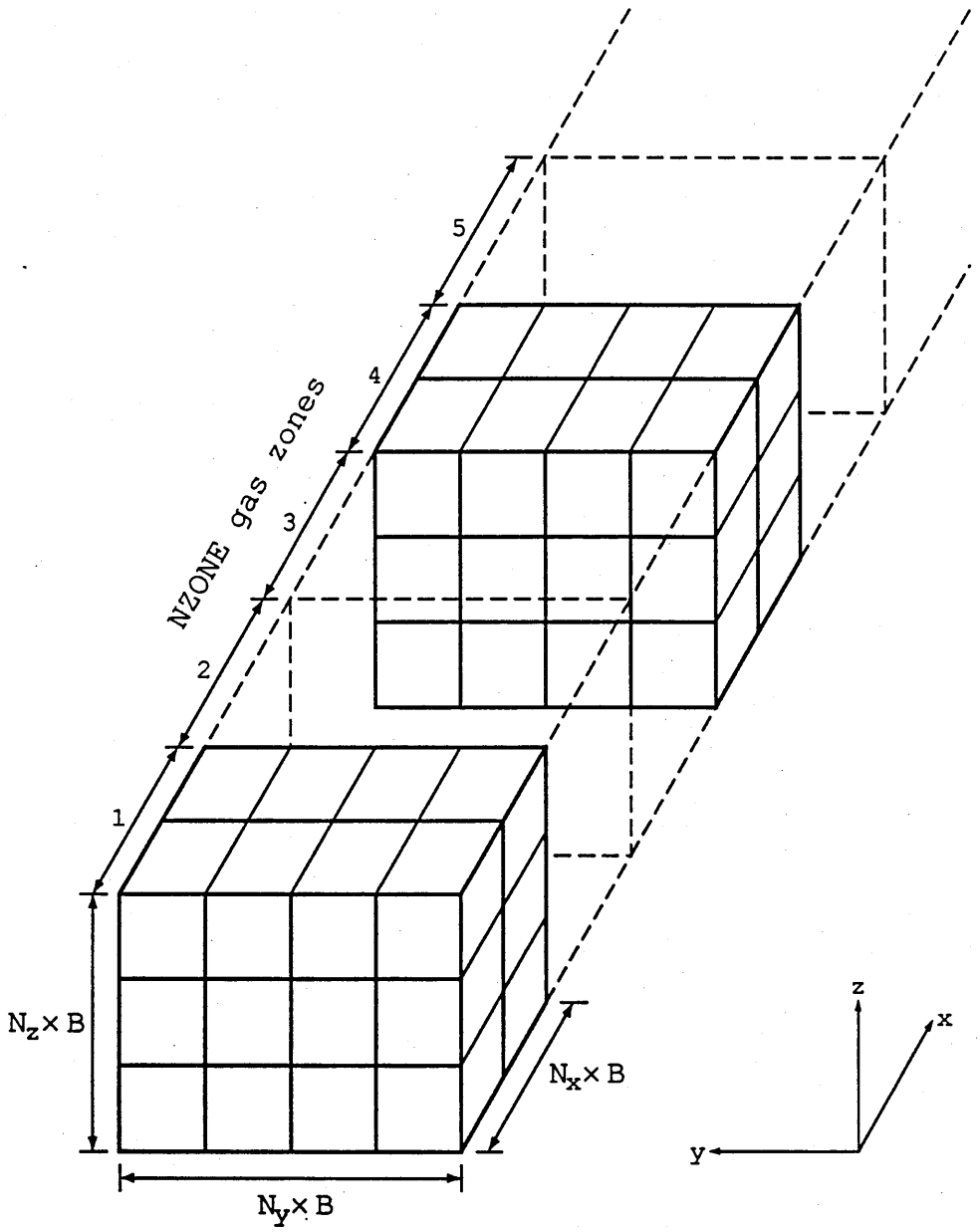

Figure 8.1. The arrangement and numbering of volume zones, and their subdivision into cubic elements for the calculation of the direct exchange areas by numerical integration.

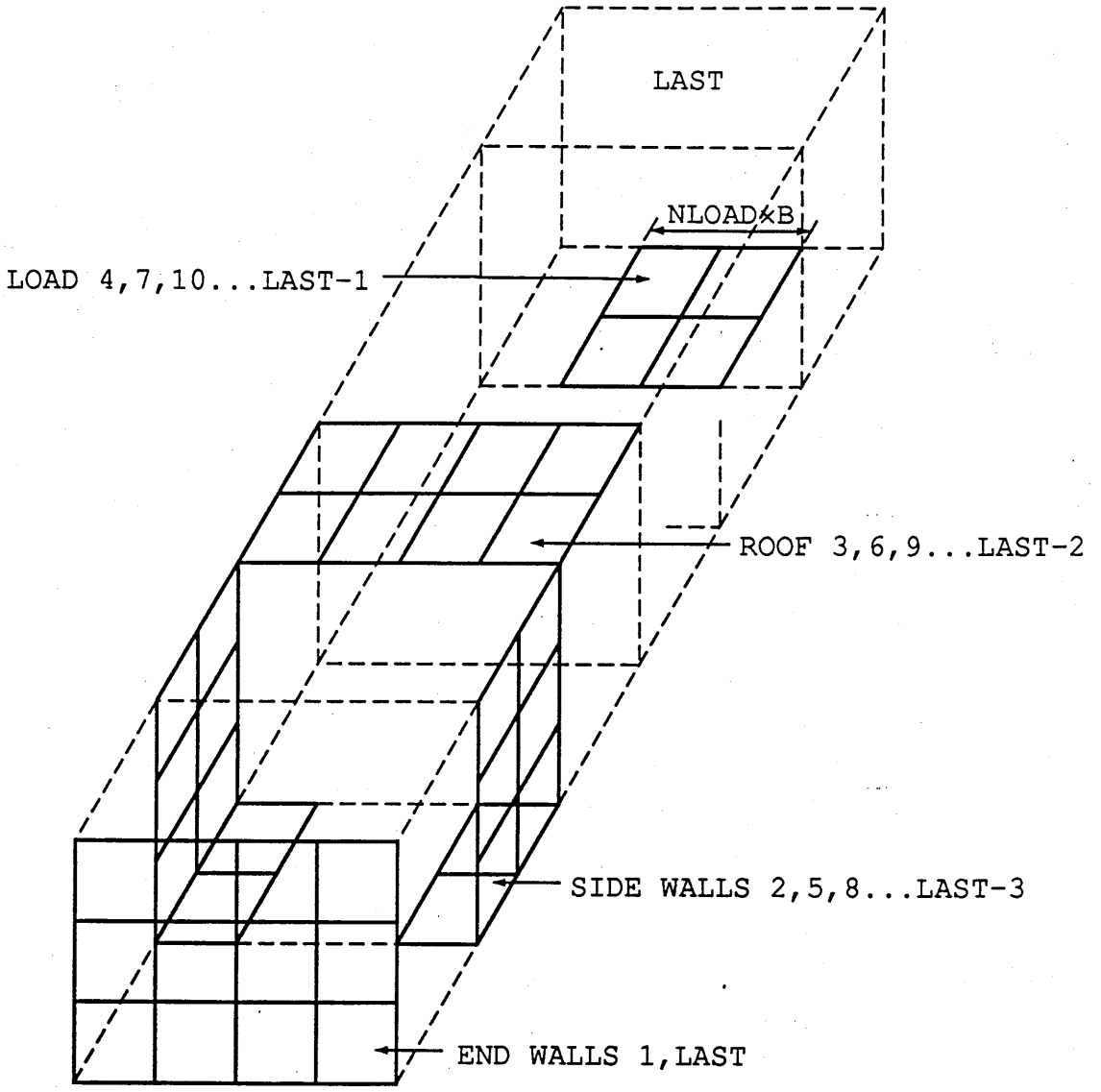

Figure 8.2. The arrangement and numbering of surface zones, and their subdivision into square elements for the calculation of the direct exchange areas by numerical integration.

component cubes and/or squares.

For greater accuracy, smaller element sizes should be used for closely spaced zones. This restriction is relaxed in the present study, by utilising accurate exchange area data published as part of this study [32] and reproduced in Appendix 3 for cubic and square elements in close proximity to each other. Rectangular geometries can then be built up from a fairly coarse arrangement of cubical and square elements.

The technique will now be described.

8.2 Gas-Gas Direct Exchange Areas

The problem of evaluating the general exchange area $\overline{g_I g_J}$ can be formulated as follows:

$$\overline{g_I g_J} = \sum_i \sum_j (\overline{g_i g_j}) \qquad 8.1a)$$

where each gas zone is subdivided into n_x x n_y x n_z cubic elements. The exchange area between any two elements (i,j) can be approximated from equation 3.15 as follows:

$$\overline{g_i g_j} = K^2 B^6 \exp\{-Kr_c\}/\pi r_c^2 \qquad 8.1b)$$

where r_c = the centre to centre separation of i,j

$$= (x^2 + y^2 + z^2)^{0.5} \qquad 8.1c)$$

This formula however assumes that the 'view' and path length for absorption are the same from all points within either element. This assumption is only valid for element pairs with a large relative separation i.e. $r_c/B >> 1$. For element pairs in close proximity to each other, the data and correlations in Appendix 3 have been applied. For gas-gas exchange these are in the form:

$$\overline{g_i g_j} \; / \; KB(\overline{gs})_b \;=\; C \exp\{-A.KB\} \qquad 8.2)$$

Where $(\overline{gs})_b$ is the direct exchange area between a cube of side B and all of its six bounding surfaces, sometimes referred to as the 'escape factor'. $(\overline{gs})_b$ is given as a polynomial expression in KB. C and A are correlation coefficients dependent on the particular relative configuration of the element pair. These are given in Table A3.4 (Appendix 3).

A subroutine (GGDEX) has been written which utilises the correlation given by equation 8.2) together with equations 8.1) to evaluate the direct exchange areas between pairs of rectangular gas zones in the model. To evaluate the matrix $\overline{gg}(I,J)$ where I,J denotes the rectangular zone pair I and J, the summation of the exchange areas between all component cubical elements within I and J is undertaken as shown in Figure 8.3.

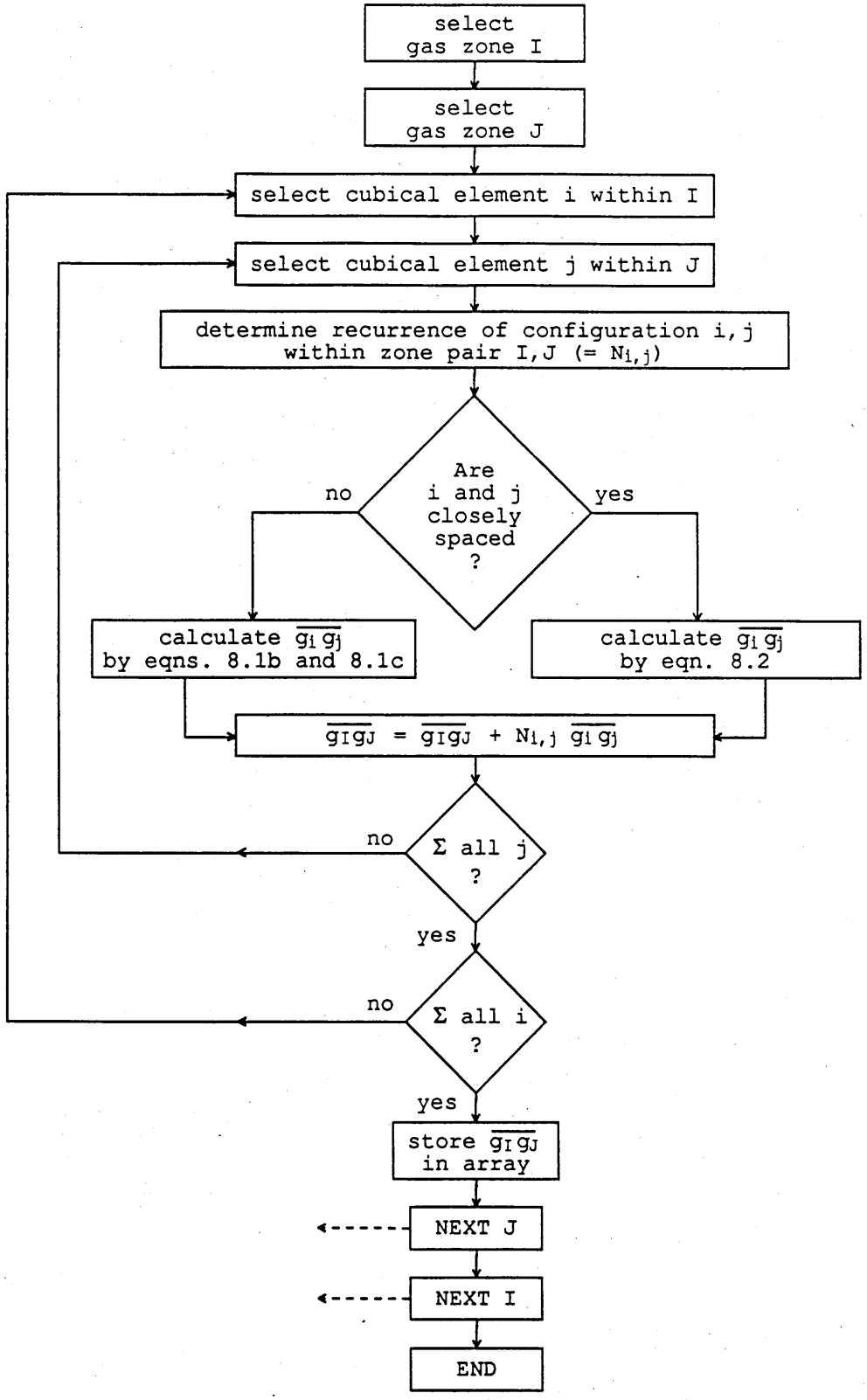

Figure 8.3. A schematic flow diagram for the calculation of gas-gas direct exchange areas between zone pair I and J in subroutine GGDEX.

Within the calculation loop, it might at first be assumed that a total of $n_x^2.n_y^2.n_z^2$ elemental exchange areas must be calculated and summated for each zone pair. In fact, the problem is reduced to the summation of just $(2n_x-1).(2n_y-1).(2n_z-1)$ unique terms. The recurrence of each unique term must however be determined. (This technique is described in Appendix 4 for the evaluation of exchange areas between cubes in close proximity to each other.) Each exchange area contains an exponential function, whose repeated evaluation can be computationally time consuming. Minimisation of the number of summations in this way is therefore very important. If $n_x = 5$, $n_y = 4$ and $n_z = 2$, then the calculation is reduced from the summation of 1600 exponential terms, to the summation of just 189 terms.

The problem is further reduced as follows:

i) By recognising that mutually displaced zone pairs in the model share the same exchange areas, thus:

$$\overline{gg}(I,J) = \overline{gg}(I+1,J+1) = \overline{gg}(I+2,J+2) \quad \text{etc.}$$

This only applies because of the assumed parallel and rectangular geometry and the assumed equal attenuation coefficient in each zone.

ii) By the requirements for reciprocity , for example $\overline{gg}(I,J) = \overline{gg}(J,I)$, calculation for zone pairs which are merely reciprocal to previously calculated zone pairs is avoided.

Consequently, GGDEX only selects gas zone 1 as the emitting zone and selects zones 1 to NZONE as receiving zones. The top line only of the matrix $\overline{gg}$ is therefore calculated and all other terms in $\overline{gg}$ follow from the governing requirements i) and ii) above. In this way, only NZONE unique exchange areas need be calculated to satisfy the matrix of $NZONE^2$ terms.

8.3 Gas-Surface Direct Exchange Areas

Gas to surface direct exchange areas between cubes and squares (of side B) in close proximity to each other are given in Appendix 3 together with a set of correlation coefficients (A and C) relating $\overline{g_i s_j}$ and KB as follows:

$$\overline{g_i s_j}/(\overline{gs})_b = C \exp\{-A.KB\} \qquad 8.3)$$

For a cube and a surface element which happens to form a bounding side of the cube, the direct exchange area is simply:

$$\overline{g_i s_j} = (\overline{gs})_b / 6 \qquad 8.4)$$

For an element pair separated by distances greater than those given in Appendix 3, the exchange area is approximated by

equation 3.13 as follows:

$$\overline{g_i s_j} = KB^5.\cos\theta.\exp\{-Kr_c\}/\pi r_c^2 \qquad 8.5)$$

where θ is the angle subtended by the volume element with the normal to the surface (see Figure 3.1b)) and where,

$$\cos\theta = \Delta z/r_c \qquad 8.6)$$

Δz is the z component of the volume-surface separation r_c (measured parallel to the normal to j).

A subroutine (GSDEX) has been written employing similar logic to that of GGDEX although in this case gas zones 1 to NZONE are selected in turn as emitting zones. A reduced matrix $\overline{gs}'(I,J)$ of dimension NZONE x 7 elementary exchange areas is initially evaluated. These are the exchange areas between each gas zone (I) and one of the seven identified surfaces (J) enclosing gas zone 1 (see Figure 8.4),

$\overline{gs}'(I,1)$		-the end wall (y - z plane)
$\overline{gs}'(I,2)$	and $\overline{gs}'(I,4)$	-the vertical side walls (x - z plane)
$\overline{gs}'(I,3)$		-the horizontal roof (x - y plane)
$\overline{gs}'(I,5)$	and $\overline{gs}'(I,7)$	-the unladen hearth (x - y plane)
$\overline{gs}'(I,6)$		-the load (x - y plane)

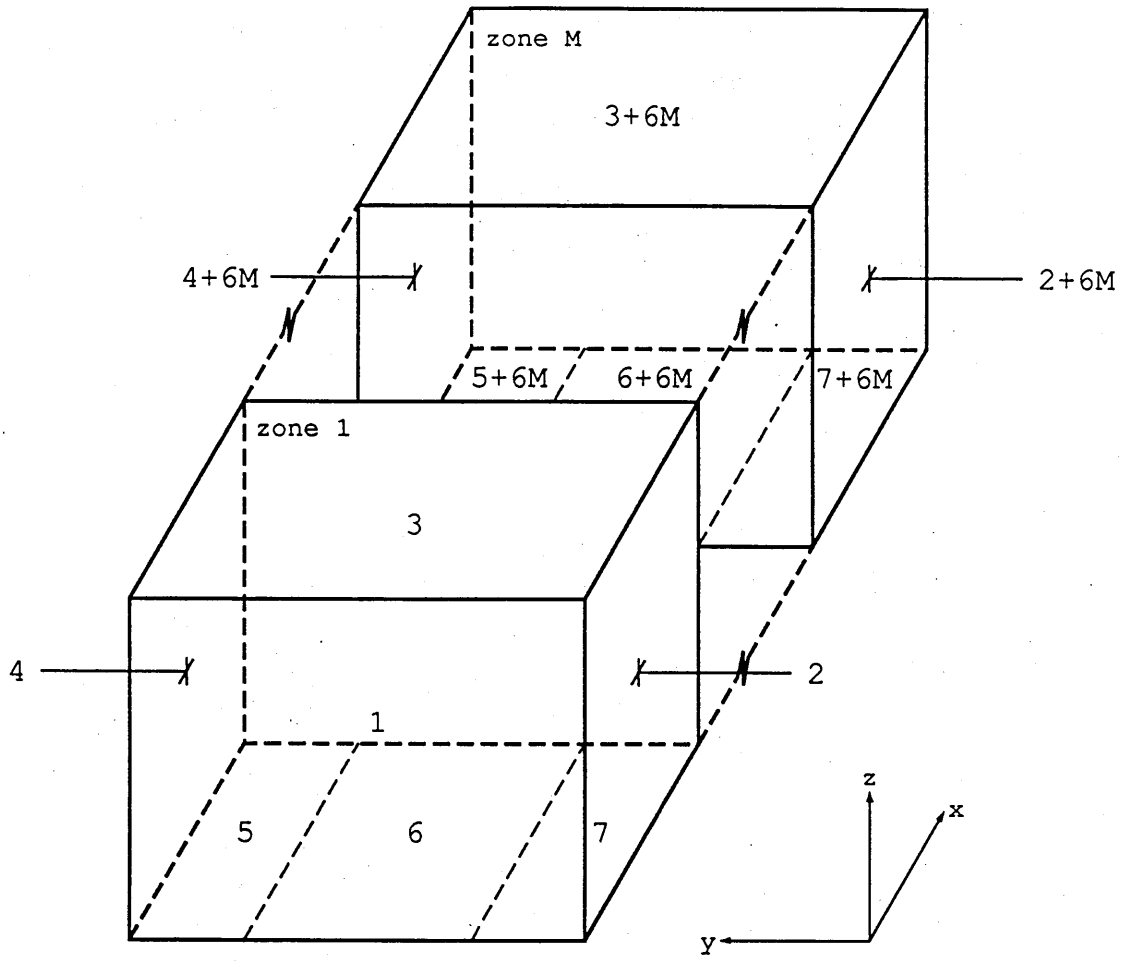

Figure 8.4. The numbering of surface zone elements adopted in subroutines GSDEX and SSDEX (for M = 0 to NZONE-1).

Once these have been evaluated, they can be grouped together according to the surface zone definitions given in Chapter 4 and the value chosen for NWALL. For example, if NWALL = 3, which assumes separate roof and wall zones, then $\overline{gs}'$ is further reduced to a matrix $\overline{gs}$ of dimension (NZONE x 4) as follows:

$$\overline{gs}(I,1) = \overline{gs}'(I,1)$$

$$\overline{gs}(I,2) = \overline{gs}'(I,2) + \overline{gs}'(I,4) + \overline{gs}'(I,5) + \overline{gs}'(I,7)$$

$$= 2\ (\ \overline{gs}'(I,2) + \overline{gs}'(I,5)\ )$$

$$\overline{gs}(I,3) = \overline{gs}'(I,3)$$

$$\overline{gs}(I,4) = \overline{gs}'(I,6)$$

This matrix is then expanded to give the lower diagonal elements of the full NZONE x LAST dimension matrix by utilising the simple relationships that:

$$\overline{gs}(I,J) = \overline{gs}(I+M,J+NWALLxM) \quad \text{for } J = 2,3 \text{ and } 4$$

$$\overline{gs}(I,1) = \overline{gs}(NZONE+1-I,LAST)$$

for I=1 to NZONE

Finally, values for the upper diagonal elements of $\overline{gs}$ are assigned from the assumed geometry and reciprocity of the problem. For example the exchange areas between gas zone 1 and the surfaces surrounding zone 2, are equal to those between gas zone 2 and the surfaces surrounding zone 1. This leads to a matrix of the structure shown in Figure 8.5.

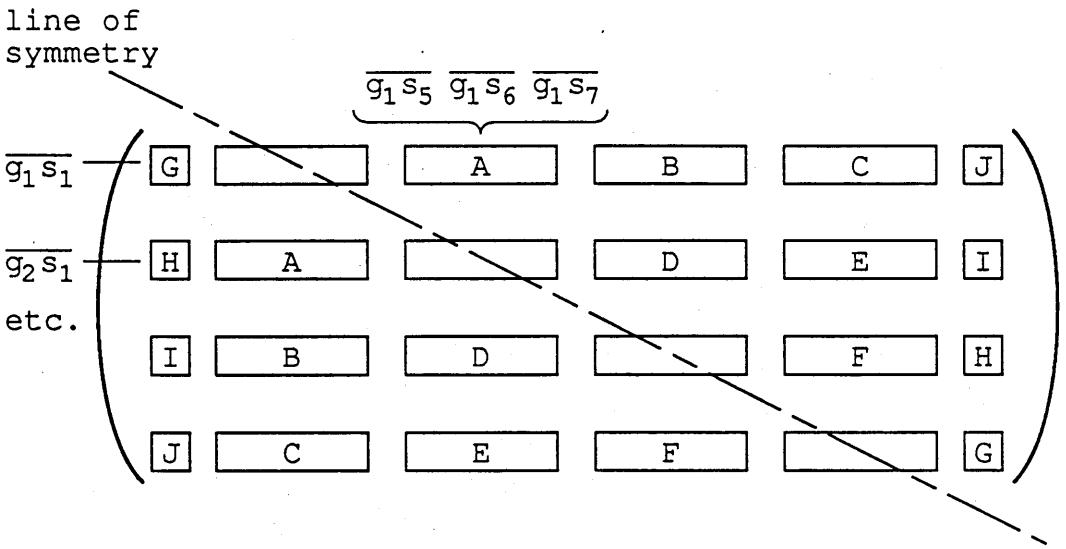

Figure 8.5. The general structure of the matrix of gas-surface exchange areas for NWALL = 3.

The above programming structure facilitates re-grouping of surface zones in the model since the direct exchange areas are built-up from their most elementary terms. The logic for NWALL=2 extends the re-grouping one stage further by assigning the side walls, empty hearth and roof as one surface.

8.4 Surface-surface direct exchange areas

Surface to surface direct exchange areas between squares (of side B) in both parallel and perpendicular configuration are given in Appendix 3 together with the set of correlation coefficients (A and C) for the following curve fit:

$$\overline{s_i s_j} / B^2 = C \exp\{-A.KB\} \qquad 8.7)$$

For an element pair separated by a distance beyond the range given in Appendix 3, the exchange area is approximated by the following equation:

$$\overline{s_i s_j} = B^4.\cos\theta_i.\cos\theta_j.\exp\{-Kr_c\}/\pi r_c^2 \qquad 8.8)$$

where θ_i, θ_j are the relative angles of orientation of the element pair (measured relative to the normal to each element). For parallel surfaces $\theta_i = \theta_j$.

A subroutine (SSDEX) has been written employing similar logic to GSDEX and GGDEX and utilising the above equations. In

SSDEX, the surfaces 1,2 and 3 as defined in Figure 8.4 are selected in turn as 'emitting' zones and surfaces corresponding to 4, 5, 6 and 7 surrounding each volume zone are selected as receiving zones.

Thus, the following matrix of elementary exchange areas ($\overline{ss}'$) is evaluated,

$\overline{ss}'(I,J)$ for I = 1 ; J = 4+6M to 7+6M and M = 0 to NZONE-1

$\overline{ss}'(I,J)$ for I = 2 ; J = 4+6M to 7+6M and M = 0 to NZONE-1

$\overline{ss}'(I,J)$ for I = 3 ; J = 5+6M to 7+6M and M = 0 to NZONE-1

SSDEX automatically checks whether the surface pair (I,J) are parallel or perpendicular and then directs the calculation to the appropriate section of the routine. The remaining exchange areas can simply be calculated by summation of the above terms for M = 0 to NZONE-1 , thus:

$$\overline{ss}'(3,4+6M) = \overline{ss}'(2,5+6M) + \overline{ss}'(2,6+6M) + \overline{ss}'(2,7+6M)$$

$$\overline{ss}'(1,2+6M) = \overline{ss}'(1,4+6M)$$

$$\overline{ss}'(1,3+6M) = \overline{ss}'(1,5+6M) + \overline{ss}'(1,6+6M) + \overline{ss}'(1,7+6M)$$

$$\overline{ss}'(2,3+6M) = \overline{ss}'(3,4+6M)$$

for M = 0 to NZONE-1

Thus, having built up the matrix of elemental exchange areas between surfaces 1 to 7 in Figure 8.4, grouping of exchange areas can then be carried out according to the surface zone

definitions given in Chapter 4.

For example if NWALL = 3,

$\overline{ss}(1,2+3M) = 2\ (\ \overline{ss}'(1,2+6M) + \overline{ss}'(1,5+6M)\ )$

$\overline{ss}(3,2+3M) = 2\ (\ \overline{ss}'(3,2+6M) + \overline{ss}'(3,5+6M)\ )$

$\overline{ss}(2,2+3M) = 2\{\ \overline{ss}'(2,4+6M) + 2[\overline{ss}'(2,5+6M)\ ) + \overline{ss}'(2,7+6M)]\}$

etc., for M = 0 to NZONE - 1

Finally , the matrix is completed by recognising that those zone pairs which are equally displaced in any given direction have equal exchange areas and that reciprocity must apply.

CHAPTER 9

Exchange Area Calculation by the Monte-Carlo Technique

9.1 Background

Numerical solution of the direct exchange area integrals is difficult for zones of complex shape or where the two zones are partially obscured (shaded) by another surface. Standard numerical techniques do not check for shading. An alternative approach to the calculation of radiation exchange areas is described based on a statistical Monte-Carlo technique for photon sampling and tracking. Although less accurate than numerical integration, this can be easily applied to irregular geometries and to shaded zone pairs. This technique therefore avoids the need to simplify the real furnace geometry by a cylindrical or rectangular zonal representation. The application of the Monte Carlo technique for calculating radiant exchange factors in enclosures containing an absorbing-emitting medium such as combustion products is well documented in the literature [33]. The use of the technique in a long furnace model is now described.

The direct exchange area between a zone pair is calculated by numerically simulating the emission of a large number of beams from one zone, and counting the fraction that intercept a surface zone or are absorbed by a gas zone. The beam origin

from within the emitting zone is selected randomly to attempt to reproduce a uniform spatial distribution of emitted photons. The direction of each beam is also selected randomly although the angular distribution of a large number of simulated beams must conform approximately to the true distribution of radiant energy emission from the gas or surface. It is convenient to resolve each beam into component vectors parallel to the x,y and z co-ordinates , since this facilitates the calculation of the point of intercept of the beam with a surface and of the path length of the beam through an intervening gas.

The technique has been developed to calculate all direct exchange areas within the long furnace model shown in Figure 9.1. The vertical height of the furnace is allowed to vary from zone to zone and can be selected to give rise to shading. The model is therefore thought to be flexible enough to represent accurately the geometry of a large number of practical furnace shapes. This is an improvement on previously published models which usually approximate the furnace shape by a rectangular or cylindrical geometry so that the exchange areas within the enclosure can be calculated by numerical integration as described for example in chapter 6. In accordance with the previous assumptions, the surfaces are assumed to be grey and diffusely reflecting.

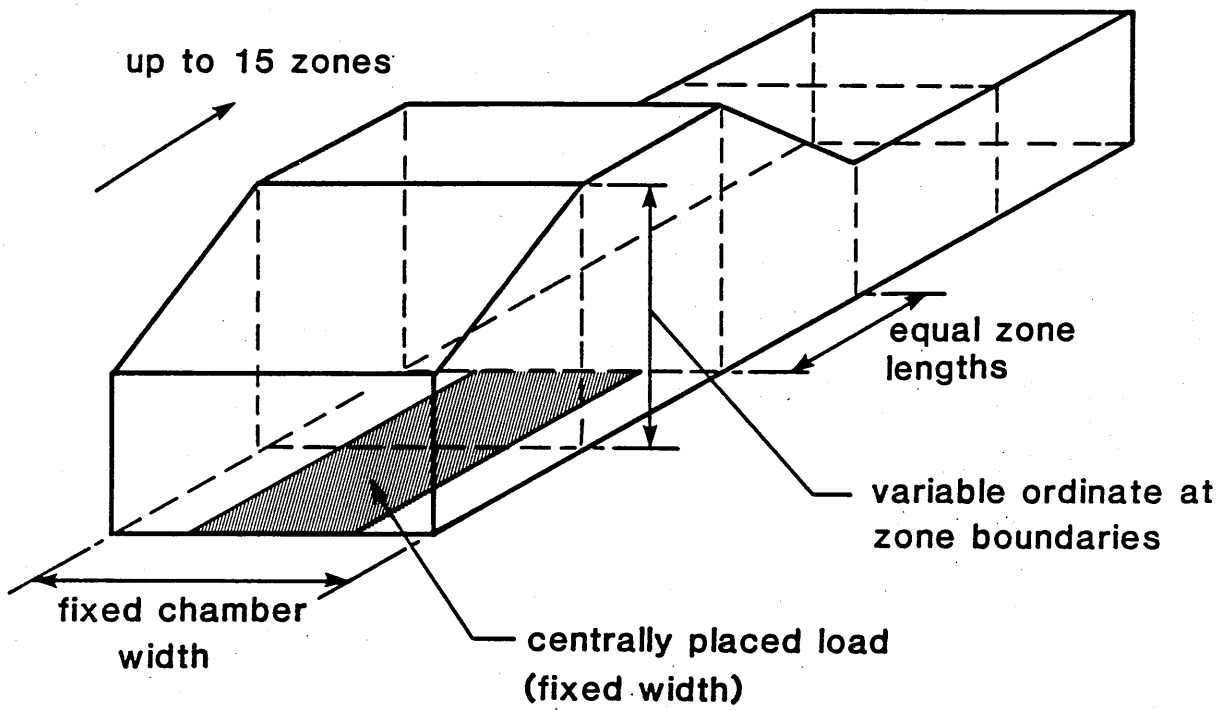

Figure 9.1 The geometry of the long furnace model simulated by the Monte Carlo technique

9.2 Outline of Method

The Monte Carlo technique is used to determine direct exchange areas by counting the fraction of randomly selected rays emitted from a zone which reach a second surface or gas zone. This involves:

i) randomly selecting the origin of emitted rays,
ii) randomly selecting their direction of emission,
iii) determining the point of direct incidence of the beam on another surface,
iv) determining the fractional attenuation of the beam through an absorbing gas if present.

These steps will now be examined in detail:

9.3 Selection of Beam Origin and Direction

Imagine a plane rectangular surface lying parallel to the x-y plane as shown in Figure 9.2. This plane may for example, represent the floor zone of the long furnace model in Figure 9.1. The origin (x_o, y_o) of a randomly selected beam can be defined by choosing just two random numbers, R_x and R_y between 0 and 1 such that:

$$x_o = R_x (x_{max} - x_{min}) + x_{min} \qquad 9.1)$$

$$y_o = R_y (y_{max} - y_{min}) + y_{min} \qquad 9.2)$$

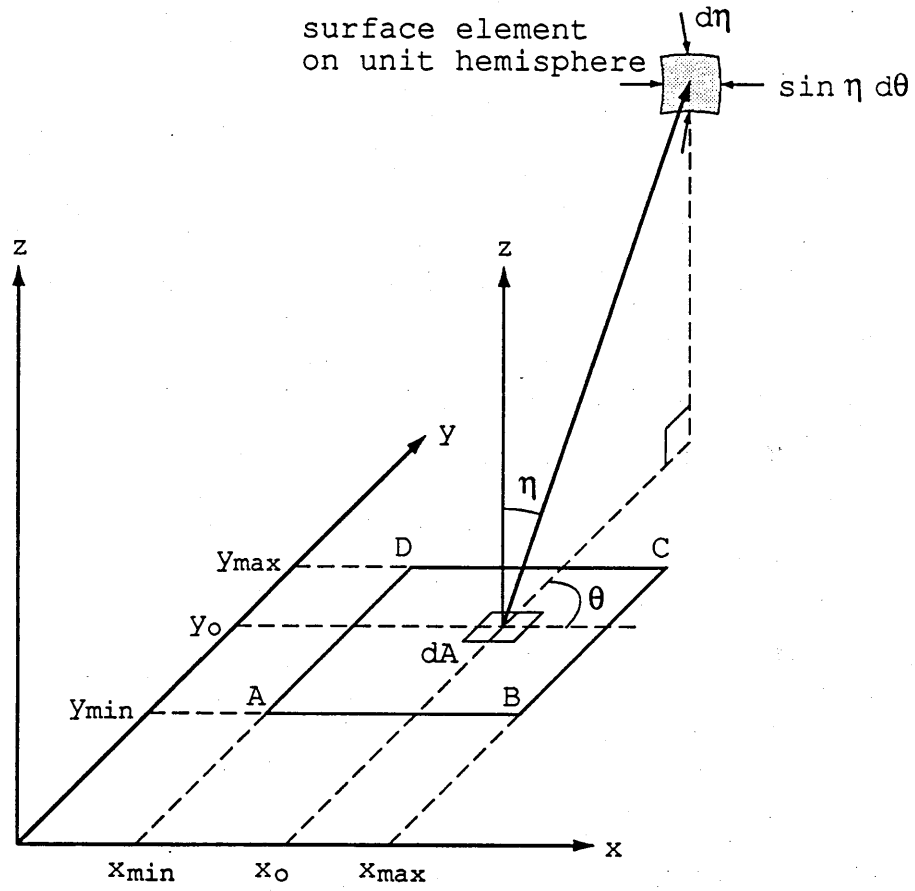

Figure 9.2. The specification of the direction and origin of a randomly selected beam from zone ABCD.

The direction of a beam emitted by the surface can be defined in terms of the circumferential (θ) and cone (η) angles as defined in Figure 9.2.

The radiant energy flux from a black surface in the (η,θ) direction is given by,

$$d\dot{q} = i_b.\cos\eta.d\omega \qquad 9.3$$

where $d\omega$ is the solid angle ($= \sin\eta.d\eta.d\theta$)

The total intensity i_b ($= \sigma T^4/\pi$) is the total rate of radiant emission over all wavelengths from a black surface, per unit elemental projected surface area normal to the beam and into unit elemental solid angle centred around the beam. It is independent of the direction of emission from a diffuse surface.

The Monte Carlo technique considers the emission of N bundles of energy leaving the finite surface from any random location (x_o,y_o). Each bundle irrespective of its direction is assumed to contain the same quantity of radiant energy. However, from equation 9.3) it is clear that there is an angular distribution of energy leaving the surface. In the Monte Carlo technique, bundles of randomly directed energy are simulated by a statistical technique that ensures an angular distribution conforming to that given by equation 9.3). The procedure for sampling N beams with the correct angular distribution uses the *cumulative distribution function*.

Consider the curve in Figure 9.3 representing schematically the relationship between $d\dot{q}$ and η . The probability that η has a value of η_1 or less is given by the cumulative distribution function as follows:

$$R_\eta = \text{prob } [\eta < \eta_1] = \frac{\int_0^{\eta_1} f(\eta)\, d\eta}{\int_0^{\pi/2} f(\eta)\, d\eta} \qquad 9.4)$$

This is represented graphically as the shaded area in Figure 9.3 as a fraction of the total area under the curve ABC. R_η is the fraction of energy flux emitted with a cone angle of η_1 or less. By selecting values of R_η uniformly distributed between 0 and 1, and equating this to the c.d.f. to determine η, ensures that the energy flux distribution with respect to η is correctly selected. Thus for N values of R_η, there are N corresponding values of η which will be distributed between $\eta = 0$ and $\eta = \pi/2$ such that $d\dot{q}$ is correctly reproduced. Applying this to equation 9.3) above gives:

$$R_\eta = \frac{\int_0^{\eta} i_b \cos\eta.\sin\eta.d\eta.d\theta}{\int_0^{\pi/2} i_b \cos\eta.\sin\eta.d\eta.d\theta} = \sin^2\eta \qquad 9.5)$$

Hence, $$\eta = \sin^{-1}(R_\eta)^{0.5} \qquad 9.6)$$

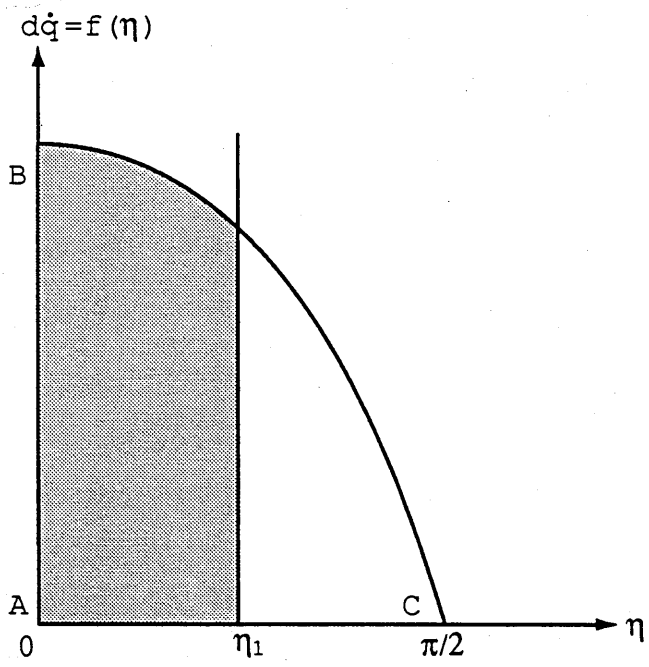

Figure 9.3. The schematic relationship between energy emission ($d\dot{q}$) and cone angle (η).

Similarly for θ,

$$R_\theta = \frac{\int_0^\theta i_b \cos\eta.\sin\eta.d\eta.d\theta}{\int_0^{2\pi} i_b \cos\eta.\sin\eta.d\eta.d\theta} = \theta/2\pi \qquad 9.7)$$

Hence, $\theta = 2\pi R_\theta$ 9.8)

Thus, by the selection of 4 random numbers, the origin and direction of emission can be determined.

9.4 Emission from a gas volume

The origin and direction of emission from within a gas volume must be selected in a similar fashion to that for a surface, such that point sources are uniformly distributed and such that the angular distribution of energy is correctly simulated. In this case, the total intensity of radiation is the energy flux emitted per unit time into elemental solid angle centred around η,θ.

$$d\dot{q} = i_b.d\omega \qquad 9.9)$$

Since we are not dealing with a plane of emission, the projected area term $\cos\eta$ is omitted, being unity for all beams within a gas zone. Furthermore, beams can be emitted in any direction such that $0 < \eta < \pi$ and $0 < \theta < 2\pi$.

The c.d.f. for η gives the following,

$$R_\eta = \frac{\int_0^\eta i_b \sin\eta . d\eta . d\theta}{\int_0^\pi i_b \sin\eta . d\eta . d\theta} = \frac{1 - \cos\eta}{2} \qquad 9.10)$$

Hence, $\eta = \cos^{-1}(1-2R_\eta)$ 9.11)

Similarly $\theta = 2\pi R_\theta$ which conforms to a uniform circumferential energy distribution.

9.5 The selection of point sources from non-rectangular zones

Uniformly distributed points can be selected from within a rectangular plane surface zone by application of equations 9.1) and 9.2). For a rectangular volume zone an additional equation for the third co-ordinate direction is required. For the non-rectangular (trapezoidal) zones shown in Figure 9.1, it is necessary to apply the cumulative distribution function to the x-z plane. For the surface zone (or x-z section through a gas zone) shown in Figure 9.4 the following cumulative distribution function ensures that the randomly selected points within the region OABC of area A are uniformly distributed,

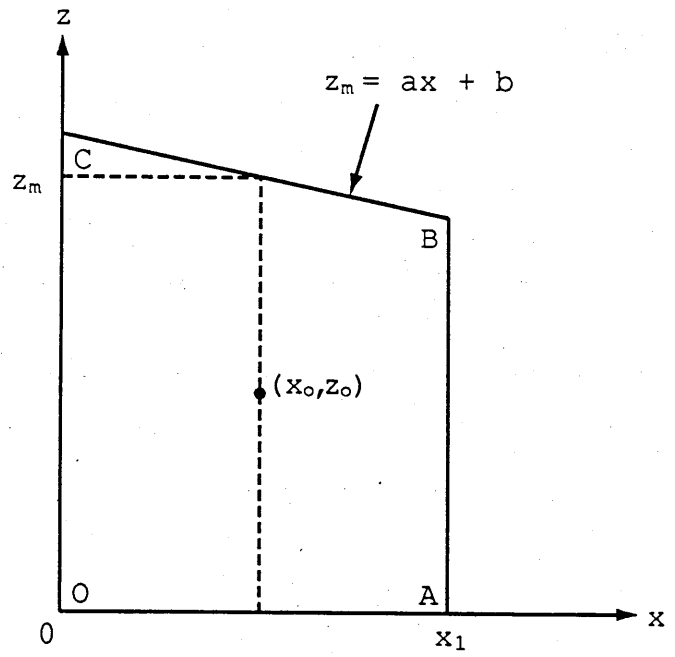

Figure 9.4. The selection of uniformly distributed points within a trapezoidal zone in the x-z plane.

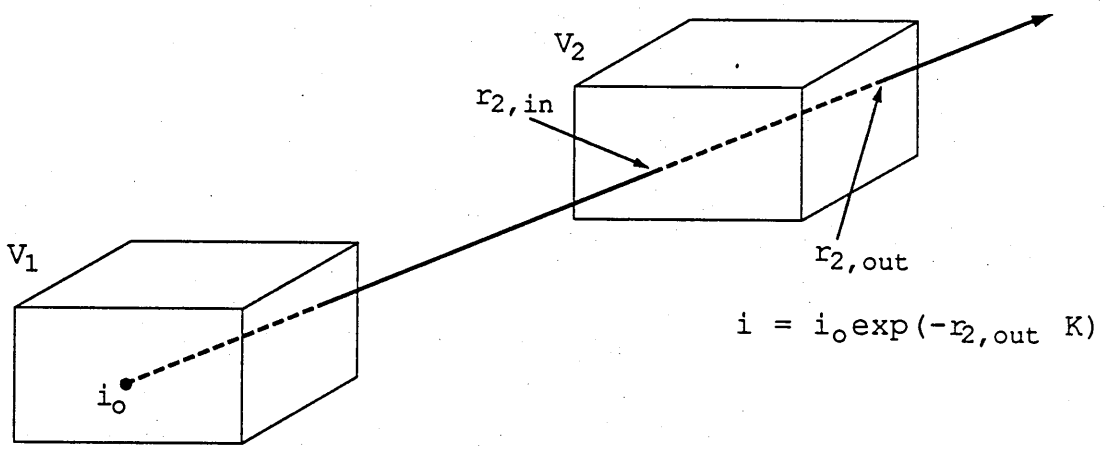

Figure 9.5. The determination of gas-gas exchange areas.

$$R_x = \frac{\int_0^{x_o} (ax+b)\,dx}{\int_0^{x_1} (ax+b)\,dx} = \left(\frac{a}{2} x_o^2 + bx_o\right)/A \qquad 9.12)$$

where $0 < R_x < 1$

For a given value of R_x, this quadratic equation is solved for x_o taking care to eliminate those roots that are outside the range $1 < x_o < x_1$. The co-ordinate z is determined from,

$$z_o = R_z z_m = R_z (ax_o + b) \qquad 9.13)$$

where $0 < R_z < 1$

9.6 Evaluation of Direct Exchange Areas

Surface-Surface Exchange - Consider two finite black surfaces A_1 and A_2. The Monte Carlo technique enables the view factor between the surfaces to be calculated by simply counting the fraction of beams leaving surface 1 which are intercepted by surface 2. The technique for determining whether a region intercepts a given beam will be described later. The view factor F_{12} is simply n/N where n is the number of beams intercepted by 2 and N the total number emitted from 1. The surface-surface direct exchange area assuming zero absorption between the surfaces is given by:

$$(\overline{s_1 s_2})_{K=0} = A_1 n/N \qquad 9.14)$$

If the two surfaces are now separated by an absorbing grey gas of uniform absorption coefficient (K), then each of the n beams arriving at 2 is partially absorbed during its passage through the gas. The fractional transmission of a beam is given by exp(-Kr) where r is its path length through the gas.

Hence,

$$\overline{s_1 s_2} = A_1/N \sum_n \exp(-Kr)_n \qquad 9.15)$$

Gas-Surface Exchange - Consider now a grey gas zone of volume V and absorption coefficient K. The direct exchange area between the gas and any surface zone A is determined by summing the fraction of each beam arriving at the surface taking into account absorption by the gas zone itself and any other intervening gas. The direct exchange area is the fraction of the total emission by the gas in 4π steradians (=4KV) ,thus:

$$\overline{gs} = 4KV/N \sum_n \exp(-Kr)_n \qquad 9.16)$$

Gas-Gas Exchange - The direct exchange area between two gas zones V_1 and V_2 is calculated by determining the fraction of each emitted beam crossing and absorbed in V_2 in its ultimate

passage to a surface in the enclosure, (see Figure 9.5). The beam at source can be assumed to have unit intensity (i_o=1). At $r_{2,in}$,the point of entry into V_2,

$$i_{in}/i_o = \exp(-r_{2,in}.K) \qquad 9.17)$$

At $r_{2,out}$,the point of departure from V_2, the fractional intensity is:

$$i_{out}/i_o = \exp(-r_{2,out}.K) \qquad 9.18)$$

The fraction of i_o absorbed in V_2 is then given by:

$$\Delta i = (i_{in}-i_{out})/i_o = \exp(-r_{2,in}.K) - \exp(-r_{2,out}.K) \qquad 9.19)$$

and the gas-gas direct exchange area is given as follows:

$$\overline{g_1 g_2} = 4KV_1/N \sum_n \Delta i \qquad 9.20)$$

where n in this case is the number of beams traversing zone 2.

9.7 The point of incidence of the beam with a surface

Having defined the beam source and direction, it is necessary to calculate its point or zone of incidence within the furnace enclosure. This is facilitated by resolving the beam into the component vectors a_i, a_j and a_k parallel respectively to the

x,y and z co-ordinate axes. Consider a unit vector OE emitted from a surface element lying parallel to the x-y plane as shown in Figure 9.6.

The component vectors are given by:

$$a_i = OA = \sin\eta\cos\theta \qquad 9.21)$$

$$a_j = OB = \sin\eta\sin\theta \qquad 9.22)$$

$$a_k = OC = \cos\eta \qquad 9.23)$$

In Table 9.1, the appropriate vectors are assigned to these expressions according to the plane of the emitting surface. Because of the slope of the roof zones in the model, the roof emitted vectors are resolved into components parallel to an x'-y'-z' co-ordinate system where the zone lies parallel to the x'-y' plane and perpendicular to the y'-z' and x'-z' planes. The roof emitted component vectors are then transformed with the x-y-z co-ordinate frame of reference. Since the y and y' co-ordinates are parallel, it is only necessary to resolve the x'-z' co-ordinates by rotation into the corresponding x-z plane of reference (see Figure 9.7)

Resolving a_i' into the corresponding vector a_i in the x-z plane of reference:

$$a_i = OA - BC = a_i'\cos\alpha - a_k'\sin\alpha \qquad 9.24)$$

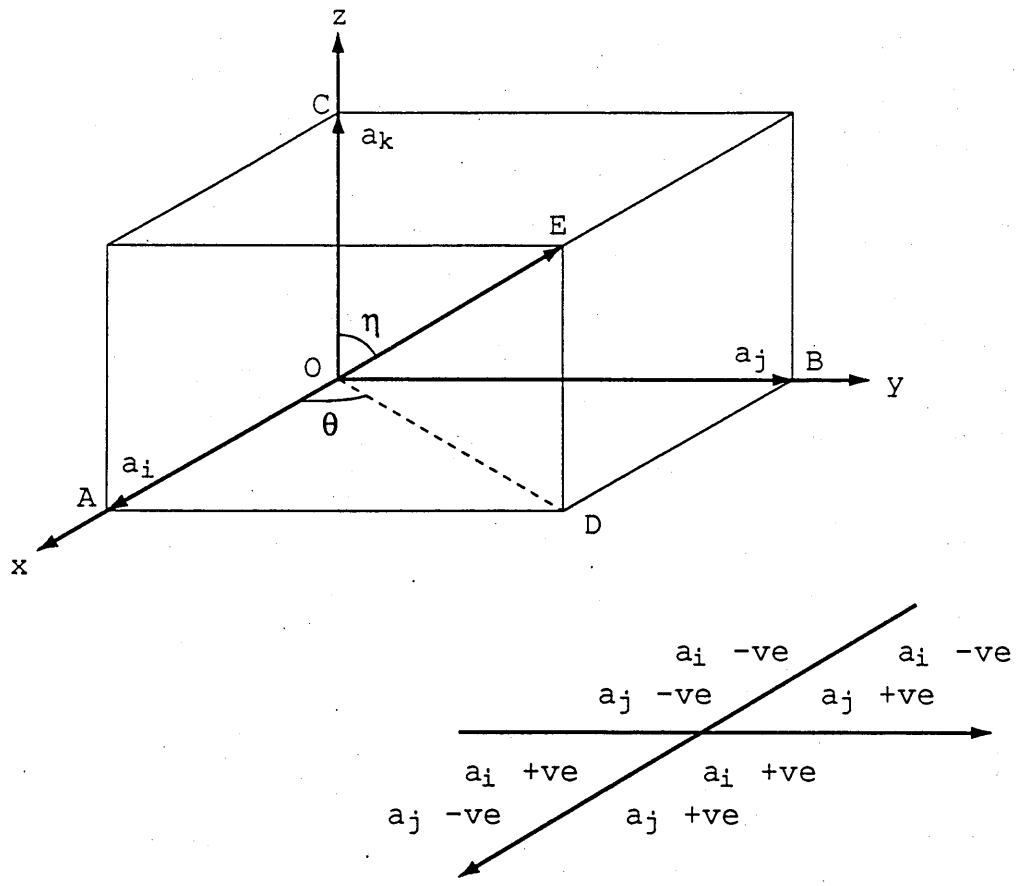

Figure 9.6. The resolution of the emitted beam into component vectors.

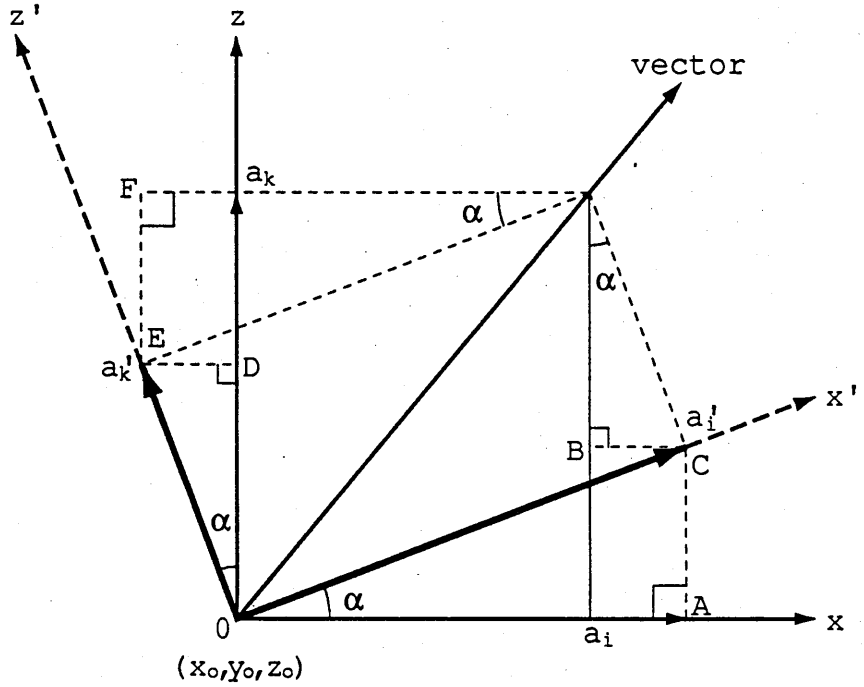

Figure 9.7. The transformation of a vector from the (x',z') to the (x,z) co-ordinate frames of reference.

Table 9.1 **The component vectors and their expressions from various zones.**

	Component Vector			
Zone Type:	Side Wall	End Wall	Floor	Roof
Plane:–	x-z	z-y	x-y	x^1-y^1
Expression:				
cosη	$\pm a_j$	$\pm a_i$	a_k	$-a_k'$
sinηcosθ	a_i	a_j	a_i	a_i'
sinηsinθ	a_k	a_k	a_j	a_j'

Resolving a_k' into a_k,

$$a_k = OD + EF = a_k'\cos\alpha + a_i'\sin\alpha \qquad 9.25)$$

The point of incidence (y,z) of a vector of components a_i, a_j, a_k with a plane surface representing for example, an end wall which is parallel to the y-z plane at $x=x_1$, is given by applying the properties of similar triangles. In the x-y plane as shown in Figure 9.8, this is given by,

$$\Delta y = y - y_o = \Delta x.(a_j/a_i) \qquad 9.26)$$

where $$\Delta x = x_1 - x_o \qquad 9.27)$$

Similarly for the x-z plane,

$$\Delta z = z - z_o = \Delta x.(a_k/a_i) \qquad 9.28)$$

Since the end wall is bounded by the limits $0 < y < y_1$ and $0 < z < z_1$ then it is a simple matter to determine whether y and z calculated by equations 9.26-9.28), fall within the boundary of the end wall.

Likewise, the determination of the point of incidence of a vector on the side wall and floor zones can be determined. The point of incidence of the beam P on a sloping roof zone is now determined. An equation describing the slope of the roof (Figure 9.9) is given as:

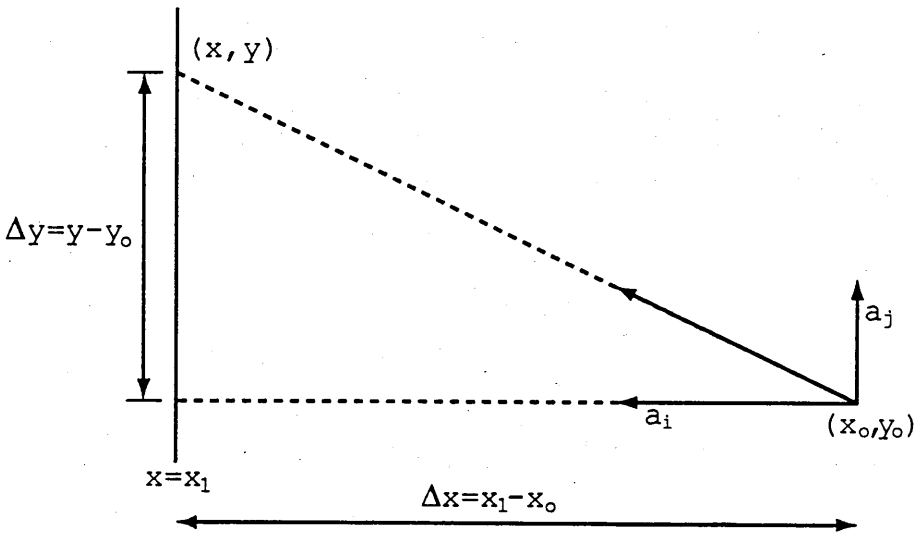

Figure 9.8. The determination of the point of incidence of a beam with a surface.

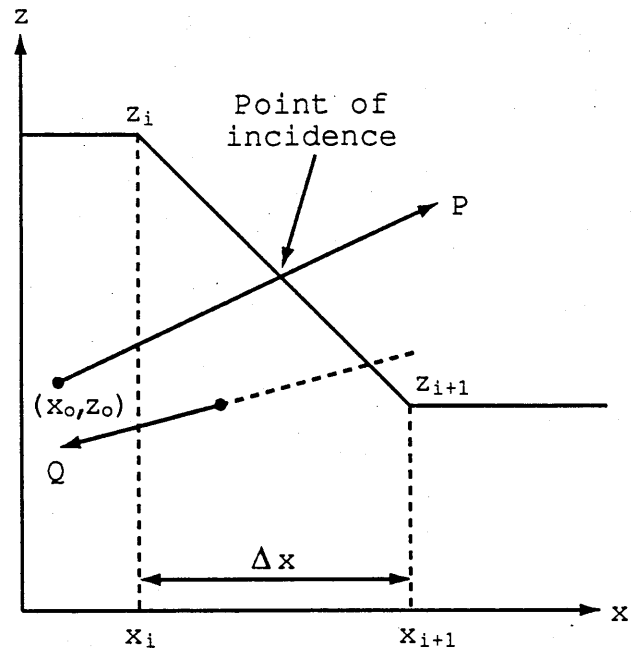

Figure 9.9. The determination of the point of incidence of beam P on a sloping roof zone.

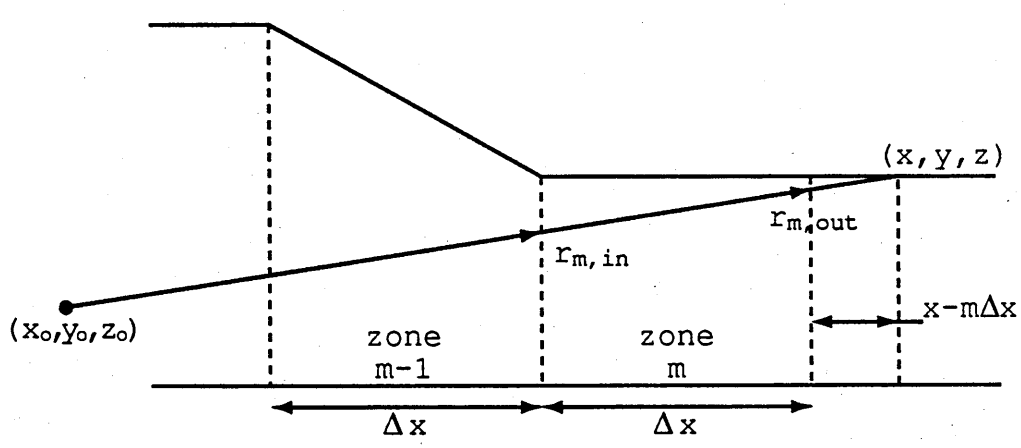

Figure 9.10. The determination of the beam length through a zone m.

$$z = b_2.x + c_2 \qquad 9.29)$$

where $b_2 = (z_{i+1} - z_i)/\Delta x$

and $c_2 = z_i - b_2.x_i$

A similar equation describing the vector P resolved as a vector parallel to the x-z plane can also be written,

$$z = b_1.x + c_1 \qquad 9.30)$$

where $b_1 = a_k/a_i$ (i.e. the vector ratios in the z and x planes respectively)

and $c_1 = z_o - b_1.x_o$

The point of intercept of these two straight lines is given by combining equations 9.29) and 9.30) thus:

$$b_2.x + c_2 = b_1.x + c_1$$

from which,

$$x = (c_1 - c_2)/(b_2 - b_1)$$

The y co-ordinate of incidence is given by:

$$y = y_o + (x - x_o).(a_j/a_i)$$

It is a simple matter to determine whether the lines cross between the limits x_{i+1} and x_i i.e. if $x_i < x < x_{i+1}$. A

check must also be made to determine whether the vector crosses the zone in a positive direction to avoid counting beams which are travelling away from the zone as exemplified by Q in Figure 9.9.

9.8 Determination of beam length

For the purposes of determining beam attenuation or absorption by a gas, the length r of each beam between its source at (x_o, y_o, z_o) and its ultimate point of incidence (x,y,z) on a surface is given by:

$$r = \{(x-x_o)^2 + (y-y_o)^2 + (z-z_o)^2\}^{0.5}$$

The partial beam length $r_{m,in}$ and $r_{m,out}$ entering and leaving gas zone m (Figure 9.10) is easily calculated by applying the property of similar triangles, thus:

$$r_{m,in} = \frac{(m-1).\Delta x - x_o}{x - x_o} \cdot r$$

$$r_{m,out} = \frac{m.\Delta x - x_o}{x - x_o} \cdot r$$

$$r_{m+1,in} = r_{m,out} \quad \text{etc.}$$

9.9 Programming logic

The computation of the zone of incidence of each beam proceeds in a logical sequence as shown in the simplified flow diagram in Figure 9.11. The principal steps in the computation are:-

1. The emitter zone is first selected within gas zone I (either a surface zone or gas zone I itself).

2. Random numbers between 0 and 1 are generated in the VAX subroutine URAN and these are used to calculate the point of emission (x_o, y_o, z_o) and the direction (η, θ) of each beam.

3. The beam is resolved into vectors a_i, a_j and a_k.

4. The surface zone of incidence is determined by a trial and error search. The point of intercept of the beam with a plane surface parallel to and containing the nearest roof zone is first determined. If this point is outside the boundary of the zone, the next roof zone (in the direction corresponding to a_i) is checked and so on i.e. the roof zones are checked sequentially from zone I through the NZONE if a_i is positive and from I to 1 if a_i is negative. This ensures that the nearest zone of incidence on the roof is determined and thereby enables an obscurring roof profile to be specified in the model.

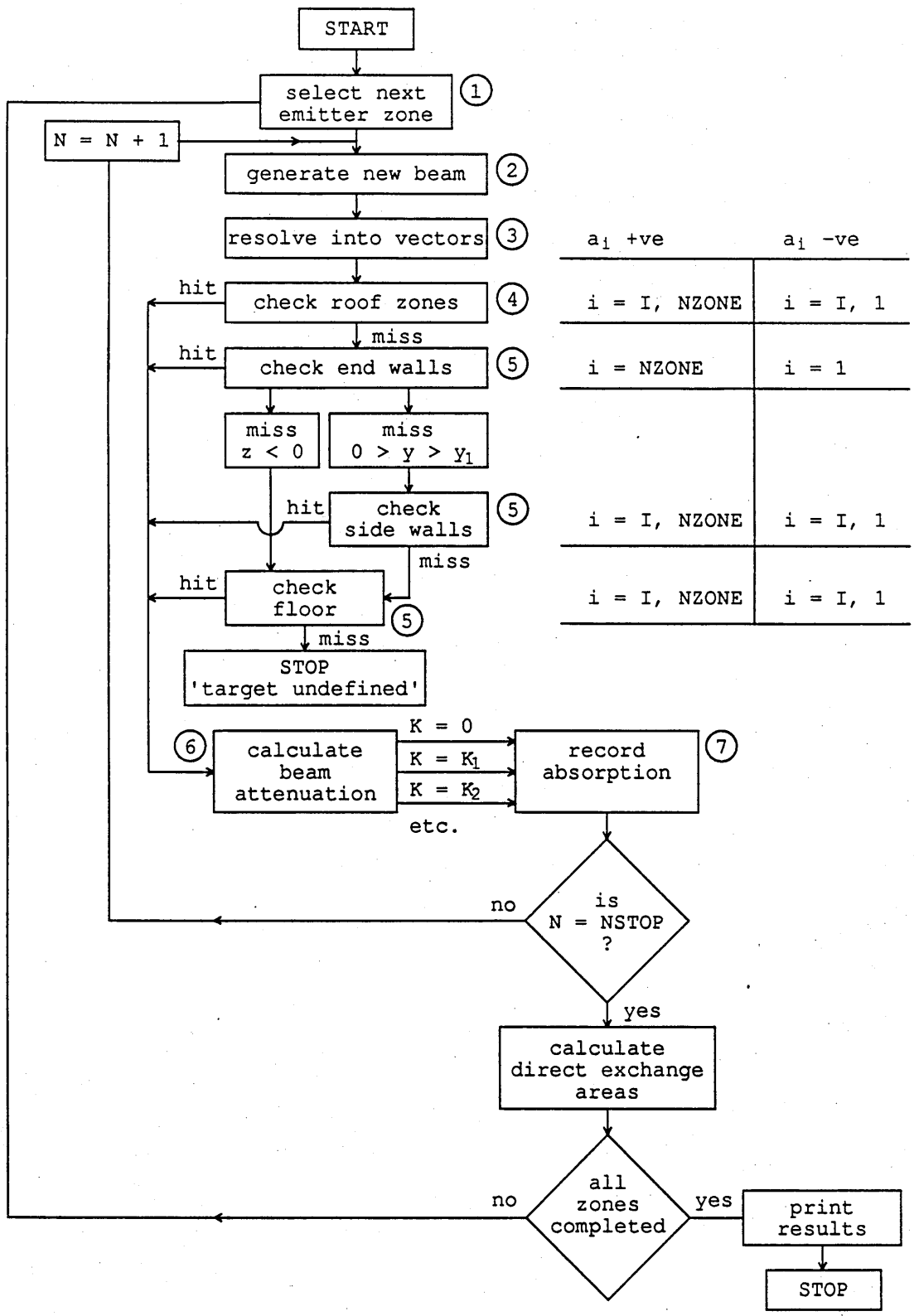

Figure 9.11. Flow diagram for the computation by the Monte-Carlo technique of the direct exchange areas in Fig. 9.1.
(numbers refer to steps in section 9.9)

5. If no 'hit is scored' on a roof zone, the incidence of the beam with a plane surface containing the appropriate end wall is determined. If the incidence is outside the zone boundary, then incidence with either a floor or side wall zone is checked according to the logic in Figure 9.11. Again if a_i is positive, floor and side wall zones from zone I to NZONE are checked (and conversely zone I to 1 if a_i is negative).

6. The path length and attenuation of each beam through the gas between its point of emission and incidence with a surface is calculated according to the value of the grey gas attenuation coefficient. When using a multiple grey gas model, attenuation of any one beam can be calculated for each component grey or clear gas. This avoids the necessity to generate and track a new beam for each individual grey gas.

7. The fraction of the beam absorbed by a receiving surface or gas zone is recorded.

8. Unless the requisite sample of beams (NSTOP) has been tracked, the next beam is selected randomly and the process is repeated.

9. When NSTOP beams have been simulated, the direct exchange areas are calculated as described in section 9.6. and then stored in the appropriate location in the exchange area array.

10. The computation is then repeated for the next emitting zone.

9.10 Verification of the Monte Carlo model

In order to verify the model, direct exchange areas have been calculated for the simple geometry comprising of 2 gas zones and 7 surfaces as shown in Figure 9.12 for K equal to 0,1 and 1.8 and some of the values have been compared to exact or accurate values derived from alternative methods as follows:

1. The charts in Appendix 3 have been used for orthogonal surface-surface or cubic gas and square surface zone pairs.

2. Exact data from analytical formulations [34,35,36] have been used for the zero K exchange areas (view factors) involving the inclined and/or triangular zones.

3. The gas-surface exchange areas involving the triangular gas zone (1) have been calculated by a numerical (Simpsons' rule) integration.

The Monte Carlo values have been calculated with N = 500, 1000, 5000, 10000 and 50000. The results are compared in Table 9.2. With N = 50000, the discrepancy compared to the accurate value is generally small (6% max, < 2.5% typical). This essentially verifies the model. Large discrepancies are

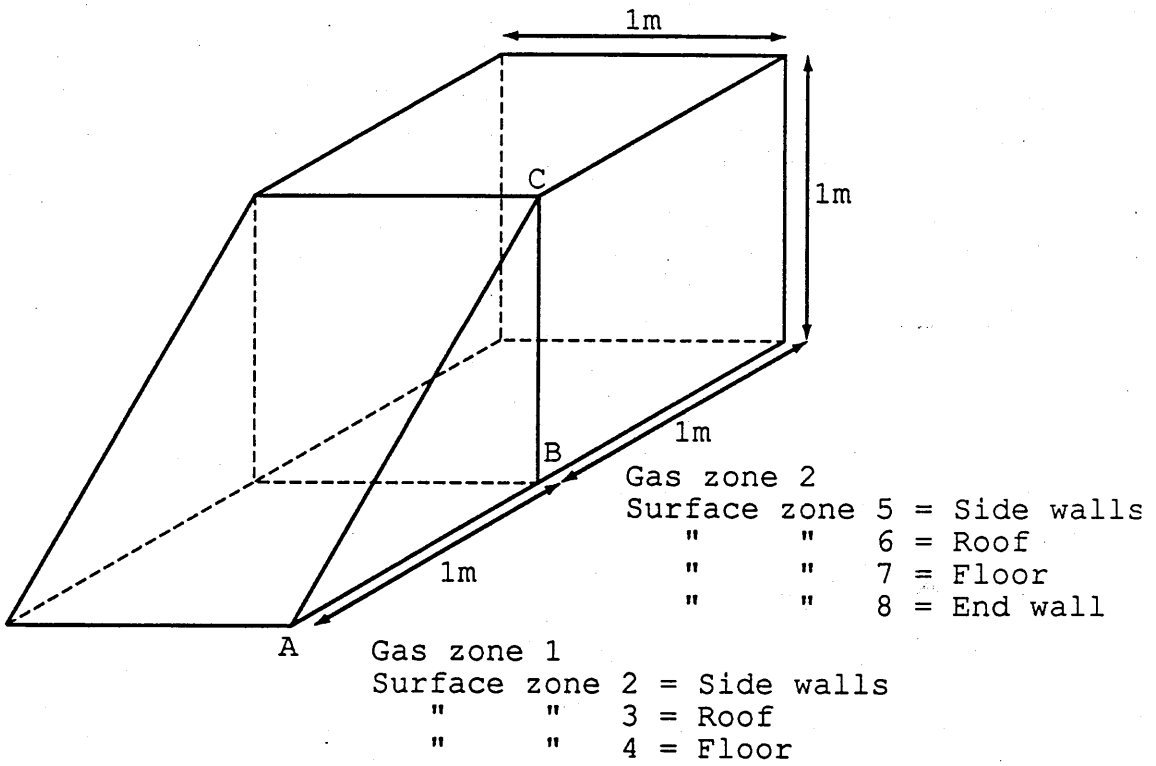

Figure 9.12. A 2 zone model for the verification of the Monte-Carlo technique for calculating direct exchange areas.

Table 9.2 Verification of the Monte Carlo Model for Direct Exchange Area Calculation

Exchange area (m^2)	Accurate Value	Monte Carlo Calculation N=500	N=1000	N=5000	N=10000	N=50000
$\overline{s_7 s_8}$ (K=0)	.200 [a]	.1880	.1975	.1956	.1999	.2023
(K=1)	.128 [a]	.1153	.1150	.1195	.1223	.1232
(K=1.8)	.090 [a]	.0841	.0813	.0870	.0893	.0895
$\overline{s_4 s_5}/2$ (K=0)	.040 [a]	.033	.0378	.041	.043	.041
(K=1)	.0165 [a]	.014	.0157	.0161	.0168	.0165
(K=1.8)	.0084 [a]	.0082	.0088	.0086	.0088	.0089
$\overline{s_4 s_6}$ (K=0)	.088 [a]	.078	.090	.087	.083	.086
(K=1)	.023 [a]	.022	.025	.024	.022	.023
(K=1.8)	.0084 [a]	.0080	.009	.0086	.0082	.0085
$\overline{s_3 s_4}$ (K=0)	.5135 [b]	.5649	.5266	.5313	.5297	.5269
$\overline{s_3 s_6}$ (K=0)	.0516 [b]	.0494	.0524	.0523	.0550	.0536
$\overline{s_4 s_2}/2$ (K=0)	.13 [c]	.1315	.1335	.1330	.1359	.1330
$\overline{s_2 s_3}/2$ (K=0)	.1803 [c]	.1758	.1828	.1770	.1740	.1764
$\overline{g_2 s_8}$ (K=1)	.45 [a]	.4730	.4162	.4579	.4268	.4495
(K=1.8)	.621 [a]	.6750	.5686	.6302	.5914	.6236
$\overline{g_2 s_4}$ (K=1)	.0589 [a]	.0847	.0799	.0617	.0630	.0602
(K=1.8)	.0597 [a]	.0898	.0821	.0642	.0657	.0624
$\overline{g_1 s_8}$ (K=1)	.0200 [d]	.0128	.0150	.0192	.0204	.0200
(K=1.8)	.0126 [d]	.0087	.0097	.0123	.0129	.0126
$\overline{g_1 s_7}$ (K=1)	.0463 [d]	.0474	.0431	.0456	.0427	.0457
(K=1.8)	.0518 [d]	.0527	.0485	.0496	.0477	.0514

Source of Accurate Values: a = Appendix 3; b = ref. 35; c = ref. 36;
d = Numerical Integration by Simpson Rule ($\Delta x = \Delta y = \Delta z = .025$m)

noticed with N = 500 particularly for some of the gas-surface exchange areas ($\overline{g_2 s_4}$ and $\overline{g_1 s_8}$), although these errors are significantly reduced when $N \geq 5000$. Thus, some caution may be needed in selecting an appropriately large sample size when computing certain exchange areas.

The accuracy of the Monte Carlo method will be discussed further in chapter 11 with particular reference to the effects of errors in direct exchange areas on computed heat transfer and thermal performance.

9.11 Sample Calculation

A sample calculation follows to illustrate the selection of the origin and direction of a beam from the triangular surface ABC in Figure 9.12, and to track it's destination and point of incidence with a surface.

1. Select beam origin and direction:
Select $R_x, R_z, R_\eta, R_\theta$ and solve for x, z, η and θ using equations 9.12), 9.13), 9.6) and 9.8) respectively.

$R_x = .921 \quad \Rightarrow \quad x_o = .9597$

$R_z = .422 \quad \Rightarrow \quad z_o = .405$

$R_\eta = .590 \quad \Rightarrow \quad \eta = .876$ radians $= 50.2^o$

$R_\theta = .867 \quad \Rightarrow \quad \theta = 5.448$ radians $= 312.1^o$

2. Resolve beam into component vectors - see Table 9.1.

$a_j = \cos\eta = .640$

$a_i = \sin\eta\cos\theta = .515$

$a_k = \sin\eta\sin\theta = -.5695$

3. Calculate point of incidence with plane parallel to floor zone.

$\Delta z = z_o = -.405$

$\Delta x/\Delta z = a_i/a_k$ from which $\Delta x = -.405 * .515/(-.5695)$

$= .366$

and hence $x = x_o + .366 = 1.3259$

$\Delta y/\Delta z = a_j/a_k$ from which $\Delta y = .455$ and $y = .455$

The values of x and y confirm incidence with the surface zone 7 in Figure 9.12.

CHAPTER 10

The Calculation of Total Exchange Areas

10.1 Introduction

Calculation of the total exchange areas from the direct exchange areas will now be described. Before they can be calculated however, the direct exchange areas must be checked and adjusted, if necessary, in order to ensure that they are consistent with the requirements of a heat balance on each zone. The direct exchange areas calculated by numerical integration and the Monte Carlo techniques described in the previous chapters, are inexact because of the approximate nature of these techniques, particularly if a course grid size or a small sample of beams are used. Consequently, adjustments must be made to the direct or total exchange areas. In this study, these adjustments are made to the direct exchange areas, although similar adjustments can be made to the total exchange areas.

10.2 Rules governing direct exchange areas.

The direct exchange areas must obey certain simple relationships in order to satisfy the criterion for radiative energy conservation at each zone.

10.2.1 Reciprocity

For thermal equilibrium to exist within an enclosure at uniform temperature, reciprocity must exist between the computed direct exchange areas.

This requires that:

$$\overline{s_i s_j} = \overline{s_j s_i} \qquad 10.1)$$

$$\overline{s_i g_j} = \overline{g_j s_i} \qquad 10.2)$$

$$\overline{g_i g_j} = \overline{g_j g_i} \qquad 10.3)$$

Reciprocity is used to advantage in the numerical integration method to avoid the repeated calculation of direct exchange areas which are merely reciprocal to those which have been previously calculated.

In the Monte-Carlo technique however, the calculation of reciprocal exchange areas cannot be avoided since the paths followed by emitted beams are not predetermined. Moreover, because of the approximate nature of the technique, the calculated reciprocal areas are not necessarily identical. Thus, to ensure conformity to the reciprocity rule, the arithmetic mean of the reciprocal direct exchange areas is determined for each zone pair.

For example, the corrected exchange area $(\overline{s_i s_j})_{corr}$ is computed from the reciprocal exchange area as follows:

$$(\overline{s_i s_j})_{corr} = (\overline{s_i s_j} + \overline{s_j s_i})/2$$

10.2.2 Sum rule checks.

For a zoned enclosure comprising of M surface and L gas zones, the arrays of exchange areas must also be consistent with the following sum rule equations:

On surface zone i:

$$A_i = \sum_{j=1}^{M} \overline{s_i s_j} + \sum_{j=1}^{L} \overline{s_i g_j} \qquad 10.4)$$

On gas zone i:

$$4K_i V_i = \sum_{j=1}^{M} \overline{g_i s_j} + \sum_{j=1}^{L} \overline{g_i g_j} \qquad 10.5)$$

With numerical integration there is necessarily some error in the calculation of direct exchange areas so that these sum rules are not initially obeyed. With the Monte Carlo technique, conservation of the simulated beams ensures

conformity with these sum rules. However, the subsequent averaging of exchange areas to ensure reciprocity, destroys the inherent agreement with the sum rules.

10.3 Adjustment of computed exchange areas.

Assuming reciprocity is obtained therefore, the direct exchange areas must be adjusted to obey the sum rule checks by a technique which does not destroy the reciprocity. Two techniques were tried and compared.

10.3.1 Adjustment to self exchange areas

In this method, adjustments were made only to the surface-surface and gas-gas self exchange areas ie. to $\overline{s_i s_i}$ and $\overline{g_i g_i}$. Correction of any of the gas-surface exchange areas was avoided since these affect both sum rule equations 10.4) and 10.5) , see Figure 10.1. The gas-surface exchange areas also govern the primary rate of radiant emission from the combustion products to a particular zone, and hence these terms have a direct influence on the predicted overall heat transfer. It was therefore considered unwise to absorb any correction in these terms once they had been calculated.
Thus, the sum rule equation for surface zone i can be written in terms of a residual error Ω_i thus (see Figure 10.1),

$$\left(\begin{array}{ccc} \overline{s_1 s_1} & \overline{s_1 s_2} & \overline{s_1 s_2} \\ & + & \\ \overline{s_2 s_1} & \overline{s_2 s_2} & \overline{s_2 s_3} \\ & + & \\ \overline{s_3 s_1} & \overline{s_3 s_2} & \overline{s_3 s_3} \\ & + & \end{array}\right)$$

$$\left(\begin{array}{ccc} \overline{g_1 s_1} + & \overline{g_1 s_2} + & \overline{g_1 s_3} \\ & + & \\ \overline{g_2 s_1} & \overline{g_2 s_2} & \overline{g_2 s_3} \end{array}\right) + \left(\begin{array}{cc} \overline{g_1 g_1} + & \overline{g_1 g_2} \\ & \\ \overline{g_2 g_1} & \overline{g_2 g_2} \end{array}\right) = 4K_1V_1 + \Omega_1$$

$$\overline{A_2+\Omega_2}$$

Figure 10.1 **A shematic illustration of the method of adjusting self exchange areas.**

$$\sum_{j=1}^{M} \overline{s_i s_j} + \sum_{j=1}^{L} \overline{s_i g_j} - A_i = \Omega_i \qquad 10.6)$$

$\overline{s_i s_i}$ is then adjusted to $\overline{s_i s_i} - \Omega_i$ so that equation 10.4) is obeyed exactly.

The sum rule equation for gas zone i is similarly adjusted by replacement of $\overline{g_i g_i}$ by $\overline{g_i g_i} - \Omega_i$ so that equation 10.5) is obeyed.

10.3.2 Least squares smoothing of direct exchange areas

The method described in the previous section, can lead to zero or low valued self exchange area becoming negative. An improved method of smoothing using a least squares technique has been described by Larsen and Howell [37]. This adjusts all exchange areas, including the gas-surface areas, in proportion to their original value, and therefore ensures that zero or low valued exchange areas remain zero or positive. This technique will now be described. The full derivation of the technique is given in reference [37].

Consider an enclosure of M surface and L volume zones. The direct exchange areas can be assembled into a single matrix **X** where,

$$\mathbf{X} = \begin{bmatrix} \overline{ss} & \overline{sg} \\ \overline{gs} & \overline{gg} \end{bmatrix}$$

($\overline{gs}$ is the transpose matrix of $\overline{sg}$)

Reciprocity requires that **X** is symmetrical. Furthermore, the sum rule equations require that the i^{th} row (or column) sums to c_i where,

$$c_i = \sum_{j-1}^{M+L} x_{ij} \qquad 10.7)$$

$c_i = A_i$ for $i \leq M$

$c_i = (4KV)_{i-M}$ for $i > M$

Assume that an estimate of **X** has been made which obeys the symmetry (reciprocity) constraints, but which does not satisfy the sum rules. The problem is to adjust **X** to satisfy the sum rules and to maintain reciprocity, but by minimising the disturbances to the original values of x_{ij} .

Larsen and Howell describe a technique for determining multipliers (λ_i and λ_j) which can be applied to the exchange areas as follows, and which satisfies the above constraints:

$$x'_{ij} = x_{ij} + w_{ij}(\lambda_i + \lambda_j) \qquad 10.8)$$

where, x_{ij} is the original estimate of the exchange area,

x'_{ij} is the adjusted exchange area,

and w_{ij} is a weighting coefficient.

The matrix **W** of weighting coefficients allows relative adjustments to be made to particular exchange areas. If w_{ij} = 1 for all i and j , then equal adjustment is made to all exchange areas.

The multipliers λ_i are calculated as follows:

$$\mathbf{r}\lambda = \delta \qquad 10.9)$$

where the elements r_{ij} (in the matrix **r**) = w_{ij} for i not equal to j , and where,

$$r_{ii} = w_{ii} + \sum_{j-1}^{M+L} w_{ij}$$

$$\delta_i = c_i - \sum_{j-1}^{M+L} x_{ij}$$

Eqn 10.9) is inverted to derive all values of λ by a Gaussian elimination technique [38].

Smoothing with $w_{ij} = x_{ij}^2$ was demonstrated by Larsen and Howell and was subsequently applied in this work. This choice of weighting coefficient avoids the occurrence of negative exchange areas.

A comparison of this technique for adjusting exchange areas with that described in the previous section has been made and this will be described in chapter 11.

10.4 Calculation of Total Exchange Areas

The arrays of adjusted direct exchange areas are substituted into equations 3.36-3.38), to derive the corresponding arrays of total exchange areas $\overline{SS}$, $\overline{SG}$ and $\overline{GG}$. The steps in the computation of the arrays representing the various terms in these equations will now be described and illustrated for a simple model comprising of 3 surface and 2 gas zones (ie. M=3,L=2).

10.4.1 Determination of R

1. The inverse matrix $\mathbf{R}^{-1}$ of order M x M is first determined as follows:

$$\mathbf{R}^{-1} = \begin{bmatrix} A_1 & 0 & 0 \\ 0 & A_2 & 0 \\ 0 & 0 & A_3 \end{bmatrix} - \begin{bmatrix} \overline{s_1 s_1} & \overline{s_1 s_2} & \overline{s_1 s_3} \\ \overline{s_2 s_1} & \overline{s_2 s_2} & \overline{s_2 s_3} \\ \overline{s_3 s_1} & \overline{s_3 s_2} & \overline{s_3 s_3} \end{bmatrix} \cdot \begin{bmatrix} \rho_1 & 0 & 0 \\ 0 & \rho_2 & 0 \\ 0 & 0 & \rho_3 \end{bmatrix}$$

$$= \begin{bmatrix} A_1 - \rho_1.\overline{s_1 s_1} & -\rho_2.\overline{s_1 s_2} & -\rho_3.\overline{s_1 s_3} \\ \text{(a)} & \text{(b)} & \text{(c)} \\ -\rho_1.\overline{s_2 s_1} & A_2 - \rho_2.\overline{s_2 s_2} & -\rho 4.\overline{s_2 s_3} \\ \text{(d)} & \text{(e)} & \text{(f)} \\ -\rho_1.\overline{s_3 s_1} & -\rho_2.\overline{s_3 s_2} & A_3 - \rho_3.\overline{s_3 s_3} \\ \text{(g)} & \text{(h)} & \text{(i)} \end{bmatrix}$$

2. This matrix is then inverted to give **R** such that

$$\mathbf{R}.\mathbf{R}^{-1} = \mathbf{I}$$

or in long-hand,

$$\begin{bmatrix} a & b & c \\ d & e & f \\ g & h & i \end{bmatrix} . \begin{bmatrix} r_{11} & r_{12} & r_{13} \\ r_{21} & r_{22} & r_{23} \\ r_{31} & r_{32} & r_{33} \end{bmatrix} = \begin{bmatrix} 1 & 0 & 0 \\ 0 & 1 & 0 \\ 0 & 0 & 1 \end{bmatrix}$$

Known matrix $\mathbf{R}^{-1}$ Unknown matrix **R** Unit matrix

where a,b,c.. etc are terms in the matrix representing $\mathbf{R}^{-1}$ above.

This is done using standard numerical techniques for solving systems of linear equations, by solving for the unknown variables (r_{ij}) in columnwise fashion ,thus:

$$\begin{bmatrix} a & b & c \\ d & e & f \\ g & h & i \end{bmatrix} \cdot \begin{bmatrix} r_{11} \\ r_{21} \\ r_{31} \end{bmatrix} = \begin{bmatrix} 1 \\ 0 \\ 0 \end{bmatrix}$$

$$\begin{bmatrix} a & b & c \\ d & e & f \\ g & h & i \end{bmatrix} \cdot \begin{bmatrix} r_{12} \\ r_{22} \\ r_{32} \end{bmatrix} = \begin{bmatrix} 0 \\ 1 \\ 0 \end{bmatrix}$$

etc.

These equations can be solved by Gaussian elimination for r_{ij}, which are then assigned to an array representing the matrix **R** of order M x M.

10.4.2 Determination of $\overline{SS}$

1. The product of the diagonal matrix **εAI** and **R** is first computed, thus,

$$\begin{bmatrix} \varepsilon_1 A_1 & 0 & 0 \\ 0 & \varepsilon_2 A_2 & 0 \\ 0 & 0 & \varepsilon_3 A_3 \end{bmatrix} \cdot \begin{bmatrix} r_{11} & r_{12} & r_{13} \\ r_{21} & r_{22} & r_{23} \\ r_{31} & r_{32} & r_{33} \end{bmatrix} = \begin{bmatrix} \varepsilon_1 A_1 r_{11} & \varepsilon_1 A_1 r_{12} & \varepsilon_1 A_1 r_{13} \\ \varepsilon_2 A_2 r_{21} & \varepsilon_2 A_2 r_{22} & \varepsilon_2 A_2 r_{23} \\ \varepsilon_3 A_3 r_{31} & \varepsilon_3 A_3 r_{32} & \varepsilon_3 A_3 r_{33} \end{bmatrix}$$

This is carried out by simply multiplying each element in row i in **R** by $\varepsilon_i A_i$. (Note that **εAI.R = R.εAI**)

2. The product $\varepsilon\mathbf{AI.R}$ is then multiplied by the array representing the matrix $\overline{\mathbf{ss}}$ by simple matrix multiplication.

3. The product matrix is then multiplied by the diagonal matrix $\varepsilon\mathbf{I}$. In this case, this is carried out by multiplying each element in column j in the product matrix by ε_j .

The resulting array represents the matrix of total exchange areas $\overline{\mathbf{SS}}$. The matrix order (M x M) is retained throughout this computation.

10.4.3 Determination of $\overline{\mathbf{SG}}$

Steps 1 and 2 in the previous section are repeated above except that the product $\varepsilon\mathbf{AI.R}$ is multiplied by the array $\overline{\mathbf{sg}}$ of order M x L to give the matrix $\overline{\mathbf{SG}}$ of total exchange areas. (Note: $\overline{\mathbf{sg}}$ and $\overline{\mathbf{SG}}$ are of identical order.)

10.4.4 Determination of $\overline{\mathbf{GG}}$

1. The product of the matrix $\overline{\mathbf{gs}}$ of order L x M and the diagonal matrix $\rho\mathbf{I}$, is first calculated thus:

$$\begin{bmatrix} \overline{g_1 s_1} & \overline{g_1 s_2} & \overline{g_1 s_3} \\ \overline{g_2 s_1} & \overline{g_2 s_2} & \overline{g_2 s_3} \end{bmatrix} \cdot \begin{bmatrix} \rho_1 & 0 & 0 \\ 0 & \rho_2 & 0 \\ 0 & 0 & \rho_3 \end{bmatrix} = \begin{bmatrix} \rho_1 \overline{g_1 s_1} & \rho_2 \overline{g_1 s_2} & \rho_3 \overline{g_1 s_3} \\ \rho_1 \overline{g_2 s_1} & \rho_2 \overline{g_2 s_2} & \rho_3 \overline{g_2 s_3} \end{bmatrix}$$

Note that the matrix order of the product is the same as $\overline{gs}$.

2. Calculate the product of this matrix with the M x M matrix **R** . Again, a product matrix of order L x M is obtained.

3. Calculate the product of this matrix with the M x L matrix $\overline{sg}$ (the transpose of $\overline{gs}$). This yields a matrix of order L x L representing the product $\overline{gs}.\rho\mathbf{I}.\mathbf{R}.\overline{sg}$

4. Add this matrix to the matrix of direct exchange areas $\overline{gg}$ to give the matrix of total exchange areas $\overline{GG}$

10.4.5 Computation Procedure

The computation procedure is outlined in Figure 10.2.
The attenuation coefficient (K_n) for each grey gas in the mixed grey gas model is given by $K_n = k_{g,n}(p_w+p_c)$. For a given fuel gas composition, and assuming fully burnt stoichiometric or fuel lean combustion products, the partial pressures are determined by the excess air level. The computation of $\overline{gs}$, $\overline{gg}$, $\overline{GS}$ and $\overline{GG}$ are bypassed for the clear gas components.

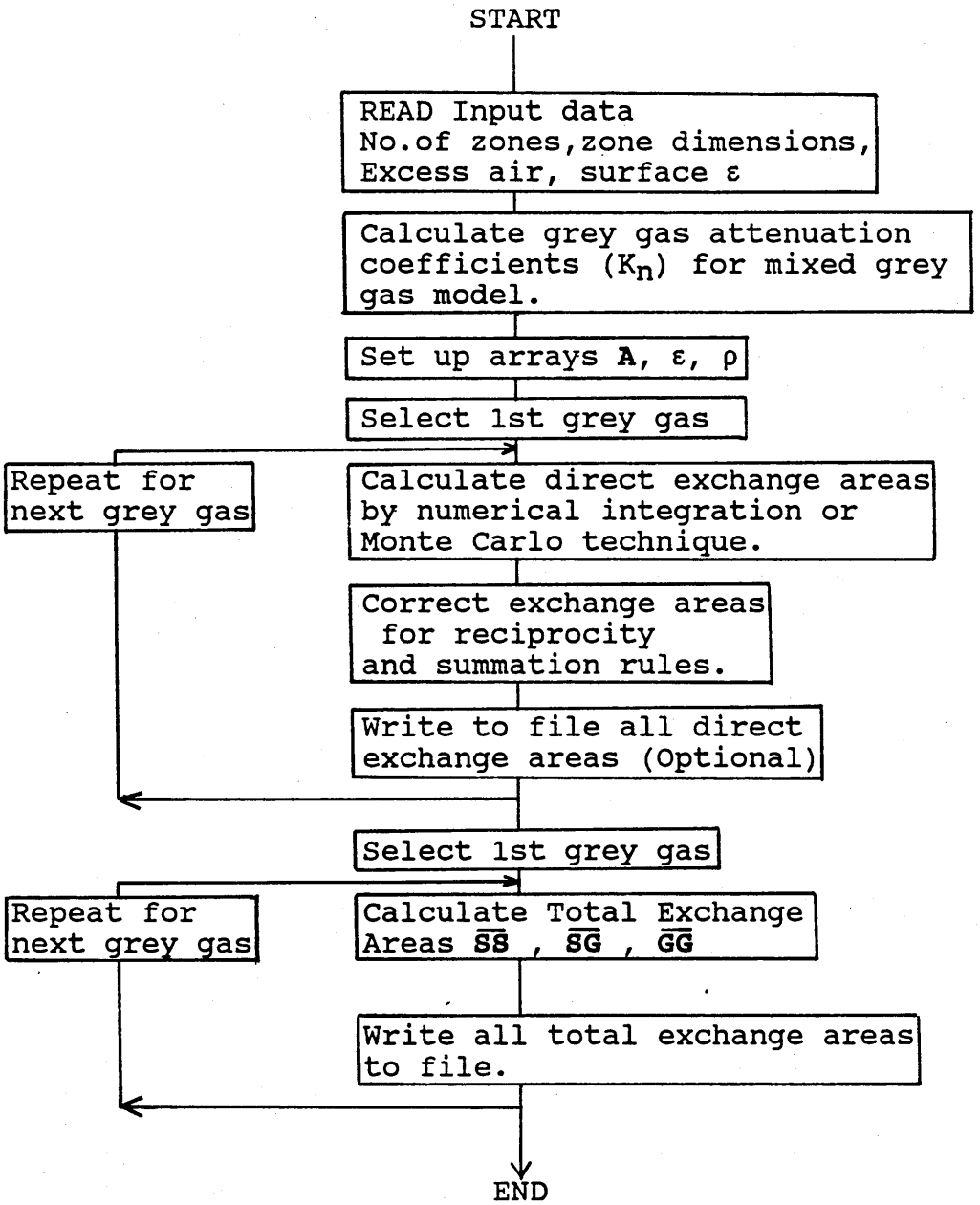

Figure 10.2 **The computation procedure for calculating total exchange areas.**

CHAPTER 11

Numerical Evaluation of the Model

11.1 Purpose of study

Two alternative techniques have been identified and developed for calculating direct exchange areas, namely:

- numerical integration (Chapter 7)
- the Monte-Carlo technique (Chapter 8)

Depending on the element size adopted, numerical integration offers a high level of accuracy. However, its method of application in this study is restricted to rectangular geometries only. The Monte-Carlo technique was developed to relax this restriction so that irregular geometries could be simulated including those where shading can occur. However, the latter technique is less accurate. In this chapter the two techniques are evaluated by:

1) Comparing the accuracy of calculation of the direct exchange areas using the Monte-Carlo technique against those calculated by numerical integration.

2) Assessing the effects of the error in the direct exchange areas on the predicted performance of a simple furnace.

3) Determining the importance of accurately representing furnace geometry for thermal performance predictions.

Also included in this study will be a comparison of the choice of smoothing technique for the direct exchange areas, and its effect on thermal predictions. Although the project has concentrated on the development of a long furnace model with interzone radiation, the effect of neglecting interzone radiation using a simple long furnace model has also been studied and is presented. Finally, a study of the effect of the number of zones on the thermal predictions is given.

11.2 Comparison of numerical integration and Monte-Carlo techniques.

Direct exchange areas were calculated by the Monte Carlo technique using beam sample sizes (N) of 500, 1000, 5000 and 10000. These were generated for a 4x1x1m rectangular enclosure zoned into 4 equal gas zones of $1m^3$ volume each (see Figure 11.1). Surface zoning comprised of 2 end walls, 4 load surface zones and 4 wall zones as shown in Figure 11.1. A furnace atmosphere corresponding to natural gas combustion products with 15% excess air was specified in the exchange area calculation. Exchange areas were generated for the 3 grey-gas model with attenuation coefficients of $K_1 = 0$, $K_2 = 0.47\ m^{-1}$ and $K_3 = 17.2\ m^{-1}$.

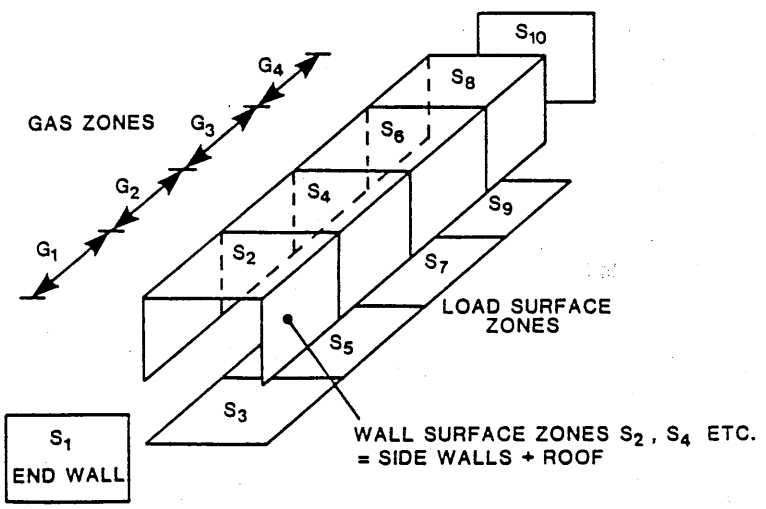

Figure 11.1 The surface and gas zone numbering system in a 4 zone long furnace model.

As a standard of comparison, a reference set of exchange areas were generated by numerical integration with an element size of 0.05 m side length giving 8000 elements per cubic gas zone. Convergence of the exchange areas to an accuracy of 0.5% was obtained in this case.

Before the comparison was made, the exchange areas generated by the Monte-Carlo technique were averaged to ensure reciprocity. Self-exchange areas were also adjusted to ensure that the sum rules were obeyed. The latter adjustment was also made to the reference set of exchange areas (generated by numerical integration), although the degree of adjustment was small in this case.

Table 11.1(a) compares values for zone pairs in close proximity to each other, i.e. where the exchange areas are of the order of $0.01m^2$ or greater. Table 11.1(b) provides comparisons for zone pairs at opposite extremes of the enclosure.

As a further indication of the accuracy of the Monte-Carlo technique, the mean absolute percentage error for groups of corresponding direct exchange areas are presented in Tables 11.2a)-d). The mean absolute error of a sample of n exchange areas is defined by,

Table 11.1

A comparison of selected direct exchange areas evaluated by numerical integration and by the Monte-Carlo technique.

Direct Exchange Area	K m^{-1}	Reference value[1] m^2	Monte-Carlo Method N=500 (% deviation from reference value)	N=1000	N=5000	N=10000
(a) Proximate zone pairs						
$\overline{s_1 s_3}$	0	.2004	3.8	-3.7	-1.0	-1.0
$\overline{s_1 s_3}$	0.47	.1565	2.9	-4.5	-0.75	-0.43
$\overline{s_1 s_3}$	17.2	.0121	11.6	8.2	9.7	7.7
$\overline{g_1 s_1}$	0.47	.2558	1.8	-8.1	-4.0	0.2
$\overline{g_1 s_1}$	17.2	.9574	-39.4	-16.4	-11.2	6.6
$\overline{g_1 g_2}$	0.47	.0579	15.4	-0.9	2.4	2.9
$\overline{g_1 g_2}$	17.2	.8836	-26.7	16.2	3.4	5.3
(b) Distant zone pairs						
$\overline{s_1 s_9}$	0	.00347	-42.4	72.9	26.8	3.7
$\overline{s_1 s_9}$	0.47	.0067	-43.3	79.1	-38.8	17.9
$\overline{g_1 s_9}$	0.47	.00070	351	-100	-41.1	12.9
$\overline{g_1 g_4}$	0.47	.00203	-30.5	-4.9	-14.8	3.5

[1] Calculated by numerical integration.

Table 11.2

A comparison of direct exchange areas generated by the Monte-Carlo technique with values derived by numerical integration - all areas averaged and adjusted for conformity with sum rules.

Table 11.2a) (N=500)

Nos. = mean absolute percentage errors (see eqn.11.1)

Nos. in brackets = sample size

		Numerical range of exchange areas m^2				
	$K(m^{-1})$	0.0001-0.001	0.001-0.01	0.01-0.1	>0.1	TOTAL
Gas-Gas	0.47	- (0)	4.7 (6)	1.5 (6)	3.9 (4)	3.3
Gas-Gas	17.2	- (0)	- (0)	- (0)	16.4 (10)	16.4
Gas-Surf.	0.47	240.0 (2)	62.7 (10)	25.0 (12)	6.9 (16)	37.9
Gas-Surf.	17.2	- (0)	- (0)	76.0 (12)	27.8 (10)	54.1
Surf-Surf.	0.0	- (0)	30.0 (12)	23.4 (32)	5.6 (38)	16.1
Surf-Surf.	0.47	2988. (6)	21.1 (28)	12.2 (24)	6.1 (26)	225.8
Surf-Surf.	17.2	72.6 (18)	- (0)	318.8 (20)	- (0)	202.2
TOTAL		754.9 (26)	28.7 (56)	81.5(106)	9.0(104)	

Table 11.2b) (N=1000)

Nos. = mean absolute percentage errors (see eqn.11.1)

Nos. in brackets = sample size

Numerical range of exchange areas m^2

	$K(m^{-1})$	0.0001-0.001	0.001-0.01	0.01-0.1	> 0.1	TOTAL
Gas-Gas	0.47	- (0)	19.8 (6)	1.3 (6)	1.6 (4)	8.3
Gas-Gas	17.2	- (0)	- (0)	- (0)	9.8 (10)	9.8
Gas-Surf	0.47	91.4 (2)	40.0 (10)	12.0 (12)	3.7 (16)	19.6
Gas-Surf	17.2	- (0)	- (0)	46.5 (12)	13.1 (10)	31.3
Surf-Surf	0.0	- (0)	37.3 (12)	12.0 (32)	3.5 (38)	11.8
Surf-Surf	0.47	2532 (6)	17.4 (28)	9.5 (24)	2.7 (26)	190.2
Surf-Surf	17.2	46.7 (18)	- (0)	214.5 (20)	- (0)	135.0
TOTAL		624.2 (26)	25.9 (56)	52.9(106)	4.8 (104)	

Table 11.2c) (N=5000)

Nos. = mean absolute percentage errors (see eqn.11.1)

Nos. in brackets = sample size

Numerical range of exchange areas m^2

	$K(m^{-1})$	0.0001-0.001	0.001-0.01	0.01-0.1	> 0.1	TOTAL
Gas-Gas	0.47	- (0)	8.1 (6)	1.3 (6)	1.4 (4)	3.9
Gas-Gas	17.2	- (0)	- (0)	- (0)	2.5 (10)	2.5
Gas-Surf	0.47	42.1 (2)	19.4 (10)	7.0 (12)	2.5 (16)	10.1
Gas-Surf	17.2	- (0)	- (0)	50.4 (12)	7.0 (10)	30.7
Surf-Surf	0.0	- (0)	10.9 (12)	6.9 (32)	1.3 (38)	4.9
Surf-Surf	0.47	1337. (6)	7.9 (28)	3.3 (24)	1.2 (26)	99.5
Surf-Surf	17.2	19.7 (18)	- (0)	121.3 (20)	- (0)	73.1
TOTAL		325.1 (26)	10.6 (56)	32.3(106)	2.2(104)	

Table 11.2d) (N=10000)

Nos. = mean absolute percentage errors (see eqn.11.1)

Nos. in brackets = sample size

Numerical range of exchange areas m^2

	$K(m^{-1})$	0.0001-0.001		0.001-0.01		0.01-0.1		> 0.1		TOTAL
Gas-Gas	0.47	-	(0)	5.3	(6)	1.6	(6)	.8	(4)	2.8
Gas-Gas	17.2	-	(0)	-	(0)	-	(0)	2.1	(10)	2.1
Gas-Surf	0.47	16.4	(2)	7.1	(10)	4.6	(12)	1.5	(16)	4.6
Gas-Surf	17.2	-	(0)	-	(0)	29.6	(12)	6.0	(10)	18.9
Surf-Surf	0.0	-	(0)	10.7	(12)	4.7	(32)	1.0	(38)	3.9
Surf-Surf	0.47	1305.	(6)	6.0	(28)	2.6	(24)	.8	(26)	96.2
Surf-Surf	17.2	19.0	(18)	-	(0)	90.1	(20)	-	(0)	56.4
TOTAL		316.2	(26)	7.1	(56)	23.0	(106)	1.6	(104)	

$$\text{Error } (\%) = \frac{100}{n} \sum_{i=1}^{N} \{(X_i - Y_i)^2\}^{0.5}/Y_i \qquad 11.1)$$

where X_i = direct exchange area calculated by the Monte-Carlo technique.

Y_i = reference value of the corresponding direct exchange calculated by numerical integration.

In Tables 11.2a)-d) the areas are grouped according to the order of magnitude of their numerical value

The main features of these comparisons (assuming the reference data are correct) are:

(a) For closely-spaced zone pairs, where K is zero or small (0.47 m^{-1}), the Monte-Carlo technique with a sample size (N) of 500 (Table 11.2a)) yields errors which are less than 25% and typically below 10%. These differences are reduced to <5% at the largest sample size, N = 10000 (Table 11.2d)).

(b) With the highly absorbing grey gas (i.e. K = 17.2 m^{-1}) the Monte-Carlo technique is less accurate. Substantial differences occur for all exchange areas, and a high sample size (N = 10000) is required to ensure errors below 10% for the most closely spaced zone pairs.

(c) The largest errors are associated with the lower-valued ranges of exchange areas. This is to be expected since the samples of received beams are obviously much smaller and therefore statistically less significant in these situations. These errors are however, unlikely to be important with regard to radiation calculations because the exchange areas are so small, so that the corresponding zone pairs play little part in the overall radiation process.

11.3 The effect of exchange area accuracy.

Thus, some of the direct exchange areas calculated using the Monte-Carlo technique are considerably less accurate than those obtained by numerical integration. It is therefore important to assess the effect of these inaccuracies on the predicted thermal performance of a furnace.

SSZONE was run to simulate a continuous counterflow steel reheating furnace. The furnace dimensions and zoning, and the furnace atmosphere were those specified in the previous section. Steel input and output temperatures of $15^{o}C$, and $1300^{o}C$ were assumed, with a throughput of 2 Te/hour, equating to a load heat transfer rate of 0.47 MW. 100% of the fuel (natural gas) was supplied and fully combusted in zone 1 with all of the combustion products flued from zone 4. All wall and roof zones were assumed to be black and adiabatic and convective heat transfer was ignored by specifying all

convection coefficients to zero. The load surface was also assumed to be black. These conditions, together with the general arrangement of the zones were such that interzone radiation exchange along the furnace was expected to be significant, thus providing a rigorous test of the radiation model and of the influence of direct exchange areas. Table 11.3 compares the thermal predictions using the reference set of direct exchange areas, to those using the Monte-Carlo derived exchange areas.

The differences in the predictions are small despite the comparatively large differences in direct exchange areas. As expected, increasing N to 10000 produces results which, in general, display closer agreement with the predictions using the reference data. All results are, however, acceptable for practical furnace design purposes. The individual gas and surface zone temperatures are also compared in Table 11.4. These only differed by a maximum of $7^{o}C$ provided N 1000. Differences of up to $14^{o}C$ were noted when N = 500. These comparisons confirmed that a long furnace model can tolerate large errors in the supplied direct exchange area data and suggest that the Monte-Carlo technique can be used with confidence.

11.4 Effect of exchange area smoothing technique.

Two alternative methods were applied for smoothing the

Table 11.3

A comparison of the steady state thermal predictions using various sets of direct exchange areas.

(Heat transfer rate to steel = 0.47 MW)

Source of exchange areas	Predicted Thermal Efficiency %	Heat flux (kW/m^2) Zone 1	Zone 2	Zone 3	Zone4
Reference set by numerical integration	37.38	64.7	110.0	154.4	157.4
Monte-Carlo (N = 10000)	37.36	63.5	109.8	154.2	159.0
Monte-Carlo (N = 5000)	37.21	64.3	109.5	153.2	159.5
Monte-Carlo (N = 1000)	37.25	63.9	109.3	152.9	160.4
Monte-Carlo (N = 500)	36.80	61.4	111.1	152.0	161.9

(NB. In all cases a solution was achieved with a heat balance error of < 0.03%)

Table 11.4 A comparison of the predicted steady-state temperatures using various sets of direct exchange areas.

Source of exchange area.	Zone 1	Zone 2	Zone 3	Zone 4
		Gas Temps (^{o}C)		
Numerical Integration:	1559	1403	1263	1146
Monte-Carlo:				
N = 10000	1559	1403	1263	1147
N = 5000	1560	1404	1265	1150
N = 1000	1560	1405	1267	1149
N = 500	1566	1405	1277	1157
		Wall Temps (^{o}C)		
Numerical Integration:	1355	1250	1109	1008
Monte Carlo:				
N = 10000	1354	1251	1109	1009
N = 5000	1355	1251	1111	1010
N = 1000	1362	1253	1114	1012
N = 500	1359	1258	1121	1010

(NB. In all cases a solution was achieved with a heat balance error of < 0.03%)

calculated direct exchange areas so that they conform to the reciprocity and sum rules. These were:

i) correction to self exchange areas $\overline{s_i s_i}$ and $\overline{g_i g_i}$
ii) least squares smoothing to all exchange areas by the technique of Larsen and Howell [37].

Direct exchange areas were calculated by the Monte-Carlo technique with N = 500 . One set of exchange areas was then corrected by the technique i) and the other duplicate set by least squares smoothing. Again, a reference set of exchange areas was also generated by numerical integration using a fine integration step. These exchange areas were smoothed by the former technique, although only minor corrections to the self exchange areas were necessary in this case. This set of exchange areas was therefore considered accurate. In Table 11.5, samples of exchange areas are compared for proximate and distant zone pairs, and for zones separated by a non-absorbing, a weakly absorbing and a strongly absorbing grey gas. This comparison revealed no evidence that least squares smoothing produced more accurate exchange areas. Larsen and Howell [37] do not in fact claim such a benefit. The exercise was repeated with N = 10000 and the same conclusion was drawn.

A comparison of the computed thermal performance data for the example given in the previous section was also made using the

Table 11.5 A comparison of the errors in computed direct exchange areas using alternative methods of correction for reciprocity and sum rule adjustment.

Direct Exchange Area	K (m^{-1})	Reference Value[1] (m^2)	Monte-Carlo method (% deviation) N = 500	N = 10000
(a) Proximate zone pairs				
$\overline{s_1 s_3}$	0	.2004	4.9 (3.8)	-0.8 (-1.0)
$\overline{s_1 s_3}$	0.47	.1565	1.6 (2.9)	-1.4 (-0.43)
$\overline{s_1 s_3}$	17.2	.0121	25.0 (11.6)	-0.4 (7.7)
$\overline{g_1 s_1}$	0.47	.2558	6.3 (1.8)	-0.6 (0.2)
$\overline{g_1 s_1}$	17.2	.9574	-0.94 (-39.4)	-0.6 (6.6)
$\overline{g_1 g_2}$	0.47	.0579	-6.0 (15.4)	1.1 (2.9)
$\overline{g_1 g_2}$	17.2	.8836	24.8 (-26.7)	7.7 (5.3)
(b) Distant zone pairs				
$\overline{s_1 s_9}$	0	.00347	-100 (-42.4)	-22.2 (3.7)
$\overline{s_1 s_9}$	0.47	.00067	-100 (-43.3)	-23.9 (17.9)
$\overline{g_1 s_9}$	0.47	.00070	-100 (35.1)	-8.6 (12.9)
$\overline{g_1 s_4}$	0.47	.00203	6.9 (-30.5)	-1.5 (3.5)

([1]) Calculated by numerical integration

Numbers = percentage error, (relative to reference value) using least squares smoothing. Numbers in brackets = percentage error using self-exchange area correction method.

reference set of direct exchange areas, and using the Monte-Carlo data smoothed by the two alternative techniques. The results are shown in Table 11.6. In these comparisons, some slight improvements in predicted efficiency and heat fluxes are indicated, although either set of predictions were acceptably close to those derived using the reference set of exchange areas.

Thus, the simpler technique of correction to the self exchange areas was found to be reliable and does not lead to significant inaccuracies in computed thermal performance data. Where programming is to be kept simple, this can be used with confidence. However, the least squares smoothing technique has been embodied in the programs since it does avoid the occurrence of negative self exchange areas. Although more complicated to program, it does not require significant additional computer storage or run time.

11.5 Effect of furnace shape.

The advantage of the Monte-Carlo technique is that it can easily be applied to furnaces of irregular geometry. Thermal performance predictions were therefore carried out to assess the importance of accurately representing geometry. Steady-state predictions were generated for the three geometries shown in Figure 11.1 for a simple steel reheating application. The furnace volume was maintained equal in all

Table 11.6 A comparison of the steady-state thermal predictions using various sets of direct exchange areas.

Source of Exchange Areas	Predicted Efficiency (%)	Heat Flux kW/m^2 Zone 1	Zone 2	Zone 3	Zone4
Numerical Integration:					
	37.38	64.7	110.0	154.4	157.4
Monte-Carlo (N=10000):					
	37.36	63.5	109.8	154.2	159.0
Monte-Carlo with lss[1] (N=10000):					
	37.42	65.0	110.3	154.2	157.0
Monte-Carlo (N=500):					
	36.80	61.4	111.1	152.0	161.9
Monte-Carlo with lss[1] (N=500):					
	37.71	67.5	110.2	154.4	154.4

([1]) lss = least square smoothing

three cases. Cases A and B represent geometries with considerable shading between zones caused by the roof.

The furnace was subdivided into 8 zones with thermal input to zone 1 and the flue at zone 8. Steel input and output temperatures of 15^{o}C and 1200^{o}C were assumed with a throughout of 4 Te/hour. The results are shown in Figure 11.2. It was found that the predicted thermal efficiency was only very slightly different in the three cases despite the very different shapes. However, comparison of the normalised heat flux profile along the furnace indicated that the rectangular geometry (C) produces lower heat flux at zone 1, a much lower peak heat flux at zone 3, and a higher flux at zone 8 where the cold load enters the furnace. This trend is expected since the effect of interzone radiation towards zone 8 is expected to be higher than in cases B and C.

This study has therefore confirmed that simplification of the geometry by a rectangular representation can lead to considerable distortion of the heat flux and temperature profile at the load surface. This can have serious practical consequences for these types of furnaces particularly those used for heating material of thick section and low conductivity. In these, the heat flux profile determines the rate of conduction into the material and its temperature uniformity at discharge. Particularly with metal reheating, the temperature history of the material through the furnace

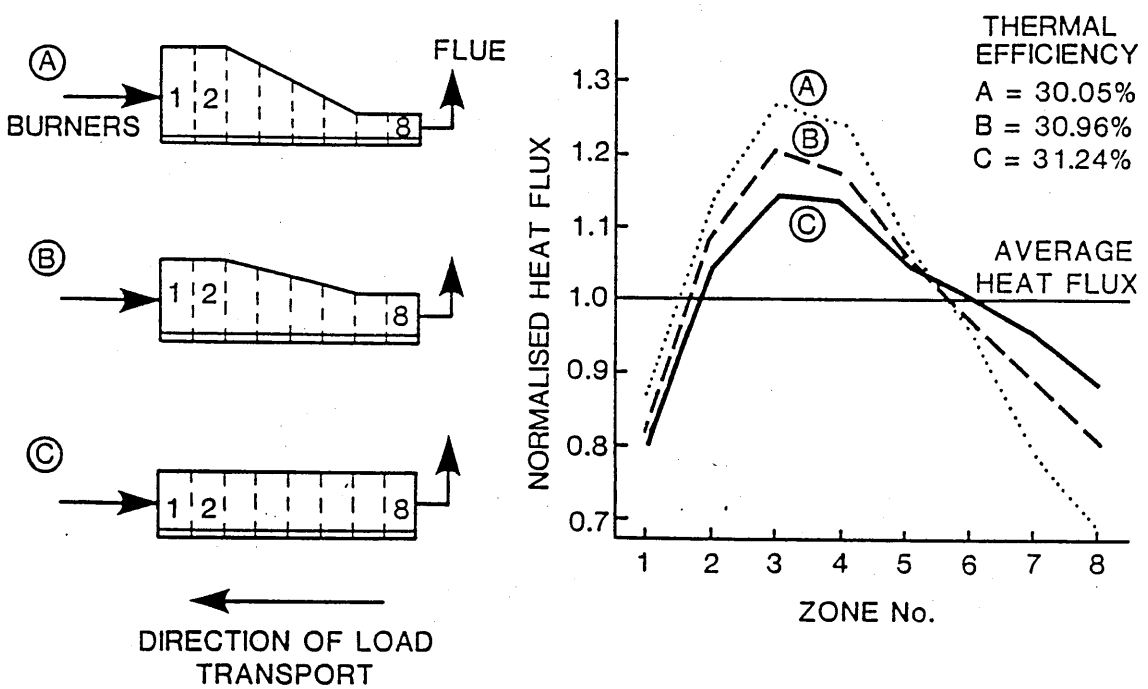

Figure 11.2 **The influence of furnace chamber shape on predicted thermal efficiency and heat flux profile. (Output=0.9MW steel at 1200°C).**

may also influence its surface condition or state of oxidation.

11.6 Effect of the number of zones.

When applying any zone model, it is important to ensure that the solution obtained is independent of the number and size of zones used to represent the radiating enclosure. This can be achieved simply by increasing the number of zones until acceptably small changes in the predictions between successive solutions are achieved (ie. convergence is achieved). The steady state model (SSZONE) was tested for a simple steel reheating application using various zoning arrangements. The data for this simulation were:

Furnace length	3m
Furnace width	1m
Furnace height	1m
Steel throughput	1000, 1500, 2000 and 3000 kg/hr
No. of zones	6, 8, 10, 12 were used.

(NWALL = 2 , roof and side walls treated as 1 surface zone)

As with the previous simulation, the fuel input was confined to zone 1 and all products were flued in the last zone. Simulations were performed without convection switched on in the model.

The predicted results are plotted in Figures 11.3 and 11.4 . The predicted steady-state efficiency (Figure 11.3) is shown to be reasonably constant for all 4 zoning arrangements, although the drop in efficiency noted when going from 8 to 6 zones may not be tolerable in some situations. Examination of the predicted heat flux profiles also show acceptable tolerance to the number of zones (Figure 11.4). A reduction from 12 to 6 zones reduces the total number of direct exchange areas needed from 1132 to 316 (a reduction by a factor of about 3.5). Thus, when machine memory or speed are limited there is advantage in using the minimum number of zones that gives a solution within acceptable accuracy.

Comparisons such as these should be carried out for every new application being modelled. It is not considered worthwhile attempting to derive general guidelines for zoning that can be used for every possible new application. The above results are therefore only illustrative.

11.7 Effect of interzone radiation.

The above steady-state predictions were repeated using a simple long furnace model which neglects interzone radiation transfer. The basis of this model, and the method of calculating exchange areas are described in chapter 7. Predictions were obtained using 6, 8, 10 and 12 zones. The corresponding results are also plotted in Figures 11.5 and

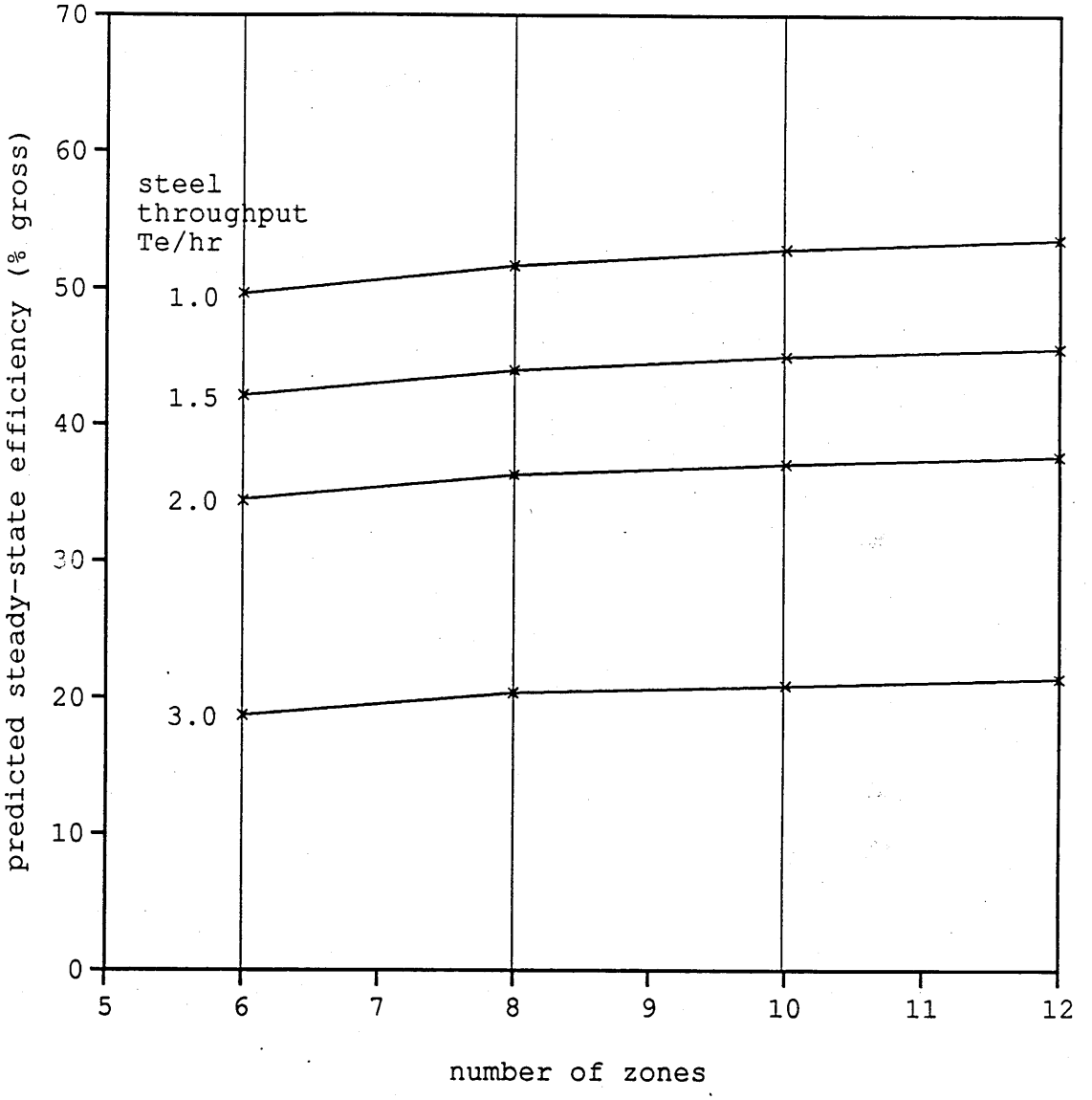

Figure 11.3. The effect of number of zones on the predicted thermal efficiency of a simple reheating furnace using SSZONE. (i.e. radiation interchange between zones included)

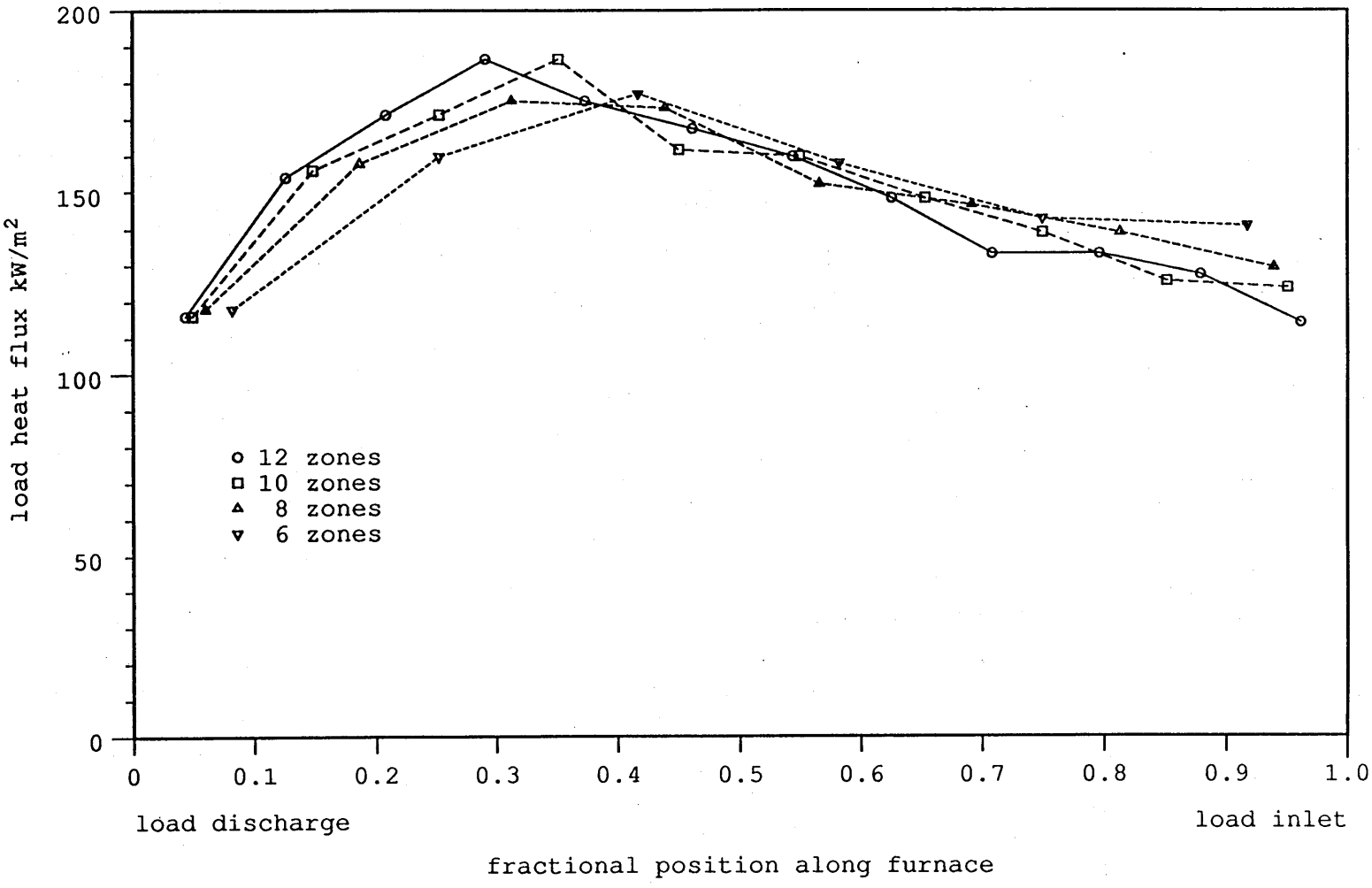

Figure 11.4. The effect of number of zones on the predicted heat fluxes in a simple reheating furnace using SSZONE. (i.e. radiation interchange between zones included). - Load throughput = 2 Te/hr.

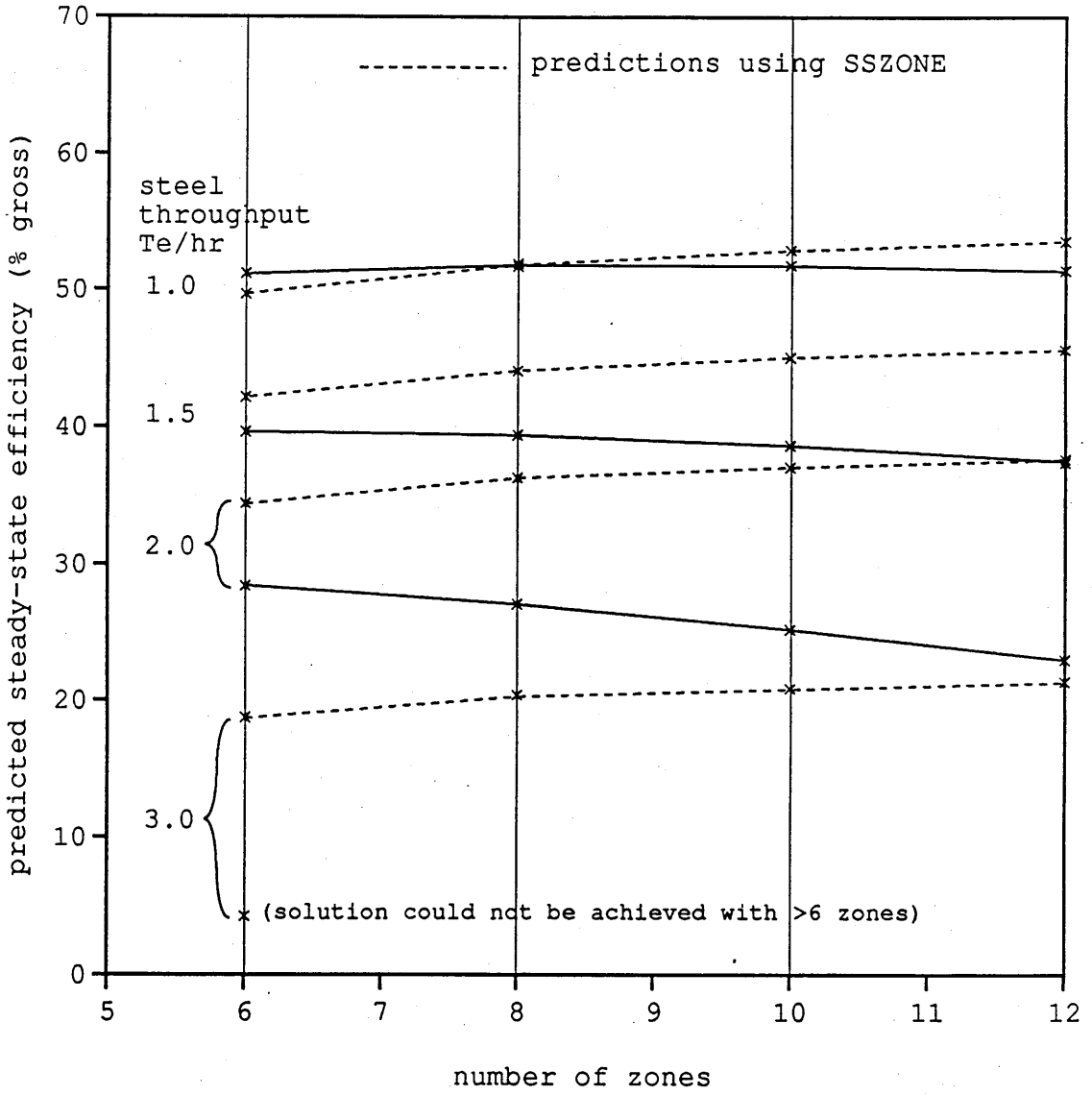

Figure 11.5. The predicted thermal efficiency of a simple reheating furnace using a long furnace model with zone interchange neglected, and comparison to predictions using SSZONE.

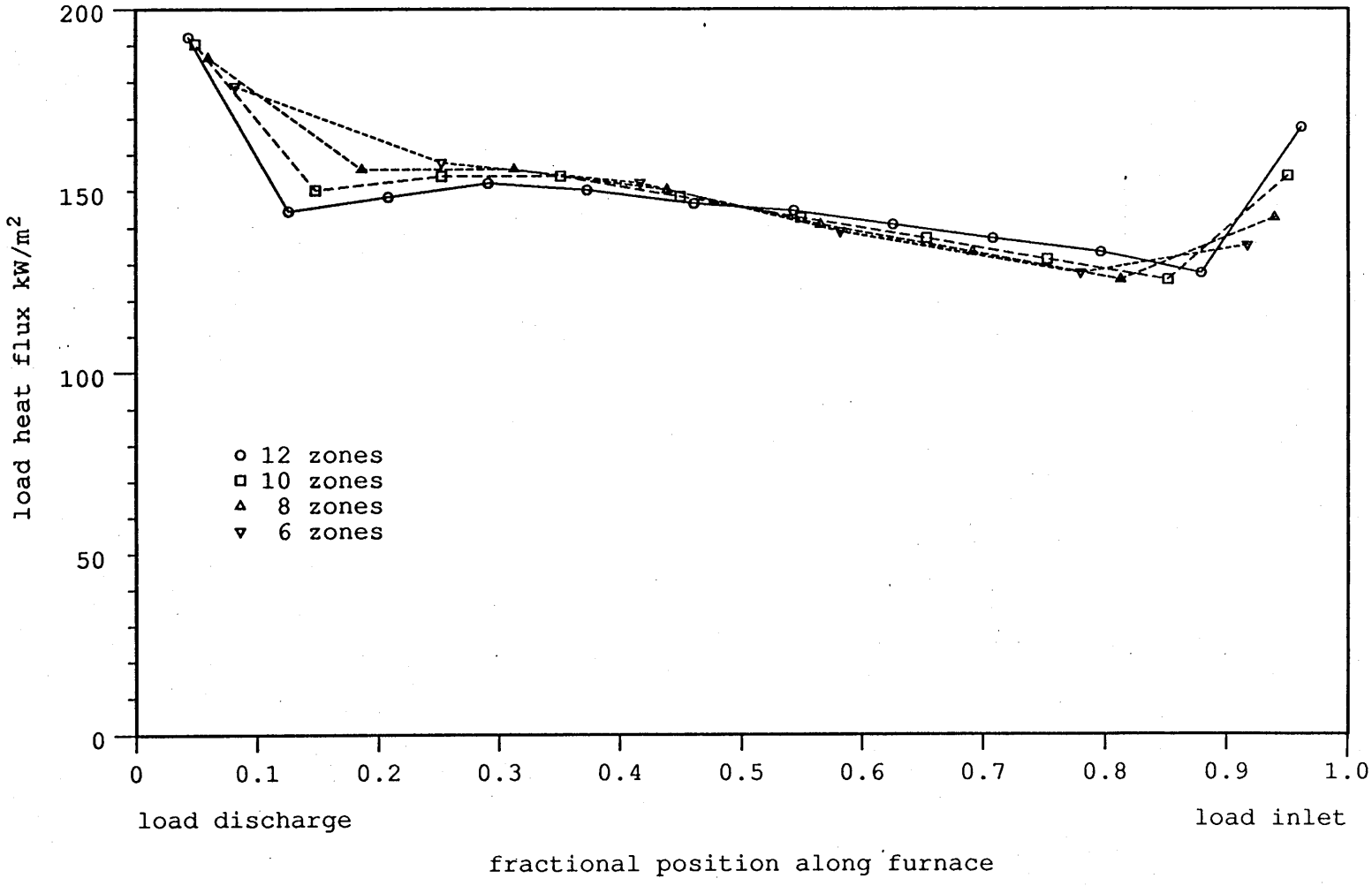

Figure 11.6. The effect of number of zones on the predicted heat fluxes in a simple reheating furnace using a long furnace model with zone interchange neglected. (conditions as for Fig. 11.4)

11.6. In Figure 11.5, the efficiencies are also compared with those using SSZONE. It is noted that the efficiency at 1500 and 2000 kg/hr are considerably lower than predicted by SSZONE. At 3000 kg/hr a stable solution could not be achieved with more than 6 zones. With 6 zones there was a very large discrepancy in predicted efficiency. Predictions at 1000 kg/hr are reasonably close to those from SSZONE. Thus, the influence of axial radiation on predicted thermal performance is most important at the higher throughputs. These results also agree with those derived for a similar type of furnace by Tucker and Lorton [2] and which are reproduced in Figures 11.7 and 11.8.

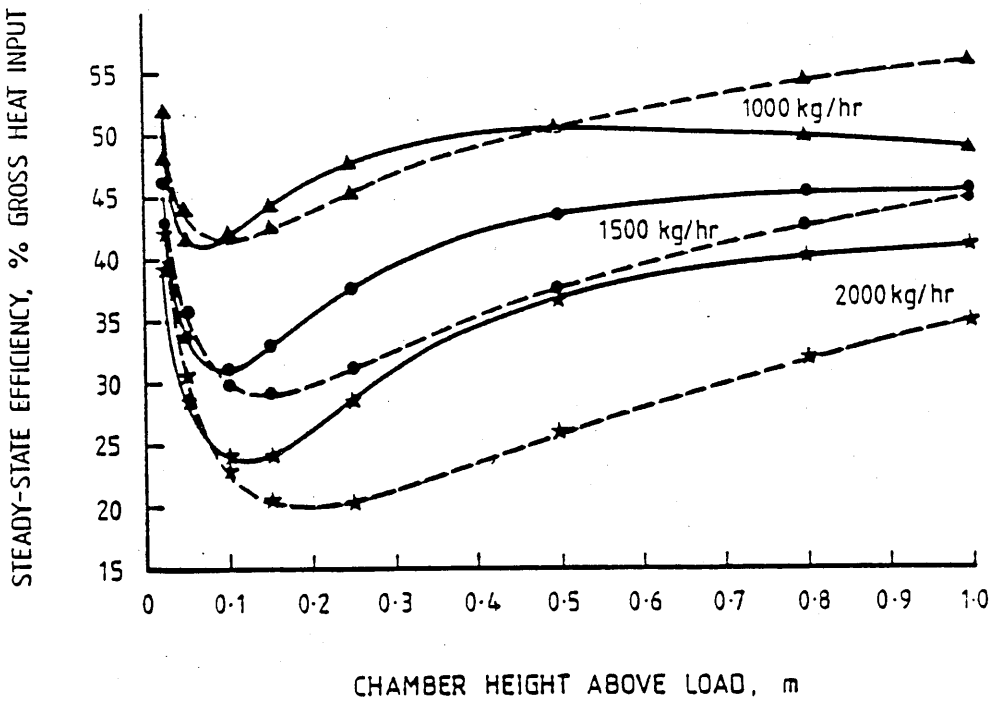

_ _ _ zero net interchange between zones

_____ interchange between zones included

Figure 11.7 **A comparison of predicted steady-state efficiencies with and without interzone radiation included [39].** (Furnace width 1.0m, length 3.0m, load discharge temperature 1250°C, load width 1.0m).

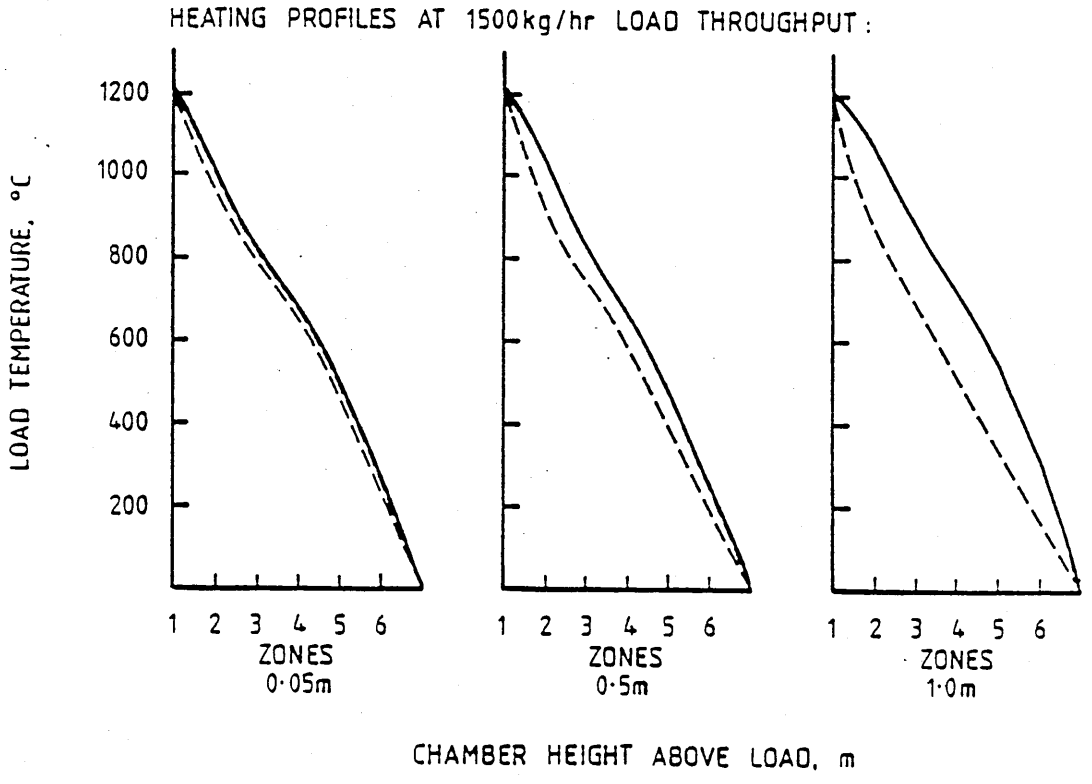

Figure 11.8 **A comparison of predicted steady-state heating profiles with and without interzone radiation included [39].** (Furnace width 1.0m, length 3.0m, load discharge temperature 1250°C, load width 1.0m)

CHAPTER 12

Model Validation Against a Continuous Furnace

12.1 Introduction

Thermal performance measurements were taken from a continuous reheating furnace in a steel rolling mill and on a batch heat treatment furnace in a forging plant. SSZONE and TRZONE were then applied to simulate these furnaces and the measured and predicted data were analysed and compared in order to validate the mathematical models and to verify their level of accuracy. This chapter describes the validation of SSZONE and TRZONE using the data from the continuous furnace. Chapter 13 describes the validation of TRZONE using the batch furnace data.

12.2 Description of the Furnace

Views of the furnace from the billet discharge end and from the loading end are shown in Figures 12.1-12.3. The main dimensions of the continuous furnace are shown in Figure 12.4. It comprises a refractory hearth and side walls cast from a 1600^{o}C grade dense castable refractory. The walls support a modular ceramic fibre roof of convoluted blanket construction. Billets or slabs of up to 2.3m length are pushed down the gently inclined hearth counterflow to the combustion products.

They drop out of the furnace through a discharge door beneath the burners and are then conveyed sideways to the first edging/de-scaling stand (see Figure 12.1). The furnace is fired by four Stordy NMG 240 burners, each nominally rated at about 1350 kW gross input of natural gas. These are mounted in line across the end wall. The combustion products are flued in a tall stack through openings in the side walls near to the billet loading position. A chain curtain is suspended across the loading end to reduce combustion product leakage and radiation transfer towards the pusher operator. The temperature of the furnace is monitored and controlled from a sheathed Platinum/Rhodium thermocouple with its junction close to the surface of the ceramic fibre roof at about 2.5m from the burners. The controller acts on a motorised valve in the main air supply line to the burner manifold and the air pressure at each burner is loaded against a governor on the gas supply line to that burner. The air-fuel ratio control however, suffers from a degree of manual intervention.

12.3 The Measurement Trial

The measurements were taken following a cold start-up on Monday 13th.February 1984 over one complete production shift.

The following data were measured and recorded:

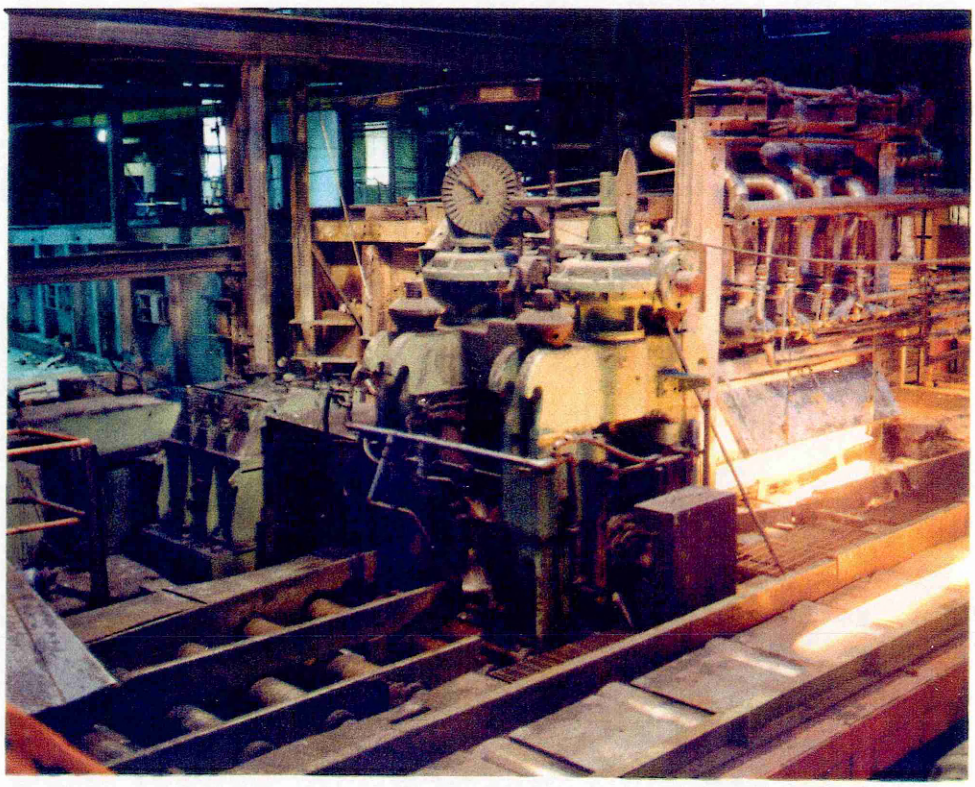

Figure 12.1 **A view of the continuous steel reheating furnace taken from the billet discharge end.** (The photograph shows the first edging and de-scaling stand in the foreground).

Figure 12.2 A view showing billets being pushed into the furnace.

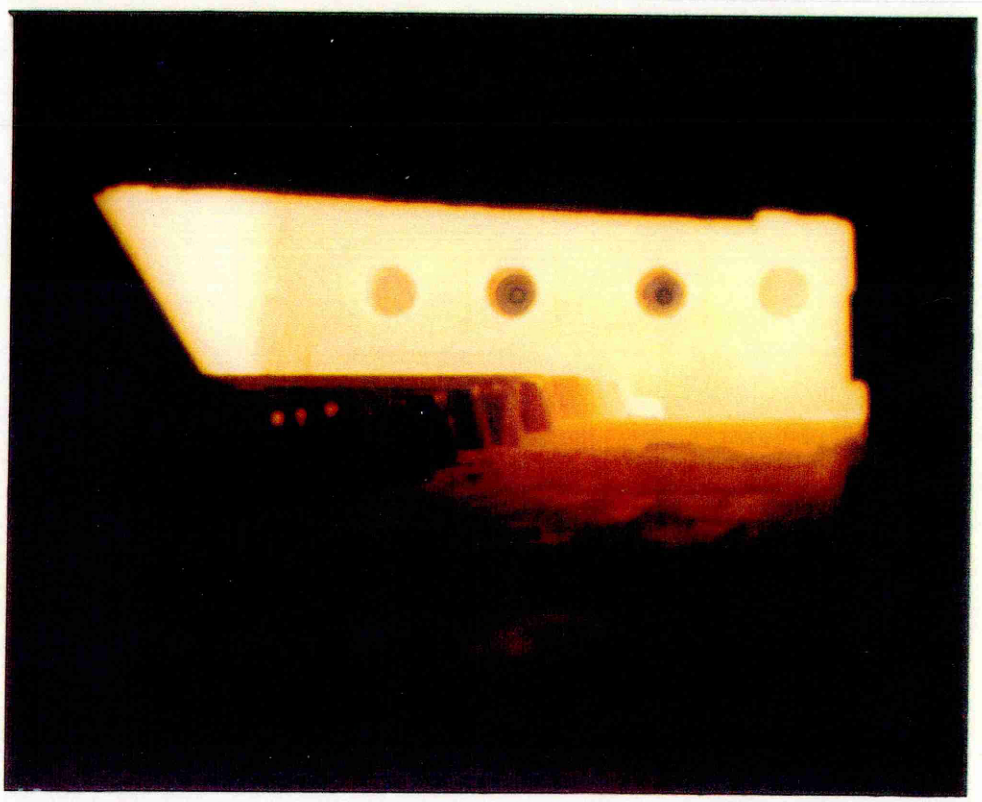

Figure 12.3 A view inside the furnace towards the four burners.

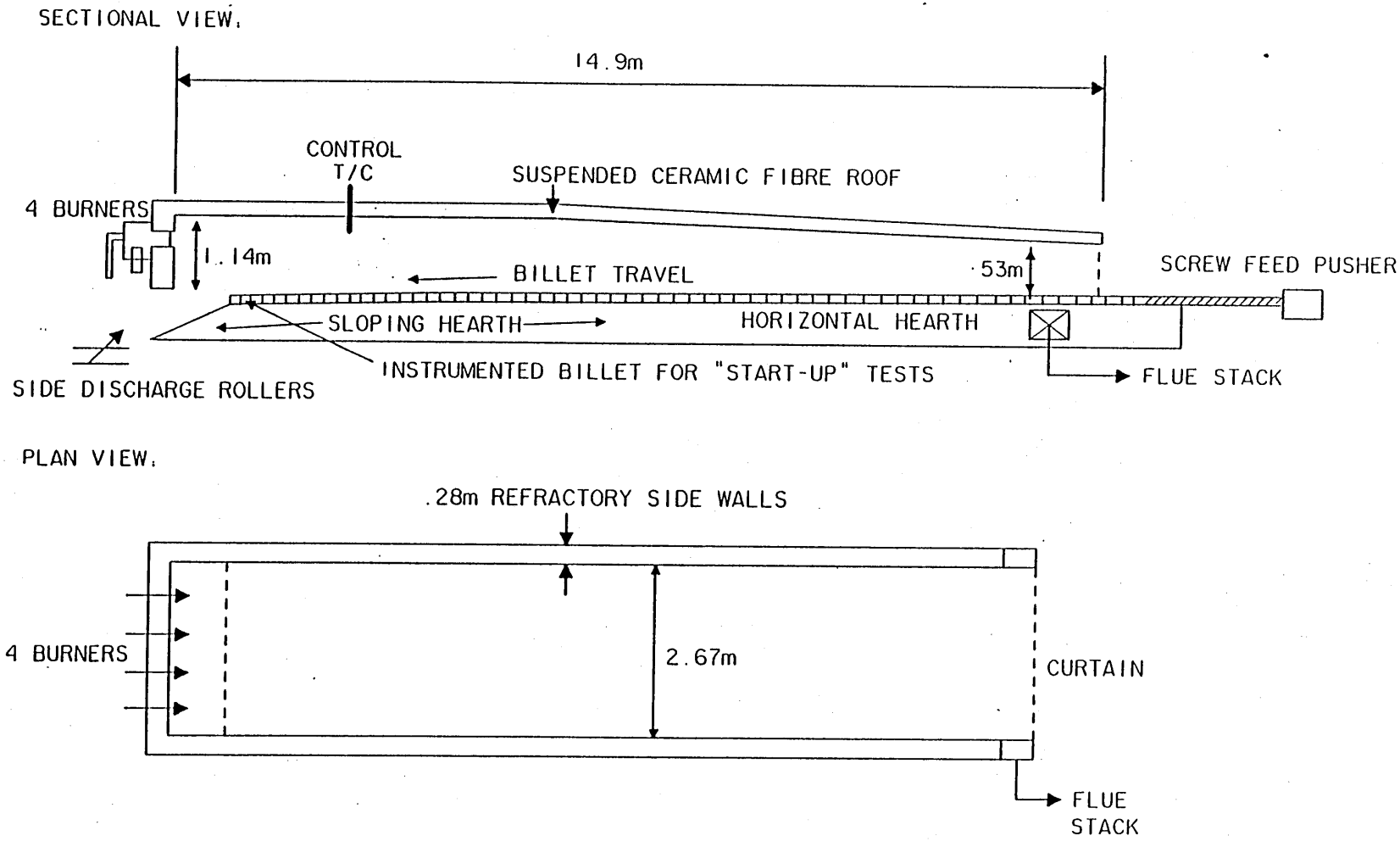

FIG. 12.4 THE GENERAL ARRANGEMENT OF THE FURNACE

i) The cumulative gas consumption from start-up.

ii) The billet discharges and temperature. The data acquisition system (DAS) detected when a billet was being pushed together with its temperature, which was measured using a tripod mounted Ircon optical pyrometer sighted on billets leaving the edging stand. The measurement is therefore made several seconds after the billet had left the furnace. At this position however, much of the scale had been removed and the measurement was not influenced by the chilled surface layer of scale, and thus the temperature measurement was considered more reliable. The billets normally took 1-2 seconds to pass the pyrometer enabling four measurements to be recorded and an average to be calculated by the DAS. The pyrometer was sighted on the side of the billet which is in contact with the hearth in the furnace and which would be expected to be colder than the hot face.

iii) The billet temperature history. Two billets were monitored each with three mineral fibre insulated type K thermocouples peened into holes in the surface of the metal. The first billet was positioned beneath the burners to record the temperature-time curve during the start-up period. The second thermocoupled billet was pushed through the furnace from the billet loading end (see Figure 12.2) during a period of steady uninterrupted production.

iv) The furnace chamber oxygen concentration.

v) The furnace control temperature and flue gas exit temperature. These were recorded manually.

12.4 Measured Results

The following operating and performance data were recorded during the trial:

i). The overall operating schedule for the furnace was as follows:

5.20 a.m.	Furnace light-up.
7.00 a.m.	1st billet discharged.
10.30 - 11.00 a.m.	Scheduled production delay. for breakfast.
14.00 p.m.	End of measurement trial.

Other unscheduled delays of shorter duration were noted during the trial.

ii). The furnace controller set point was maintained constant at $1380^{o}C$.

iii). A chamber oxygen concentration of 0.5% indicated an excess air level of about 2.5% .

iv). Steel throughput, billet sizes, gas consumption and calculated efficiencies are given in Table 12.1 grouped according to the scheduled stock sizes discharged from the furnace. Billet temperatures recorded ranged from less than 1100^{o}C to 1216^{o}C. The efficiency data in Table 12.1 however assumes a mean billet temperature of 1150^{o}C (equivalent to 760 MJ/Te). Overall efficiency equals the ratio of heat output in the hot steel to the gross energy input in the fuel since light-up. The running efficiency equals the ratio of output to input over the duration of each group of billets. The high running efficiency after start of production and after the delay periods, arises because the average firing rate during these periods is lower since the billets contain considerable stored energy from the preceding periods when the load is stationary.

12.5 Furnace Representation by Model

The representation of the furnace by TRZONE and SSZONE is illustrated in Figure 12.5 showing its subdivision into 10 zones of equal length with separate roof, wall and load (billet) surfaces in each zone (ie.NWALL = 3). One simulation using TRZONE employing a 20 zone representation was also carried out to test the sensitivity of the predictions to the number and size of zones. In order to improve the representation of the furnace, the following features were incorporated in both models.

Table 12.1 Recorded output and efficiency data.

ELAPSED TIME (mins)	GAS USED (GJ,gross)	BILLETS DISCHARGED (No)	(Te)	OVERALL EFFICIENCY (% gross)	BILLET SIZES (mm) LGTH x WDTH x TH.	THR.PUT (Te/hr)	RUNNING EFFICIENCY (% gross)
Start of Trial @ 5.20 a.m.							
107	31.8	Start of Production					
167	51.4	74	15.7	23.2	} 2080 x 216 x 60	15.7	60.9
179	56.3	74	15.7	21.2	} 13 min delay	-	-
188	59.7	85	18.0	22.9	} 2080 x 216 x 60	15.3	51.4
212	68.8	110	23.7	26.2	} 2360 x 216 x 57	14.1	47.8
244	81.2	138	29.7	27.8	} 2210 x 210 x 60	11.4	37.2
275	92.8	168	34.7	28.4	} 1850 x 190 x 60	9.7	32.2
287	97.7	168	34.7	27.0	} 13 min delay	-	-
309	105.1	184	39.7	28.7	} 2460 x 216 x 76	13.6	51.4
339	112.7	184	39.7	26.8	} Breakfast delay (30 mins)		-
366	121.0	208	44.8	28.1	} 1650 x 216 x 76	11.0	46.6
519	173.1	334	71.3	31.3	} 1650 x 216 x 76	10.5	38.7

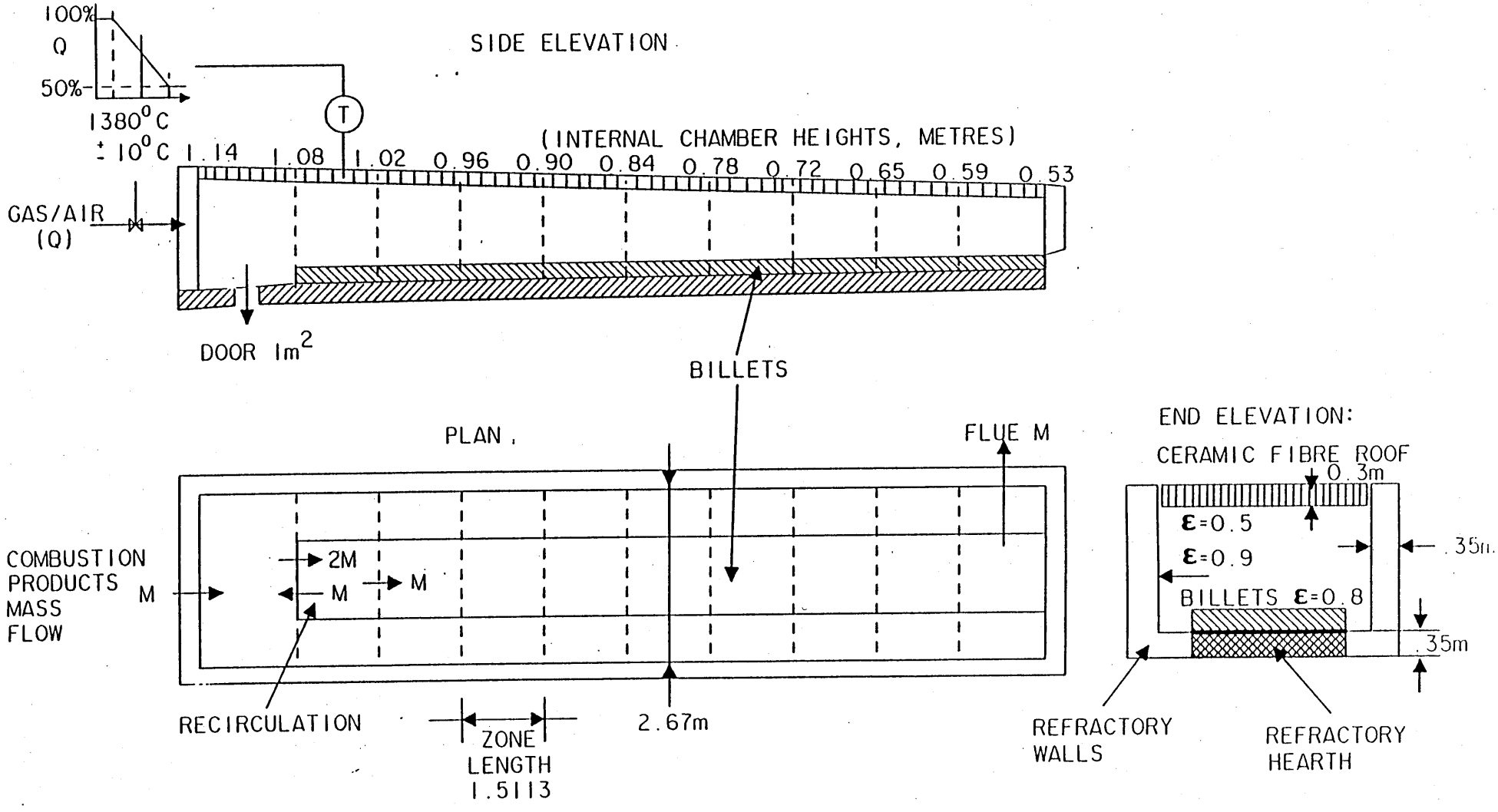

FIG. 12.5 A 10 ZONE LONG FURNACE MODEL REPRESENTATION OF THE FURNACE

i) A region of exposed hearth was assumed to exist in front of the burners. In the 10 zone model, the first zone was assumed to be empty. With 20 zones, the first two zones were empty. Billets were assumed to be discharged from zones 2 and 3 in the respective models.

ii) Because of the presence of a permanently open discharge door beneath the burners, an opening of variable area for radiation loss from the floor of zone 1 to the ambient environment was incorporated in the models.

iii) Since the billets are resting directly on the hearth, the area for contact conductance is considered high and so conduction as well as radiation were included for the billet-hearth heat transfer calculation. Assuming unit emissivity for the two surfaces, the heat flux ($\dot{q}_h$) into the hearth is calculated by:

$$\dot{q}_h = \sigma(T_b^4 - T_h^4) + C_c(T_b - T_h) \qquad 12.1)$$

where T_b and T_h are the adjacent cold face billet and hearth surfaces.

Values for the contact conductance C_c between a metal and a refractory are not available. Data have been published however for the contact conductance between billets and

water-cooled skid rails [40]. These are reproduced in Figure 12.6 as a function of the average temperature $T = (T_b+T_h)/2$. The following approximation to this has been applied to both models to test the sensitivity of the predictions to the inclusion of contact conductance.

$$T < 350^{o}C \; ; \; C_c = 5000 \; W/m^2K \qquad 12.2)$$

$$T > 350^{o}C \; ; \; C_c = 500 \; W/m^2K \qquad 12.3)$$

iv) Some recirculation of combustion products immediately downstream of the burners was assumed. This was derived by application of the Craya-Curtet formula for confined jet flow [41] as follows:

The maximum combustion products recirculation (ϕ) downstream of a confined burner jet is given by the Craya-Curtet parameter (η) :

$$\phi = \frac{\dot{m}_{r,max}}{\dot{m}_g + \dot{m}_a} = .430(\eta^{0.5} - 1.65) \qquad 12.4)$$

where,

$$\eta = \frac{\dot{G}_g}{\dot{G}_\infty} + \frac{\dot{G}_a}{2\dot{G}_\infty} - 0.5$$

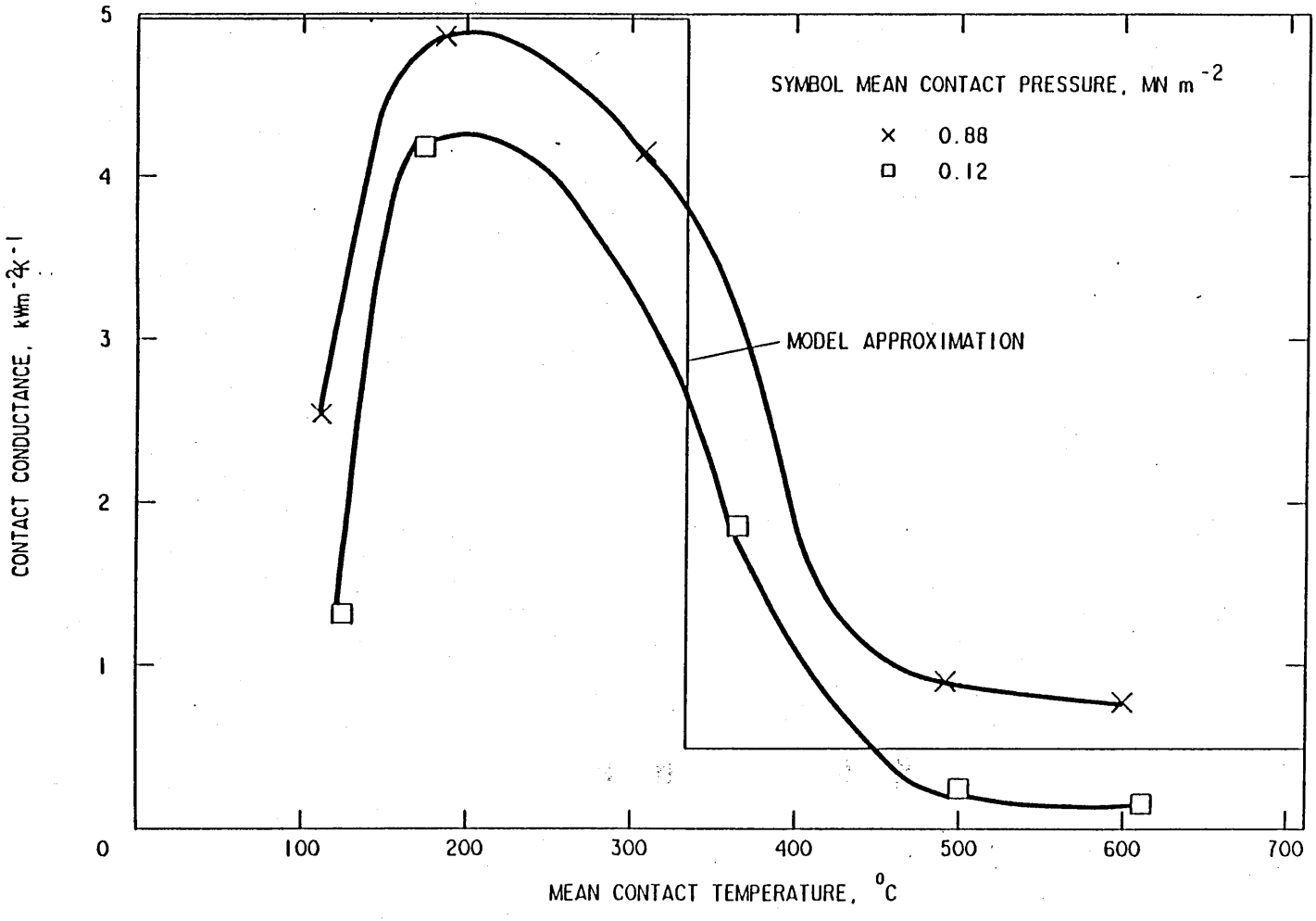

FIG. 12.6 THE CONTACT CONDUCTANCE BETWEEN HOT BILLETS AND WATER COOLED SKID RAILS [40]

$\dot{G}_g$, $\dot{G}_a$ and $\dot{G}_\infty$ are the momentum fluxes of the primary jet (the burner tunnel exit), a secondary air stream (nonexistent in this case) and the fully expanded jet, and $\dot{m}_g$ and $\dot{m}_a$ are the mass flow rates of the jet and secondary stream, and $\dot{m}_{r,max}$ is the maximum mass flow rate of recirculating combustion products.

Calculation of $\dot{G}_g$ and $\dot{G}_\infty$ now follows:

The natural gas supply rate to one burner is .0375 $m^3(s)/s$ and the tunnel exit diameter is .241m. Assuming an exit temperature of 2000 K and an excess air level of 2.5%, the mass flow rate of the jet ($\dot{m}_g$) is .486 kg/s and its exit velocity is 62.8 m/s.

Therefore, $\dot{G}_g = \dot{m}_g u = .486 \times 62.8 = 30.5$ N

Assuming a cross sectional area of 2.88 m^2 and a temperature of 1800K, the mean velocity of the combustion products in the near downstream region of the burners is 3.58 m/s.

Hence, $\dot{G}_\infty = .486 \times 3.58 = 1.74$ N

Thus, $\eta = 30.5/1.74 - 0.5 = 17$

giving, $\phi = 1.06$

Thus, the recirculation of combustion products equals approximately that of the input mass flow rate of fuel and air to the furnace. With 10 zones, recirculation between zones 1 and 2 was specified (see Figure 12.5). With 20 zones, this was extended to include recirculation between zones 2 and 3.

TRZONE was initially applied to simulate the start-up period from cold, up to the commencement of pushing (Runs 1 & 2). In this simulation, the gas consumption pattern was force fitted to the measured pattern by an appropriate polynomial expression relating total gas consumed with time. The same model was then used (Run 3) to simulate start-up and production up to and including the 30 mins delay for breakfast (i.e. the first 39.7 Te of production), and including the two shorter delays preceding this (see Table 12.1). In this case, the gas input rate was varied with time during the simulation to control the internal roof surface above the discharge zone at the observed set point temperature of 1380^{o}C, thereby simulating the temperature control of the furnace. A high fire-rate of 5.8 MW gross of natural gas was assumed with a turn down range of 50% over a proportional band of 10^{o}C. The high fire rate was chosen to equal the observed maximum firing rate during start-up before the controller was responding. The discharge rate of billets from the furnace was also varied during the simulation in accordance with the observations. The assumed operating schedule in the model for this period is shown schematically in Figure 12.7 with a

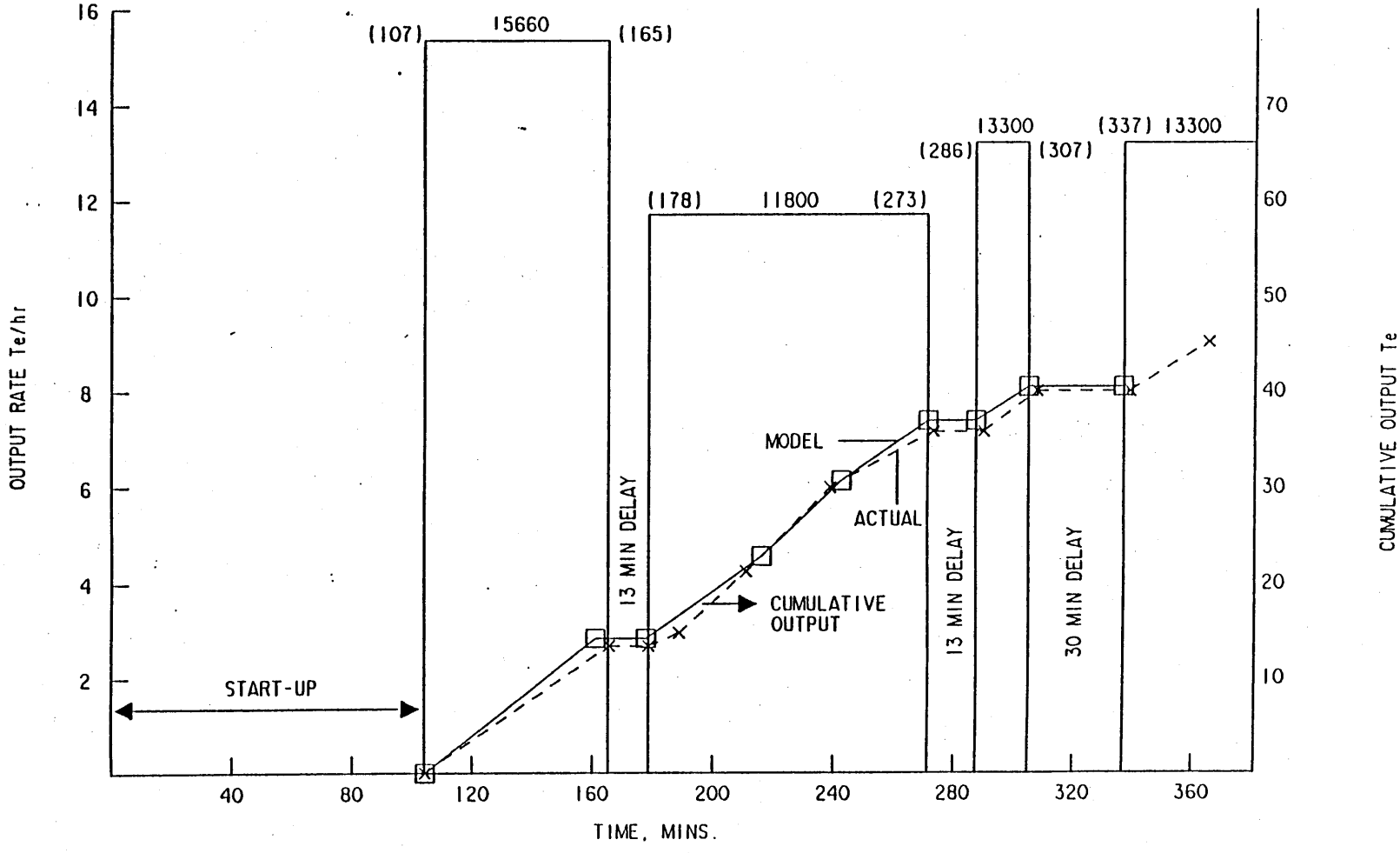

FIG. 12.7 FURNACE OUTPUT DURING THE EXPERIMENTAL TRIAL

comparison of the simulated and actual output pattern.

After the breakfast delay, the length of the billets pushed through the furnace were significantly shorter (see Table 12.1). TRZONE cannot easily represent a change in billet size during production since the total exchange areas are calculated once for a specified furnace geometry and load size and these are specified as input to the model. It would be possible to re-calculate and input new total exchange areas as the shorter billets replace the longer billets at each push, although this would impose a heavy computational burden on the model. Since the billet size and throughput remained approximately constant for nearly 3 hours during this period, it was assumed that approximately steady-state thermal performance was being achieved. The 10 zone model was therefore run for an extended period simulating 8.65 hrs of production (Run 4), in order to predict the quasi-steady-state performance on the shorter billets. SSZONE using a 10 zone representation was also run for these same conditions.

The input data for TRZONE relating to the pre-breakfast and post-breakfast simulations are shown in Table 12.2.

Table 12.2a)

Input Data For Reheating Furnace Simulation

	Start-up plus first 39.7 Te production		Final 3hrs. of production
RUN No.	1,2,3	5	4
No. of zones	10	20	10
Zone length (m)	1.5113	.7556	1.5113
Furnace width (m)	2.667	2.667	2.667
Load width (m)	2.0883	2.0883	1.651
Steel throughput (Te/hr)	(variable with time - see Figure 12.4)		10.5
Excess Air (%)	2.5	2.5	2.5
High fire rate (MW gross)	5.8(a)	5.8	5.8
Set Point Temp (^{O}C)	1380(a)	1380	1380
Proportional Band (^{O}C)	$\pm$10(a)	$\pm$10	$\pm$10
Turn Down	1/2(a)	1/2	1/2
Calculation time step (secs)	5	5	5

Note (a) : Run 3 only ; see text.

Table 12.2b)

Details of Wall, Roof, Steel and Hearth Representation

		Load	Roof	Walls	Hearth
Material (See Appendix B)		Steel	Ceramic Fibre	Wilkinson Brick	Stein Brick
Density (kg/m^3)		7800	128	2060	2600
Thickness (mm)	60.3	(76.2[a])	300	350	350
Finite Difference Spacing (mm)	6.03	(7.62[a])	60	70	70
Hot Face Emissivity		0.8	0.5	0.9	-

Note [a]: Run 4 only.

12.6 Results

12.6.1 Start-up Simulation

From the start-up simulations using TRZONE, it was evident that the door area selected in the model had the most marked effect on predicted final billet temperature. The door area for radiation loss is not easy to define precisely from the furnace geometry. An area of $1m^2$ however gave a sensible prediction of the final surface temperature of the billet in the discharge zone although this was higher than indicated by the thermocoupled billet (see Figure 12.8). The measurements are somewhat suspect however, due to the high values at the start of monitoring and the fluctuating values towards the end of the start-up period. This may be caused by preheating of the thermocouple leads by the hot combustion products beneath the burners.

12.6.2 Production Simulations

Assuming therefore a door area of $1m^2$, and (in TRZONE) allowing the gas input rate to modulate from start-up to control furnace set point temperature at $1380^{o}C$, the following simulations were performed :

i) A simulation of the period up to and including the breakfast delay using TRZONE with 10 zones (Run 3).

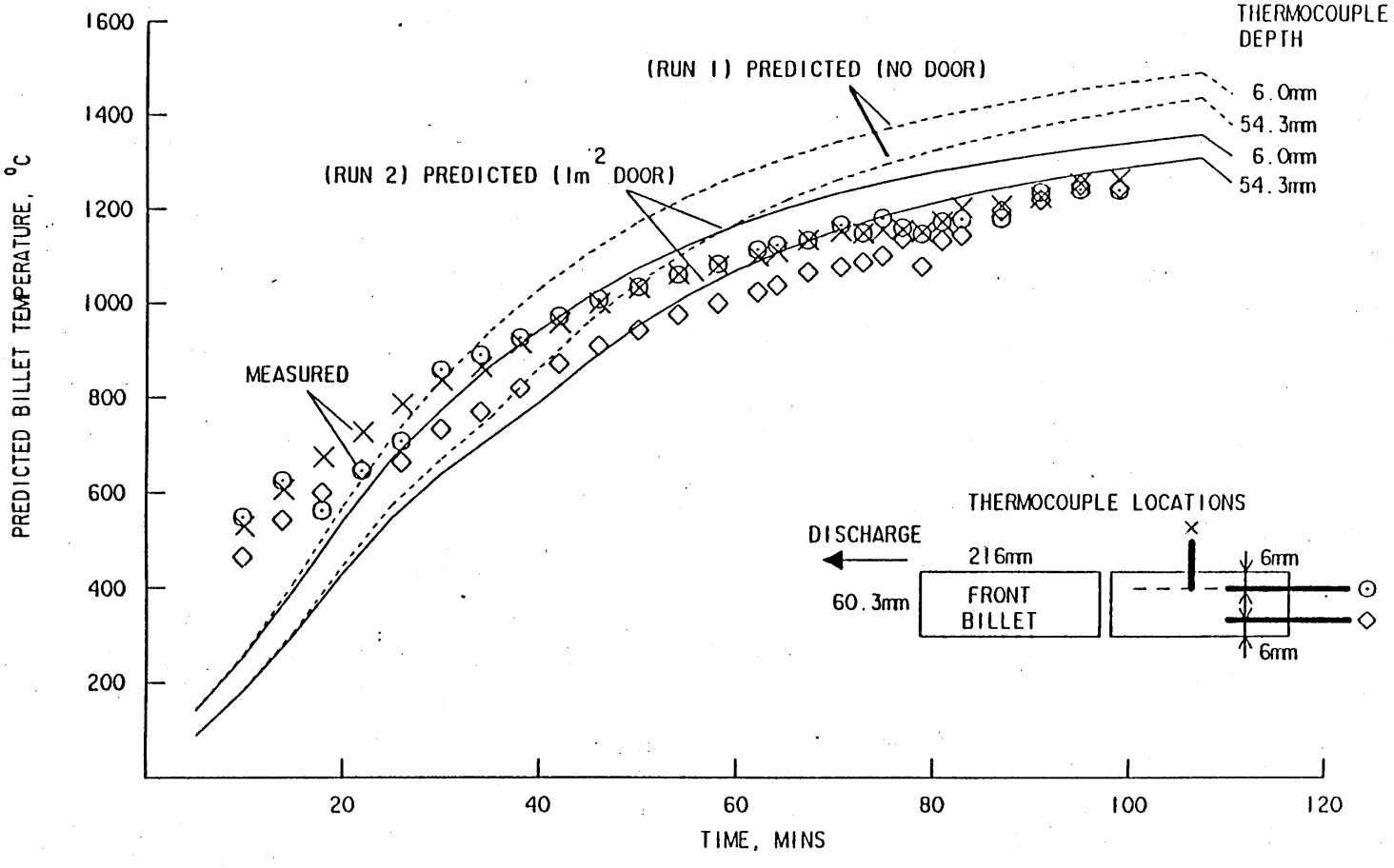

MODEL INPUT PARAMETERS - NO. ZONES = 10 BILLET LENGTH = 2.083m
GAS CONSUMPTION FORCE FITTED TO MEASURED RATE
EXCESS AIR = 2.5%

FIG. 12.8 PREDICTION AND MEASUREMENT OF BILLET TEMPERATURE DURING START-UP

Acceptable agreement with the measured gas consumption output pattern is obtained (Figure 12.9) with the measured consumption during start-up and the production delays accurately simulated. A plot of the predicted energy balance over this period is shown in Figure 12.10. The heat transfer to the load includes the energy stored in the load residing in the furnace, as well as the energy output in discharged billets. These predictions indicate the significance of the wall and hearth losses during the early part of the trial period. From the shape of the curves, it also appears that by the end of the simulation period, a state of thermal equilibrium has been closely approached.

Predicted hot face and cold face billet temperatures at discharge are plotted in Figure 12.11. It is seen that temperatures vary from a maximum hot face value of 1360^{o}C to a minimum of 1180^{o}C with corresponding cold face temperatures of 1320 and 1030^{o}C respectively. The range of observed cold face billet temperatures (measured after the first edging stand) is indicated for comparison. Excepting the high temperature over-prediction at start-up and immediately after the breakfast delay, agreement is otherwise acceptable. The predictions show a sharp increase in temperatures after the 3 simulated delays. This is not unexpected and was certainly observed in practice.

ii) A repeat of Run 3 using TRZONE with 20 zones (Run 5).

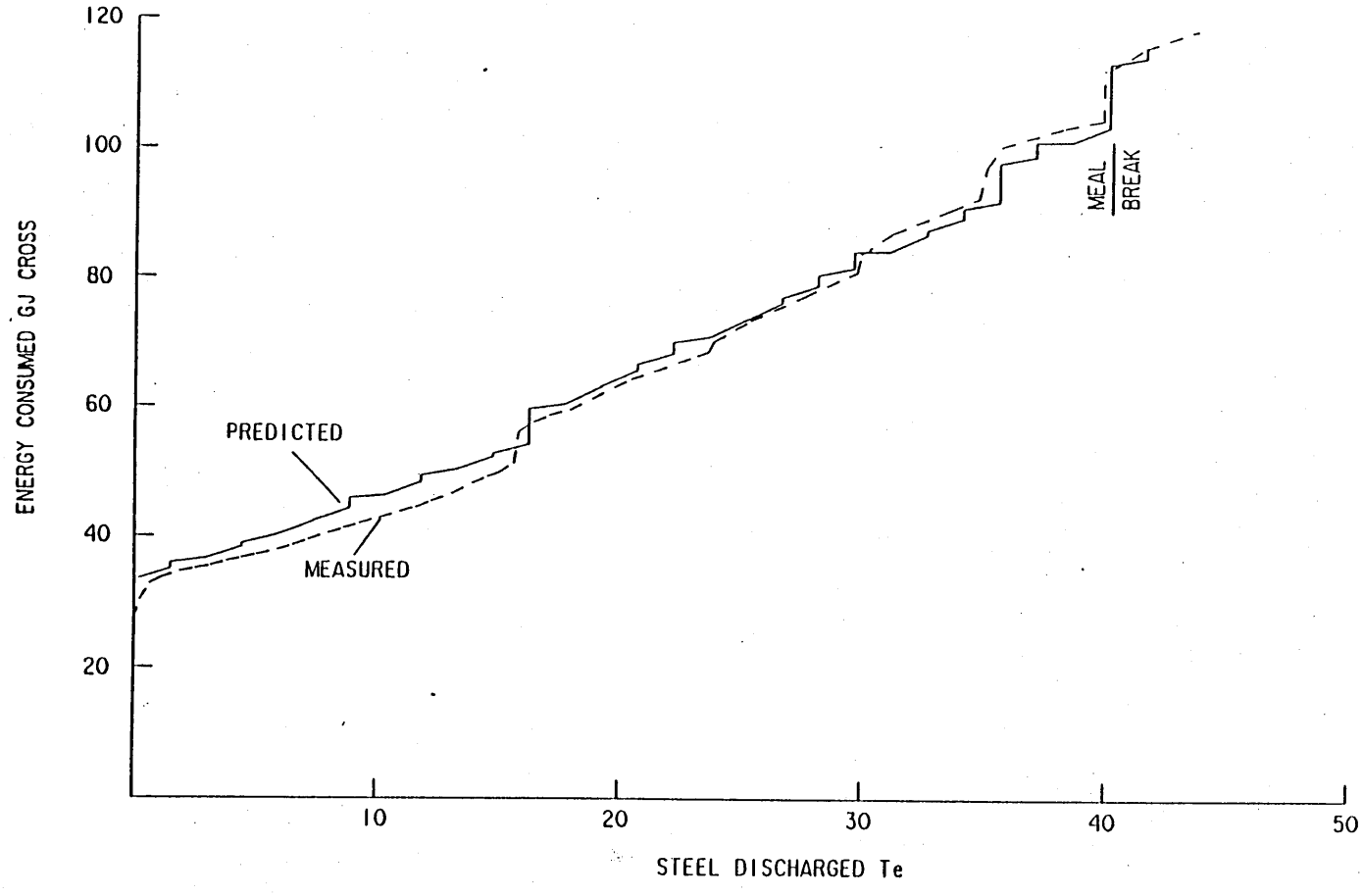

MODEL INPUT PARAMETERS - NO. ZONES = 10 BILLET LENGTH = 2.083m
HIGH FIRE RATE = 5.8 MW GROSS
EXCESS AIR = 2.5% SET POINT TEMPERATURE = 1380 ^{0}C

FIG. 12.9 PREDICTED AND MEASURED ENERGY CONSUMPTION (RUN 3)

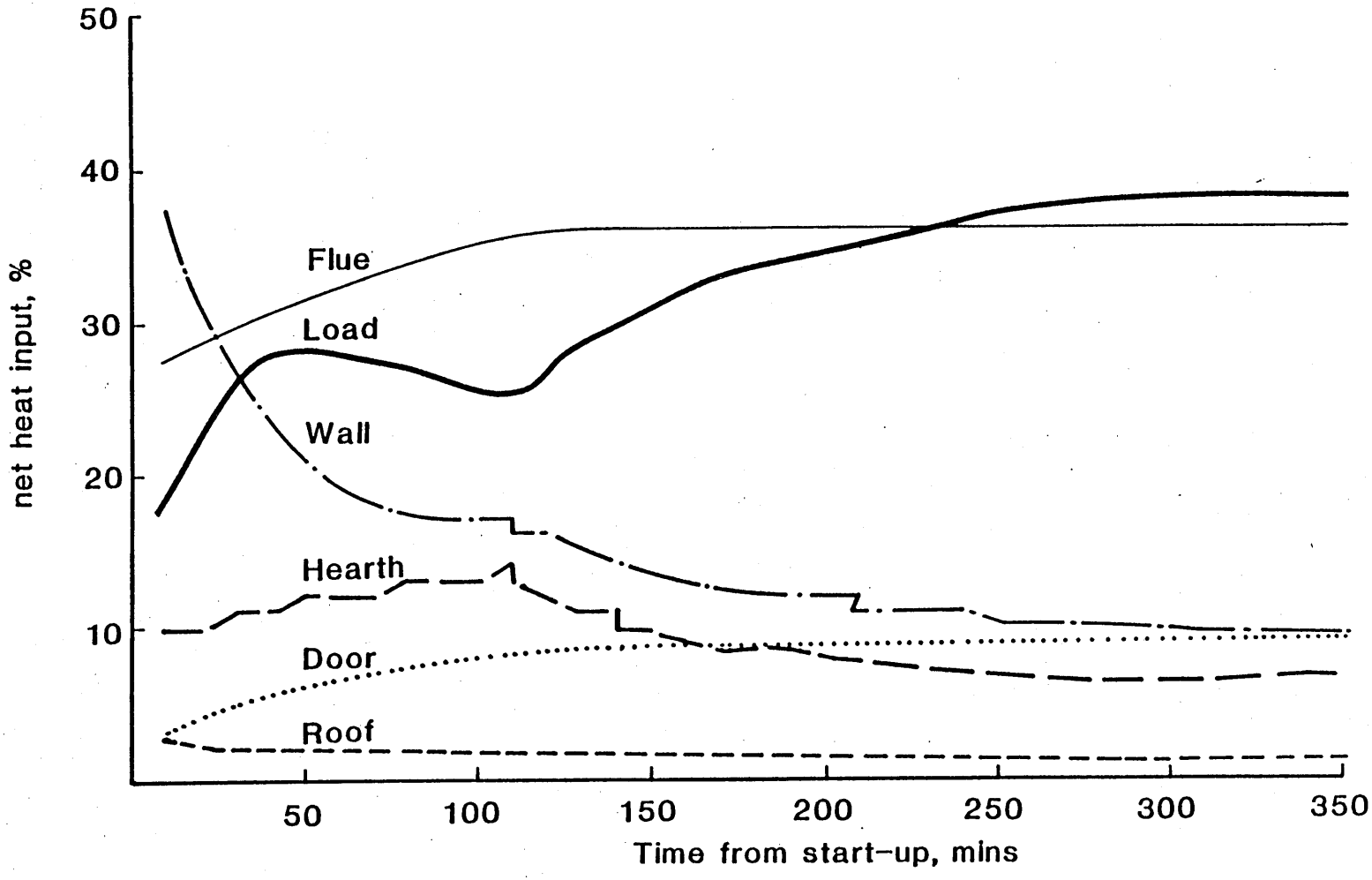

Figure 12.10 The predicted energy balance for trial period

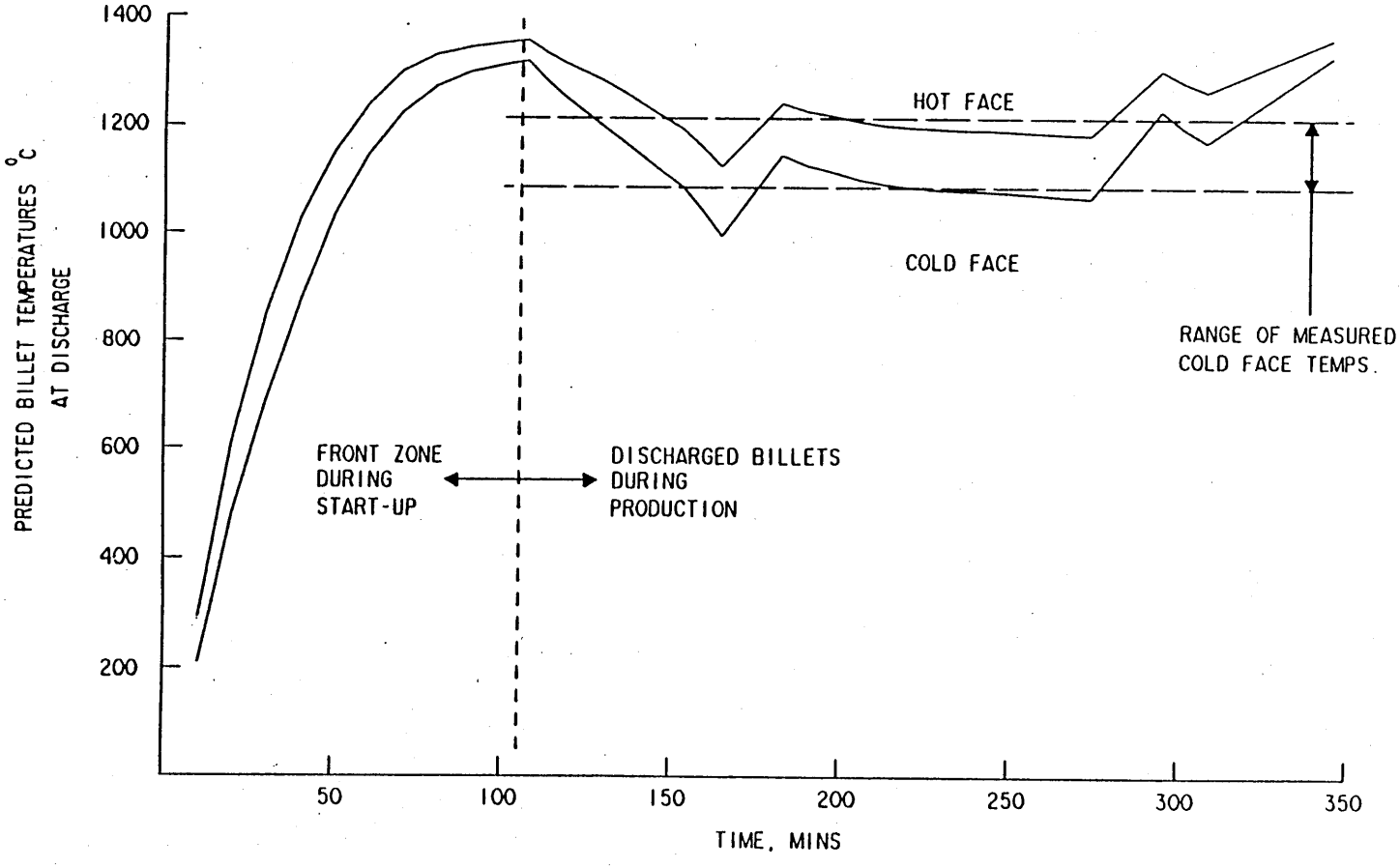

MODEL INPUT PARAMETERS - NO. ZONES = 10 BILLET LENGTH = 2.083m
HIGH FIRE RATE = 5.8 MW GROSS
EXCESS AIR = 2.5% SET POINT TEMPERATURE = 1380 °C

FIG. 12.11 PREDICTED AND MEASURED BILLET TEMPERATURES

Comparison with Run 3 (Figure 12.12) shows a slightly lower predicted gas-consumption at any given output. Billet temperatures at discharge closely agree with those predicted using the 10 zone model. The 20 zone model took 205 CPU minutes on a Vax 11/780 compared to the 10 zone model which took 51 CPU minutes. Thus, computing time is proportional to the square of the number of zones. For economy of computing, the 10 zone model is obviously preferred and appears to give acceptable accuracy.

iii) A transient simulation of the total trial with shorter billets corresponding to the latter half of the trial (Run 4).

It was only valid to compare results from after the breakfast delay in this case. For this reason the predictions after the delay are presented in Figure 12.13 and Figure 12.14 as a continuation of the data from Run 3. Acceptable agreement in the consumption output pattern is again obtained (Figure 12.13) and predicted billet temperatures at discharge are comparable to the range of observed values (Figure 12.14).

iv) A simulation using SSZONE. Assuming a discharge billet temperature of 1200^{o}C corresponding to the hot face values predicted by the transient model, a simulation using SSZONE of the later half of the trial predicted a specific fuel consumption of 1.892 GJ/Te (17.93 therms/Te) which is comparable to a measured value during the period of 1.930

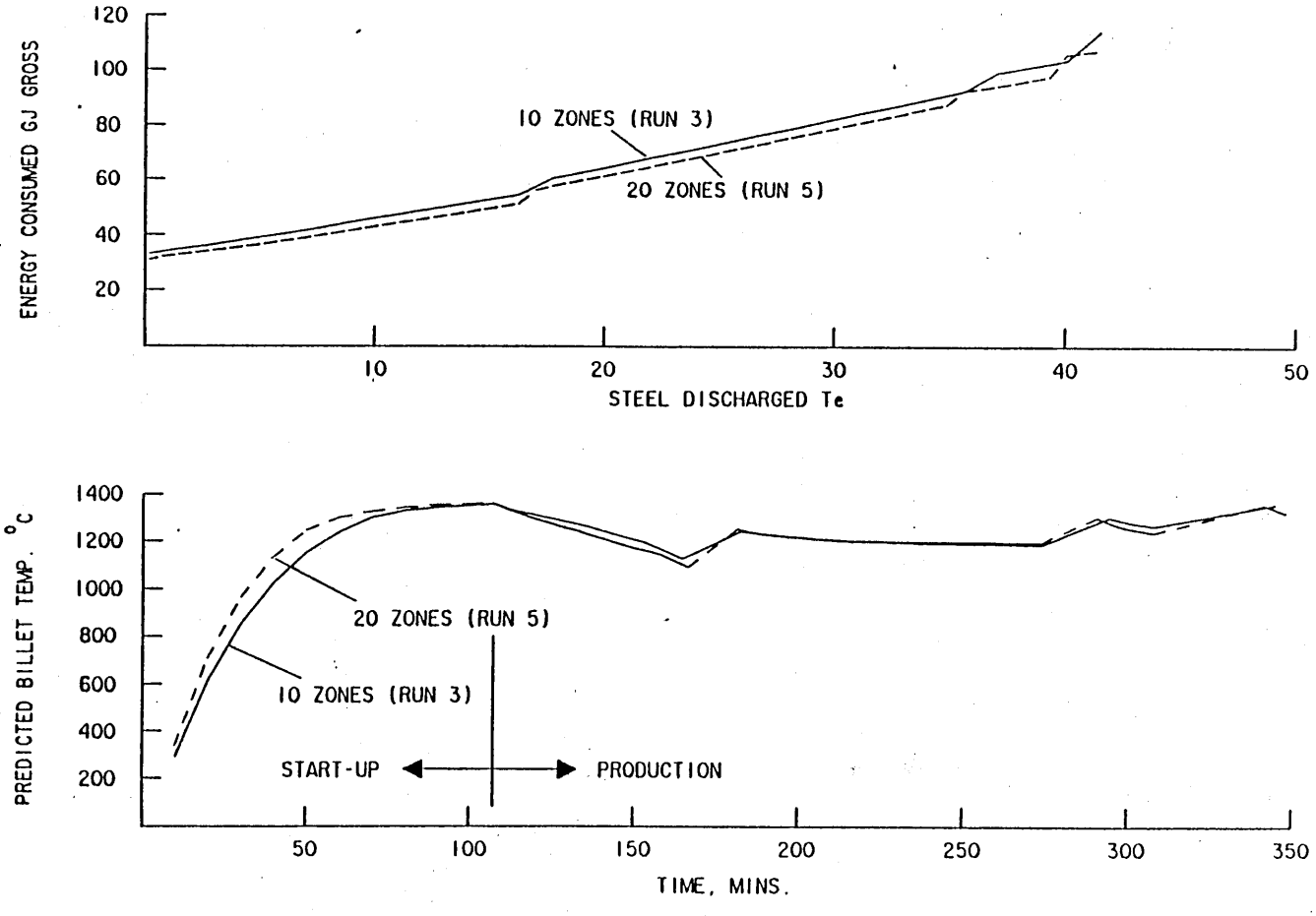

MODEL INPUT PARAMETERS - BILLET LENGTH = 2.083m
HIGH FIRE RATE = 5.8 MW GROSS
EXCESS AIR = 2.5% SET POINT TEMPERATURE = 1380 °C

FIG. 12.12 THE EFFECT OF THE NUMBER OF ZONES

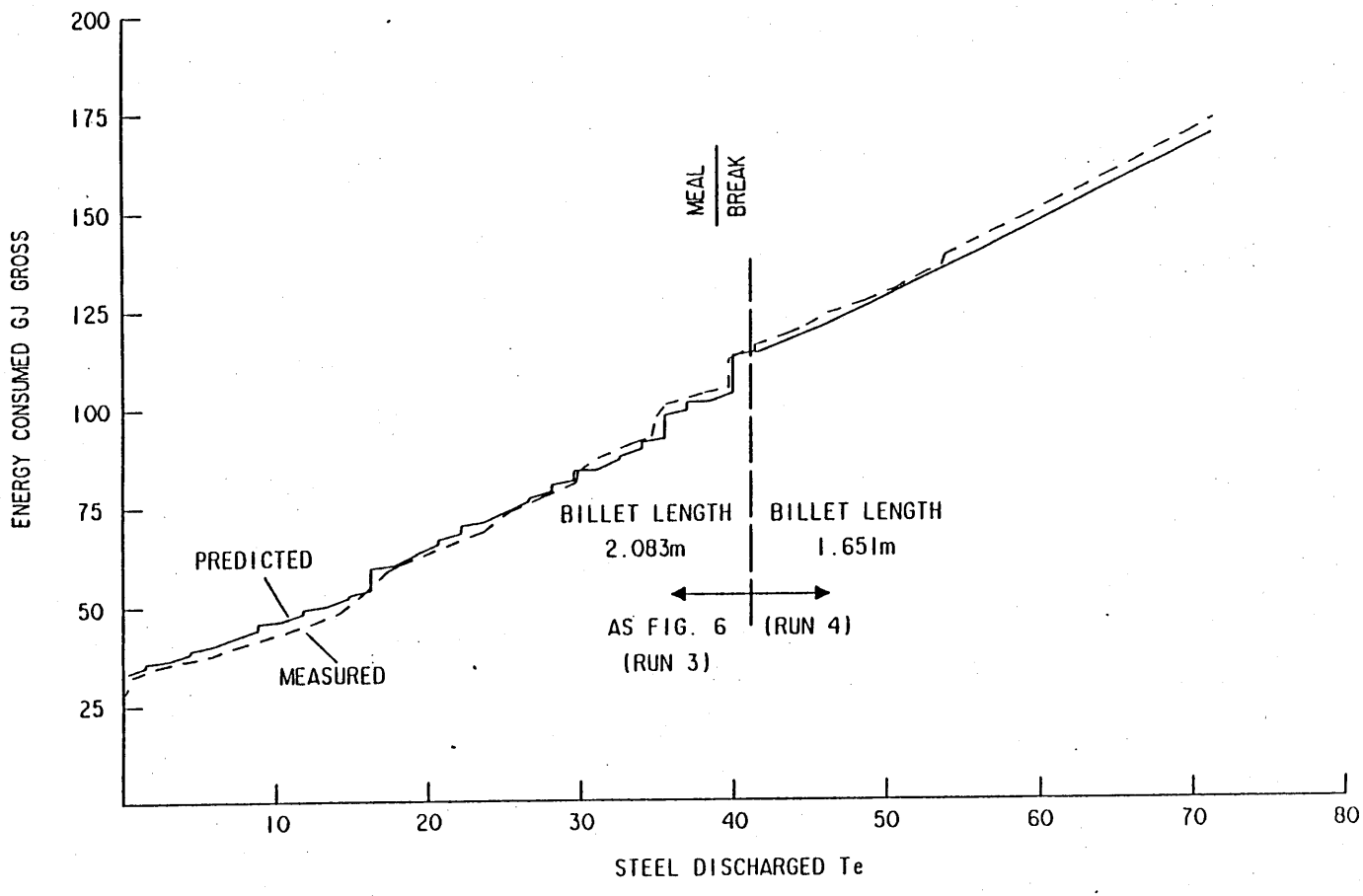

MODEL INPUT PARAMETERS - NO. ZONES = 10
HIGH FIRE RATE = 5.8 MW GROSS
EXCESS AIR = 2.5% SET POINT TEMPERATURE = 1380 °C

FIG. 12.13 PREDICTED AND MEASURED GAS CONSUMPTION FOR TOTAL TRIAL PERIOD

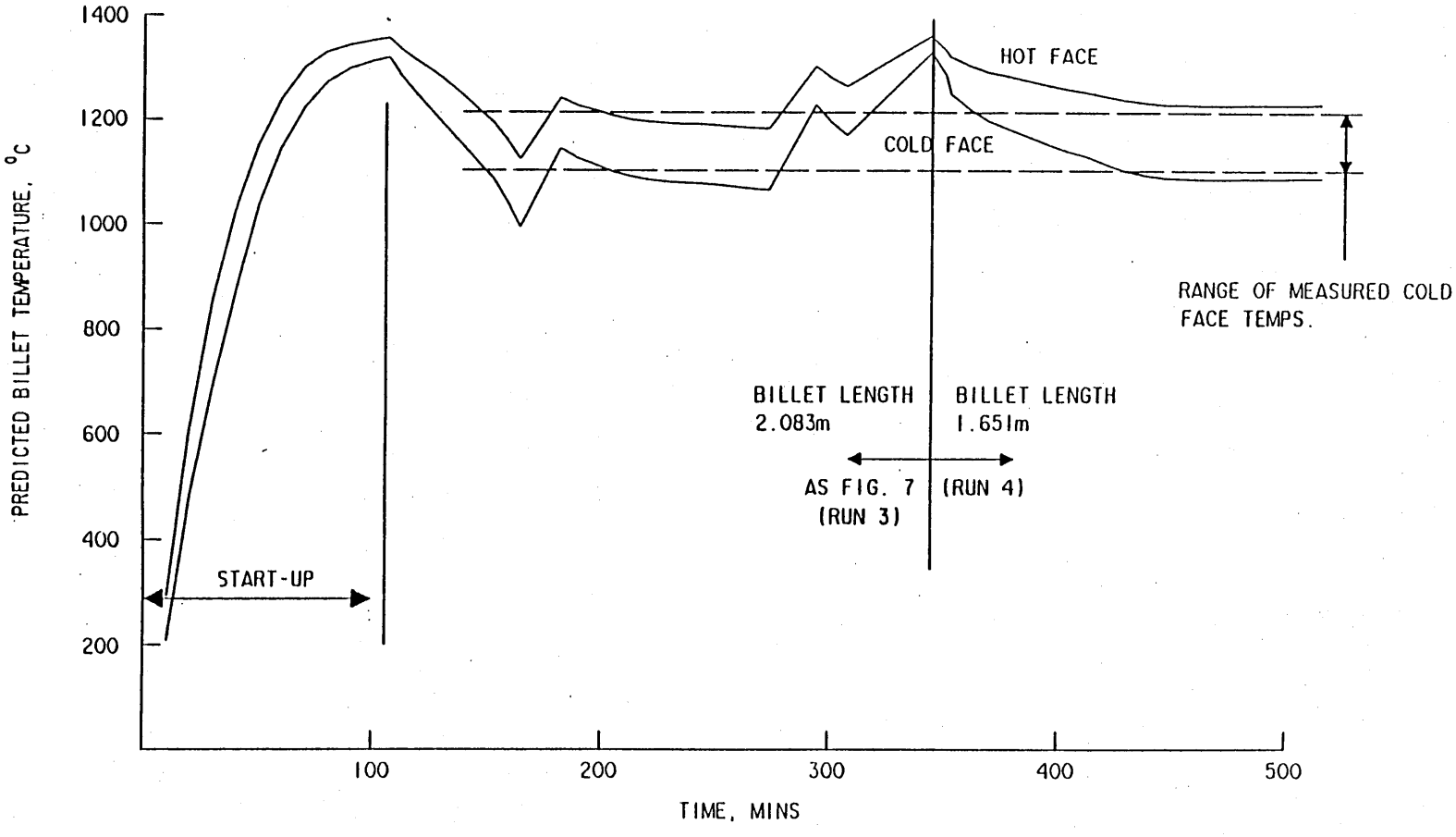

MODEL INPUT PARAMETERS - NO. ZONES = 10
HIGH FIRE RATE = 5.8 MW GROSS
EXCESS AIR = 2.5% SET POINT TEMPERATURE = 1380 °C

FIG. 12.14 PREDICTED AND MEASURED BILLET TEMPERATURES FOR TOTAL TRIAL PERIOD

GJ/Te (18.3 therms/tonne). A $\pm 50^{o}C$ variation in discharge temperature produced a variation in specific fuel consumption of +7% and -6% respectively. A summary of the predicted and measured specific fuel consumption during this period is given in Table 12.3.

12.6.3 Billet Temperature Profile Through the Furnace

The second thermocoupled billet was pushed through the furnace after the breakfast delay period when the furnace was discharging billets of 1.651m length. The recorded surface temperatures are compared in Figure 12.15 to the SSZONE predictions of billet temperature in each zone and the TRZONE predictions (Run 4) for the corresponding period of furnace operation. Unfortunately, the thermocouples failed at about $800^{o}C$ when the billet was 75% through the furnace. The measurements up to this point, agree closely with the steady-state temperature profile which assumes infinite conductivity in the steel and therefore zero differential between the top and bottom surfaces of the billet. If the measurements are regarded as a true representation of the hot face of the billet, TRZONE is seen to overpredict temperatures along the furnace. In general however, agreement would be considered acceptable for practical furnace design.

Table 12.3

The predicted and measured performance during the latter half of the trial

	Specific fuel consumption GJ/Te		
Period	Observed	Predicted	
		TRZONE	SSZONE
Breakfast - End of Trial([a])	1.931	1.920	
422 mins - End of Trial([a])	1.973	1.952	1.892
466 mins - End of Trial([a])	2.036	1.952	

([a]) = 519 mins.

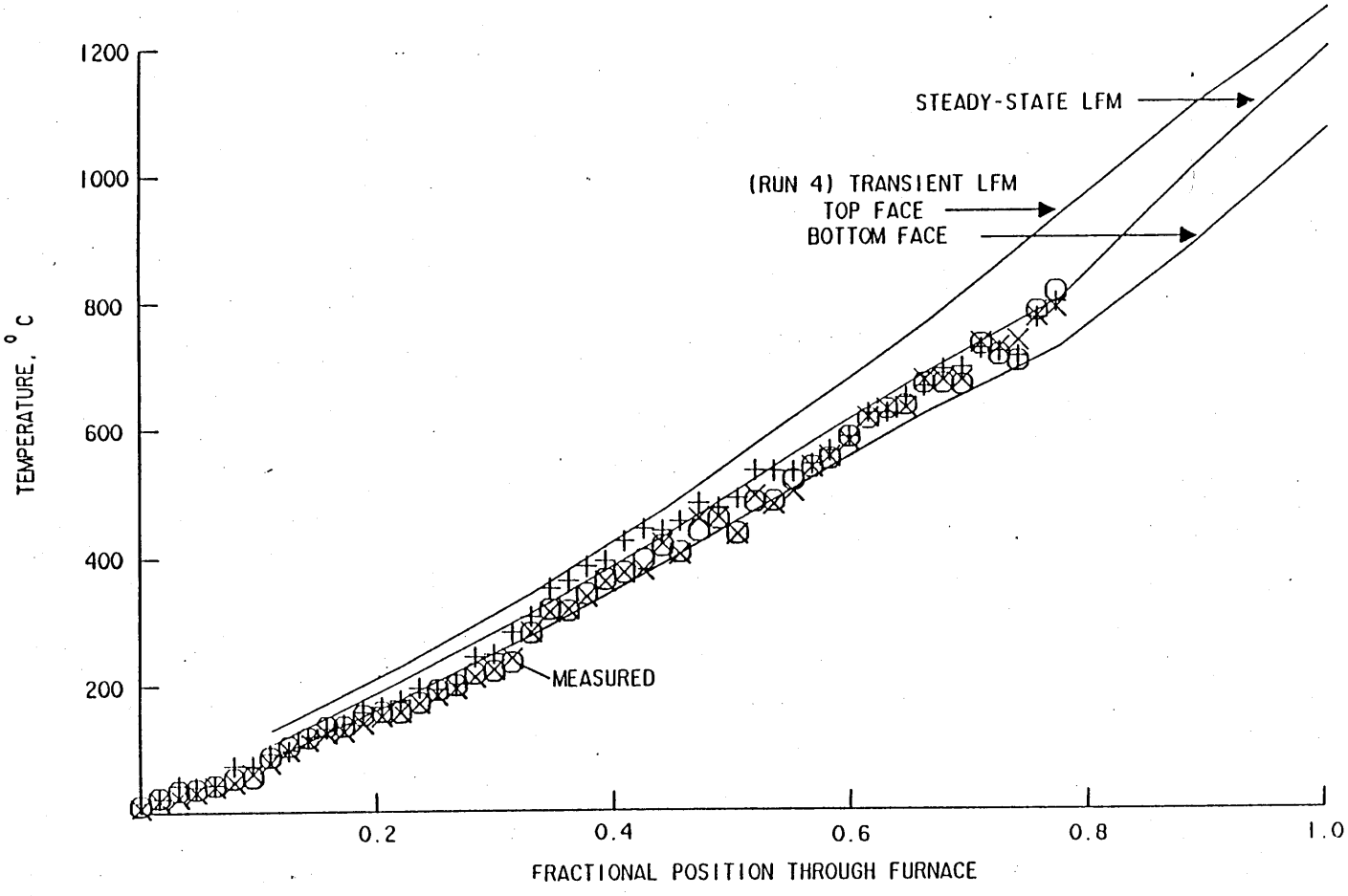

FIG. 12.15 PREDICTED AND MEASURED BILLET TEMPERATURE PROFILES THROUGH THE FURNACE

12.7 Application of the Model and Sensitivity Analysis

Taking Run 3 as a reference case, the models were applied to study the influence of the following factors on the overall thermal performance:

1. Furnace Control on Billet Temperature (Run 6).

In this run, the simulated gas input rate is controlled on the hot face billet temperature in zone 2 (the discharge zone). A set point of 1200^{o}C was selected with delay on discharge if the billet in zone 2 is below set point. Consequently some unscheduled delays were simulated and the overall throughput up to the start of the breakfast delay was 34.1 Te compared to 40 Te in Run 3. A reduction in the start-up energy consumption of 7.24 GJ (20%) is predicted (Figure 12.16) which decreases to a 4.6 GJ reduction at the end of the simulation period. This is due to the lower average rate of energy consumption during production in Run 3 which is in part a consequence of the significant overheating of billets during start-up.

2. Production at constant rate (Run 7).

This is a repeat of Run 6 with control on billet temperature, but with all scheduled delays removed and a constant push rate of 10.26 Te/hr simulated. Comparison between Runs 6 and 7 show

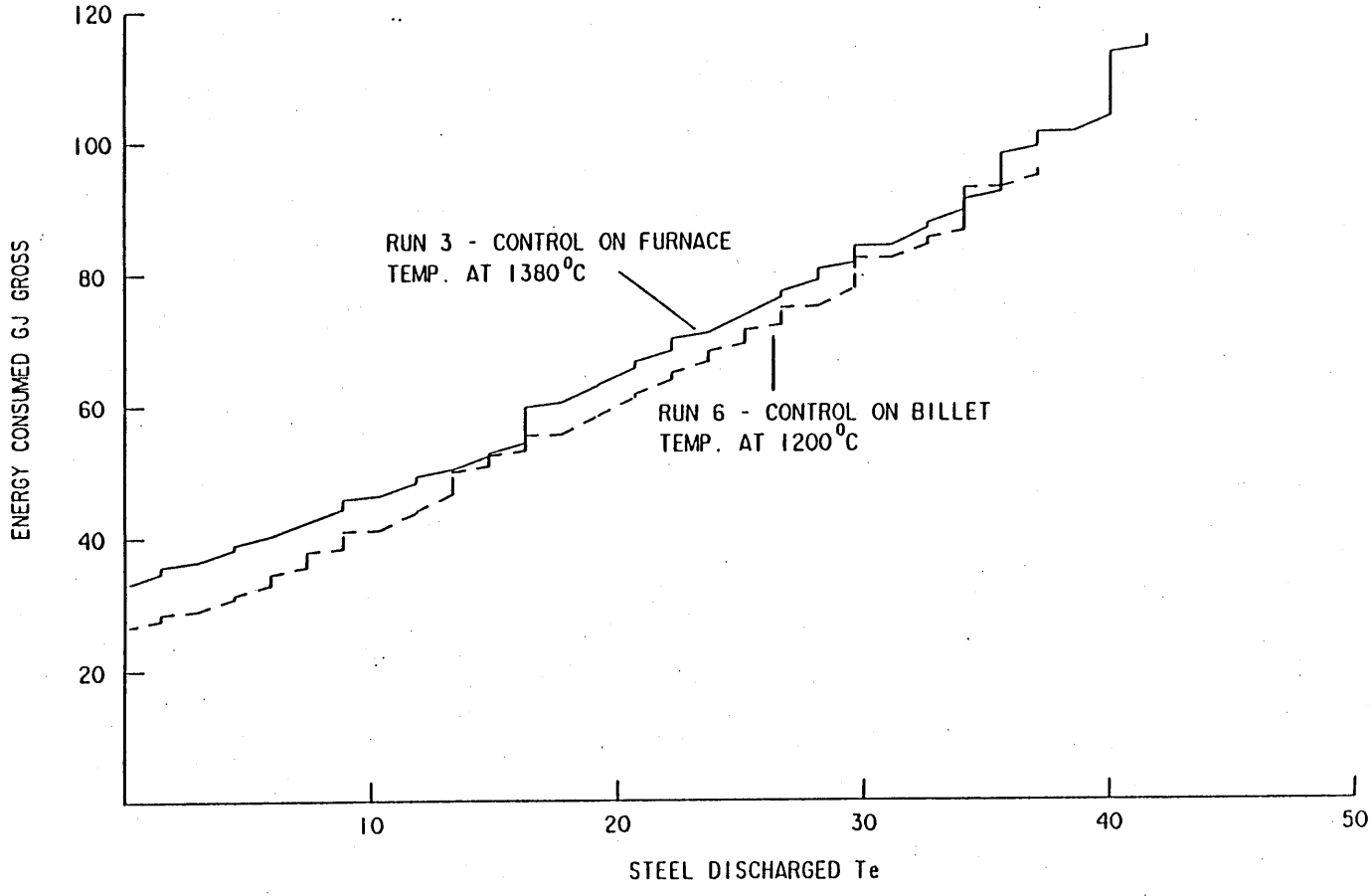

MODEL INPUT PARAMETERS - NO. ZONES = 10
HIGH FIRE RATE = 5.8 MW GROSS
EXCESS AIR = 2.5%

FIG. 12.16 THE PREDICTED EFFECT OF CONTROL ON BILLET TEMPERATURE

that there is insignificant effect of delays on the overall energy consumption - output pattern (Figure 12.17).

3. Billet emissivity (Run 8).

Because the surface emissivity of steel is so dependent on its state of oxidation, there is inevitable uncertainty in the value assumed in the model. Run 7 was therefore repeated with billet emissivity reduced from 0.8 to 0.7. An increase in start-up energy consumption and running consumption of just 3% is predicted (see Table 12.4). A similar increase in predicted steady-state performance is also shown.

4. Ceramic fibre roof emissivity (Run 9).

There is also considerable uncertainty regarding the emissivity of ceramic fibre. Run 7 was repeated with roof emissivity increased from 0.5 to 0.9. The decrease in start-up, running and steady-state consumption (Table 12.4) is shown to be insignificant.

12.7 Conclusions

1. The simulation of the start-up and production period for the furnace, shows that acceptable predictive accuracy is achieved. By simulating the control of the roof temperature, the energy consumption, billet discharge temperatures and load

Table 12.4

The predicted effects of steel surface emissivity and of ceramic fibre roof emissivity.

Run No.	Steel Emissivity	Roof Emissivity	Start-Up Gas (GJ) TRZONE	Steady-state Consumption (GJ/Te) TRZONE	SSZONE
(7)	0.8	0.5	27.655	1.839	1.775
(8)	0.7	0.5	28.377	1.897	1.836
(9)	0.8	0.9	27.300	1.815	1.750

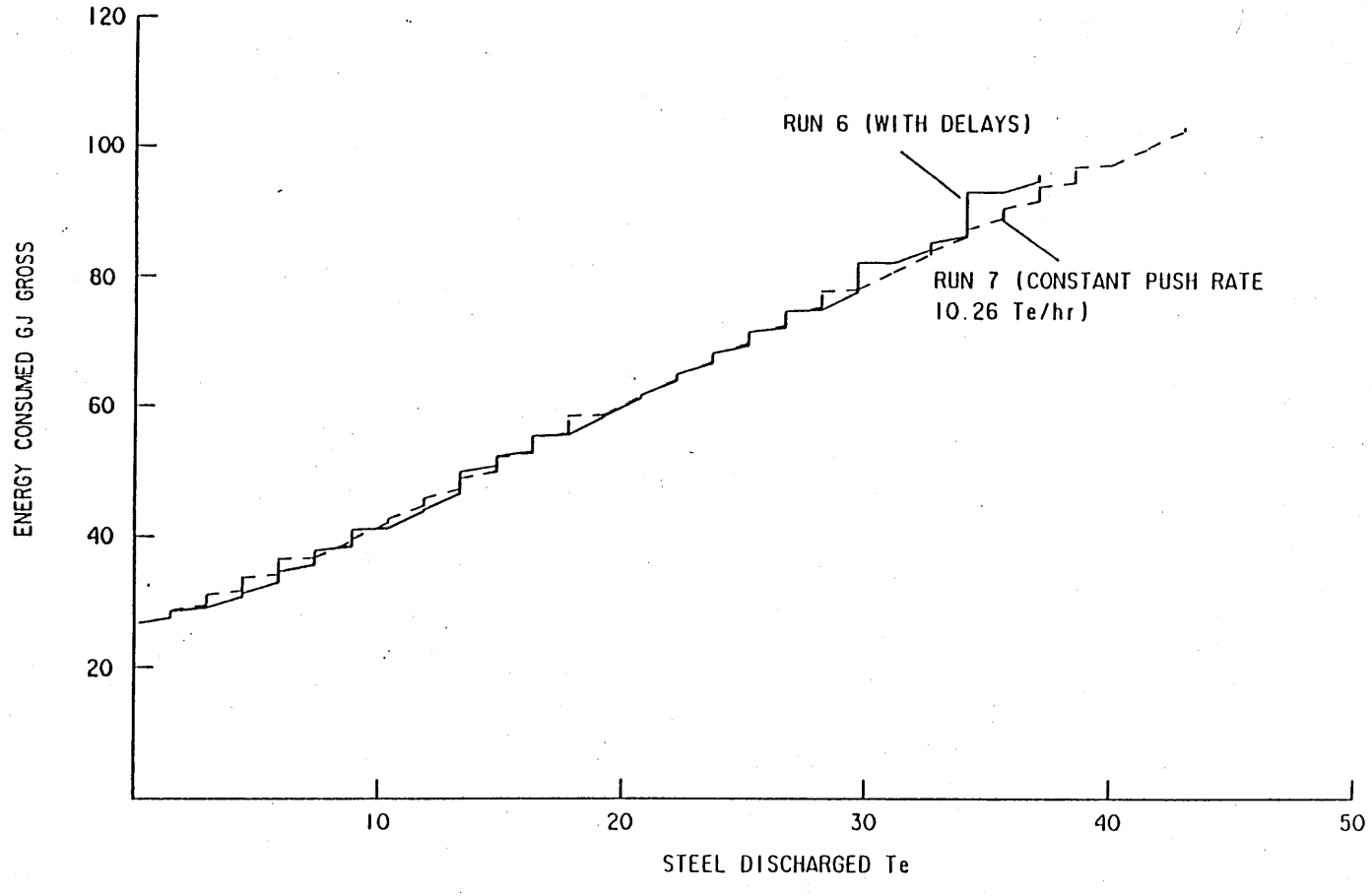

MODEL INPUT PARAMETERS - NO. ZONES = 10
HIGH FIRE RATE = 5.8 MW GROSS
EXCESS AIR = 2.5% SET POINT TEMPERATURE = 1200 °C (BILLET)

FIG. 12.17 THE PREDICTED EFFECT OF OPERATION AT A CONSTANT THROUGHPUT RATE

temperature profile through the furnace were all reliably predicted by TRZONE. The thermal performance under steady production conditions was also closely predicted by SSZONE.

2. The use of TRZONE to simulate production delays and changes in throughput has been demonstrated. After each delay, the model simulates a significant increase in discharged billet temperature. This was observed in practice. The effect of the delays on overall energy consumption was predicted to be small however.

3. Uncertainty in the surface emissivities of both the load and hot face of the ceramic fibre roof in the models has been shown to have small effect on the predicted energy consumption pattern.

CHAPTER 13

Model Validation Against a Batch Furnace

13.1 Introduction

Chapter 12 described the validation of TRZONE and SSZONE against a continuous reheating furnace starting from cold. Although the accuracy of the predictions throughout the production period was acceptable, there was some discrepancy and uncertainty in the start-up period with predicted billet temperatures higher than measured (see section 12.6.1). This was thought to be in part due to measurement inaccuracies, and to uncertainty into the area for radiation loss presented by the open door. Thus, further validation of TRZONE, particularly simulating a cold start-up period, was considered worthwhile.

TRZONE was also written to simulate batch furnaces. An opportunity was therefore taken to carry out controlled heating tests on a production batch heat treatment furnace. This furnace was newly built and of modern construction. It also operated at a lower temperature (<1000^{o}C) than the continuous furnace described above, and incorporated a tightly fitting door. The trial therefore provided an improved set of data with which to test the model. The testing of TRZONE against a batch furnace, also completes the validation of the

model for two main categories of furnaces.

13.2 Description of the Furnace and Measurement Trial

The main dimensions of the furnace are shown in Figure 13.1. It comprises an arched ceramic fibre roof, and insulating brick side walls with 50 mm of fibre veneer on the hot face. In normal use, the load which comprises of randomly packed automotive castings, rests on a tray to be loaded and removed from the furnace by a manually operated 'fork-lift' conveyor. The hearth is constructed of dense cast refractory. The combustion products are flued through pigeon hole slots in the piers with the objective of encouraging some flow of gases between the castings. The furnace is fired by two Nu-Way Multi-plex medium velocity tunnel burners positioned as shown in Figure 13.2. The tunnel exit on each burner is angled to encourage a strong torroidal recirculation of combustion products above the load with the objectives of achieving good temperature uniformity. The primary mission of the tests was to determine the influence of various firing arrangements on load temperature uniformity.

For this purpose an artificial load was constructed comprising of 41 mild steel bars of 50 mm square section. Thermocouples were inserted at a depth of 6 mm below the surface of selected bars at positions indicated in Figure 13.2. These were linked to a data acquisition system and subsequent processing of the

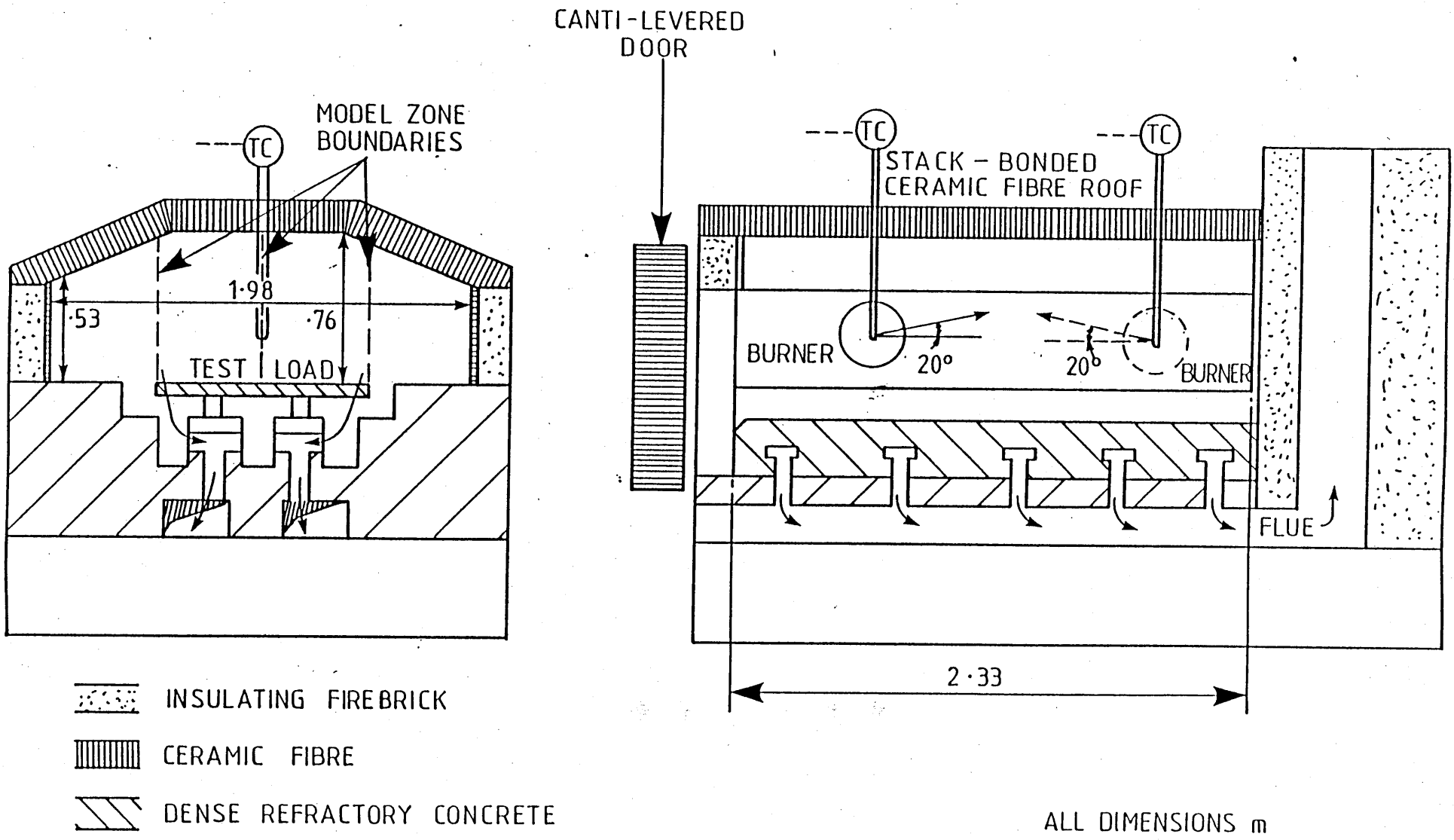

FIG. 13.1 SECTIONAL VIEWS OF THE BATCH FURNACE

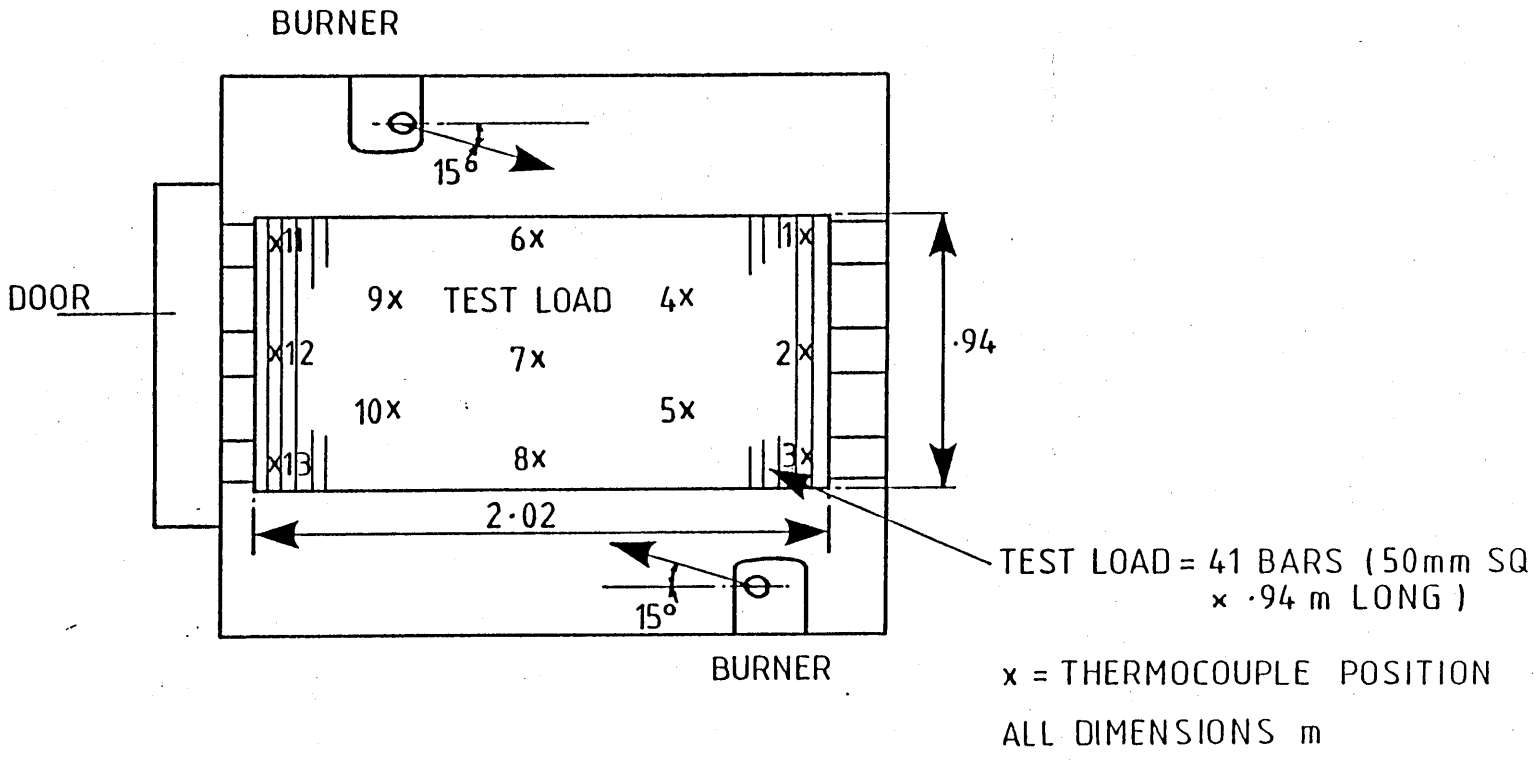

FIG. 13.2 PLAN VIEW OF THE FURNACE AND THE TEST LOAD

data produced files of maximum, minimum and average load surface temperature with time. Each test was carried out with the door firmly closed, and furnace pressure controlled at ±.5 mm water gauge. The risk of air ingress into the chamber influencing the results was therefore considered small. The firing rate of each burner was controlled by two roof inserted thermocouples positioned as shown in Figure 13.1. When the burners were on high fire, oxygen analysis of the flue gases indicated an excess air level of between 10 and 12.5%. When the burners turned down, this increased to 20-35% due to limitations of the control system to maintain constant ratio over different firing rates. During each test, the totalised gas input was monitored manually and subsequently inputted into the temperature-time files. Although a total of seven tests were carried out, only the first three were considered to provide suitable data to rigorously test against the mathematical model. These were:

Test 1. The furnace and load were heated from cold to 650^{o}C (as indicated by the control thermocouples), and then held at this temperature for a period. This was followed by an increase in set point temperature to 900^{o}C and holding at temperature.

Test 2. The furnace was preheated empty to 650^{o}C, the cold load was inserted and heated to 650^{o}C and then held at this temperature.

Test 3. The furnace was preheated empty to 900°C, the cold load was inserted and heated to 900°C and then held at this temperature.

13.3 Furnace Representation by Model

The furnace chamber was represented by TRZONE using 4 zones as indicated in Figure 13.3. The load was assumed to occupy zones 2 and 3 (the centre two zones only) with zones 1 and 4 assumed to be exposed hearth. Since the load is supported above the hearth with little direct contact with the refractory, the heat transfer from the underside of the steel to the hearth surface was assumed to be by radiation only. Load thickness of 55 mm was assumed in the model to allow for the extra mass of steel work which supported the 50 mm square bars above the hearth.

The two end walls and the side walls in each zone were treated separately from the roof because of their very different materials of construction. Each simulation was carried out with the gas input force fitted to the measured consumption pattern thus eliminating the need to simulate the control thermocouples. The gas consumption for each test is plotted in Figure 13.4. An excess air level of 10% was assumed for all three simulations. A high degree of combustion product recirculation was assumed (Figure 13.3) in accordance with observations using wood dust as a flow visualisation medium

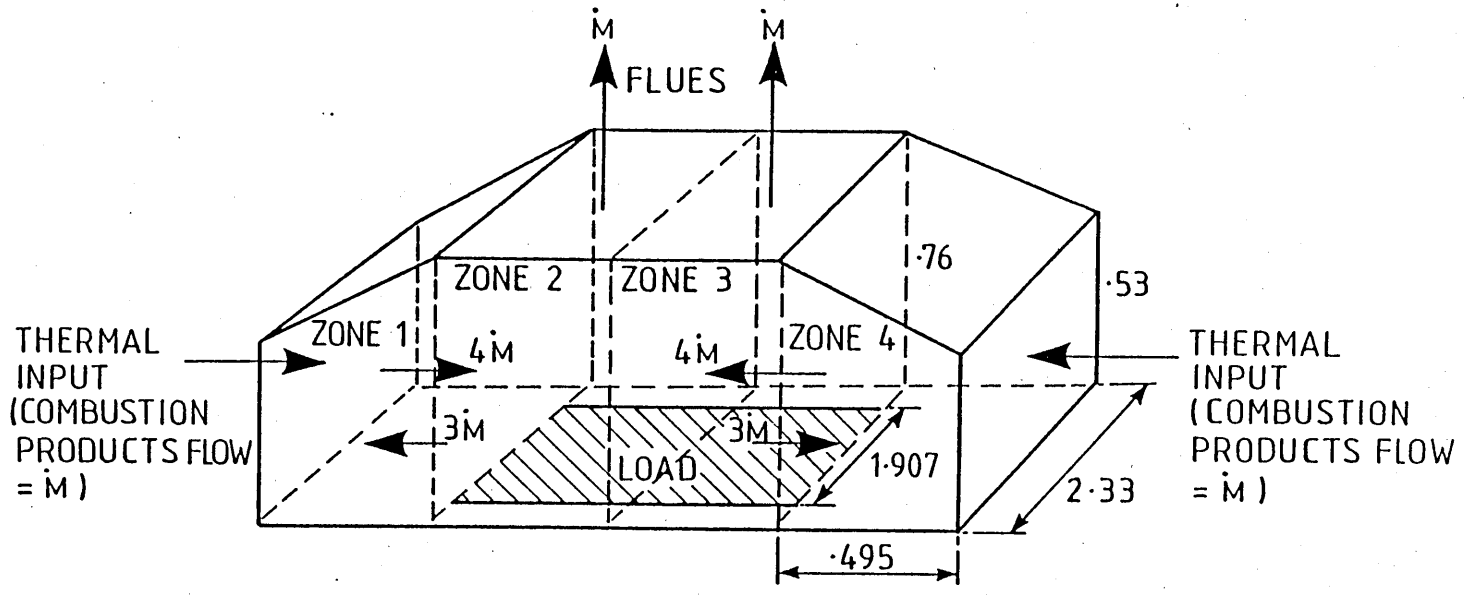

	CONSTRUCTION	DENSITY(kg/m^3)	HOT FACE EMISSIVITY
END & SIDE WALLS	50mm C.F. VENEER	128	0·5
	ON 180mm I.F.B.	880	—
ROOF	240mm STACK BONDED C.F.	128	0·5
HEARTH	350 mm REFRACTORY	2600	0·8
LOAD	55 mm MILD STEEL	7800	0·8

FIG. 13.3 THE REPRESENTATION OF THE FURNACE BY TRZONE
(ALL DIMENSIONS IN METRES)

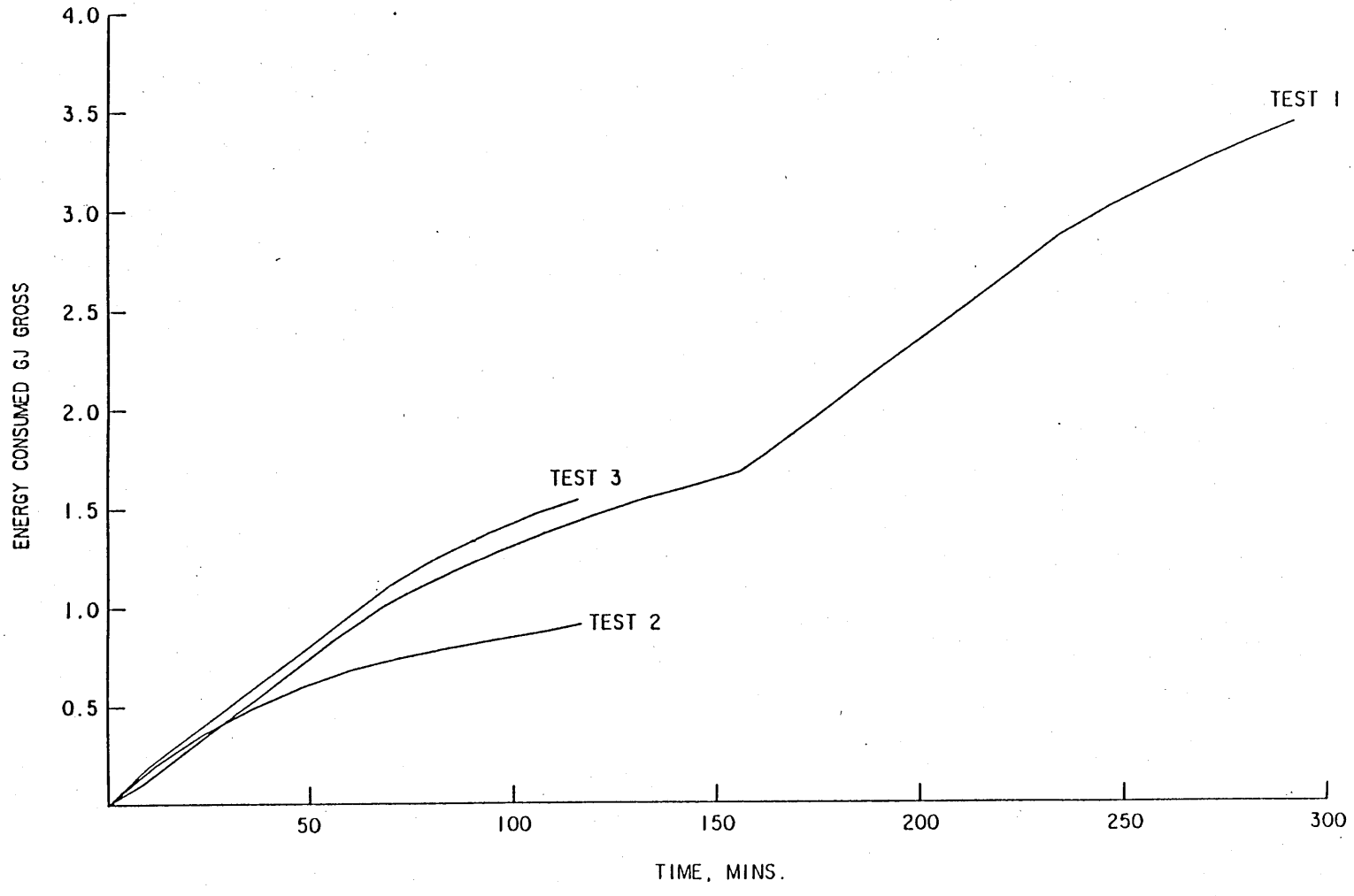

FIG. 13.4 THE MEASURED ENERGY CONSUMPTION FOR THE THREE TESTS

thrown into the furnace during firing with the door open. The model is symmetrical about the plane separating zones 2 and 3. A calculation time step of 2.5 seconds was selected after ensuring that a stable solution of the transient wall conduction was being achieved. If the time step is too large, oscillation of the nodal temperatures in the one-dimensional finite difference solution can occur, particularly when modelling conduction through ceramic fibre. CPU time on a VAX 11/780 simulating the 290 minutes furnace operation of test 1 was 470 secs.

13.4 Results

The comparison of the predicted and measured charge temperatures corresponding to tests 1, 2 and 3 are given in Figures 13.5, 13.6 and 13.7 respectively. The measured results are the maximum, average and minimum values for the 13 thermocouples. The transient conduction into the charge was modelled using a one-dimensional finite difference solution with nodes at 11 mm spacings. The predicted curve is the average of nodes 1 and 2 in the charge, thus corresponding approximately to the position of the thermocouples below the surface of the charge. Predicted temperature differences between the top and bottom of the charge were never greater than $60^{o}C$. Excellent predictive accuracy is achieved for test 1 up to $650^{o}C$ with an over prediction of the temperature rise to $900^{o}C$. An analysis of the computed energy balance at the

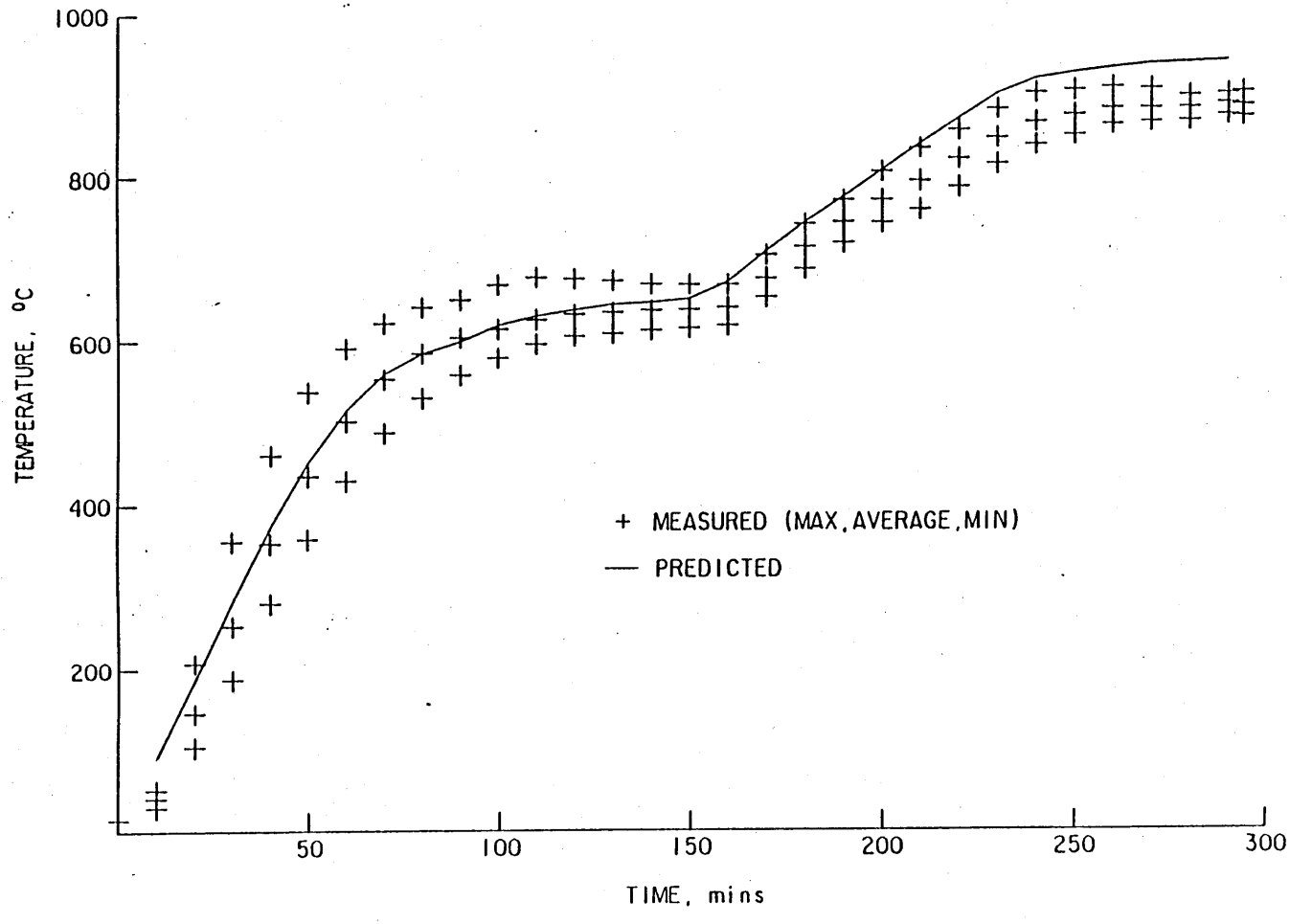

FIG. 13.5 A COMPARISON OF THE PREDICTED AND MEASURED LOAD TEMPERATURES (COLD START TEST 1)

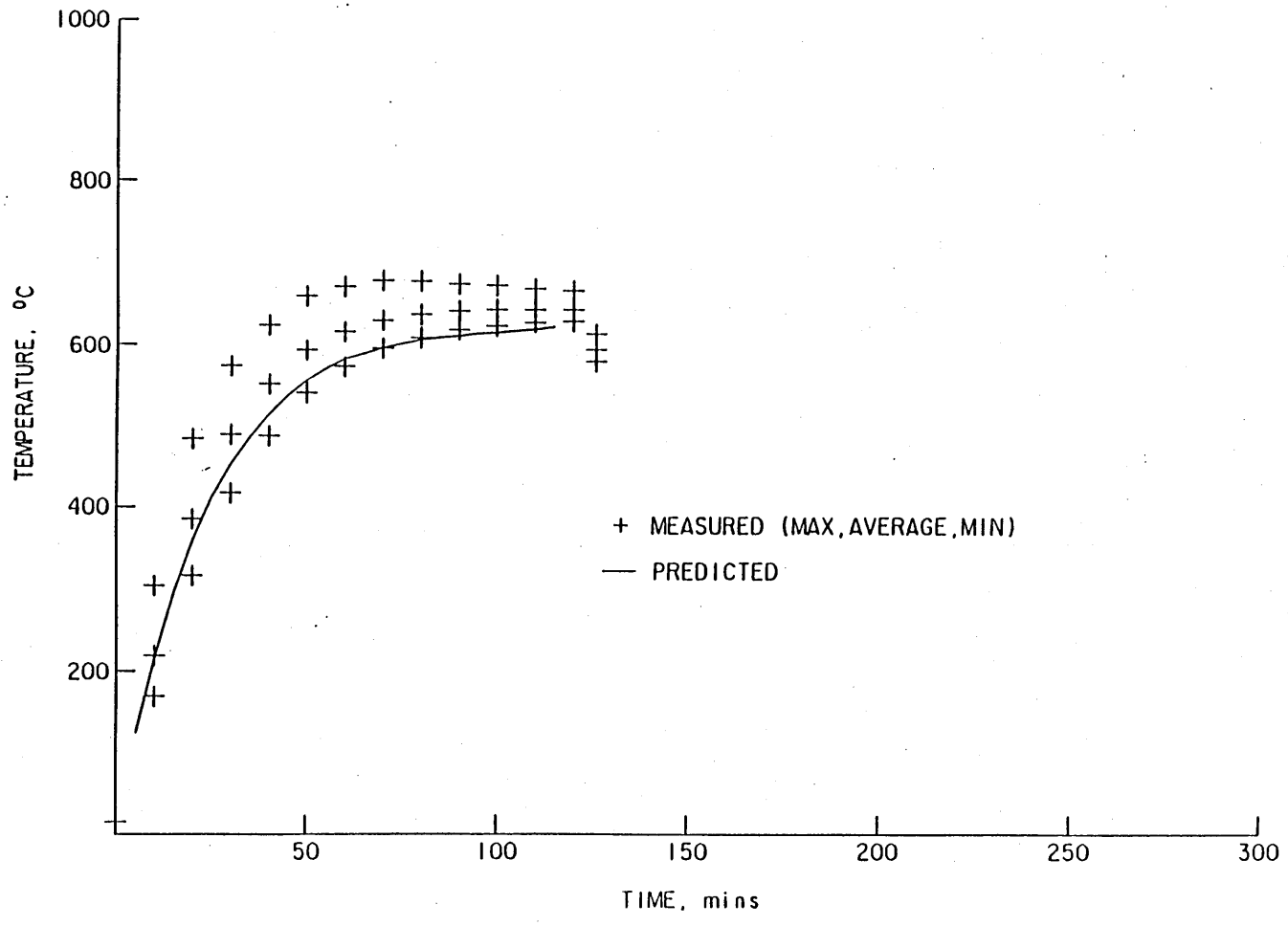

FIG. 13.6 A COMPARISON OF THE PREDICTED AND MEASURED LOAD TEMPERATURES (WARM START TEST 2)

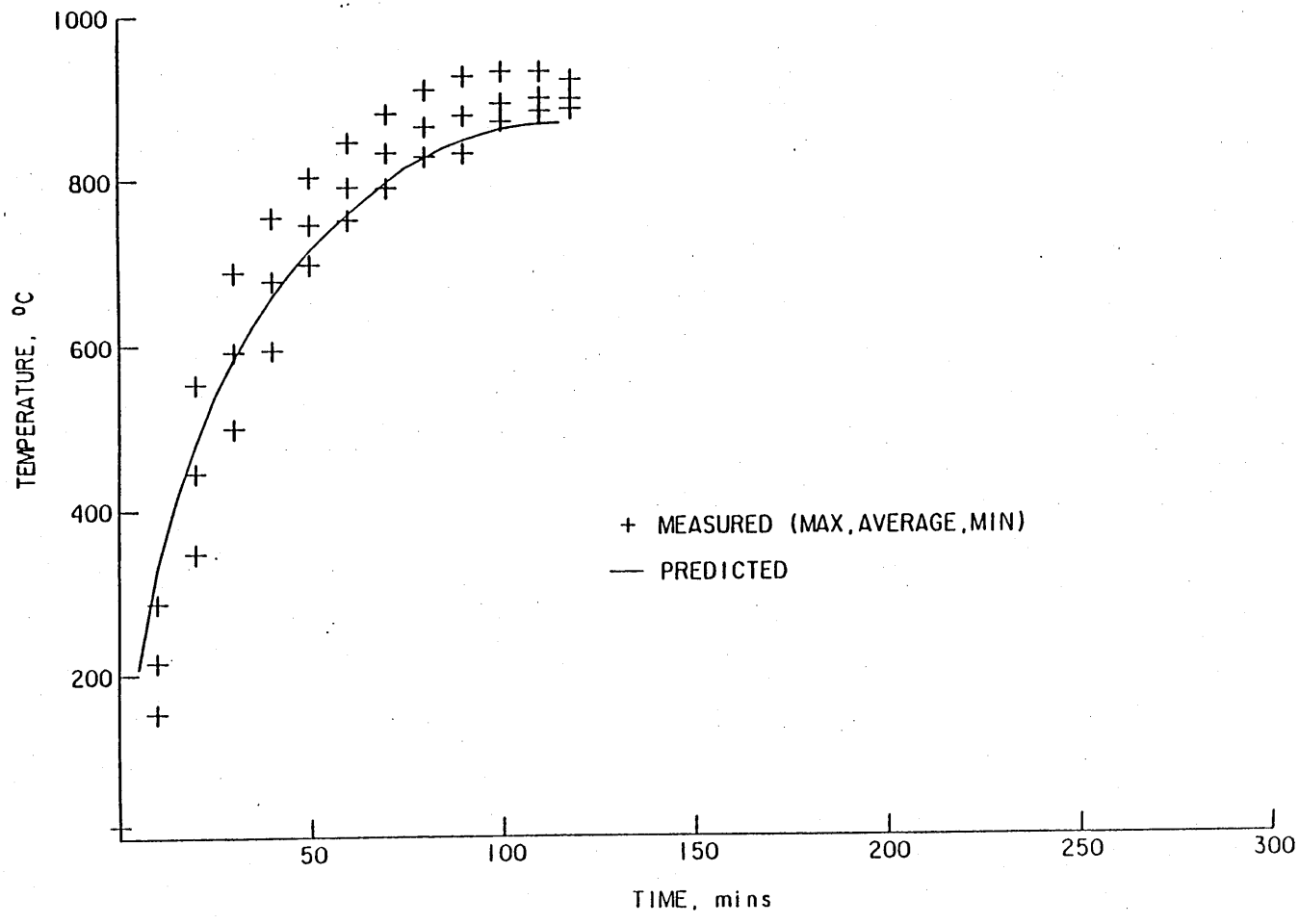

FIG. 13.7 A COMPARISON OF THE PREDICTED AND MEASURED LOAD TEMPERATURES (WARM START TEST 3)

end of this test is given in Table 13.1. This shows the significant heat absorption by the hearth.

In tests 2 and 3, the empty furnace was preheated to 650^{o}C and 900 ^{o}C respectively, prior to charging. This was simulated in the model as follows:

1) The heat up of the empty furnace was initially simulated with gas input controlled to maintain the roof surface in zones 2 and 3 at 650^{o}C or 900^{o}C. A total simulation time of 3 hrs was applied to ensure that the furnace structure had reached thermal equilibrium.

2) The predicted roof, wall and hearth temperature profiles in each zone were stored and appended to the input data files for tests 2 and 3.

3) Tests 2 and 3 were then simulated using the temperatures derived above as initial conditions. In these simulations the gas input was again force fitted to the measured consumption pattern.

In each test there is a slight underprediction of the measured temperatures. The agreement is however acceptable in view of the possible inaccuracies in specifying initial conditions. The energy balance analysis for these tests (Table 13.1) shows a significant reduction in the percentage of heat transferred to the hearth for these two warm start tests.

Table 13.1

The computed energy balance for cold start test 1 at 290 mins

	MJ	(%)
Energy Input (net CV)	3092	
Charge (810 kg, T = 945^{O}C)	900	(29)
Flue Loss	1315	(43)
Walls	241	(8)
Roof	105	(3)
Hearth	530	(17)

The computed energy balance for warm start test 2 at 115 mins

	MJ	(%)
Energy Input (net CV)	812	
Charge (810 kg, T = 624^{O}C)	329	(41)
Flue Loss	299	(37)
Walls	59	(7)
Roof	18	(2)
Hearth	107	(13)

The computed energy balance for warm start test 3 at 115 mins

	MJ	(%)
Energy Input (net CV)	1381	
Charge (810 kg, T = 871^{O}C)	521	(38)
Flue Loss	620	(45)
Walls	86	(6)
Roof	25	(2)
Hearth	130	(9)

13.5 Sensitivity Analysis

There is considerable uncertainty in the thermal property data and surface emissivity of ceramic fibre. Since this furnace comprises both a fibre roof and fibre veneered walls, the effects of fibre conductivity, density and emissivity on the predicted billet temperature rise was determined.

Because of the compressibility of ceramic fibre, its density when installed is thought to vary. Shrinkage during subsequent heating may also affect the final density. Test 1 was therefore repeated with fibre density reduced by 25% from 128 kg/m^3. The conductivity of stack-bonded ceramic fibre has also been shown by Junot *et al*. [42] to be higher than quoted by the fibre suppliers. The fibre conductivity used in the simulations above used a curve fit to the Junot data. Test 1 was repeated therefore with conductivity reduced to values corresponding approximately to the range of manufacturers quoted data.

The results of these simulations are shown in Figure 13.8a). Clearly, the large uncertainty in thermal properties for the ceramic fibre in this particular furnace has little overall effect on the predicted billet temperature rise.

The above exercise was repeated for the hearth and for the insulating fire brick in the side walls with similar

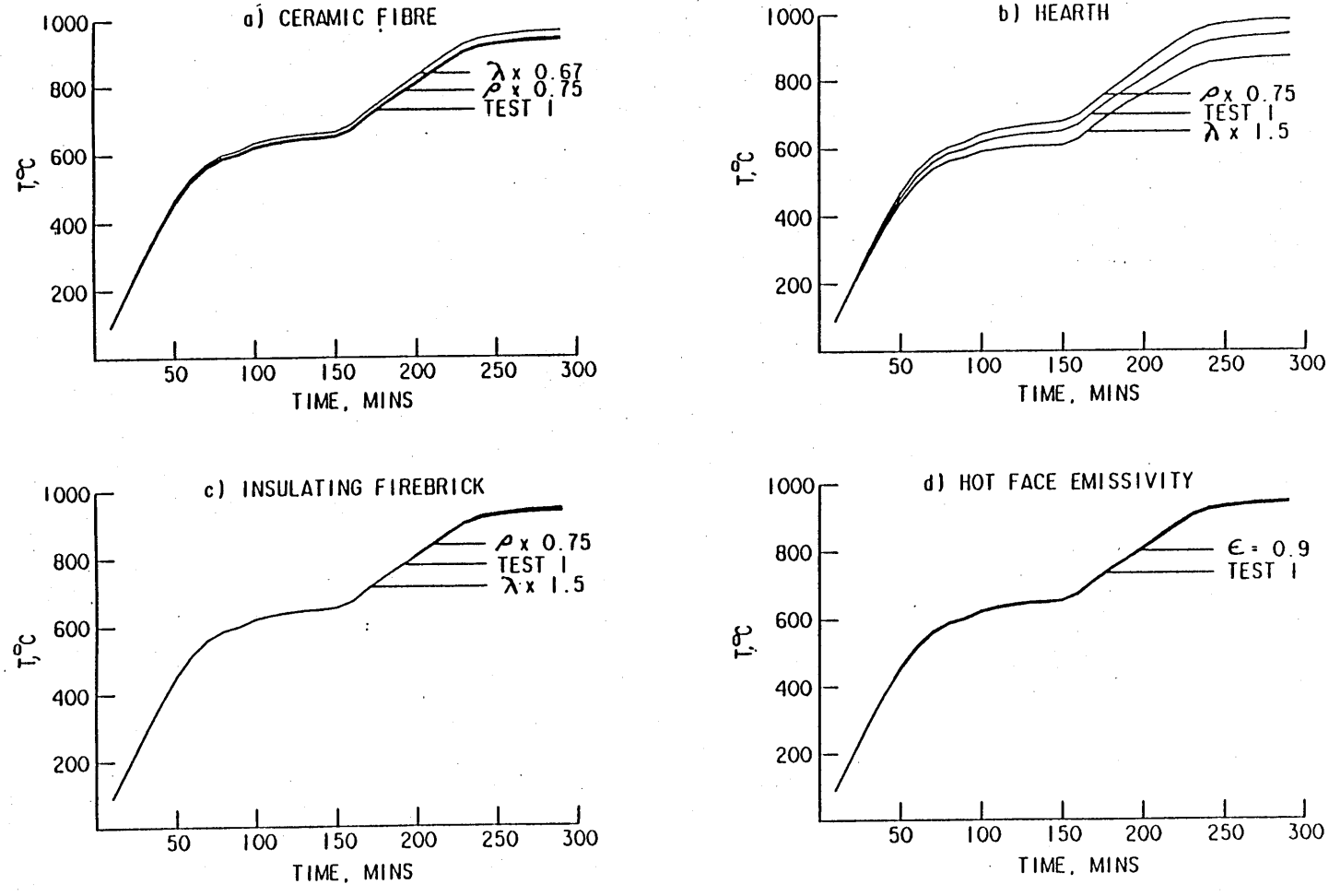

FIG. 13.8 THE INFLUENCE OF INSULATION AND REFRACTORY PROPERTIES ON THE PREDICTED LOAD TEMPERATURES

percentage changes in thermal conductivity (λ) and density (ρ) applied in turn (Figures 13.8b) and 13.8c)). As expected, variations in the hearth properties have the most sensitive effect on the predicted billet temperature curves since the hearth does absorb a significant quantity of energy during a cold start. Variations in the properties of the insulating fire brick in the walls has less effect than the ceramic fibre properties even though a greater quantity of heat is absorbed in the walls. Since the walls are veneered with ceramic fibre, it can be inferred that the properties at the hot face of the walls are more important.

Finally, the hot face emissivity (ε) of the fibre walls and roof was increased from 0.5 to 0.9 covering the current range of uncertainty of ceramic fibre emissivity. Negligible influence on the billet temperature curves was predicted (Figure 13.8d)).

13.6 Conclusions

1. The simulation of the 3 tests by TRZONE, show that acceptable agreement with the measured load temperature-time data is obtained. In particular, its application to a transient batch heating process is demonstrated wherein the furnace structure is known to absorb a significant fraction of the energy input to the process, and wherein the walls, roof and hearth interact strongly with the load heat transfer.

2. Large uncertainty in the ceramic fibre properties can be tolerated in the model. The predictions are also insensitive to variations in the thermal properties of the insulating fire brick beneath the fibre veneered walls.

3. Since the hearth can absorb a large quantity of energy in batch furnaces, especially over the first heating cycle, the predicted billet temperature rise is sensitive to its thermal properties.

4. The hot face surface emissivity of the fibre walls and roof is predicted to have negligible influence on the temperature curves.

CHAPTER 14

Application of the models

14.1 Introduction

SSZONE and TRZONE have been verified by comparison with measurements from a continuous steel reheating furnace and a batch heat treatment furnace. In both cases, the agreement has been satisfactory. A number of applications of the models were then tried in order to demonstrate the use of the models for practical furnace design and investigation. Because there are so many design and operating parameters to consider, this study has been based on just two application examples:

1. The continuous steel reheating furnace described in Chapter 12 which was used to validate the models. This was used to study alternative methods of flue gas heat recovery on continuous furnaces.

2. The models have also been applied to study the influence of wall emissivity on thermal performance. This latter case has been reported previously by Tucker and Docherty [43].

14.2 Flue Gas Heat Recovery on a Continuous Furnace

14.2.1 Introduction

Three methods of improving the thermal performance by flue gas heat recovery were considered:

- Flue stack recuperation
- Recuperative burners
- Regenerative burners

The furnace geometry and construction are described in Chapter 12. For each case a 10 zone representation of the continuous furnace shown in Figure 12.1 was used with billet discharge from zone 2, and allowance for radiation losses through a $1m^2$ open door in zone 1. For this particular study, the following operating specification was assumed:

- Billet size 1650 x 213 x 76 mm
- Throughput 15 Te/hr (50 secs/push)
- Output temperature 1200 ^{o}C
- Excess air 10 %

These parameters differ from those measured and were chosen in order to provide a better base case for this study. The throughput is higher than the maximum recorded during the trial. However, a 50 seconds push interval represents a

realistic maximum production rate in a steel rolling mill. The excess air level is thought to represent a more sustainable level on a well maintained furnace than the 2.5 % measured during the trial.

The results are tabulated in Table 14.1. The simulations are numbered 1 to 10 ; run 1 is the base case with no heat recovery. SSZONE was used to predict the gross steady-state thermal efficiency. The gross heat input is also predicted and tabulated. TRZONE was run for selected cases to determine:

i) The predicted efficiency under continuous and steady pushing (ie. the quasi-steady-state efficiency). TRZONE was run for an extended period (approx.350 mins) until a steady-state solution was achieved.

ii) The billet temperature uniformity (surface-centre temperature difference) and the load temperature profile through the furnace under the same conditions as for i).

iii) The gas consumption following a cold start-up and for a typical production period.

14.2.2 Flue Stack Recuperator

In this case, all of the thermal input was applied to zone 1 and all combustion products were flued from zone 10. The

Table 14.1 **A comparison of the predicted performance of a continuous furnace employing different forms of flue gas heat recovery.**

(Efficiencies are steady-state, gross values)

Run no.	Simulation	Heat Recovery Effectiveness (%)	SSZONE Predictions		TRZONE Predictions	
			Efficiency (%)	Input (MW_{gross})	Efficiency (%)	ΔT_L (^oC)
1	Base case - no heat recovery	0	36.4	9.241	33.3	234
2	Flue Recuperator	20	43.3	7.767	-	-
3	Flue Recuperator	40	49.6	6.778	44.0	254
4	Flue Recuperator	60	55.6	6.051	-	-
5	Recup.Burner (Scheme A)	40	32.1	10.472	-	-
6	Recup.Burner (Scheme B)	40	34.8	9.675	-	-
7	Recup.Burner (Scheme C)	40	38.7	8.697	36.0	160
8	Flue Recup. (Scheme C)	40	46.8	7.188	-	-
9	Regen.Burner (Scheme C)	80	59.8	5.63	-	-
10	Regen.Burner (Scheme C) - High Recirculation	80	60.5	5.56	55.1	171

performance of the flue stack recuperator was specified by a temperature effectiveness value (η_{eff}) defined by,

$$\eta_{eff} = (T_{a,out}-T_{a,in})/(T_{c,in}-T_{a,in}) \qquad 14.1)$$

where,

$T_{a,out}$ = air outlet temperature from recuperator,

$T_{a,in}$ = air inlet temperature to recuperator,

$T_{c,in}$ = combustion products temperature to recuperator.

For simulating a flue stack recuperator, $T_{c,in}$ is set equal to the gas temperature in zone 10 of the model (see chapter 5, section 5.6).

In runs 2,3 and 4 values of η_{eff} of 20,40 and 60% were specified in SSZONE. The predicted results are compared in Table 14.1 to the base case (run 1) with no heat recovery. An effectiveness of 40% represents a typical value which is likely to be attained in a commercially available metallic flue stack recuperator. The predictions indicate that a substantial improvement in thermal efficiency is possible. However, inspection of the load temperature profile through the furnace (Figure 14.1) shows that the rate of heat transfer towards the discharge zone is increased as higher levels of heat recovery are applied. The expected increase in billet surface to cold face temperature difference (ΔT_L) due to the change in heating profile is confirmed by the predictions from

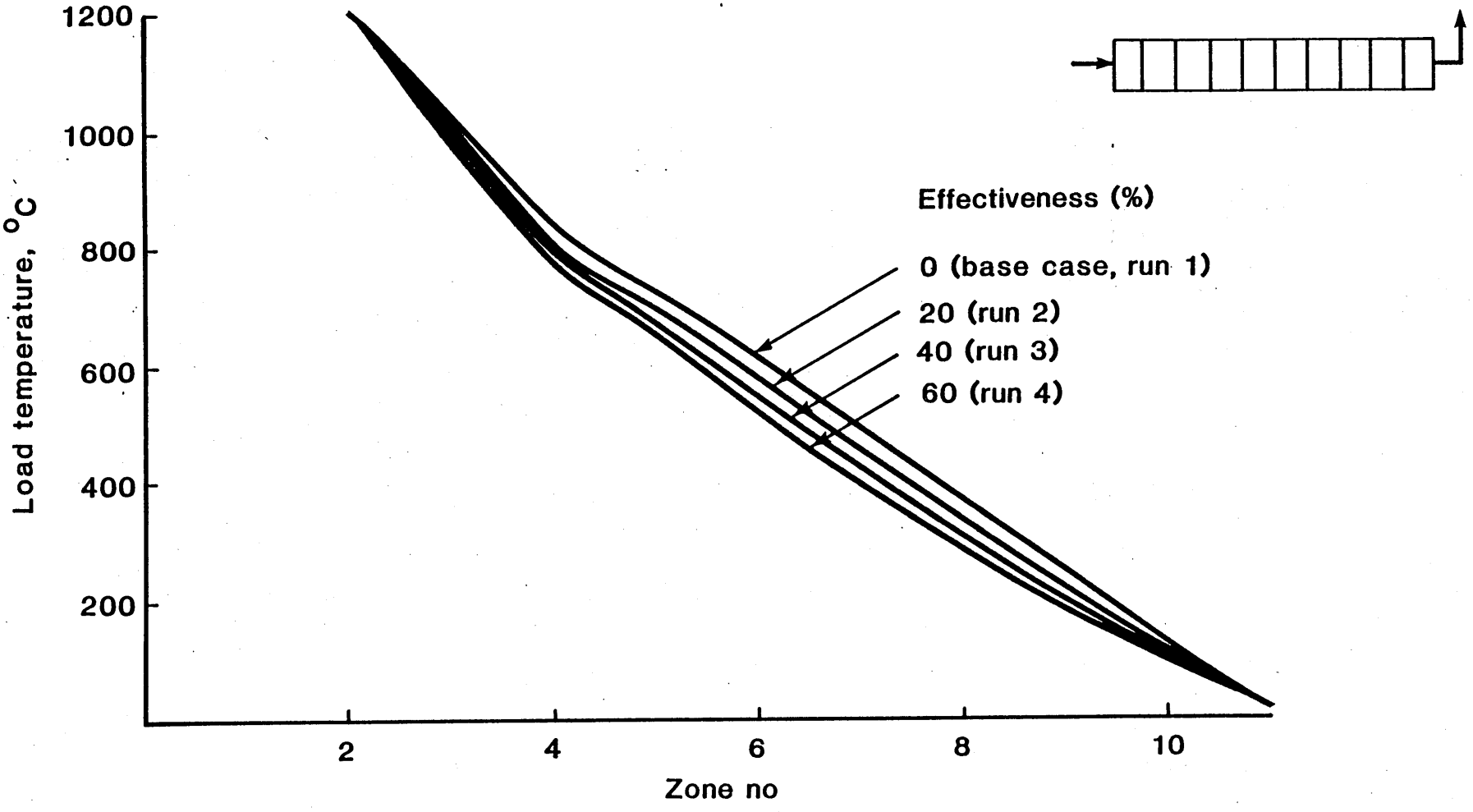

Figure 14.1 Predictions from SSZONE of load temperature profiles in a continuous steel reheating furnace with stack recuperation. (Runs 1,2,3,4 Table 14.1)

TRZONE which was run for the base case (run 1) and for the case with a 40% effective recuperator (run 3). The steady-state efficiencies predicted by the two models are compared in Table 14.1. The lower efficiency predicted by TRZONE is due to a higher steady-state heat loss through the walls, roof and hearth than the 1500 W/m^2 specified in the input data to SSZONE. A comparison of the thermal heat balances for run 1 predicted by the two models illustrates this point,

	Predicted Heat Transfer Rate (% gross heat input)	
	SSZONE	TRZONE
Load	36.4	33.3
Walls + roof + hearth	1.8	5.1
Door	5.9	5.8
Flue	55.9	55.8

If the total percentages to the load plus the walls, roof and hearth are compared, then close agreement between the two models is achieved, 38.2% in the case of SSZONE , and 38.4% in the case of TRZONE.

The steady-state load temperature profiles predicted by the two models are also worth comparing. Figure 14.2 compares the TRZONE and SSZONE predictions for the base case with no recuperation. As expected, TRZONE gives a higher surface

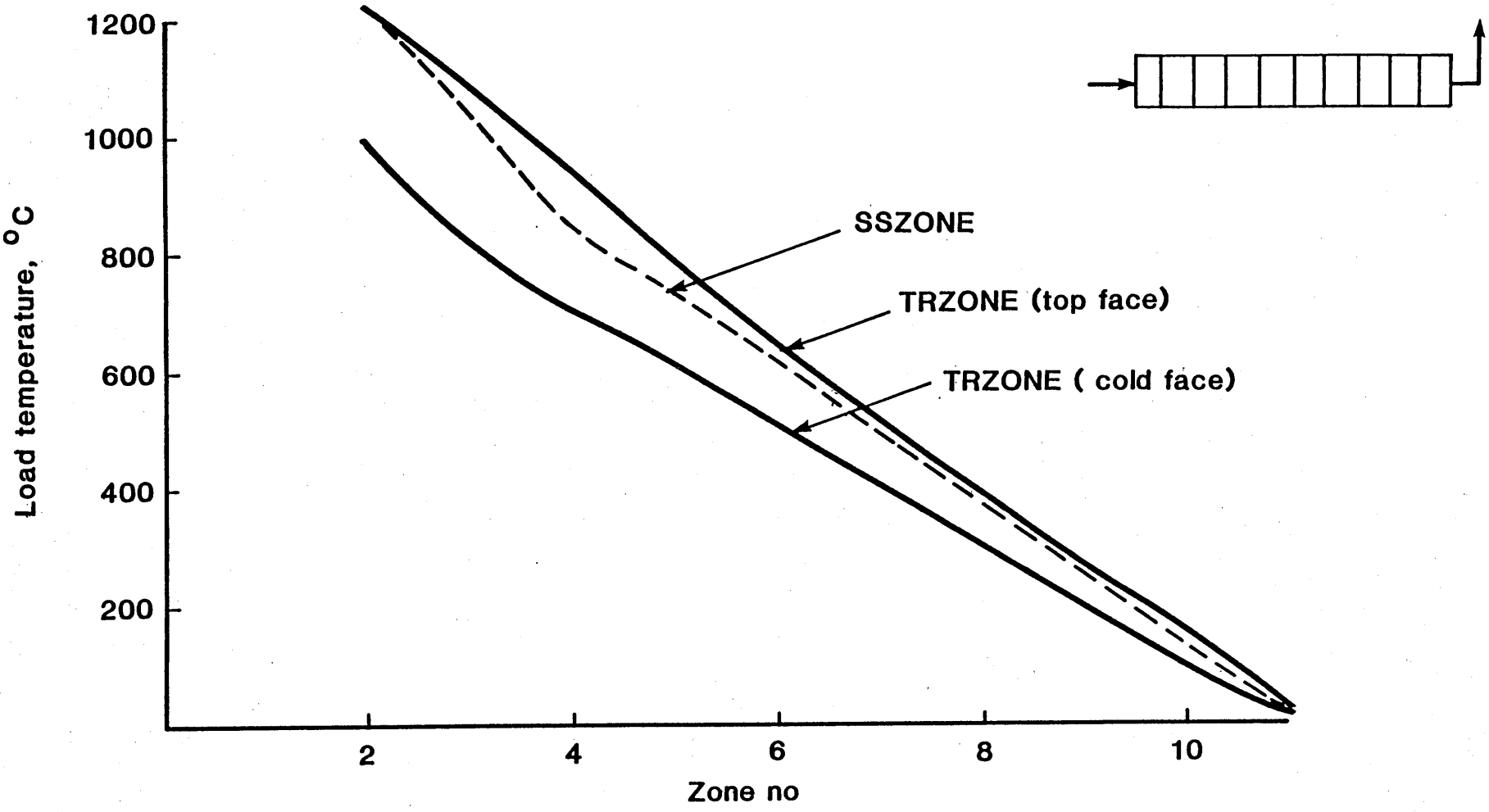

Figure 14.2 Predicted steady-state load temperature profiles using SSZONE and TRZONE for a continuous furnace without heat recovery. (Run 1 Table 14.1)

temperature throughout the furnace. The predicted surface to cold face temperature difference at discharge is 234 ^{o}C.

As with SSZONE, when recuperation is applied, the heat flux to the load predicted by TRZONE increases towards the discharge zones, giving a steeper temperature gradient and a higher surface to cold face temperature difference, Figure 14.3. From a practical view point, the increased surface to cold face temperature difference may not be tolerable, although the change in heating profile would yield lower rates of scaling of the steel.

14.2.3 Recuperative Burners

In this case, the thermal input was distributed to a number of zones along the furnace length, and the air preheat to each fired zone is based on the combustion products temperature in the respective zone ie. $T_{c,in}$ is equal to the local zone gas temperature (see chapter 5, section 5.6). Three firing arrangements were modelled as follows:

Scheme A : 66% fuel input to zone 1 ; 33% fuel input to zone 4
Scheme B : 33% fuel input to zone 1 ; 66% fuel input to zone 4
Scheme C : 25% fuel input to each of zones 1,3,5 and 7

In schemes A and B, 75% of the flue products were pulled back to the firing zones, and the remaining 25% was flued from zone

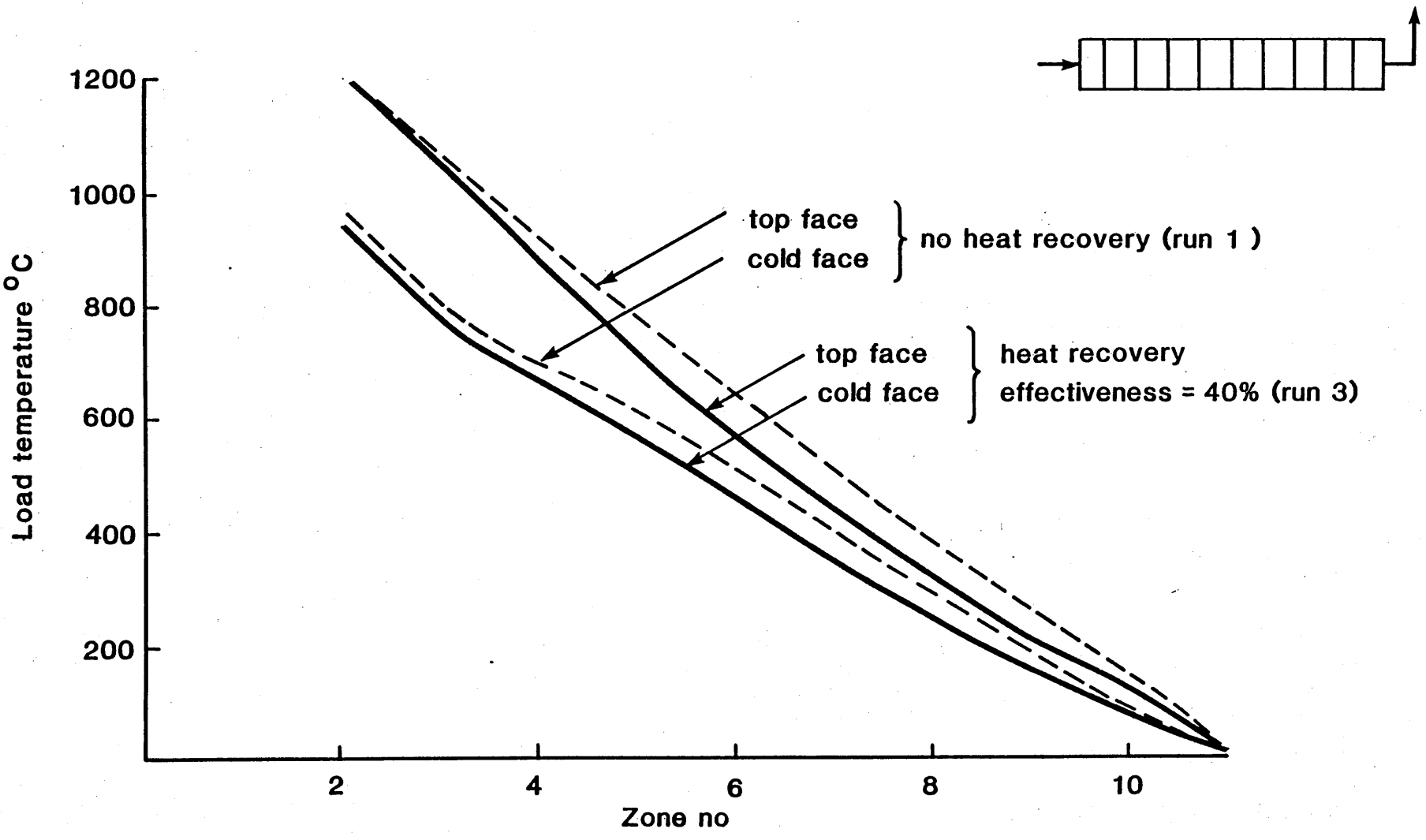

Figure 14.3 Predicted load temperature profiles using TRZONE for a continuous furnace with and without flue stack recuperation. (Runs 1,3 Table 14.1)

10. In scheme C, 80% pull-back was employed. It is common practice to allow some products to flow to the ends of the furnace in order to maintain a positive pressure in the chamber. A 75 % pull-back is usually tolerable within a recuperative burner without causing a significant drop in recuperator effectiveness (as defined in equation 14.1) and air preheat temperature. A constant recuperator effectiveness of 40% was assumed.

Only scheme C (run 7) was predicted by SSZONE and TRZONE to yield an improvement in steady-state thermal efficiency on the base case without any heat recovery (run 1). The increase in efficiency was small. Thus, the effect of pulling gases out of the furnace to individual recuperative burners instead of allowing them to travel to the main flue does, in this particular application, eliminate the benefits of the heat recovery. However, the surface to cold face load temperature difference is significantly reduced due to the change in load temperature profile through the furnace (see Figure 14.4). Applying the firing distribution in scheme C, but with 100% of the combustion products flued from zone 10 (run 8), and a 40% effective flue stack recuperator, SSZONE predicts a higher efficiency and an improved load temperature profile. Although this option is theoretically better, no consideration has been taken of the thermal losses involved in distributing hot air from a single flue stack recuperator to a number of burners. The installation costs compared to fitting individual

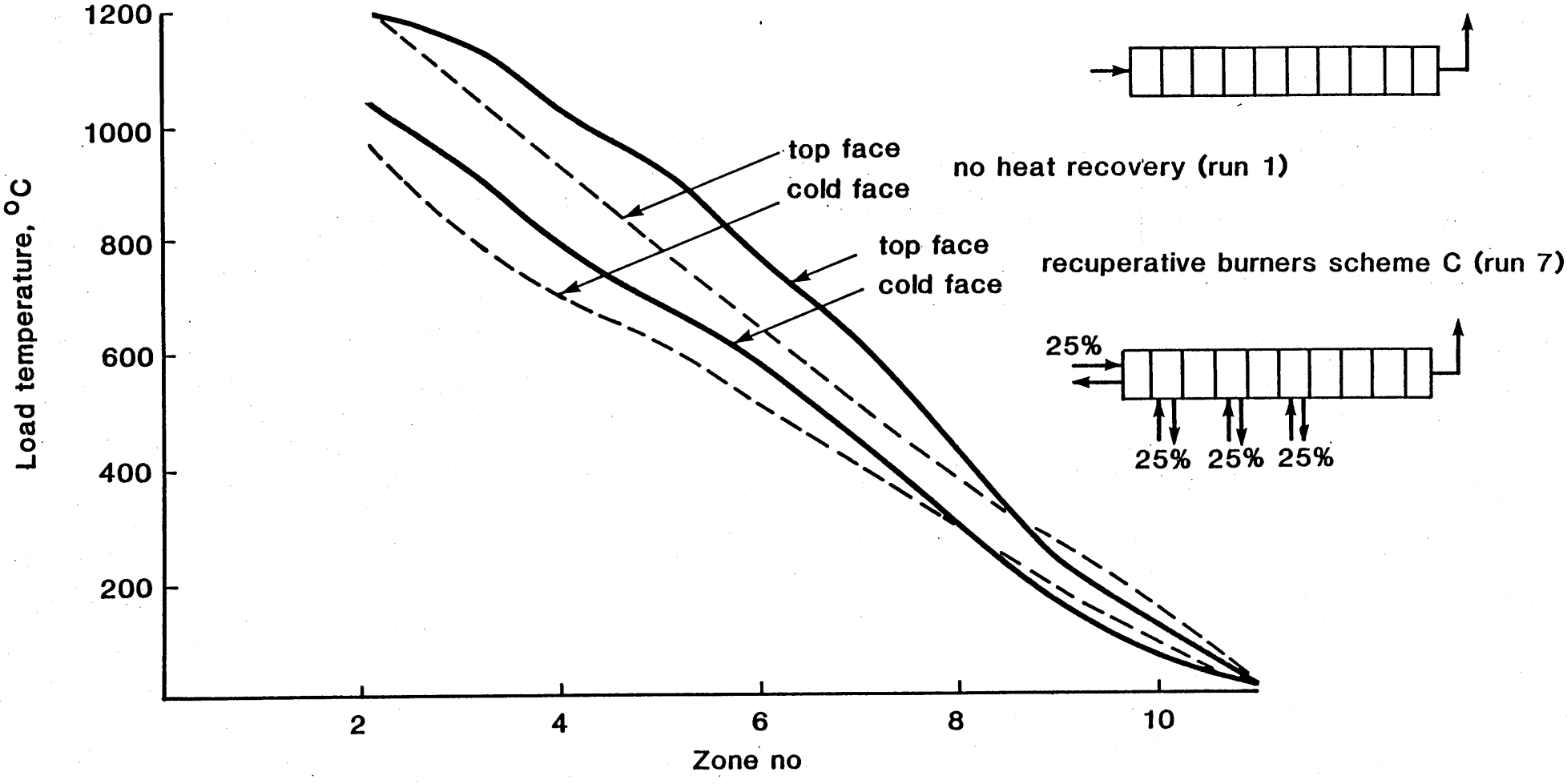

Figure 14.4 Predicted load temperature profiles using TRZONE for an end – fired continuous furnace without recuperation, and for the same furnace with recuperative burners. (Runs 1,7 Table 14.1)

recuperative burners would also need to be compared in a complete design study.

14.2.4 Regenerative Burners

In this case only firing scheme C was simulated and a heat recovery effectiveness of 80% was assumed which is typical of the operating performance of commercially available regenerative burners [44]. SSZONE predicts an efficiency of 59.8% (run 9). However, inspection of the calculated air preheat temperatures indicated a value of 1328°C to zone 1. This is a consequence of the high combustion products temperature of 1657°C predicted in this zone, which in turn is a consequence of there being no load in this zone, and there being no recirculation of combustion products between this zone and the cooler zone 2. The simulation was therefore repeated (run 10) with a high level of combustion product recirculation between all fired zones, in an attempt to reduce the high peak zone temperatures. A small increase in efficiency to 60.5% was predicted with a maximum air preheat temperature of 1295°C occurring in zone 1. Inspection of the load temperature profiles predicted in runs 9 and 10 showed that this was also insensitive to the degree of recirculation. Checks such as these are necessary to increase predictive confidence particularly where some of the input parameters cannot be specified with any certainty.

The predicted load temperature profile with regenerative burners was similar to that with recuperative burners (run 7); a very slight increase in heating rate towards zone 1 was predicted which produced a slight increase in the surface to cold face temperature difference at discharge.

14.2.5 Conclusions

This study has demonstrated how SSZONE and TRZONE can be used to compare various options for flue gas heat recovery on the same furnace. In this particular example, because the furnace employs a significant level of load heat recovery, the use of recuperative burners does not lead to a significant improvement in thermal efficiency, and with some firing configurations, they may actually reduce efficiency. This is because the gain in performance due to heat recovery by the combustion air is largely eliminated by the loss in load heat recuperation. It is only by installing regenerative burners on this furnace, with a much higher effectiveness, that significant gains in thermal efficiency are predicted.

The cumulative gas consumption following a cold start-up is shown in Figure 14.5, for the four transient runs carried out (runs 1,3,7 and 10). This shows that the predicted start-up energy consumption of the recuperative burner option is higher. During start-up however, the load along the furnace achieves a higher temperature than the level during continuous

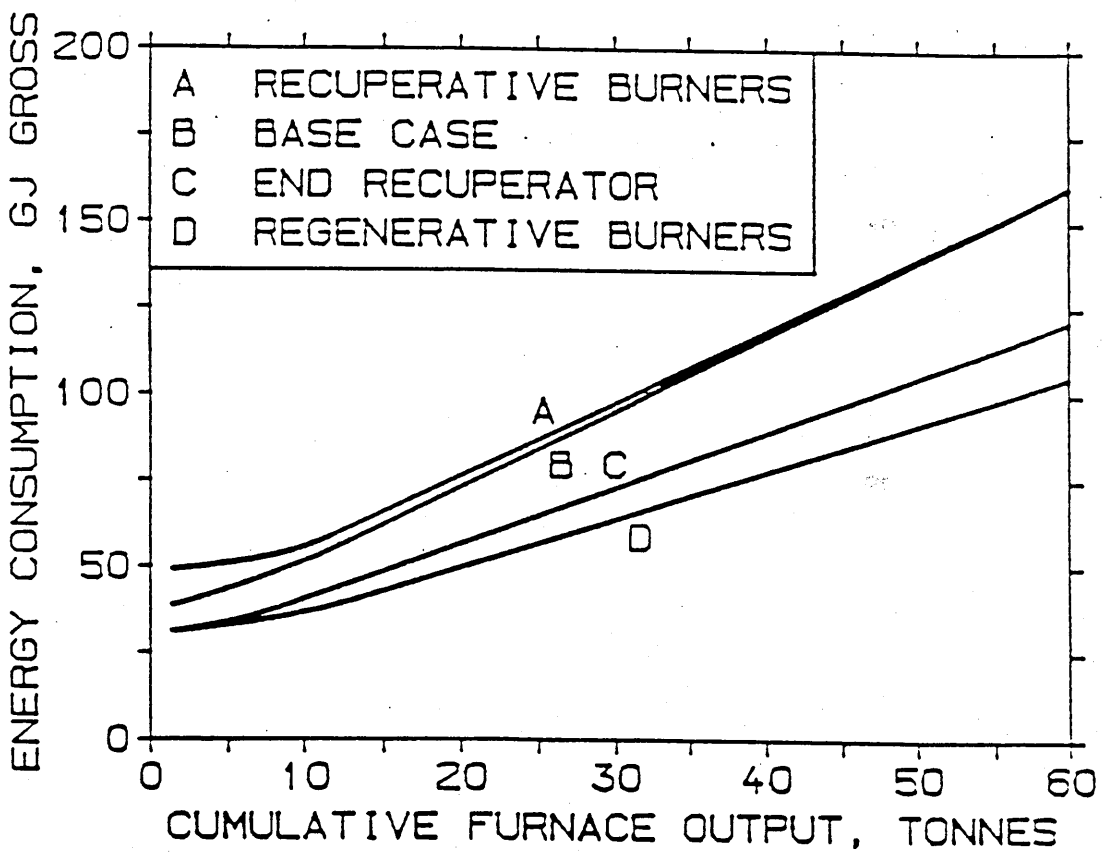

Figure 14.5 The predicted energy consumption on a continuous furnace using various forms of heat recovery.

production. Consequently, the gas rate to the furnace turns down once production commences and until the hot billets have been discharged from the furnace. An improved burner start-up strategy could be applied here as discussed by Saimbi and Tucker [22], with the light-up of some of the recuperative burners along the furnace delayed to avoid overheating of the load. This would reduce the start-up gas consumption and yield a curve closer to that for the base case. For the flue stack recuperator and regenerative burner options, the start-up consumption, and the consumption during pushing are both considerably reduced relative to the base case.

14.3 The influence of furnace wall emissivity

14.3.1 Introduction

Ceramic coatings are available which when applied to the hot face insulating walls of furnaces are claimed to raise their surface emissivity, and to lead to improvements in overall heat transfer and thermal performance [45]. The interchange of radiation between the combustion gases and the surfaces in a furnace enclosure will obviously be affected by a change in any surface emissivity. However, the effect on overall performance can only be estimated by application of a mathematical model of the furnace radiation heat transfer.

The mechanism of radiation interchange within a gas fired furnace is discussed in Chapter 1, section 1.4. It is postulated that an increase in wall emissivity will lead to an increase in the proportion of radiation that can be transmitted through the combustion products to the load. The grey body emission from the wall, increases the intensity of radiation at those wavebands which can pass unattenuated through the combustion gases. (The radiation originating from the combustion products which is reflected off the wall will be attenuated by the combustion products before it arrives at the load). This effect will lead to an increase in the radiation originating from the combustion products, which arrives at the load. Conversely, if the furnace atmosphere has a continuous spectral absorptivity over the wavelengths of interest (0.5-20μm), as typified by a luminous flame for example, radiation from the wall at all wavelengths is attenuated by the combustion products. In this case it is postulated that if the furnace atmosphere is grey, then an increase in wall emissivity will have no effect on overall heat transfer. SSZONE and TRZONE were therefore applied to test these hypotheses. Using the mixed grey gas model described in chapter 3, these models simulate the non-grey spectral character of the combustion products, and therefore should be capable of simulating the effects being investigated.

14.3.2 Application of SSZONE

SSZONE was applied to simulate emissivity changes on a continuous steel reheating furnace of dimensions 3x0.5x0.5 m with a load of width 0.5 m along the furnace length. Wall emissivity was varied from 0.01 to 1.0 and the effect on predicted gas consumption determined. The walls were assumed to be adiabatic (ie. zero conductivity). Since wall losses in a well maintained furnace is usually less than 5% of the thermal input, this assumption is justified.

Predictions were carried out for a steel discharge temperature of 1250 ^{o}C. The results are given in Figure 14.6 with gas consumption normalised to the predicted consumption with a wall emissivity of 0.5. These results also indicted that wall emissivity is more important at low levels of ε_w. An increase in emissivity from 0.5 to 1.0 gives a predicted 17% reduction in fuel consumption in this particular case.

SSZONE was also run to compare predictions with a mixed grey gas model of the combustion products to predictions assuming a single grey gas. The results (Table 14.2) support the hypothesis above that wall emissivity will have no effect on thermal performance if the gas is grey. This conclusion has also been arrived at independently by Elliston *et al.* [46], using both a simple mixed grey gas model, and a more detailed spectral radiation model for the gas.

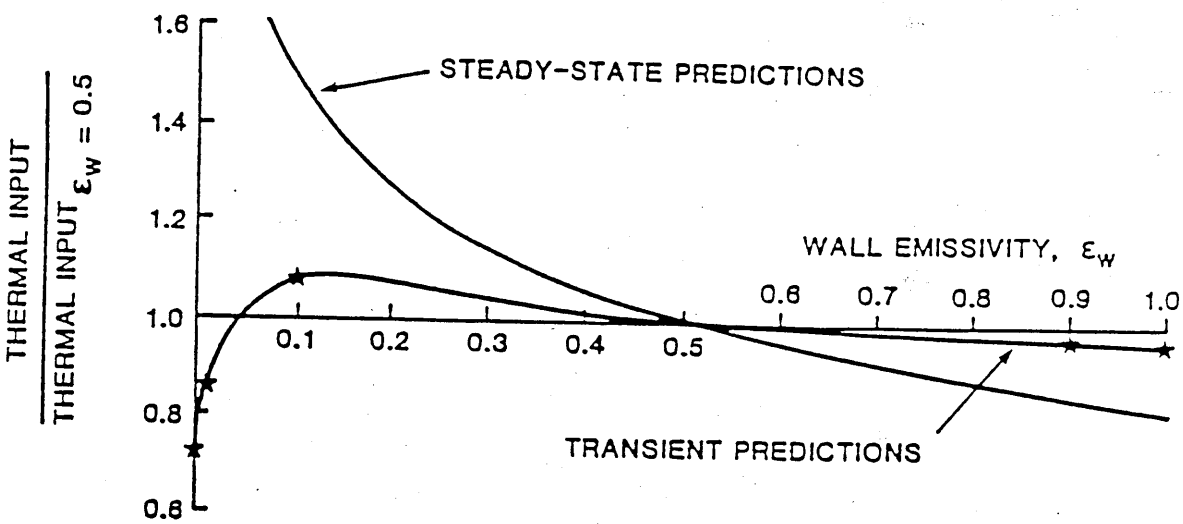

Figure 14.6 The effect of wall emissivity on predicted steady-state and transient energy consumption.

Table 14.2 Prediction of the effect of wall emissivity using SSZONE - the influence of non-grey gas behaviour.

Wall emissivity	Thermal efficiency % gross	
	Grey-gas model[1]	Non-grey-gas model[2]
1.0	51.76	48.28
0.9	51.76	47.91
0.5	51.74	45.83
0.1	51.79	41.41
0.01	51.85	39.29

(1) k_g=1.88 $m^{-1}atm^{-1}$

(2) Mixed grey gas model:

$kg,_1$=0.0 $kg,_2$=1.88 $kg,_3$=68.8 $m^{-1}atm^{-1}$

Again, applying SSZONE to a steel reheating furnace, the effects of a number of design and operating parameters on the predicted savings were investigated, as follows. For each run, ε_w was increased from 0.5 to 1.0 and the percentage drop in fuel consumption was noted. The results are summarised in Table 14.3. The fuel saving was found to depend on the following factors:

i) The original furnace efficiency.

Comparing cases A,B,C and D, the fuel saving achieved by increasing ε_w is dependent on the original efficiency of the furnace at the lower emissivity. By varying the steel throughput, the efficiency of the base case (ε_w = 0.5) can be adjusted. A low efficiency furnace corresponds to a high flue gas exit temperature. A change in wall emissivity increases the heat transfer from the combustion products to the load as discussed above, and therefore has most effect on those processes with an initially high flue gas exit temperature.

In the subsequent comparisons, furnace efficiency for the base case was maintained at approximately 23%.

ii) Furnace size.

Comparing cases E,C and F, the predicted saving is smaller for the larger furnaces and appears to reach a limiting value. It

Table 14.3 **The influence of design and operating conditions on predicted steady-state fuel savings.**

Case	Furnace Size,m (LxWxH)	Steel Output kg/hr	Steel Output °C	Steel emissivity	Predicted efficiency % gross ε_w = 0.5	Predicted efficiency % gross ε_w = 1.0	Potential Fuel Saving %
A	3x0.5x0.5	400	1250	0.8	46.1	48.3	4.6
B	3x0.5x0.5	700	1250	0.8	35.0	38.5	9.1
C	3x0.5x0.5	1000	1250	0.8	23.5	28.1	16.3
D	3x0.5x0.5	1300	1250	0.8	11.5	17.1	32.9
E	3x0.5x0.1	415	1250	0.8	23.4	30.6	23.6
F	15x2.5x2.5	42500	1250	0.8	24.0	28.4	15.5
G*	3x0.5x0.1	750	1250	0.8	23.3	26.3	11.5
H	3x0.5x0.5	435	1250	0.2	23.4	25.3	7.8
I	3x0.5x0.5	1800	800	0.8	23.2	28.3	17.9

* Includes convective heat transfer; all other cases convection ignored.

is postulated that this limit is reached when the absorbing components of the mixed grey gas model become opaque.

iii) Convective heat transfer.

In many natural gas fired processes, the forced convection between the combustion products and the wall and load surfaces is significant. In the cases so far considered, convective heat transfer has been ignored. In cases G and E, two furnaces of the same size and base case efficiency were compared with and without convection included. In case G, radiation from the combustion products accounts for only half of the total heat transfer to the load. Since radiation transfer from the combustion products is less significant, the predicted fuel savings are smaller.

iv) Load emissivity.

Comparing cases C and H, a furnace heating a material of low surface emissivity is predicted to yield a reduced fuel saving. There is an increased reflection at the load surface of the clear gas component of radiation from the wall. This radiation is subsequently re-absorbed and emitted (at all wavelengths) by the wall, and some of this becomes re-absorbed by the combustion products.

v) Load temperature.

Comparing cases C and I, the load temperature is predicted to have little effect on the potential fuel saving.

14.3.3 Application of TRZONE

It can be postulated, that if heat loss into or through the furnace wall is high, then an increase in emissivity may lead to an increase in fuel demand by the furnace. Circumstances where wall heat losses are significant arise on intermittently operated furnaces, particularly when they are first switched on from cold. These effects can be tested by application of TRZONE which was applied to simulate a batch furnace of volume $1m^3$ comprising of dense refractory walls and heating a steel mass per charge of 393 kg to 1250°C. The simulation included a thermal soak at 1250°C for 30 mins. Convective heat transfer was neglected. Predicted flue temperature through the heating cycle were similar to those cases in Table 14.3 operating with a base case steady-state efficiency of 23%. This was considered important in order to enable a direct comparison to be made between some of the steady-state and the transient predictions. The predicted results shown in Figure 14.6 relate to the fuel consumption during heating of the 4th charge of billets after the furnace had been turned on from cold. The consumption is again normalised to the consumption with ε_w = 0.5. In contrast to the steady-state predictions, a much

smaller fuel saving is predicted. At very low values of ε_w (<0.1), the wall heat loss effect dominates any improvement in radiation heat transfer within the chamber. Increasing emissivity under these conditions, increases wall heat loss, and hence the fuel consumption per cycle. This result also indicates potential savings by using very low emissivity materials for the wall.

14.3.4 Conclusions

From this theoretical study, it is concluded that:

i) An improvement in heat transfer by increasing wall emissivity is only theoretically verifiable if the non-grey character of the combustion products is taken into account by the model.

ii) The predicted savings are dependent on the original furnace efficiency, with low efficiency furnaces offering greatest potential savings.

iii) Where wall heat losses are significant, such as in many transient processes, lower savings are predicted.

CHAPTER 15

Conclusions

The following conclusions can be drawn from this study:

1) The zone method for radiation analysis provides an accurate and flexible method on which to base both steady-state and transient mathematical models of industrial furnaces. In particular, the long furnace model has been demonstrated to be an adequate model for practical furnace design problems. Comparison of predictions against data from both a batch and a continuous steel reheating furnace, have verified that a long furnace model can accurately simulate both the transient start-up and the continuous steady-state operation of these types of furnaces.

2) For accuracy in both the prediction of furnace efficiency and of load temperatures, it is important that allowance for radiation interchange between zones is included in the long furnace model. Simpler models which neglect interzone radiation can, for some operating conditions, yield inaccurate predictions of important performance parameters. The predictions from these simpler models are also more sensitive to the number of zones chosen to represent the furnace enclosure.

3) In order to allow fully for zone interchange, a large number of direct exchange areas between the zones must be calculated. Accurate techniques such as numerical integration can only handle regular geometries such as rectangular furnace enclosures. However, the Monte Carlo technique has been successfully used in this study to calculate exchange areas in more complex geometries, including those where shading can occur.

4) The Monte Carlo technique can produce large errors in some of the calculated exchange areas compared to the numerical integration technique. However, the effects of these errors on the computed thermal performance of a furnace using a long furnace model has been demonstrated to be insignificant.

5) The model developed in this study can be easily applied to evaluate alternative methods of firing furnaces, such as the use of recuperative and regenerative burners, as well as changes to the furnace control or construction.

6) The models have shown that increasing wall emissivity in a furnace can improve the heat transfer to the load by increasing the proportion of radiation transmitted through the clear bands in the absorption spectrum of the combustion products. The effects are more significant on furnaces where wall heat loss is small, such as a continuously operated furnace.

APPENDIX 1

The Numerical Solution of Non-Linear Equations

Because of the occurrence of terms in T and T^4 in the energy balance equations in SSZONE and TRZONE, these equations are described as non-linear in temperature. Their solution can be carried out by the Newton iterative procedure which is well suited to machine computation. The technique as applied to a single equation in one unknown variable and to a set of n simultaneous non-linear equations in n variables is described.

Solution of a Single Equation

Consider for example, a simple heat balance equation of the form,

$$aT^4 + bT = c$$

where a, b and c are constants. It is necessary to find the values of T (there may be up to 4) which satisfy this equation.

The problem can be generalised to finding the roots to the non-linear function $f(x) = 0$ in any unknown variable x. The problem formulated in this way lends itself to many standard

methods of solution of which Newton's method is just one. Suppose $x = x_1$ is a known approximation to the root of $f(x) = 0$. If the exact root is x (where $x = x_1 + h$) then $f(x_1 + h) = 0$. This can be expanded by Taylor's theorem to give,

$$f(x_1+h) = 0 = f(x_1) + h\, f'(x_1) + h^2/2\ \ f''(x_1) + \ldots\text{etc.}$$

Where f', f'' represent the first and second order derivatives of $f(x)$ with respect to x (i.e. df/dx, d^2f/dx^2 etc.).
$f(x_1)$ is called the residual of f at x_1.

If h is small, terms in $f''(x)$ and above can be neglected giving,

$$h = -f(x_1)/f'(x_1)$$

Consequently a second approximation to the root is given by

$$x_2 = x_1 + h = x_1 - f(x_1)/f'(x_1) \qquad \text{A1.1)}$$

which is Newton's formula for improving the approximate root of $f(x) = 0$. This formula can be applied repeatedly to improve the approximation until the value of h is acceptably small. A convergence criterion must be defined in order to limit the number of iterations. This is defined by a tolerance (tol) such that solution is assumed to be achieved

when $h \leq tol$.

Equation A1.1) can be derived by considering $f'(x_1)$ as the slope of the tangent to the curve at x_1. This is equal to $f(x_1)/(x_1-x_2)$ from which the improved approximation x_2 can be derived.

In practice it may often be impossible to differentiate $f(x)$. In order to calculate the derivative $f'(x)$ at any value of x, it is necessary to find a linear approximation to $f'(x_1)$ as follows:

$$f'(x_1) = (f(x_1) - f(x_1 - \Delta x))/\Delta x \qquad \text{A1.2)}$$

where Δx equals an incremental change in x about x_1.

A generalised procedure for finding the root to the equation $f(x) = 0$ can now be written:

1. Guess an initial value x_1 to start the procedure. This must be a sensible guess particularly if more than one real root exists. Set $k = 1$.

2. Calculate $f(x_k)$

3. Calculate a linear approximation to $f'(x_k)$ by equation A1.2).

4. Calculate the improved approximation x_{k+1} from equation A1.1).

5. If x_{k+1} and x_k differ by more than an acceptable tolerance (tol), then repeat from step 2) with x_{k+1} in place of x_k. Increment k by 1.

The Gauss-Seidel method.

This involves the following steps:

i) Guess all unknown temperatures T_j and assign to array.

ii) Select zone 1 and its appropriate heat balance equation which is of the form,

$$f_1(T_1) = 0$$

and includes terms in T_1^4 and T_1.

iii) Solve this equation for T_1 by Newton-Raphson method, keeping all other temperatures constant, to yield a new estimate of $T_1 = T_1^1$, and replace T_1 in array by T_1^1.

iv) Repeat procedure from step ii) for next zone (zone 2).

Solution for all NX temperatures in this way is called a cycle. The cycle is then repeated starting with the current

array of temperatures T_j until two consecutive cycles yield a set of temperatures which differ by less than a prescribed tolerance (TOL) or convergence criterion , ie.

$$\max \left| T_i - T_i^1 \right| < TOL$$

Solution of Simultaneous Non-Linear Equations.

In the formulation of the energy balance equations, the balance at any one zone is a function of the temperature of all other zones representing the enclosure. Hence it is impossible to isolate and solve the balance on any zone without simultaneously solving for all other zone temperatures.

The problem can be generalised to solving the following set of n non-linear functions in n unknown variables x_1, x_2 ...x_n.

$$f_1(x_1, x_2, x_3, \ldots x_n) = 0$$
$$f_2(x_1, x_2, x_3, \ldots x_n) = 0$$
$$f_n(x_1, x_2, x_3, \ldots x_n) = 0$$

or in short-hand notation $F(x) = 0$

Newton's method for improving the k^{th} approximation is generalised to a form analogous to equation A1.1). In the 1-D

case the procedure is defined by,

$$x_{k+1} = x_k - f(x_k)/f^1(x_k)$$

but in n dimensions this becomes,

$$X_{k+1} = X_k - F(X_k).H^{-1}(X_k) \qquad \text{A1.3)}$$

where X_k and X_{k+1} are the vectors of n unknown variables at the k^{th} and $(k+1)^{th}$ iterations respectively.

e.g.
$$X_k = \begin{bmatrix} x_1 \\ x_2 \\ . \\ . \\ x_n \end{bmatrix}_k$$

$F(X_k)$ is the vector of function residuals at the k^{th} iteration (equal to zero when solution is achieved),

$$F(X_k) = \begin{bmatrix} f_1 \\ f_2 \\ . \\ . \\ f_n \end{bmatrix}_k$$

and $H^{-1}(X_k)$ is the inverse of the matrix of partial derivatives $\delta f_i/\delta x_j$ ($i = 1,n$ and $j = 1,n$) evaluated at X_k. $H(X_k)$ is known as the Jacobian and can be expanded thus,

$$H(X_k) = \begin{bmatrix} \delta f_1/\delta x_1 & \delta f_1/\delta x_2 & \delta f_1/\delta x_n \\ \delta f_2/\delta x_1 & \delta f_2/\delta x_2 & \delta f_2/\delta x_n \\ . & . & . \\ . & . & . \\ \delta f_n/\delta x_1 & \delta f_n/\delta x_2 & \delta f_n/\delta x_n \end{bmatrix}_k$$

If equation A1.3) is rewritten thus,

$$E = X_k - X_{k+1} = F(X_k)\ H^{-1}(X_k) \qquad \text{A1.4)}$$

$$\text{then } H(X_k)\ E = F(x_k) \qquad \text{A1.5)}$$

which is now a system of linear equations which can be easily solved for E by standard procedures for matrix manipulation (e.g. Gaussian Elimination and Back Substitution [38]. Once E has been solved, then the vector of improved approximations X_{k+1} can easily be evaluated.

As in the 1 - dimensional case, the problem of evaluating the partial derivatives at each iteration arises. They can be approximated by a linear approximation, thus,

$$\left(\frac{\delta f_i}{\delta x_j}\right)_k = \left(\frac{f_i(x_j) - f_i(x_j + \Delta x_j)}{\Delta x_j}\right)_k \qquad \text{A1.6)}$$

where Δx_j is a small perturbation to the k^{th} approximation to x_j.

A criterion for acceptable convergence must be defined by the user. It is necessary to specify a realistic stopping criterion to avoid excessive iteration. An example might be,

$$\max \left| x_{i,k+1} - x_{i,k} \right| / x_{i,k} \leq \text{tol}$$

ensuring that the maximum absolute adjustment to any one of the variables is less than an acceptable tolerance.

When convergence has been satisfied, it is also advisable to calculate the vector of residuals F to ensure that each energy balance equation is satisfied to acceptable accuracy.

Since the partial derivatives in H are calculated according to the linear approximation (equation A1.6), it is possible to solve for any unknown variable provided n <u>independent</u> equations exist for n unknown variables and provided sensible initial guesses are made for these variables. In the zone energy balance formulation, some of the temperatures may be known (e.g. the load discharge temperature) and during solution these can be substituted by alternative unknown variables (e.g. fuel input rate, load throughput etc.). The

energy balance equations (if defined correctly) are a well behaved independent system of equations and no problems arise in defining H and H^{-1}. This method fails if the equations are inconsistent or not independent.

APPENDIX 2

Finite Difference Solution of Transient Conduction Problems

A method is required to predict the non-steady-state conduction into the hearth, insulating walls and the load in the transient furnace models. Due to the wide temperature range through which these materials pass in their normal heating from ambient conditions, and due to the large temperature gradients and heat fluxes that can arise, the temperature dependence of conductivity and specific heat must be taken into account in any calculation. Furthermore, the furnace walls and hearth may comprise of two or more layers of graded insulation of differing thermal properties (eg.ceramic fibre on brick).

Analytical solution of transient conduction problems are restricted to simple geometries with a constant temperature, constant flux or a convective boundary condition. The thermal properties of the material are also assumed to be invariant with temperature and position. The application of analytical solutions to conduction problems in furnaces and fuel fired plant is therefore limited. Numerical methods using finite difference approximation techniques or finite element modelling can be applied for solving both steady-state and transient 1-D and multidimensional conduction problems and these allow all of the features described above to be

simulated. Finite elements are widely applied to multi-dimensional modelling of heat flow in complex bodies. The majority of furnace walls and loads can be reasonably closely modelled assuming temperature variation in one dimension only with the material represented as an infinite slab or as a cylinder. For 1-D modelling, the finite difference technique is therefore preferable since it is simple to formulate and can be easily integrated with other models.

A subroutine to calculate the 1-D transient conduction through a plane multi-layer wall with temperature dependent thermal properties was therefore written for integration into TRZONE.

The 1-D transient conduction equation,

$$(C_p\rho)\ \frac{\delta T}{\delta t} = \frac{\delta}{\delta x}\left(\lambda\ \frac{\delta T}{\delta x}\right) \qquad \text{A2.1)}$$

is a parabolic partial differential equation in that it is defined in part by system boundary conditions and in part by an initial condition. Its solution by finite differencing is marched forward in discrete time steps from the initial condition. At each step however, solution is constrained by the boundary conditions. Steady-state problems give rise to elliptic partial differential equations which are constrained

by boundary conditions only, over the extremes of the region of integration. Because, for transient problems, the solution is marched forward in discrete time steps, different boundary conditions can be applied at each step and the thermal properties can be updated in accordance with their known temperature dependency. This method of solution is easily incorporated into mathematical models which simulate other time dependent variables and events (such as a change in firing rate or a discharge of load) which themselves produce step changes in the thermal boundary conditions.

A Finite Difference Formulation of a Plane Wall Transient

The first step in the finite difference formulation of equation A2.1) is to subdivide the x direction into nodes spaced Δx apart as shown in Figure A2.1 . As an approximation, the temperature of each node m is assumed to represent the temperature of a thin slice of thickness Δx surrounding the node (the shaded area in Figure A2.1). An energy balance about m can then be written in terms of the temperatures of the surrounding nodes m-1 and m+1. Considering a section of the wall of unit area (measured normal to the direction of heat flow), then:

$$(\rho C_p)\Delta x \frac{dT_m}{dt} = \frac{\lambda_m^-}{\Delta x}(T_{m-1}-T_m) - \frac{\lambda_m^+}{\Delta x}(T_m-T_{m+1}) \qquad \text{A2.2}$$

where λ_m^-, λ_m^+ are the conductivities of the solid evaluated at the mean temperatures of the adjacent nodes, i.e. $(T_m+T_{m-1})/2$ and $(T_m+T_{m+1})/2$ respectively. C_p is evaluated at the temperature T_m.

The partial differential equation A2.1) has been reduced to a set of ordinary differential equations, one for each node through the solid. The problem is further subdivided into equal time intervals Δt apart enabling the LHS of equation A2.2) to be rewritten, thus:

$$(\rho C_p)\Delta x \frac{dT_m}{dt} = (\rho C_p)\Delta x(T_m^1-T_m^o)/\Delta t \qquad \text{A2.3)}$$

where T_m^o and T_m^1 are the initial and final temperatures of node m over the time interval t to $t+\Delta t$.

If the derivatives in the RHS of equation A2.2) are written in terms of temperature at time t, then T_m^1 can be expressed explicitly as a function of all temperature at time t $(T^o_{m-1}, T^o_m\ T^o_{m+1})$. An explicit method of solution (the Euler method) is therefore achieved. It is however, more accurate to use the arithmetic mean of the derivatives at the beginning and the end of the time interval. This approach, known as the Crank-Nicolson solution [47], leads to a system of algebraic equations with all temperatures T^1 expressed implicitly.

Equation A2.2) then becomes,

$$(\rho C_p)\Delta x(T_m^1-T_m^o) = \frac{\Delta t}{2\ \Delta x}\{\lambda_m^-(T_{m-1}^1-T_m^1)-\lambda_m^+(T_m^1-T_{m+1}^1)$$

$$+\lambda_m^-(T_{m-1}^o-T_m^o) - \lambda_m^+(T_m^o-T_{m+1}^o)\}$$

All thermal properties are evaluated at the initial temperatures. Provided the time steps are sufficiently small that the temperature rise $(T_m^1-T_m^o)$ does not significantly affect conductivity at m, then this simplification in the finite difference equation is valid. The variation of λ with position is however included since large spatial temperature gradients can exist during transient heating.

Defining the parameters,

$$K_m^- = \frac{\Delta t\lambda_m^-}{2\Delta x} \qquad K_m^+ = \frac{\Delta t\lambda_m^+}{2\Delta x} \qquad \alpha_m = \rho\Delta x(C_p(T_m^o)$$

where $C_p(T_m^o)$ is the specific heat at temperature T_m^o .

Then,

$$\alpha_m(T_m^1-T_m^o) = K_m^-(T_{m-1}^1-T_m^1) - K_m^+(T_m^1-T_{m+1}^1)$$
$$+ K_m^-(T_{m-1}^o-T_m^o) - K_m^+(T_m^o-T_{m+1}^o) \qquad \text{A2.5)}$$

Rearranging with all T^1 terms on the LHS and all T^o terms on the RHS,

$$T_{m-1}{}^1(-K_m^-) + T_m{}^1(\alpha_m+K_m^-+K_m^+) + T_{m+1}{}^1(-K_m^+) =$$
$$T_{m-1}{}^o(K_m^-) + T_m{}^0(\alpha_m-K_m^--K_m^+) + T_{m+1}{}^o(K_m^+) \qquad \text{A2.6)}$$

Equation A2.6) gives the finite difference formulation for an internal point within a homogeneous material. Although the derivatives are evaluated at the mean of the initial and final temperatures, the properties are evaluated at a representative average temperature at time t . ie. K_m^- is evaluated with conductivity λ at a temperature $(T_{m-1}{}^o+T_m{}^o)/2$, and α_m with C_p at a temperature $T_m{}^o$. It is possible to evaluate properties at the mean of the initial and final temperatures in each case but additional numerical iteration becomes necessary at each time step. The proposed method is considered acceptable provided the time steps and temperature changes at each time step are not too large.

Finite difference equations can similarly be derived for the surface nodes incorporating the specified boundary conditions, and also for the node representing the interface between two different materials.

Hot face boundary

A constant flux $\dot{q}$ at the hot face boundary is assumed. If this flux is applied at m=1 for the duration of the time step Δt then a finite difference form of the hot face boundary condition can be derived by considering an energy balance on the slice of thickness $\Delta x/2$ adjacent to the surface (see Figure A2.2). Again, applying the mean of the derivatives at times t and $t+\Delta t$, the following finite difference equation for this slice can be written,

$$(\rho C_p)\frac{\Delta x}{2}(T_{0.5}^{1}-T_{0.5}^{o}) = \Delta t\left(\dot{q} - \frac{\lambda_1^{+}}{2\Delta x}(T_1^{1}-T_2^{1}) - \frac{\lambda_1^{+}}{2\Delta x}(T_1^{o}-T_2^{o})\right) \qquad A2.7)$$

Letting, $K_1^{+} = \dfrac{\Delta t \lambda_1^{+}}{2\Delta x}$ and $\alpha_1 = \dfrac{\rho \Delta x C_p(T_{0.5}^{0})}{2}$

then,

$$\alpha_1(T_{0.5}^{1}-T_{0.5}^{o}) = \dot{q}\Delta t - K_1^{+}(T_1^{1}-T_2^{1}) - K_1^{+}(T_1^{o}-T_2^{o}) \qquad A2.8)$$

Assuming a linear temperature variation between nodes 1 and 2, then the representative temperature of this slice is given by,

$$T_{0.5} = .75T_1 + .25T_2 \qquad A2.9)$$

Substituting T_1 and T_2 for $T_{0.5}$ and rearranging all T^1 terms on the LHS,

$$T_1^1(0.75\alpha_1+K_1^+) + T_2^1(0.25\alpha_1-K_1^+)$$
$$= \dot{q}\Delta t + T_1^o(0.75\alpha_1-K_1^+) + T_2^o(0.25\alpha_1+K_1^+) \qquad A2.10)$$

Although $\dot{q}$ is considered constant in the above equation, it can be varied from time step to time step enabling time dependent boundary conditions to be simulated.

Cold face boundary

It is assumed that heat transfer by convection occurs at the cold face node m = L at a rate equal to $h(T_L^o-T_\infty)$ where h is the convection coefficient (assumed constant over the duration of each time step), and T_∞ is the surrounding fluid temperature. Applying the same reasoning as for the hot face boundary, the following finite difference equation at L can be written.

$$\alpha_L(.75T_L^1+.25T_{L-1}^1-.75T_L^o-.25T_{L-1}^o) = K_L^-(T_{L-1}^1-T_L^1)$$
$$+ K_L^-(T_{L-1}^o-T_L^o) - h(.5T_L^1+.5T_L^0-T_\infty)\Delta t \qquad A2.11)$$

where, $K_L^- = \dfrac{\Delta t\lambda_L^-}{2\Delta x}$ and $\alpha_L = \dfrac{\rho\Delta x c_p(T_{0.5}^o)}{2}$

and, $T_{0.5}^{o} = .75\ T_L^{o} + .25\ T_{L-1}^{o}$

Rearranging,

$$T_{L-1}^{1}(0.25\alpha_L - K_L^{-}) + T_L^{1}(0.75\alpha_L + K_L^{-} + .5h\Delta t) =$$

$$T_{L-1}^{o}(0.25\alpha_L + K_L^{-}) + T_L^{o}(0.75\alpha_L - K_L^{-} - .5h\Delta t) + h\Delta t T_\infty \qquad \text{A2.12)}$$

Interface between two layers

Consider the node i at the interface between two different materials 1 and 2 as shown in Figure A2.3 , with finite difference steps $(\Delta x)_1$ and $(\Delta x)_2$ in the two materials. The finite difference equation around point i can be written,

$$\left(\frac{\Delta x}{2}\rho C_p(T_{0.5}^{1} - T_{0.5}^{o})\right)_{\text{layer1}} + \left(\frac{\Delta x}{2}\rho C_p(T_{0.5}^{1} - T_{0.5}^{o})\right)_{\text{layer 2}} =$$

$$\Delta t\left(\frac{.5\lambda_i^{-}}{\Delta x_1}(T_{i-1}^{1} - T_i^{1} + T_{i-1}^{o} - T_i^{o}) - \frac{.5\lambda_i^{+}}{\Delta x_2}(T_i^{1} - T_{i+1}^{1} + T_i^{o} - T_{i+1}^{o})\right)$$

A2.13)

Let, $K_i^{-} = \dfrac{\Delta t \lambda_i^{-}}{2\ \Delta x_1}$ $\qquad K_i^{+} = \dfrac{\Delta t \lambda_i^{+}}{2\ \Delta x_2}$

and, $\alpha_1 = [\rho \Delta x C_p(T_{0.5}^{o})]_{\text{layer1}}/2$

$\alpha_2 = [\rho \Delta x C_p(T_{0.5}^{o})]_{\text{layer2}}/2$

and let, $[T_{0.5}]_{\text{layer 1}} = .75T_i + .25T_{i-1}$

and, $[T_{0.5}]_{\text{layer 2}} = .75T_i + .25T_{i+1}$

Substitution for $T_{0.5}$ into equation 2.13) and rearranging gives,

$$T_{i-1}^{1}(.25\alpha_1 - K_i^-) + T_i^{1}(.75(\alpha_1+\alpha_2) + K_i^- + K_i^+) + T_{i+1}^{1}(.25\alpha_2 - K_i^+)$$
$$= T_{i-1}^{o}(K_i^- + .25\alpha_1) - T_i^{o}(K_i^- + K_i^+ - .75(\alpha_1+\alpha_2)) + T_{i+1}^{o}(K_i^+ + .25\alpha_2) \quad \text{A2.14)}$$

Solution of the finite difference equations

The algebraic equations (A2.6), (A2.10), (A2.12) and (A2.14) are all expressed in the following general form,

$$a_{i-1,i}T_{i-1}^{1} + a_{i,i}T_i^{1} + a_{i+1,i}T_{i+1}^{1} = d_i$$

where d_i is a function of temperature T^o

For all points i = 1 to L, the following tri - diagonal matrix equation can be written:

$$\begin{bmatrix} a_{11} & a_{21} & 0 & 0 & \cdots \\ a_{12} & a_{22} & a_{32} & 0 & \cdots \\ 0 & a_{23} & a_{33} & a_{43} & \cdots \\ 0 & 0 & \cdots & \cdots & \cdots \\ : & : & & & \\ : & : & & & \end{bmatrix} \cdot \begin{bmatrix} T_1{}^1 \\ T_2{}^1 \\ T_3{}^1 \\ : \\ : \\ : \end{bmatrix} = \begin{bmatrix} d_1{}^1 \\ d_2{}^1 \\ d_3{}^1 \\ : \\ : \\ d_L{}^1 \end{bmatrix}$$

or in short hand notation,

$$\mathbf{A}.\mathbf{T}^1 = \mathbf{D} \qquad \text{A2.7)}$$

A is a tri-diagonal matrix because the temperature at any node depends only on the temperatures at its two adjacent nodes. The Gaussian elimination technique with back substitution can be used to solve this set of simultaneous equations in T^1[38].

Choice of Δt and Δx

It is to be expected that if smaller time steps are assumed in the finite difference technique, then closer agreement with the exact solution will be achieved. In practice, in order to reduce computing time, one usually tries to select as large a time step as possible. Large time steps however, can introduce some unwanted numerically induced oscillations. The selection of Δt and Δx is discussed by Myers [48], for the fully explicit and for the Crank-Nicolson methods of solution of a 1-D transient problem with a step change in temperature

on one face and the other face fully insulated. The following criteria for stability are derived,

The explicit (Euler) method $$\frac{\overline{\Delta t}}{\overline{\Delta x}} < 0.5$$

The Crank-Nicolson method $$\frac{\overline{\Delta t}}{\overline{\Delta x}} < 1.0$$

where, $$\overline{\Delta t} = \left(\frac{\lambda}{\rho C_p}\right) \frac{\Delta t}{L^2} \quad \text{and} \quad \overline{\Delta x} = \frac{\Delta x}{L}$$

and L is the radius or semi-thickness of the system.

Although the Crank-Nicolson method is more stable than the Euler method, the wrong selection of Δt and Δx can lead to stable oscillations that merely cause error in the calculated temperatures rather than an abortive failure of the solution. When the Euler method fails, it usually produces unstable oscillations.

The above stability criteria will differ according to the boundary conditions. For example a more restrictive criterion applies to the Euler method if a convective boundary condition is imposed. In practice it is advisable to repeat any finite difference solution at an alternative time step in order to test for numerical accuracy.

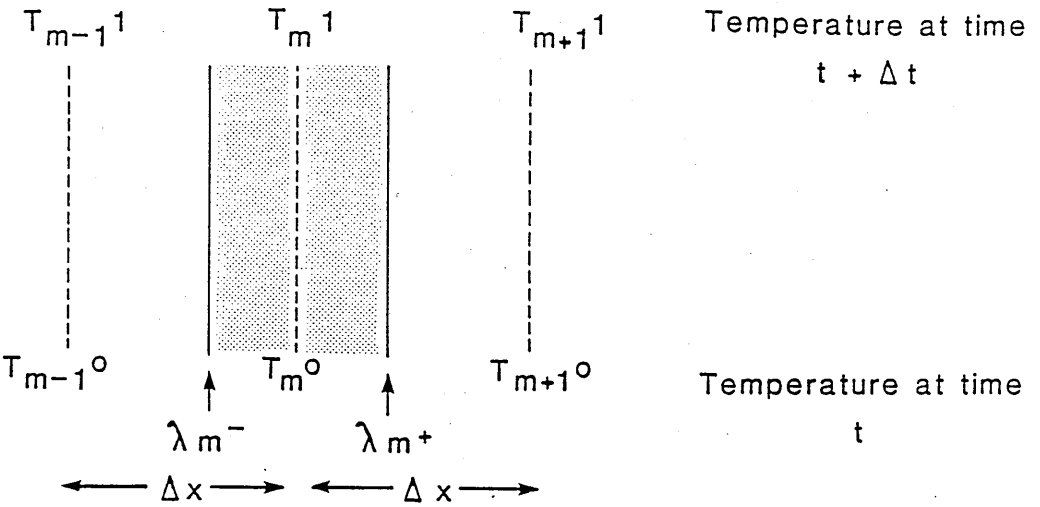

FIG. A2.1 HEAT BALANCE ON AN INTERNAL POINT m

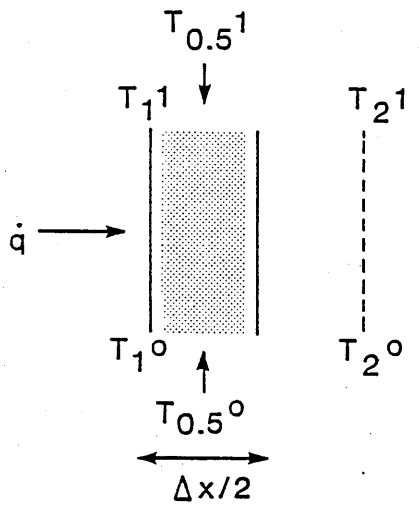

FIG. A2.2 HEAT BALANCE ON THE HOT FACE BOUNDARY

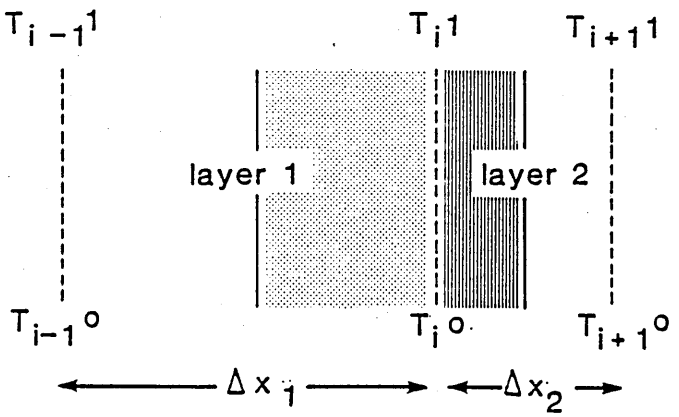

FIG. A2.3 HEAT BALANCE AT THE INTERFACE BETWEEN TWO LAYERS

APPENDIX 3

Direct Exchange Areas Between Cubic Volume and/or Square Surfaces in a Rectangular Framework

Exchange areas for cubes and/or squares in close proximity to each other and for values of KB up to 1.4 have been published in graphical form by Hottel and Cohen [21]. In all multiple grey gas models for combustion product emissivity or absorptivity, K for the highest absorptivity grey gas component can often exceed 20 m^{-1} thereby limiting the range of application of the above graphs to cubes or squares of maximum linear dimension (B_{max}) of 0.07 m. Furthermore, Becker [49] identified minor inaccuracies in the graphs for some of the configurations. For the purposes of this study therefore, new data for cubes and/or squares were generated covering a wider range of KB from zero up to 18 (B_{max} = 0.9m). The data are also expressed in the form of simple exponential correlations which can be easily implemented into a computer file or subroutine [32].

Numerical integration of the multiple integrals describing surface-surface, gas-surface and gas-gas direct exchange areas (equations 3.8, 3.13 and 3.15) was carried out using a modified form of Simpson's rule. An example of the method is described in Appendix 4 for gas-gas exchange area

calculation. The data are presented graphically in Figures A3.1 to A3.5 and as simple correlations in Tables A3.1 to A3.4, where:

K = the attenuation or extinction coefficient of the gas
= $k_g p$ m^{-1}

B = the cube or square side, m

A = B^2

V = B^3

The exchange areas are presented in normalised form as follows:

1. Gas-gas exchange areas are normalised by $KB(\overline{gs})_b$ where $(\overline{gs})_b$ is the exchange area between a cube of gas and its six bounding surfaces.

2. $(\overline{gs})_b$ is presented graphically in Figure A3.1, and is normalised by the unit emittance 4KV in 4π steradians of solid angle about the cube of volume V.

3. Gas-surface exchange areas are normalised by $(\overline{gs})_b$.

4. Surface-surface exchange areas are normalised by B^2.

The exponential correlation given in Tables A3.1-A3.4 are best fit expressions. For most zone pairs, acceptable accuracy is provided by a correlation of the form,

$$\phi = C \exp(-A.KB)$$

where C is the intercept at KB = 0 and A the slope of the function ϕ on a log-linear plot against KB. For closely spaced zone pairs, some of the curves are non-linear and the coefficient A in these cases is expressed as a polynomials expression in KB. This non-linearity is not evident in the charts of Hottel and Cohen [21].

The correlations have been implemented into DATA statements in the subroutines SSDEX, GSDEX and GGDEX (see Chapter 8) where they are applied to carry out the coarse integrations to yield exchange areas between rectangular zones in SSZONE and TRZONE.

Verification of the Integration Techniques

The surface-surface exchange areas with KB = 0 can be compared to view factors for which exact values can be derived by analytical techniques. This comparison provides a level of verification of the numerical integration technique. It has been applied to assess the accuracy of the exchange areas

between mutually perpendicular square surface zones, and in particular those closely configured zones with a common side or corner. Errors in the numerical integration technique will be higher for the closely configured zones.

The analytical formulae for mutually perpendicular and displaced squares are given below with reference to the numbering convention in Figure A3.6.

$$A_{10}F_{10-3} = (\overline{s_{10}s_3})_{k=0}$$

$$= (A_3+A_6)\left(F_{(3+6)-(10+11)}-F_{(3+6)-11}\right) - A_6\left(F_{6-(10+11)}-F_{6-11}\right)$$

where F_{i-j} is the view factor between surfaces i and j.

The view factors in this equation are expanded to the following expressions:

$$F_{(3+6)-(10+11)} = \frac{A_{10}+A_{11}}{A_3+A_6} \cdot F_{(10+11)-(3+6)}$$

$$= \frac{A_{10}+A_{11}}{A_3+A_6} \left\{ \frac{A_3+A_6}{A_{10}+A_{11}} \left(\frac{1}{2(A_3+A_6)} \right. \right.$$

$$\left[(A_7+A_8+A_9+A_{10}+A_{11}+A_{12}) \cdot F_{(7+8+9+10+11+12)-(1+2+3+4+5+6)} \right.$$

$$- (A_3+A_6) \cdot F_{(3+6)-(9+12)}$$

$$- (A_1+A_2+A_4+A_5) \cdot F_{(1+2+4+5)-(7+8+10+11)}$$

$$- (A_7+A_8+A_9) \cdot F_{(7+8+9)-(1+2+3+4+5+6)}$$

$$+ (A_3+A_6) \cdot F_{(3+6)-9}$$

$$\left. \left. + (A_1+A_2+A_4+A_5) \cdot F_{(1+2+4+5)-(7+8)} \right] \right) \right\}$$

$$F_{(3+6)-11} = \frac{A_{11}}{A_3+A_6} \cdot F_{11-(3+6)}$$

$$= \frac{A_{11}}{A_3+A_6} \left\{ \frac{A_3+A_6}{A_{11}} \left(\frac{1}{2(A_3+A_6)} \right. \right.$$

$$\left[(A_8+A_9+A_{10}+A_{12}) \cdot F_{(8+9+11+12)-(2+3+5+6)} \right.$$

$$- (A_3+A_6) \cdot F_{(3+6)-(9+12)} - (A_2+A_5) \cdot F_{(2+5)-(8+11)}$$

$$- (A_8+A_9) \cdot F_{8+9-2+3+5+6} + (A_3+A_6) \cdot F_{(3+6)-9}$$

$$\left. \left. + (A_2+A_5) \cdot F_{(2+5)-8} \right] \right) \right\}$$

$$F_{6-(10+11)} = \frac{A_{10}+A_{11}}{A_6} \cdot F_{(10+11)-6}$$

$$= \frac{A_{10}+A_{11}}{A_6} \left\{ \frac{A_6}{A_{10}+A_{11}} \left(\frac{1}{2A_6} \right. \right.$$

$$\left[(A_7+A_8+A_9+A_{10}+A_{11}+A_{12}) \cdot F_{7+8+9+10+11+12-4+5+6} \right.$$
$$- A_6F_{6-(9+12)} - (A_4+A_5) \cdot F_{(4+5)-(7+8+10+11)}$$
$$\left. \left. - (A_7+A_8+A_9) \cdot F_{7+8+9-4+5+6} + A_6F_{6-9} + (A_4+A_5) \cdot F_{4+5-7+8} \right] \right) \Bigg\}$$

$$F_{6-11} = \frac{A_{11}}{A_6} \cdot F_{11-6}$$

$$= \frac{A_{11}}{A_6} \left\{ \frac{A_6}{A_{11}} \left(\frac{1}{2A_6} \right. \right.$$

$$\left[(A_8+A_9+A_{11}+A_{12}) \cdot F_{(8+9+11+12)-(5+6)} \right.$$
$$- A_6F_{6-9+12}$$
$$- A_5F_{5-(8+11)}$$
$$\left. - (A_8+A_9) \cdot F_{8+9-5+6} + A_6F_{6-9} + A_5F_{5-8} \right] \Bigg) \Bigg\}$$

These expressions contain view factors between perpendicular surfaces with a common side and which can all be calculated by use of the expression given in Figure A3.7 [33]. A programme was written to evaluate the view factor between the general pair of mutually perpendicular surfaces of unit area in Figure A3.6. The results are given in Table A3.5 to six decimal places and are compared to the values derived by numerical integration which is shown to be accurate to 4 decimal places.

The exchange area between a cubic gas zone and its bounding surfaces $(\overline{gs})_b$ has been computed for increasing values of n (the integration step, see Figure A4.1, Appendix 4) to check the convergence of $(\overline{gs})_b/4KB^3$ to unit value at KB = 0.0. The results are given in Table A3.6, and confirm that convergence to within 0.5% is achieved with n = 170 although the rate of convergence is slow.

The sensitivity of $(\overline{gs})_b/4KB^3$ to n for finite values of KB has also been checked. The results given in Table A3.7 indicate that numerical error increases as KB increases. This is to be expected since exchange between contiguous elements in the integration is more significant as KB increases.

The above checks verify that the numerical integration technique is accurate provided a sufficient number (n) of integration steps are selected. The checks have been made on configurations where closely spaced elements in the integration are likely to be significant and where consequential errors are therefore likely to be highest. Fuller verification of the numerical integration techniques is demonstrated in Chapter 10 where exchange area sum rule checks are presented for arrays of computed exchange areas in a simple surface geometry.

Table A3.1 **Correlation coefficients for direct exchange areas between parallel square surfaces.**

$$\overline{ss}/B^2 = C \exp(-A.KB)$$

X/B	Y/B	Z/B	C	A	X/B	Y/B	Z/B	C	A
1	1	1	.1998	1.1053	1	1	4	.0191	4.0396
2	1	1	.0861	1.3014	2	1	4	.0171	4.1475
3	1	1	.0153	1.9987	3	1	4	.0126	4.4615
4	1	1	.0036	2.9351	4	1	4	.0082	4.9529
2	2	1	.0433	1.5172	2	2	4	.0153	4.2538
3	2	1	.0105	2.1959	3	2	4	.0114	4.5627
4	2	1	.0029	3.0880	4	2	4	.0076	5.0464
3	3	1	.0045	2.7513	3	3	4	.0088	4.8569
4	3	1	.0018	3.5187	4	3	4	.0061	5.3190
4	4	1	.0009	4.1511	4	4	4	.0045	5.7494
1	1	2	.0686	2.0710	1	1	5	.0124	5.0322
2	1	2	.0481	2.2368	2	1	5	.0115	5.1224
3	1	2	.0206	2.7286	3	1	5	.0093	5.3863
4	1	2	.0080	3.4595	4	1	5	.0068	5.8053
2	2	2	.0351	2.4015	2	2	5	.0107	5.2114
3	2	2	.0164	2.8812	3	2	5	.0087	5.4720
4	2	2	.0068	3.5899	4	2	5	.0065	5.8861
3	3	2	.0093	3.3165	3	3	5	.0073	5.7232
4	3	2	.0046	3.9625	4	3	5	.0055	6.1231
4	4	2	.0027	4.5268	4	4	5	.0043	6.5018
1	1	3	.0330	3.0512	1	1	6	.0087	6.0271
2	1	3	.0274	3.1838	2	1	6	.0082	6.1042
3	1	3	.0168	3.5683	3	1	6	.0071	6.3310
4	1	3	.0090	4.1582	4	1	6	.0056	6.6951
2	2	3	.0230	3.3140	2	2	6	.0078	6.1805
3	2	3	.0146	3.6906	3	2	6	.0067	6.4052
4	2	3	.0081	4.2680	4	2	6	.0054	6.7658
3	3	3	.0101	4.0432	3	3	6	.0059	6.6235
4	3	3	.0061	4.5855	4	3	6	.0048	6.9744
4	4	3	.0040	5.0783	4	4	6	.0039	7.3105

Table A3.2 **Correlation coefficients for direct exchange areas between perpendicularly orientated square surfaces.**

$$\overline{ss}/B^2 = C \exp(-A.KB)$$

$$A = a_o+a_1(KB)+a_2(KB)^2+a_3(KB)^3+a_4(KB)^4$$

X/B	Y/B	Z/B	C	a_0	a_1	a_2	a_3	a_4
1	1	1	.2000	.5390	-.615E-01	.429E-02	-.151E-03	.206E-05
2	1	1	.0406	.9965	-.878E-1	.419E-02	-.773E-04	.000E+00
3	1	1	.0043	1.906				
1	2	1	.0328	1.571	-.391E-01	.208E-02	.000E+00	.000E+00
2	2	1	.0189	1.751				
3	2	1	.0059	2.384				
1	3	1	.0089	2.502				
2	3	1	.0069	2.665				
3	3	1	.0036	3.129				
1	2	2	.0329	2.055				
2	2	2	.0230	2.245				
3	2	2	.0101	2.780				
1	3	2	.0159	2.860				
2	3	2	.0129	3.010				
3	3	2	.0076	3.435				
1	3	3	.0124	3.481				
2	3	3	.0107	3.609				
3	3	3	.0073	3.976				

Table A3.3 **Correlation coefficients for direct exchange areas between cubic gas zones and square surface zones.**

$$\overline{gs}/(\overline{gs})_b = C \exp(-A.KB)$$

$$A = a_o + a_1(KB) + a_2(KB)^2$$

X/B	Y/B	Z/B	C	a_0	a_1	a_2
2	1	1	.0337	.4563	-.311E-01	.824E-03
3	1	1	.0048	1.457		
2	2	1	.0137	.8332	-.469E-01	.103E-02
3	2	1	.0034	1.674		
3	3	1	.0017	2.251		
1	1	2	.0313	1.062		
2	1	2	.0200	1.292		
3	1	2	.0078	1.933		
2	2	2	.0135	1.514		
3	2	2	.0062	2.089		
3	3	2	.0037	2.602		
1	1	3	.0120	2.033		
2	1	3	.0098	2.210		
3	1	3	.0060	2.666		
2	2	3	.0083	2.366		
3	2	3	.0053	2.806		
3	3	3	.0037	3.201		

Table A3.4 **Correlation coefficients for direct exchange areas between pairs of cubic gas zones.**

$$\overline{gs}/KB(\overline{gs})_b = C \exp(-A.KB)$$

$$A = a_o+a_1(KB)+a_2(KB)^2+a_3(KB)^3$$

X/B	Y/B	Z/B	C	a0	a1	a2	a3
2	1	1	.0949	.3784	-.331E-01	.174E-02	-.360E-04
3	1	1	.0203	1.430			
2	2	1	.0445	.8190	-.599E-01	.235E-02	-.347E-04
3	2	1	.0161	1.657			
3	3	1	.0099	2.263			
2	2	2	.0283	1.147	-.620E-01	.132E-02	.000E+00
3	2	2	.0132	1.866			
3	3	2	.0090	2.458			

Table A3.5

A verification of view factors between mutually perpendicular and displaced squares calculated by numerical integration.

Configuration (see Table A3.2)	Exact Value	Value by Numerical Integration
1 1 1	.200000	.2000
2 1 1	.040592	.0406
2 2 1	.018928	.0189
2 3 1	.006863	.0069
2 2 2	.023039	.0230
2 3 2	.012908	.0129
2 3 3	.010711	.0107
3 1 1	.004315	.0043
3 2 1	.005860	.0059
3 3 1	.003618	.0036
3 2 2	.010057	.0101
3 3 2	.007627	.0076
3 3 3	.007267	.0073

Table A3.6

The sensitivity of the numerical integration technique to step size for a cube (KB=0).

Integration step ,n :

30	50	70	90	110	130	170
$\{(\overline{gs})_b/4KB^3\}_{KB=0}$:						
1.02443	1.01450	1.01030	1.00799	1.00652	1.00551	1.00420

Table A3.7

The sensitivity of the numerical integration technique to step size for a cube with various values of KB.

(n = integration step)

	$(\overline{gs})_b/4KB^3$		% change
KB	n=100	n=150	
0.2	.92318	.92078	.26
0.5	.81594	.81356	.29
1.0	.67612	.673776	.35
2.0	.49206	.48975	.47
5.0	.25946	.25727	.84
10.0	.14417	.14216	1.39
18.0	.08546	.08367	2.09

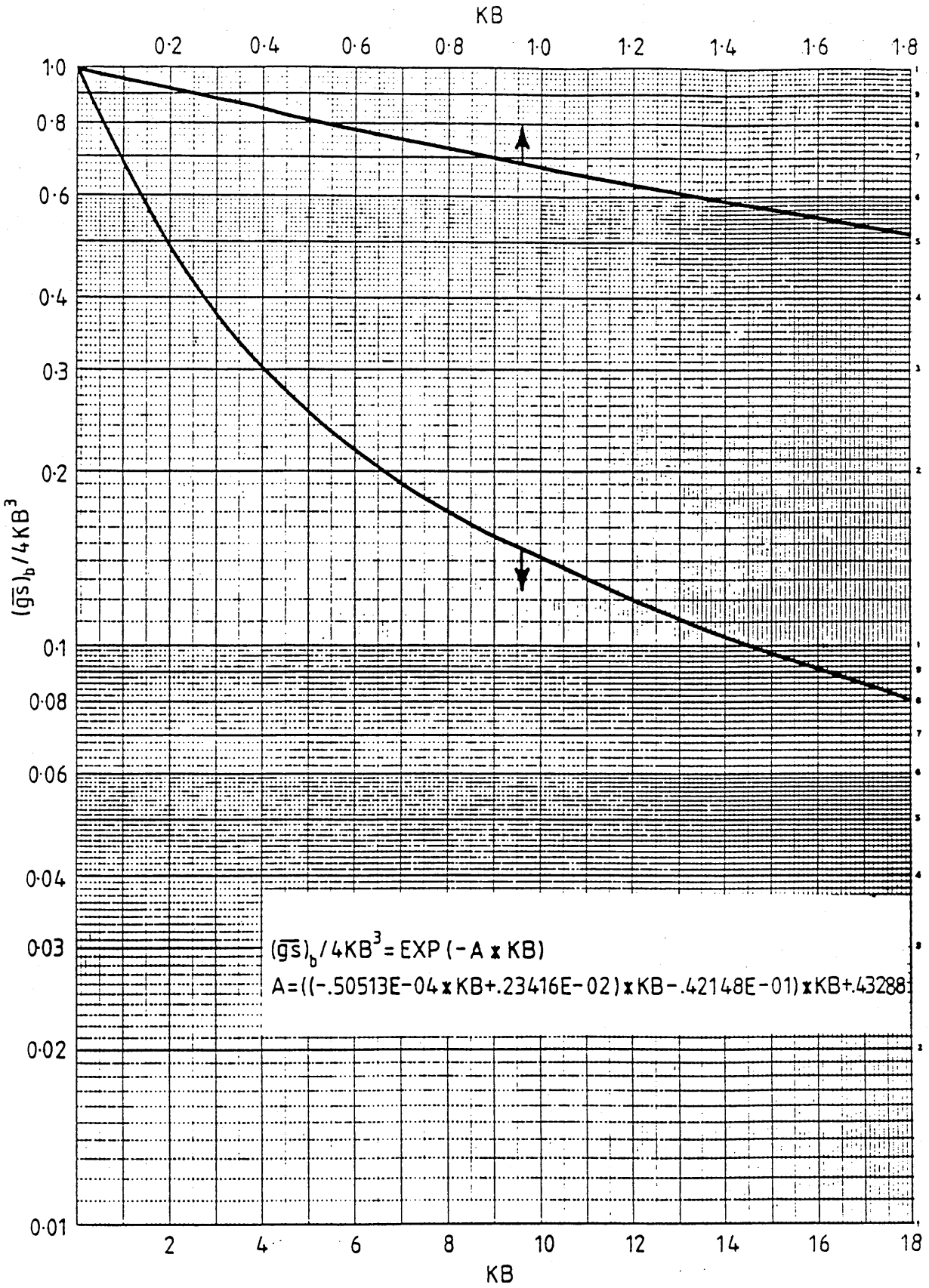

Figure A3.1 The exchange area $(\overline{gs})_b$ between a cube of edge B and its six bounding surfaces.

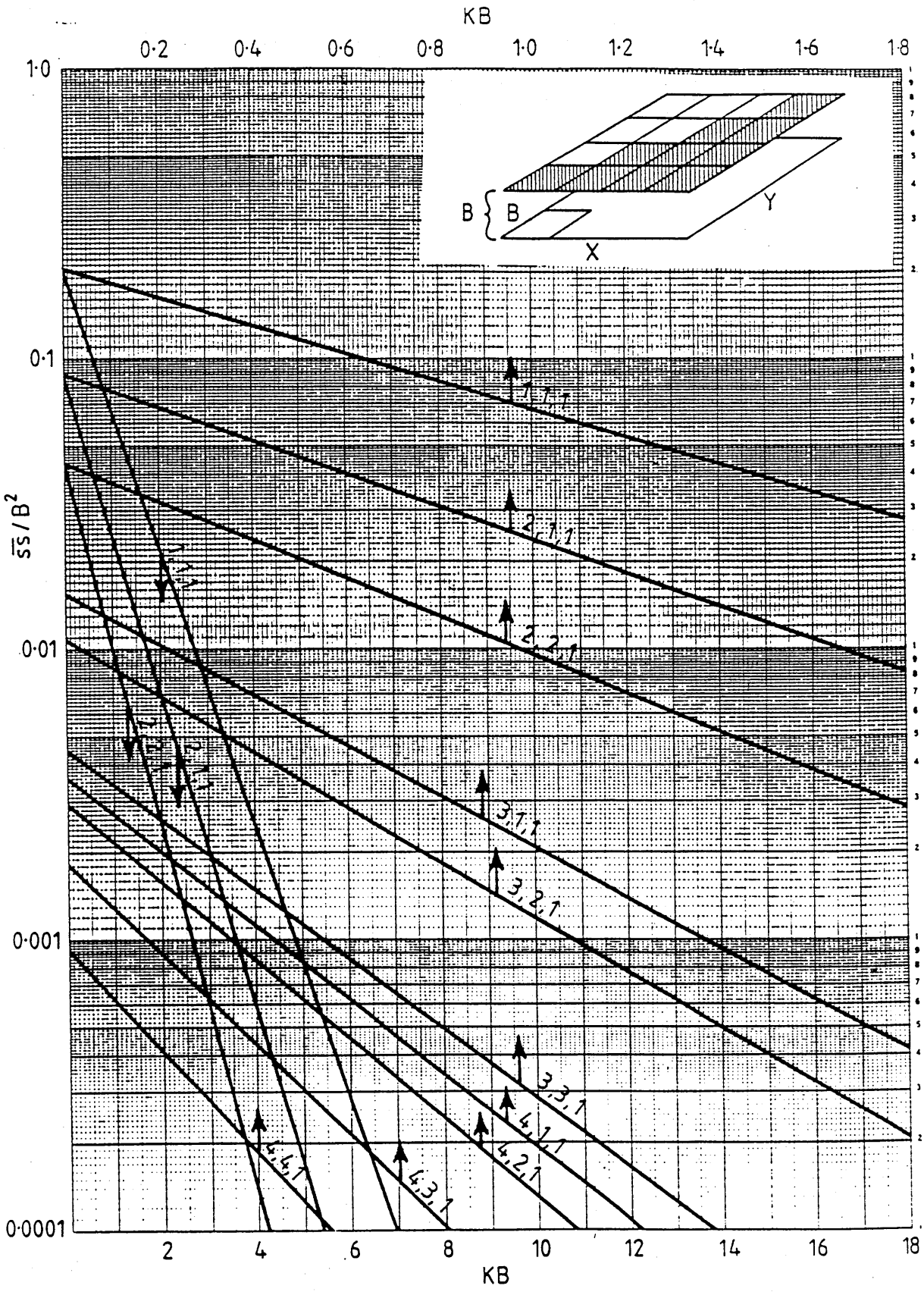

Figure A3.2 **Direct exchange areas between parallel square surfaces in close proximity** (numbers on curves are X/B, Y/B, Z/B where B=the square side).

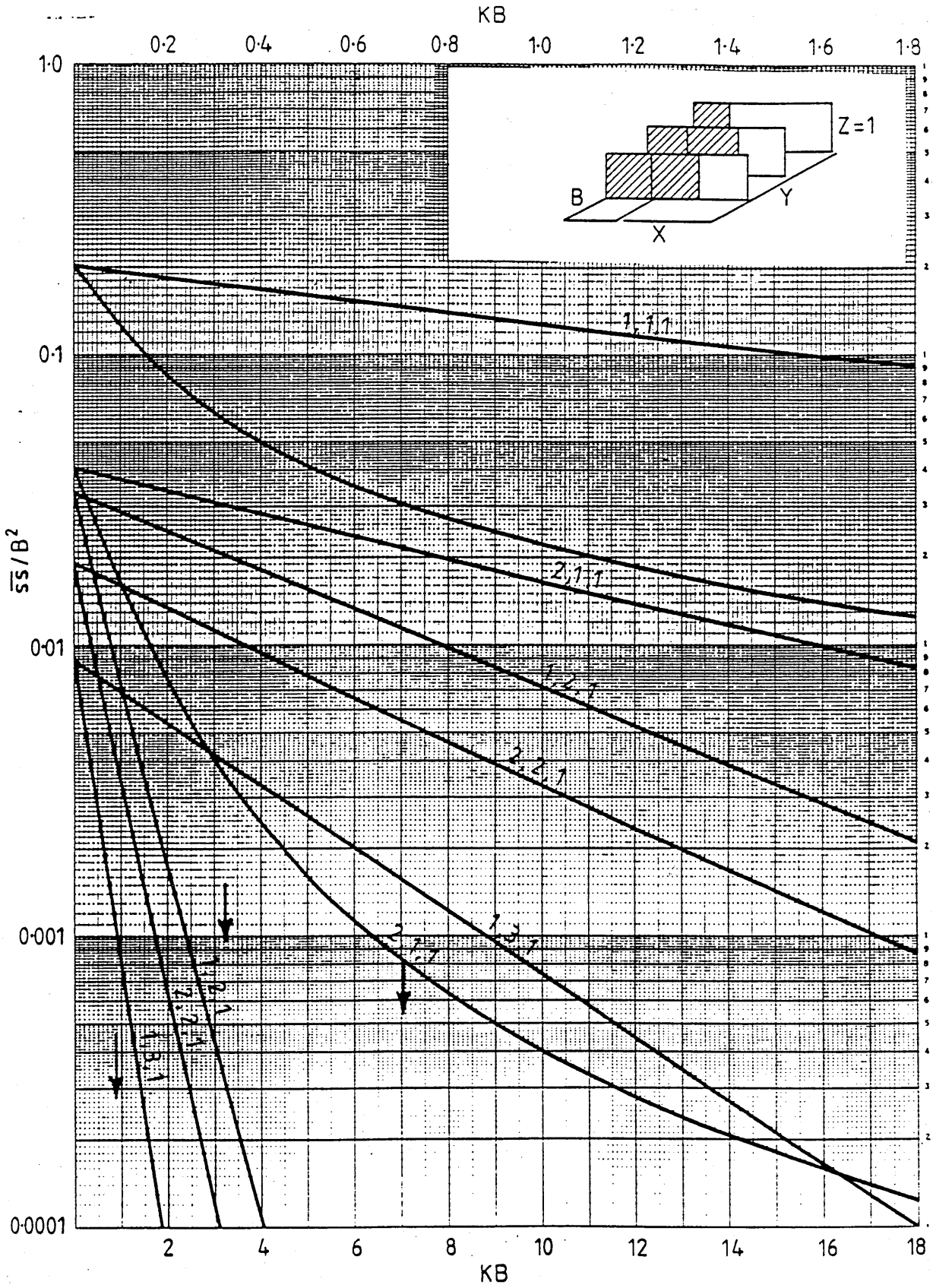

Figure A3.3 **Direct exchange areas between perpendicular square surfaces in close proximity** (numbers on curves are X/B,Y/B,Z/B where B=the square side).

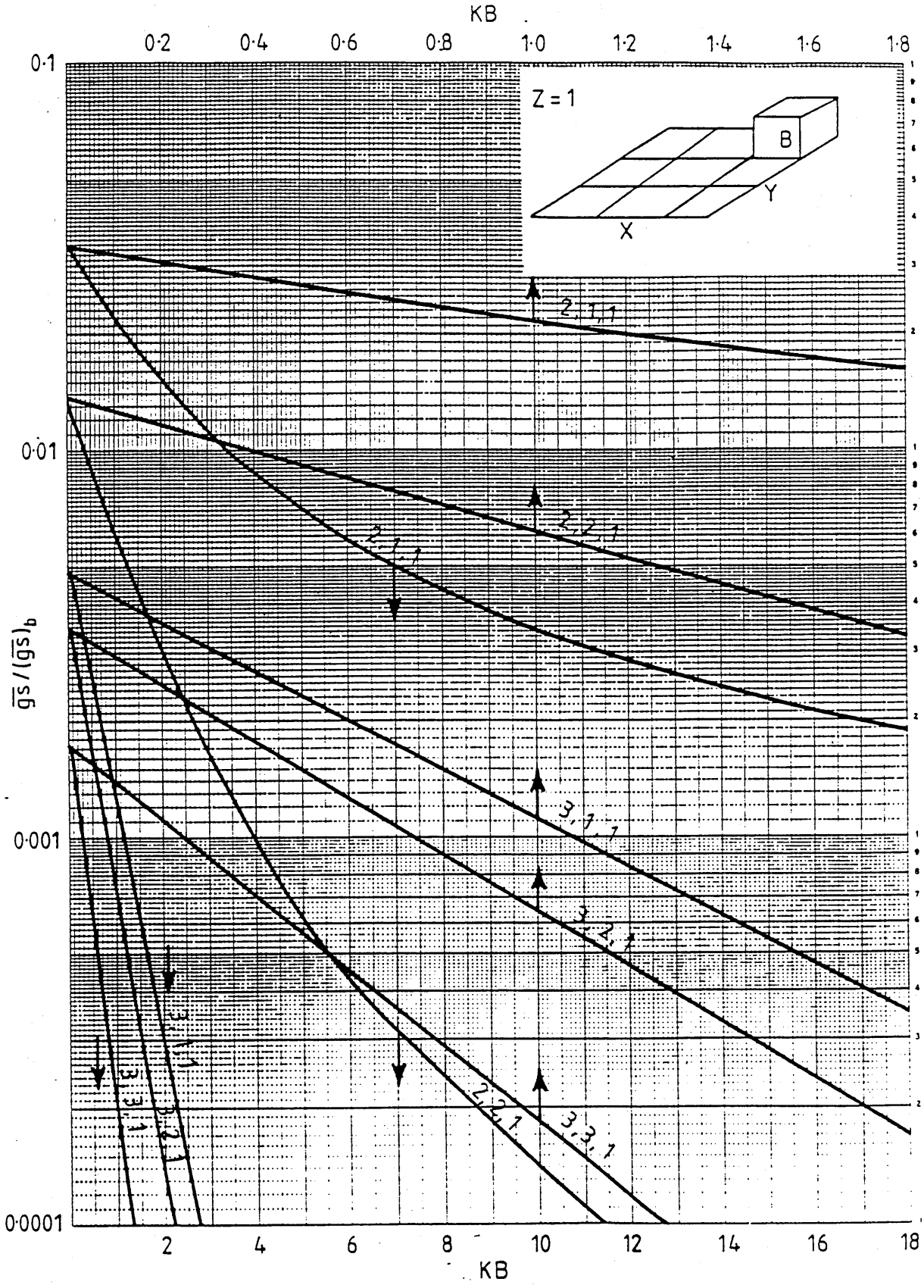

Figure A3.4 **Direct exchange areas between cubes and square surfaces in close proximity** (numbers on curves are X/B, Y/B, Z/B where B=the square side).

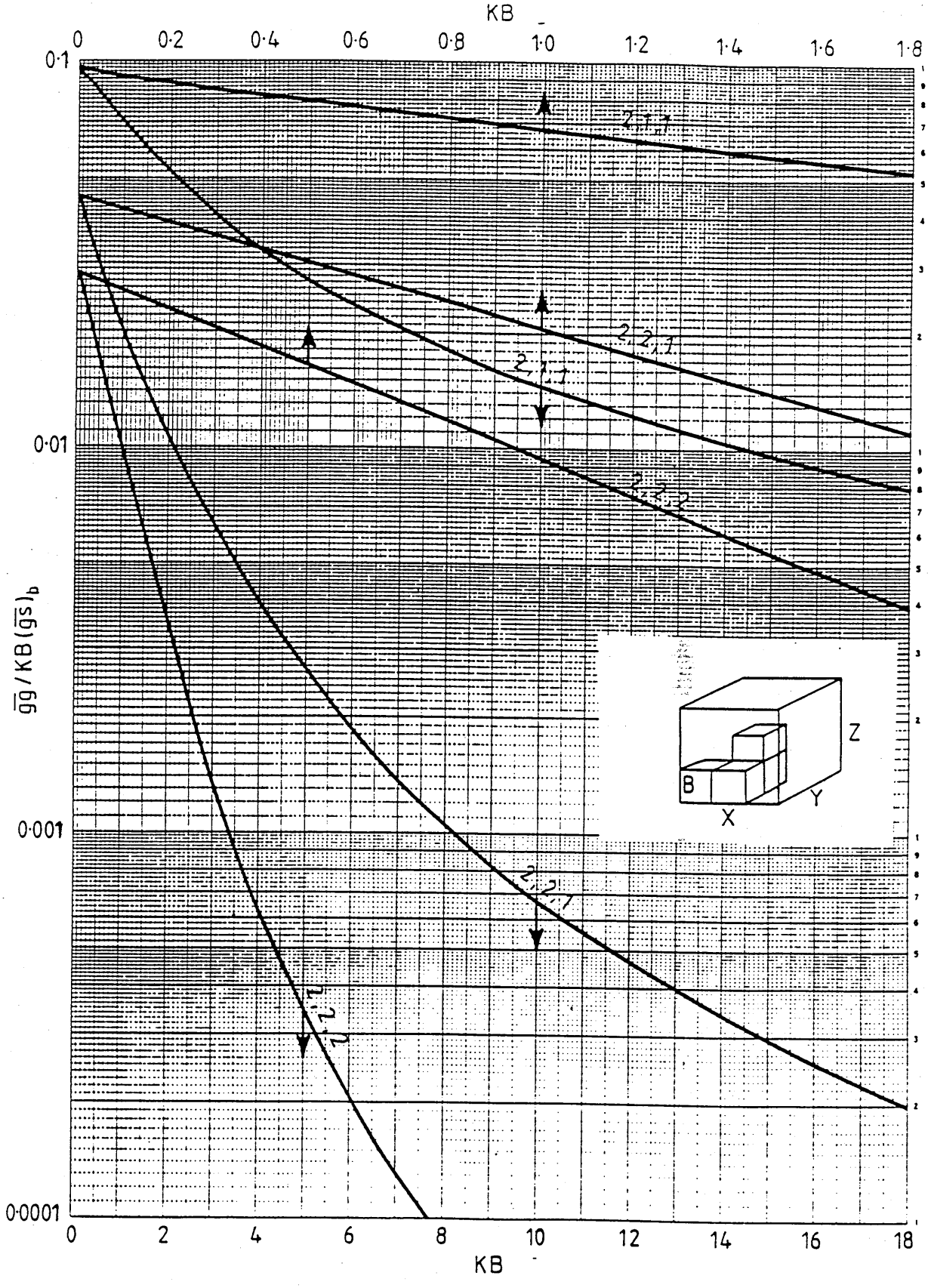

Figure A3.5 **Direct exchange areas between cubes in close proximity** (numbers on curves are X/B, Y/B, Z/B where B=the cube side).

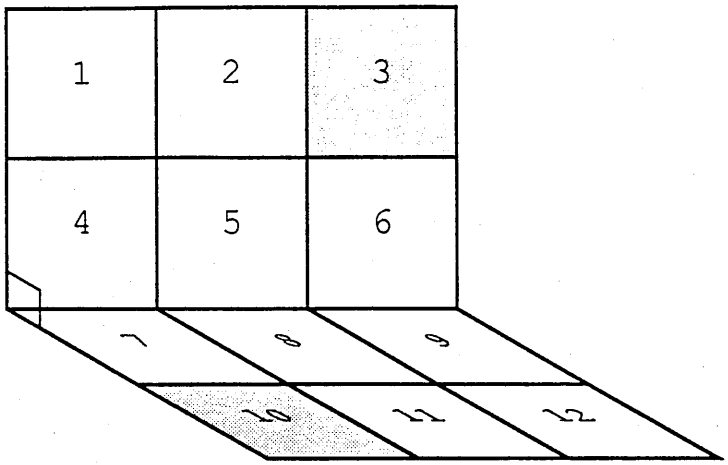

Figure A3.6 The numbering convention for the calculation of view factors between mutually perpendicular and displaced squares.

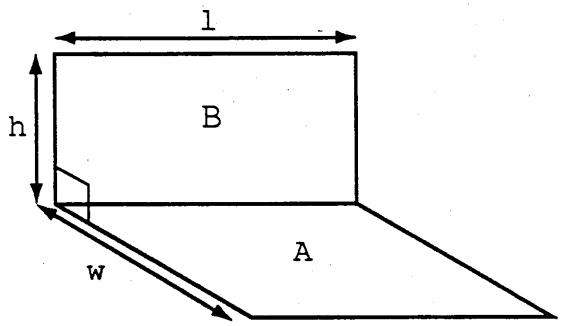

$$F_{A-B} = \frac{1}{\pi W}\left(W \tan^{-1}\frac{1}{W} + H \tan^{-1}\frac{1}{H} - \sqrt{(H^2+W^2)}\tan^{-1}\frac{1}{\sqrt{(H^2+W^2)}} \right.$$
$$\left. + \frac{1}{4}\ln\left\{ \left[\frac{(1+W^2)(1+H^2)}{(1+W^2+H^2)}\right] \left[\frac{W^2(1+W^2+H^2)}{(1+W^2)(W^2+H^2)}\right]^{W^2} \left[\frac{H^2(1+H^2+W^2)}{(1+H^2)(H^2+W^2)}\right]^{H^2} \right\} \right)$$

Figure A3.7 The view factor between mutually perpendicular rectangles having a common edge (H = h/l, W = w/l).

APPENDIX 4

The numerical evaluation of the multiple integral expression for cubical gas-gas direct exchange areas.

Consider a pair of cubical gas zones i and j of side B and separated as shown in Figure A4.1. If each zone is subdivided into n^3 incremental volume elements, the multiple integral for the gas-gas direct exchange area can be approximated by the following expression:

$$\overline{g_i g_j} = \frac{K^2}{\pi} \frac{B^6}{n} \sum_{X_i=1}^{n} \sum_{X_j=a}^{nN_X} \sum_{Y_i=1}^{n} \sum_{Y_j=b}^{nN_Y} \sum_{Z_i=1}^{n} \sum_{Z_j=c}^{nN_Z} \exp(-Kr)/r^2$$

where, $a = n(N_X-1)+1$; $b = n(N_Y-1)+1$; $c = n(N_Z-1)+1$

and $r = B/n\{(X_j-X_i)^2+(Y_j-Y_i)^2+(Z_j-Z_i)^2\}^{0.5}$

In this expression, the K^2 term is removed from the summation since it is assumed that the system has a uniform absorption coefficient.

At first inspection, a total of n^6 terms must be summed to derive $\overline{g_i g_j}$. However, many of these terms will be of identical

value to each other since many of the configurations of incremental elements will be repeated. By identifying the repeated configurations, the number of terms can easily be reduced to $(2n-1)^3$ terms. This is achieved by considering each zone as n slices in mutual exchange as shown in Figure A4.2.

The configuration of slices a and e (ae) is repeated in (bf), (cg) and (dh). Likewise (af) is repeated in (bg) and (ch). It is possible to complete the matrix of n^2 exchange areas for each slice pair by determining just (2n-1) terms since all terms on an upper left to lower right diagonal are identical. Thus, the exchange area between each cube can be computed from a summation of 2n-1 exchange areas between slices.

Similarly, the exchange area between any two slices (a and e for example) can be computed from a summation of 2n-1 terms for exchange between columns a′ to d′ and e′ to h′, and the exchange area between any two columns (a′ and e′ for example) can be computed from a summation of 2n-1 terms for exchange between elements a′′ to d′′ and e′′ to h′′. Thus, the overall problem is reduced to an evaluation of $(2n-1)^3$ terms.

The surface to surface integration can similarly be reduced to a summation of $(2n-1)^2$ terms and the volume to surface integration to $n(2n-1)^2$ terms.

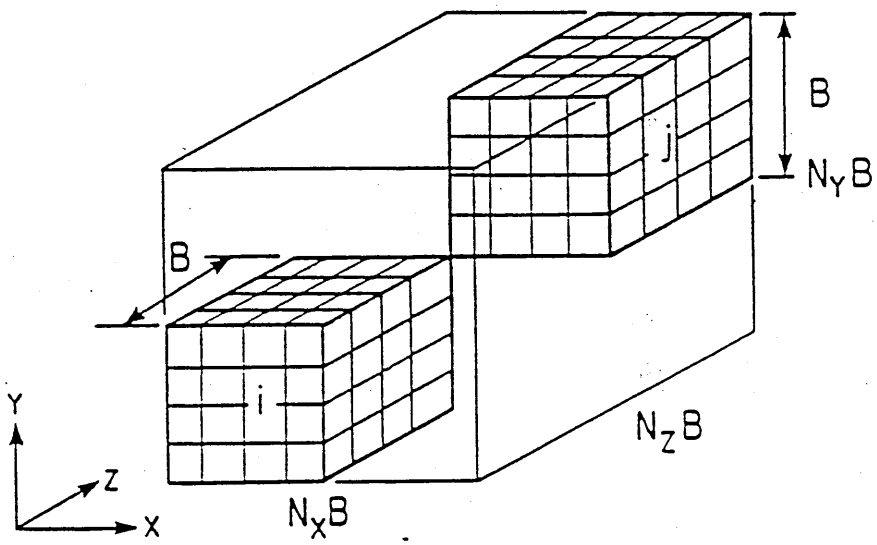

Figure A4.1 The arrangement of a pair of cubical gas zones and their subdivision into elements.

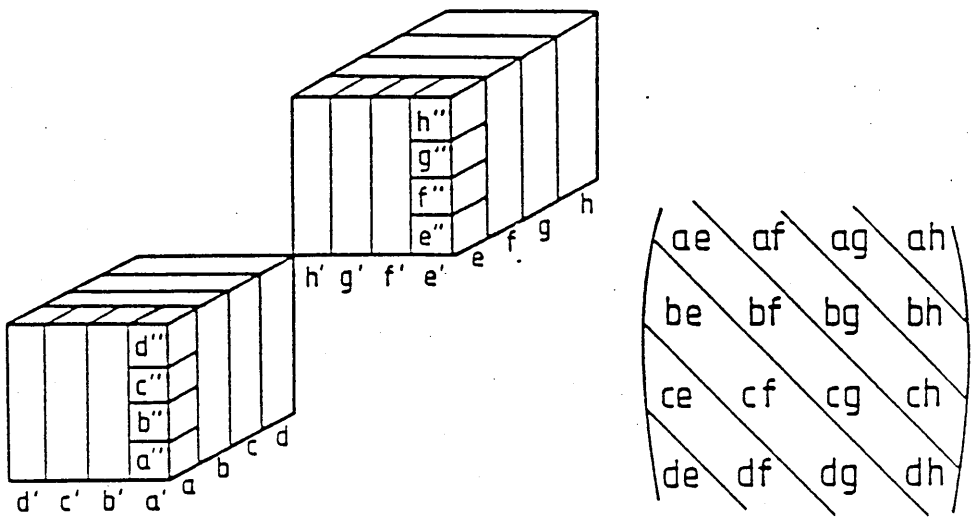

Figure A4.2 The identification of repeated element configurations in a pair of cubical gas zones by grouping elements into slices (a-h) and columns (a′-h′).

REFERENCES

1. R.Hardcastle, *The Pattern of Energy Use in the U.K. 1980*, No.2 Energy Efficiency Series, Published by the Energy Efficiency Office, D.o.E., HMSO, 1984.

2. *Energy Efficiency Demonstration Scheme - A Review*, No.1 Energy Efficiency series, Published by the Energy Efficiency Office, D.o.E., HMSO, 1984.

3. Pritchard R., Guy J.J., Conner N.E., *Industrial Gas Utilisation - Engineering Principles & Practice*, Bowker Publishing Company, 1977.

4. Trinks W., *Industrial Furnaces*, Vol.2, 4th. Edition, John Wiley & Sons, 1967.

5. Fricker N., Pomfret K., Waddington J., *Rapid heating in perspective*, Institute of Gas Engineers, Communication 1072, November, 1978.

6. M.H.Mawhinney, *Heat transfer in industrial heating furnaces*, Industrial Heating, Jan 1956, p54.

7. Trinks W., *Industrial Furnaces*, Vol.1, 4th. Edition, John Wiley & Sons, 1951.

8. Hottel H.C. and Egbert R.B., *The radiation of furnace gases*, Trans A.S.M.E., May 1941, p297-307.

9. Heisler M.P., *Temperature charts for induction and constant-temperature heating*, Trans.A.S.M.E., April, 1947, pp.227-236.

10. Viskanta R. and Menguc M.P., *Radiation heat transfer in combustion systems*, Prog.Energy Combustion Science, 1987, Vol 13, pp 97-160.

11. Hottel H.C. and Sarofim A.F., *Radiative Transfer*, McGraw-Hill, New York, 1967.

12. Beer J.M., *The significance of modelling*, Proc. 3rd. Symposium on Flames and Industry, ppB1-B8, The Institute of Fuel, 1967.

13. Hottel H.C., *Burning in laminar and turbulent fuel jets*, Proc.4th. Symposium (International) on Combustion, pp97-113, 1953.

14. Lucas D.M., *Prediction of the performance of rapid heating furnaces using physical and mathematical modelling techniques*, PhD Thesis, University of Aston in Birmingham, June 1971.

15. Khalil E.E., Spalding D.B., Whitelaw J.H., *The calculation of local flow properties in two-dimensional furnaces*, Int.J.Heat Mass Transfer, Vol 18, pp 775-791, 1975.

16. Khalil E.E., *Modelling of Furnaces and Combustors*, Abacus Press, 1982.

17. Siddal R.G., *Flux methods for the analysis of radiant heat transfer*, J.Inst.Fuel, June 1974, pp 101-109.

18. Lockwood F.C. and Shah N.G., 18th.Symposium (International) on Combustion, pp 1405-1414, The Combustion Institute, 1981.

19. Salter F.M. and Costick J.A., *Mathematical model of the heat transfer within a reheating furnace*, Proc. 4th. Symp. on Flames in Industry: Predictive Methods for Industrial Flames, Institute of Fuel, 1972.

20. Fitzgerald F. and Sheriden A.T., *Prediction of temperature and heat flux distribution in gas-fired pusher reheating furnaces*, Proc. 4th. Symp. on Flames in Industry: Predictive Methods for Industrial Flames, Institute of Fuel, 1972.

21. Hottel H.C. and Cohen E.S., *Radiant heat exchange in a gas-filled enclosure*, AIChE J.Heat Transfer, Vol 4, March 1958, p3.

22. Saimbi M.S. and Tucker R.J., *Mathematical modelling of the thermal performance of furnaces operating under non-steady-state conditions*, Proc. International Gas Research Conference, 1983 (British Gas Midlands Research Station report MRS E407).

23. Klima R., Kuck A., Sucke D., *A simple mathematical model for heat transfer and its application for continuous type reheating furnaces*, Gas Warme International, 32, No.4, pp138-145, 1983.

24. Lucas D.M., Masters J., Toth H.E., *Prediction of the performance of rapid heating furnaces*, Inst.Gas Engineers, Research Communication GC 151, Nov 1968, British Gas Midlands Research Station Report MRS E123.

25. Lucas D.M. and Barber A.J., *Transient thermal response of rapid heating furnaces*, J.Iron and Steel Inst., October 1971, pp790-796.

26. Noble J.J., *The zone method: Explicit matrix relations for total exchange areas*, Int.J.Heat Mass Transfer, Vol 18, pp 261-269, 1975.

27. Taylor P.B. and Foster P.J., *The total emissivities of luminous and non-luminous flames*, Int.J.Heat and Mass Transfer, Vol.17, pp1591-1605, 1974.

28. Truelove J.S., *A mixed grey gas model for flame radiation*, United Kingdom Atomic energy Authority Report, AERE-R-8494, Harwell, 1976.

29. McAdams W.H., *Heat Transmission*, 3rd.Ed , McGraw-Hill, New York, 1954.

30. Rhine J.M. and Tucker R.J., *Modelling of Gas-Fired Furnaces and Boilers*, McGraw-Hill, 1990.

31. Jeffrey A., *Mathematics for Engineers and Scientists*, Nelson, 1969.

32. Tucker R.J., *Direct exchange areas for calculating radiation transfer in rectangular furnaces*, ASME J.Heat Transfer, August 1986, Vol 108, pp707-710.

33. Siegel R. and Howell J.R., *Thermal Radiation Heat Transfer*, McGraw-Hil, 1972 (Chapters 11 and 18).

34. Howell J.R., *A Catalog of Radiation Configuration Factors*, McGraw Hill 1982.

35. Feingold A., *Radiant-Interchange Configuration Factors Between Various Selected Plane Surfaces*, Proc. R. Soc. London, ser.A., vol. 292, no.1428, pp 51-60, 1966.

36. Sauer H.J., *Configuration Factors for Radiant Energy Interchange with Triangular Areas*, ASHRAE Trans., vol.80, part 2, no. 2322, pp.268-279, 1974.

37. Larsen M.E. and Howell J.R., *Least-squares smoothing of direct exchange areas in zonal analysis*, ASME J.Heat Transfer, Vol 108, Feb.1986, pp239-242.

38. R.L.Johnson, *Numerical Methods - A Software Approach*, John Wiley, 1982.

39. Tucker R.J. and Lorton R., *Mathematical modelling of load recuperative gas-fired furnaces*, Proc.1st UK National Heat Transfer Conference, Leeds, 1984, Institute of Chemical Engineers, Symposium Series No.86, pp1035-1046.

40. Howells R.I.L., Ward J., Probert S.D., *Thermal conductances of contacts at high temperatures*, J.Iron and Steel Institute, March 1973, pp193-196.

41. GEFGN Fiche Technique No.7, Review Generale de Thermique, 13, pp537-542, 1974.

42. Junot H. *et al.*, *Fibrous refractories for industrial furnaces*, Revue Generale de Thermique, 204, Dec 1978, pp935-950.

43. Docherty P. and Tucker R.J., *The influence of wall emissivity on furnace performance*, J.Inst.Energy, March 1986.

44. Ward T. and Webb R.J., *Regenerative burners for use in high temperature furnaces*, Inst.Gas Engineers, Communication 1273, 1985.

45. Lasday S.B., *Nature of ceramic coatings and their benefits in thermal processes*, Industrial Heating, August 1982, p49.

46. Elliston D.G., Gray W.A., Hibberd D.F., Ho T-Y, Williams A., *The effects of surface emissivity on furnace performance*, J.Inst.Energy, Dec 1987, p155.

47. Crank J. and Nicolson P., *A practical method for numerical evaluation of solutions of partial differential equations of the heat conduction type*, Proc.Camb.Phil.Soc., 43, 50-67, (17), 1947.

48. Myers G.E., *Analytical Methods in Conduction Heat Transfer*, McGraw-Hill, 1971.

49. Becker H.B., *A Mathematical Solution for Gas-to-Surface Radiative Exchange Area for a Rectangular Parallelepiped Enclosure Containing a Grey Medium*, ASME J Heat Transfer, Vol 99, May 1977.

Published papers arising from this study

1. Tucker R.J. and Lorton R.L., *Mathematical Modelling of Load-Recuperative Gas-Fired Furnaces*, Proc.1st.U.K.National Heat Transfer Conference, Leeds, 1984.

2. Tucker R.J., *Direct Exchange Areas for Calculating Radiation Heat Transfer in Rectangular Furnaces*, A.S.M.E.Journal of Heat Transfer, 1986.

3. Tucker R.J. and Ward J., *Use of a Monte-Carlo Technique for the Determination of Radiation Exchange Areas in Long Furnace Models*, Proc.8th.International Heat Transfer Conference , San Francisco, 1986.

4. Docherty P. and Tucker R.J., *The Influence of Wall Emissivity on Furnace Performance*, J.Inst.Energy, March 1986.

5. Docherty P. and Tucker R.J., *The Influence of Wall Emissivity on the Thermal Performance of Furnaces*, Proc.International Gas Research Conference, Toronto, 1986

6. Tucker R.J. and Ward J.O., *Application of a Long Furnace Model to a Continuous, Gas-Fired, Steel Reheating Furnace*, Proc. First European Conference on Industrial Furnaces and Boilers, Lisbon, March 1988.